Heidelberg, September 2011

-Star Formation in the COSMOS Field-

A radio view on the build-up of stellar mass over 12 billion years

---

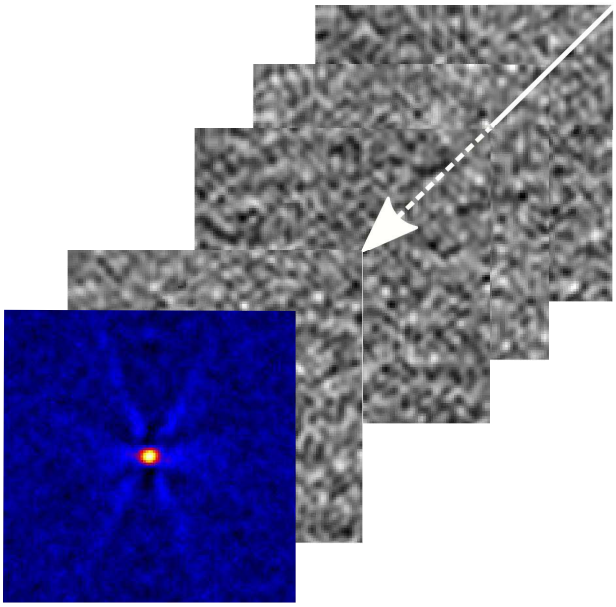

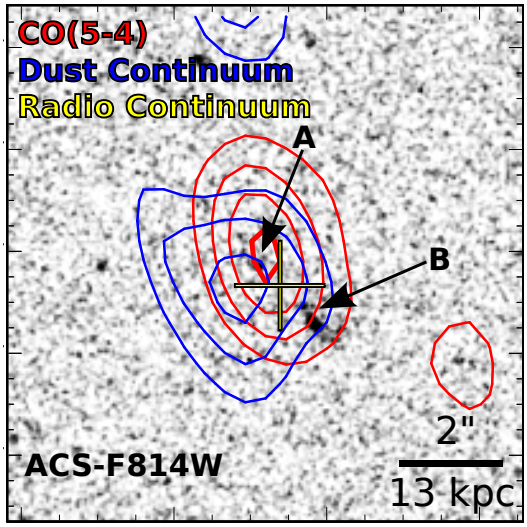

Alexander Karim

Dissertation

submitted to the

Combined Faculties of the Natural Sciences and Mathematics

of the Ruperto-Carola-University of Heidelberg, Germany

for the degree of

Doctor of Natural Sciences

Put forward by

Dipl. Phys. Alexander Karim

born in: Mönchengladbach, Germany

Oral examination: 23rd of November, 2011.

–Star Formation in the COSMOS Field–
A radio view on the build-up of
stellar mass over 12 billion years

Referees:
Prof. Dr. Hans-Walter Rix (MPIA Heidelberg)
Prof. Dr. Ralf Klessen (ITA Heidelberg)

Stellares Massenwachstum über 12 Milliarden Jahre aus Radiosicht

In der vorliegenden Arbeit wird die Evolution von Galaxien im Hinblick auf ihre Fähigkeit Sterne zu bilden untersucht, wobei die vorhandenen umfangreichen Multi-Wellenlängen Datensätze im 2 Quadratgrad grossen COSMOS Feld genutzt werden. Tiefe Beobachtungen im Radiokontinuum mit dem Very Large Array bei einer Frequenz von 1.4 GHz (entprechend einer Wellenlänge von 20 cm) bilden das Fundament einer Analyse der kosmischen Sternentstehungsgeschichte, die nicht durch Staub verfälscht wird. Ein neu entwickelter Bildstapelalgorithmus ermöglicht einen einmalig repräsentativen Einblick in die Evolution der mittleren Sternentstehungsrate bis hin zu Galaxien von geringem (stellaren) Massengehalt seit einer Rotverschiebung von $z \sim 3$ (ca. 2 Milliarden Jahre nach dem Urknall). Die Ergebnisse stimmen gut mit denen anderer Sternentstehungsdiagnostiken überein, welche oftmals von grossen Staubkorrekturen und signifikant schlechterer Statistik geprägt sind. Ein Hauptergebnis dieser Dissertation ist die Identifikation einer konstanten charakteristischen Masse sternbildender Galaxien. Es legt nahe, dass Galaxien von ähnlicher Masse wie unsere Milchstrasse stets die Hauptschauplätze von Sternbildung waren. Oft diskutierte Szenarien, in denen diese charakteristische Masse im Laufe der kosmischen Zeit abnehmen sollte, werden damit widerlegt. In dieser Arbeit wurde zudem erfolgreich nach den extremsten sternbildenden Umgebungen im frühen Universum ($\lesssim 1.5$ Milliarden Jahre nach seiner Entstehung) gesucht. Jene stellen wichtige Objekte zur Eingrenzung der kosmischen Strukturbildung und der durch Staub verdeckten Sternentstehung zu frühesten Zeiten dar. Eine detaillierte Fallstudie enthüllt grosse Mengen an molekularem Gas aber auch einen versteckten aktiven Galaxienkern in einem solchen extrem sternbildenden Objekt. Dieses Ergebnis demonstriert die Vielfalt dieser kosmologisch wichtigen Galaxienpopulation.

A radio view on the build-up of stellar mass over 12 billion years

In this thesis I study the evolution of galaxies with a special focus on their star forming ability by using the extensive multi-wavelength data sets available for the 2 square degree COSMOS deep field. The deep radio continuum data from Very Large Array observations at a frequency of 1.4 GHz (a wavelength of 20 cm) form the basis of my analysis of the cosmic star formation history unaffected by dust obscuration. A newly developed stacking algorithm enabled an unprecedentedly representative view on the evolution of the average star formation rate within galaxies down to low limiting (stellar) masses since a redshift of $z \sim 3$ (i.e. ~ 2 billion years after the Big Bang). My findings are in good agreement with results from different star formation diagnostics that often suffer from large dust corrections or significantly worse statistics. A main result of this thesis is the identification of a constant characteristic mass for star forming galaxies. It implies that galaxies with masses similar to our Milky Way have always been the main sites of star formation. Therefore the often debated 'downsizing scenario' where the characteristic mass decreases with cosmic time is ruled out. In the young universe ($\lesssim 1.5$ billion years of cosmic age) I successfully searched for the most extreme star forming environments. These provide critical constraints on cosmic structure formation and dust enshrouded star formation at early times. A detailed case study not only reveals large amounts of molecular gas but also a powerful hidden active galactic nucleus in one such massive starburst. This finding demonstrates the diversity of this cosmologically important galaxy population.

Die Straße nämlich,
die Hauptstraße des Dorfes,
führte nicht zum Schloßberg,
sie führte nur nahe heran,
dann aber, wie absichtlich,
bog sie ab,
und wenn sie sich auch vom Schloss nicht entfernte,
so kam sie ihm doch auch nicht näher.

Franz Kafka, *D*as Schloß

Contents

List of Figures

List of Tables

1. Introduction

Understanding the evolution of the universe on large scales is a major challenge in astrophysics. Observationally, the analysis is mostly restricted to luminous matter and hence visible structures. Galaxies therefore constitute the key-element in observational cosmology. Understanding their formation but also revealing their evolution over long timescales is an essential prerequisite to insights into cosmic evolution as a whole. Clearly, even the properties of a single galaxy and the physical processes by which its baryonic constituents interact are of vast complexity. Galaxy evolution therefore is a broad research field with a large number of very different foci.

The light emitted by stars is a longstanding key diagnostic in celestial observations and in studying entire galaxies. The process of star formation within galaxies is therefore of fundamental importance. It is the aim of this thesis to investigate the process of how stars formed in galaxies over cosmic time. We will thereby build on previous work that found the essential calibrations needed to measure the rate of star formation in galaxies and concentrate on the evolution of this quantity with respect to other global galaxy properties. Large samples of galaxies are needed hereby to obtain a representative view of the entire galaxy population over a substantial range in cosmic time.

At the earliest cosmic epochs the study of individual objects with exceptionally high star formation rates is vital to understand how cosmic structures form and how the first massive galaxies assemble. This thesis therefore deals with both, large data sets of galaxies as well as those of individual sources that reside at the earliest times and are of special interest in their own right. While we will make use of the emission of galaxies over a wide range of the electromagnetic spectrum a clear focus of this thesis is at radio wavelengths from the sub-millimeter to centimeter regime (i.e. several hundreds of gigahertz down to a few). This Chapter is meant to give the reader an overview of the essential scientific context, the state of this research field and the most important tools needed for galaxy evolution studies. The reader might wish to obtain deeper methodological and physical insights into the topics covered in the scientific Chapters of this thesis: Fundamental laws and their derivation based on the important assumptions that are used in this thesis are therefore presented in Appendix B.

1.1. Panchromatic galaxy evolution in a dark universe

The universe as we find it today is a dark place. A (hypothetic) present day space-traveller would encounter a single particle of baryonic matter[1] – on average – only every fourth cubic meter along his way. Dark matter, on the other hand is claimed to be about five times more abundant but its origin and nature remains elusive. The by far dominant content of the present universe is supposed to be of dark origin in the same sense: While being of

[1] I.e. the kind of matter he is used to from daily life experience.

exceptional importance as the driver for the (nowadays even accelerated) expansion[2] of the universe this so-called dark energy – possibly related to vacuum energy – is not directly observable.

Perhaps humans tend to focus on what is obvious, what they already know and, particularly, what they know to handle. Celestial observations therefore have a longstanding tradition in focussing on electromagnetic waves, in particular visible light. Other parts of the electromagnetic spectrum, however, are of vast and partially growing importance for modern observational astrophysics. Despite their advantages (see below), electromagnetic wave observations are inevitably restricted to phenomena that involve the electromagnetic force. To our knowledge this excludes the possibility to study all sorts of dark phenomena by direct observations of electrodynamically driven emission and it explains why those phenomena are actually referred to as being dark. In other words, only the baryonic world is accessible to direct observations with instruments that are sensitive to electromagnetic emission.

Photons, the carriers of electromagnetic emission, have the advantage that they are comparatively easy to detect because they interact with matter but not as rapidly as massive particles. Hence, they can travel substantial distances without significant disturbance before being caught in any adequately designed man-made device. Photons are abundant in the cosmos. Other particles like neutrinos which are barely massive, might also be abundant but they hardly interact with matter. Moreover, it is the panchromatic view that makes photons exceptional. Over all wavelengths they carry an ubiquitous variety of information, involving high energy processes (often taking place at the smallest scales), emission and absorption features due to the presence of individual atomic or molecular species to all sorts of thermal and non-thermal phenomena. The variety of physical processes that produce photons thereby explains their abundance. Finally, the finite but constant speed of light enables a view into the cosmic past when observing distant objects.[3] Thus, it is the electromagnetic (baryonic) universe that literally sets a colorful contrast against the energetically dominant dark side of the cosmos. Both worlds are solely connected through gravity and the details on how and why constitute perhaps the toughest remaining mystery in our understanding of the cosmos.

Galaxies as well as groups and clusters of galaxies are unique structures to reflect this dichotomy in the most vital way. Any individual galaxy consists of (luminous) baryonic material[4] but is hosted by a halo of dark matter (White and Rees 1978) and it is the grav-

[2] Cosmic expansion can be measured using a variety of diagnostics with the same underlying requirement of measuring cosmological distances to highest possible accuracy. The calibration of observable distance indicators on different distance scales against each other (the so-called distance ladder) therefore is a critical prerequisite. For an excellent summary on recent (combined) results and on the different methods starting from Cepheid stars, type Ia supernovae (acting as 'standard candles' out to substantial distances due to their known luminosity) to global galaxy scaling relations the reader is referred to Freedman et al. (2001).

[3] Strictly speaking, not the full cosmic past can be explored based on photonic observations. The universe was practically opaque at the earliest times when radiation and matter plasma were in thermal equilibrium. After the cosmologically short phase of recombination the universe was predominantly neutral. The mean free path of energetic photons emerging from the relatively rare first population stars as well as quasars was hence short. This resulted in a high opacity at short wavelengths. It is common practice and in the spirit of this introduction to refer to this epoch as the 'dark ages'. As a result, our full panchromatic view is thought to reach out to a few hundred millions of years after the Big Bang (i.e. a redshift of $z \ll 10$).

[4] Note that it is the author's opinion that a galaxy is an object that needs to contain baryonic material. An absolutely clear definition of what a galaxy is does not exist at the time of writing this thesis. For an

itational potential of this dark halo that enables the funneling of baryonic material to the central parts of the galaxy. On adequately large scales dark as well as baryonic matter are distributed homogeneously and isotropically[5] in the present day universe while on smaller scales the baryonic matter follows the filamentary structure of the dark matter distribution (the so-called cosmic web).

This homogeneity and isotropy is the reason why in our modern view of the universe no observer (in particular no observer located on earth or any other point of our solar system) is exceptional or preferred.[6] Asides small initial density fluctuations, meant to be the seeds of the gravitationally driven hierarchical assembly of the cosmic web (White and Rees 1978) and imprinted in the cosmic microwave background as observed today (e.g. Smoot et al. 1992; Spergel et al. 2003, 2007; Komatsu et al. 2009), the universe is also thought to have been homogeneous at earliest times after the Big Bang.

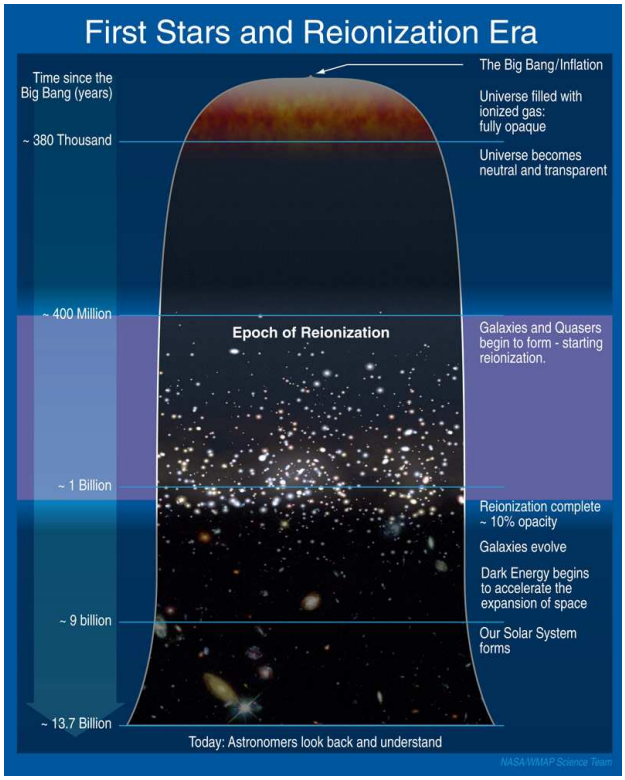

Figure 1.1. – The artist's view on cosmic history with a non-linear time axis. While this sketch has a certain focus on the epoch of reionization it summarizes the essential phases in cosmic evolution that result from the observationally supported dark energy dominated universe and that are mentioned in this Section. Image courtesy of the NASA/WMAP Science Team.

It is of marginal importance for this thesis how these initial inhomogeneities are thought to have been produced, in an early cosmic epoch cosmologists refer to as inflation. The puzzling quest for an observer rather is how the comparatively simple structural agglomerations of luminous matter (manifesting themselves in a well classifiable zoo of local galaxies) emerged from a vastly homogeneous and dense mix of neutral primordial hydrogen gas and dark matter residing in an initially hot environment. The processes that shape the morphologies of galaxies can – in principle – be understood within well established modern standard physical

overview on possible definitions we refer the critical reader to Forbes and Kroupa (2011).

[5] Cosmic isotropy on large scales is an observable since the present day cosmic microwave background, observationally discovered by Penzias and Wilson (1965), is found to be globally isotropic (e.g. Spergel et al. 2003, or the results from any other space-based measurements of the cosmic microwave background).

[6] On cosmic scales gravity clearly is the dominant force so that cosmic evolution and structure formation is described in a purely gravitational framework assuming large scale homogeneity and isotropy. This framework is given by Einstein's theory of general relativity. For a thorough introduction starting from the general relativistic field equations prominent textbooks (e.g. Padmanabhan 1993) should be consulted. The geometrical consequences that are most important for this thesis are presented in Appendix B.1 along with our observationally supported assumptions.

paradigms. Moreover, these processes can be observed in the way described above. As the luminous matter, essentially in form of galaxies, follows the global dark matter distribution, it is the observational study of galaxies over time that is the key diagnostic to understand cosmic evolution regardless if the latter is predominantly driven by dark phenomena. Finally, the study of the intrinsic evolution of the galaxy population enables us to identify cosmic turning points and key epochs in the gravitational interplay of baryonic and dark matter.

A question of fundamental importance for galaxy (and hence cosmic) evolution research is how hydrogen gas is converted into the fundamental building blocks of the luminous universe, namely stars. Stars are of critical important because of various reasons: It is stellar emission that tells us about a galaxy's age and most other galaxy properties of interest. The composition of stellar populations within a galaxy shed light on its history and its past ability to form stars. It is the (young) stars that predominantly illuminate and thereby heat their surrounding medium, producing to a large extent the global cosmic infrared emission observed (see Hauser and Dwek 2001, for a review on the cosmic infrared background).

Studying star formation over time and revealing its globally most important drivers will therefore yield key insights into the evolution of luminous matter on galaxy scales and set tight constraints on the interplay of baryonic and dark matter and the growth of cosmic structure. It is the aim of this thesis to investigate galaxies with respect to their star formation over a broad baseline in cosmic time and, in particular, to connect their star formation activity to their intrinsic global properties. Due to the exceptional role gravity plays in connecting dark and baryonic matter a particular focus of this thesis will be on how star formation activity in galaxies is related to their observationally accessible (i.e. stellar) mass content. The observational results presented in this thesis, based on a multi-wavelength view on an unprecedentedly rich galaxy sample, are the basis for constraining theoretical models of matter and structure formation in the universe. Those models, in turn, constitute the fundament of our current state of knowledge on cosmic evolution in this dark universe.

1.2. Tools to study cosmic evolution: From simulations to multi-wavelength deep field surveys

Surprisingly few parameters are needed to describe – in principle – the cosmos and its evolution and they are constrained by observations of the cosmic microwave background combined with established distance indicators (e.g. Spergel et al. 2003, 2007; Komatsu et al. 2009). These measurements favor a set of parameter values that describes a cold dark matter model with cosmological constant, the so-called concordance or ΛCDM cosmology (see also Appendix B.1). As mentioned above, the total matter budget is clearly dominated by dark matter which is used to theoretically predict structure formation and evolution based on (N-body) computer simulations (e.g. Springel et al. 2005). Those simulations form the basis of our understanding of matter agglomeration and evolution in the universe. They reveal the important physical scales in terms of matter density as a function of cosmic time (see, e.g., Springel et al. 2006, for comprehensive insights into the cosmic large scale structure found in simulations compared to observational results). They also quantify the hierarchical merging of individual dark matter halos, a prerequisite for predicting merger

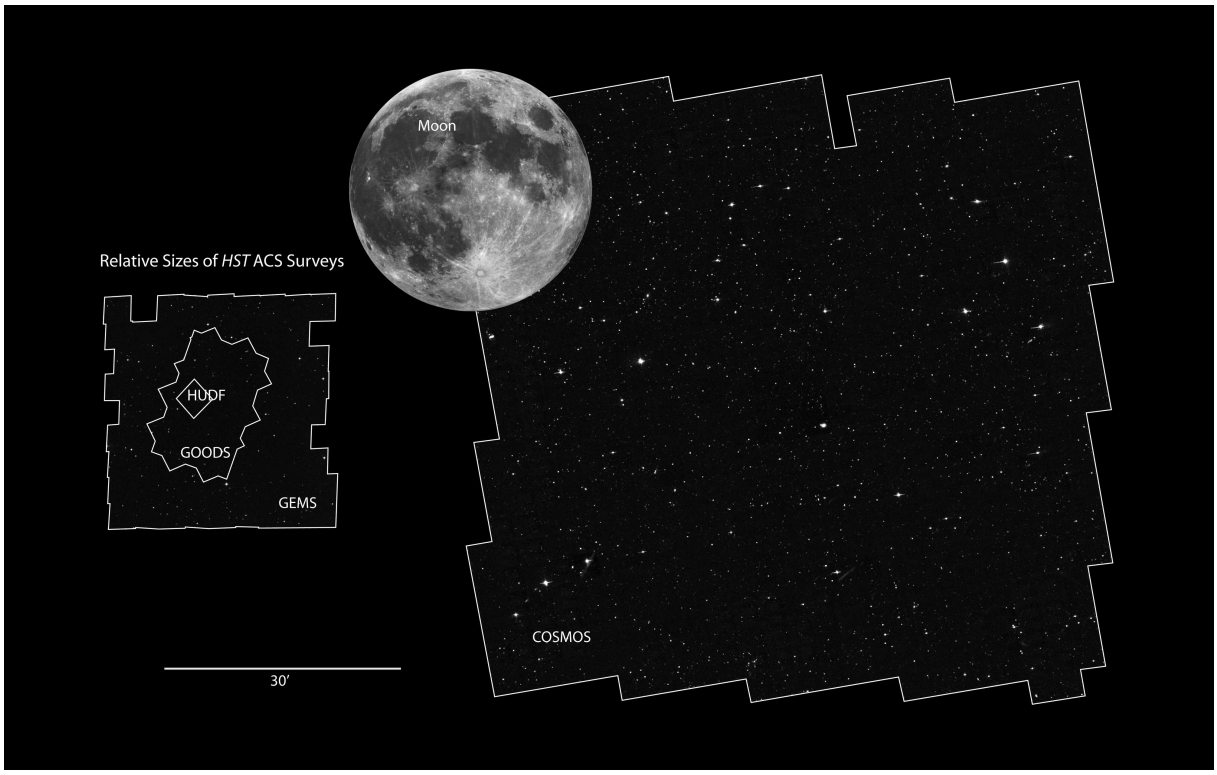

Figure 1.2. – The full COSMOS Hubble Space Telescope (HST) survey, the largest contiguous HST deep field survey ever undertaken. The celestial area covered by the Advanced Camera for Surveys (ACS; Ford et al. 2003) observations corresponds to slightly less than 2 deg^2, the angular area achieved or even exceeded by most other space- and ground-based observing efforts in the COSMOS field. For size comparison other prominent HST deep field surveys (see explanations in the text) are indicated as well as the full moon to scale with respect to the survey fields. Image courtesy of NASA, ESA and Z. Levay (Space Telescope Science Institute).

rates of galaxies.

Two diagnostics are essential to observationally probe the simulated structures. First, the technique of (weak) gravitational lensing can be used to reveal the total matter distribution (see, e.g., Bartelmann and Schneider 2001, for an introduction and review). Second, directly observed galaxies trace the density field of luminous matter which is supposed to follow the walls of the dark cosmic web (e.g. Kovač et al. 2010, for recent results). Both diagnostics require similar observational efforts, namely deep imaging of a (preferably) contiguous and sufficiently large patch of the sky, a so-called deep-field survey.

However, by far not only (large scale) structural studies are of interest but, as outlined above, especially an understanding of the evolution of baryonic matter within the dark matter environment is a key challenge. Semi-analytical modeling techniques are a road to theoretically incorporate interactions other than gravity in N-body simulations and hence make predictions on baryonic galaxy properties (e.g. Kauffmann et al. 1999; Croton et al. 2006; Somerville et al. 2008). Direct hydrodynamical simulations are a valuable alternative to the expense of substantially higher computational effort (e.g. Springel and Hernquist 2003, for an application of hydrodynamic simulations in a research area well connected to this thesis). Generally, it is the vast complexity of physical processes underlying the intrin-

sic growth and evolution of galaxies that limits any theoretical approach and explains the necessity of testing model predictions against real data. Galaxy evolution and in particular the processes through which stellar mass builds up over time therefore clearly needs to be constrained observationally.

1.2.1. Redshift surveys and deep fields

Due to the variety of processes by which the baryonic constituents of a galaxy (mainly stars as well as interstellar gas and dust) interact or evolve, different portions of the electromagnetic spectrum carry different information on the global state of a given galaxy and only the multi-wavelength view reveals the full picture.

Given all aspects discussed so far an observational program to study the evolution of the baryonic universe in broad variety and in detail requires in the ideal case

1. a survey over a large and possibly contiguous celestial area in order to
   a) identify statistically meaningful samples of galaxy populations.
   b) study aspects of large scale structure by weak lensing methods and by the directly observed clustering of individual galaxies.
2. panchromatic observations of this celestial area – hence requiring very different observing instruments in order to
   a) characterize individual galaxies as well as their surrounding intergalactic medium in detail.
   b) determine redshifts and hence distances for large data sets of galaxies[7].
   c) assure a certain lookback potential, implying that galaxies over a wide range of cosmic epochs need to be traced which requires sufficiently high sensitivities at all wavelength[8].

It is therefore apparent that panchromatic deep field surveys for lookback studies demand tremendous observational programs constituting one of the largest collaborative efforts in modern observational astronomy. Various such survey programs have been carried out, especially over the last decade, differing in area, depth as well as in celestial position. Despite the ideal survey design listed above, the variety of different survey programs has a number of advantages. Survey design follows the 'wedding cake' picture in which on top small area ('pencil-beam') observations are carried out to highest depth while very large area and shallow surveys form the bottom. Very large lookback times can be assessed this way even for rather normal galaxies (e.g. in the Hubble Ultra Deep Field (HUDF); Beckwith et al. 2006) but, on the other hand, also a larger local volume can be sampled enabling a virtually complete view of the (near) present day galaxy population (e.g. the Sloan Digital Sky Survey, SDSS; York et al. 2000). Intermediate panchromatic surveys typically aim at a statistically meaningful sampling of the galaxy population residing at various cosmic

[7] The concept of redshift and consequences for light emitted at a given wavelength are discussed in Appendices B.1 and B.2.

[8] Aspects concerning the choice of the depth of survey data are discussed in Chapter 3.1.

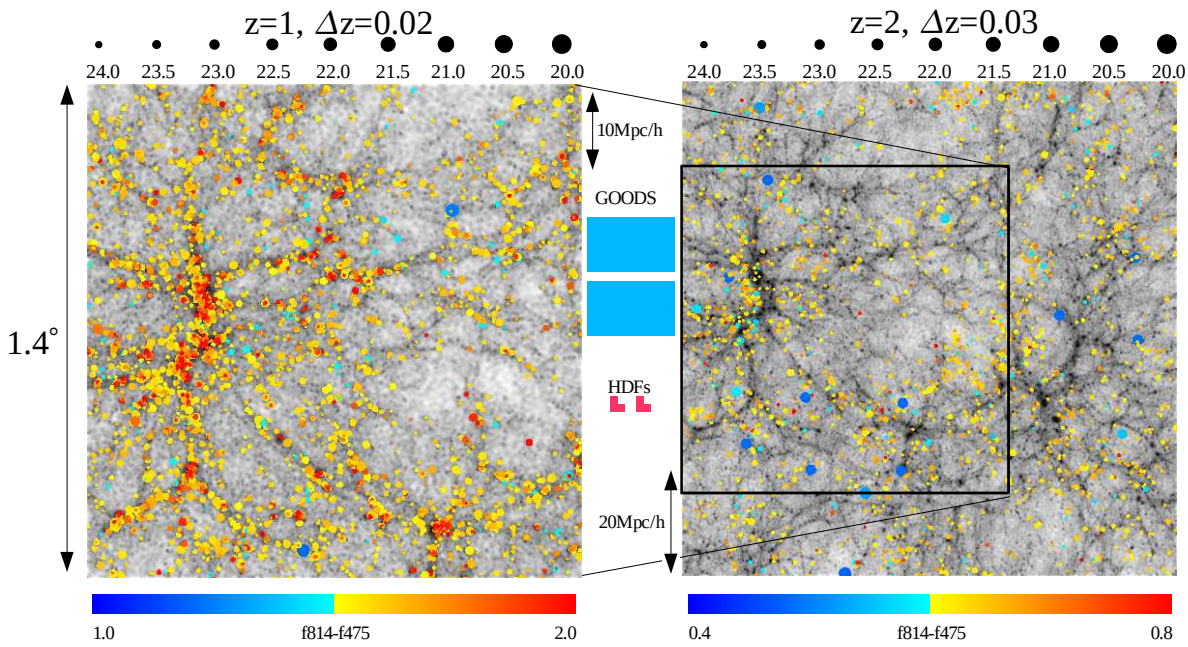

Figure 1.3. – Cosmological simulation results for two redshift slices over a 2 square degree field of view (the angular extent of the COSMOS field). For comparison the areal coverage of other prominent deep field surveys are indicated as well as the physical scale (normalized to the dimensionless Hubble parameter $h = H_0/(100\ \mathrm{km\,s^{-1}\ Mpc^{-1}})$ assumed to be $h = 0.7$ in this thesis). The simulations have been carried out in the ΛCDM framework by the VIRGO CONSORTIUM (Frenk et al. 2000). The background gray scale indicates the simulated dark matter distribution, clearly showing the cosmic web consisting of overdense filaments and underdense voids. Symbols denote individual galaxies that are color-coded according to their colors predicted by semi-analytical models. The simulations motivate the comparatively large observational time investment for surveying a 2 deg^2 field in order to probe the effects of large scale structure and avoid cosmic variance. IMAGE TAKEN FROM Scoville et al. (2007d).

epochs, hence enabling evolutionary studies of global galaxy properties. The most prominent surveys of this kind[9] are based on observations of the survey field with the Hubble Space Telescope (HST) in at least one band and completed by panchromatic observations over a spatially coinciding area of similar size, typically from X-ray to far-infrared and radio wavelengths. The high angular resolution of HST observations allow for morphological studies of galaxies at optical to ultraviolet wavelengths in their rest-frame, thereby revealing interacting or merging galaxy systems.

This thesis is based on the panchromatic data acquired in the COSMOS field (Scoville et al. 2007d) which covers an on-sky area of 2 square degrees (deg^2 in the following). It is the largest of the prominent HST deep field surveys (see Figure 1.2). This size is motivated

[9]To name a few, these are the GEMS (Galaxy Evolution from Morphologies and SEDs) survey (Rix et al. 2004) with ancillary data from the COMBO-17 (Classifying Objects by Medium-Band Observations in 17 filters) survey (Wolf et al. 2001), the Great Observatories Origins Deep Surveys (GOODS; Giavalisco et al. 2004) with survey fields in the northern and southern sky and various ancillary observing programs as well as the Cosmic Evolution Survey (COSMOS; Scoville et al. 2007d). Both, the GOODS-South as well as the GEMS fields partially coincide with the (extended) Chandra Deep Field South ((E)CDFS; Giacconi et al. 2001) and contain the Hubble Ultra Deep Field (HUDF; Beckwith et al. 2006). The GOODS-North field contains the northern Hubble Deep Field (HDF; Williams et al. 1996).

by cosmological simulations that predict the largest structures at a redshift of $z = 1$ to show a comparable angular extent corresponding to about 40 Mpc in comoving units (see Figure 1.3). COSMOS therefore traces cosmic structures at and above this redshift in a representative way, thereby minimizing the effect of cosmic variance[10]. The large number of $\sim 2 \times 10^6$ galaxies residing in the COSMOS field and the vast panchromatic ancillary data[11] enable an unprecedented rich view of galaxy evolution at high statistical accuracy.

1.3. The global population of galaxies over time

Redshift surveys provide the opportunity to investigate changes of the galaxy population over time in a statistical sense. Since we cannot directly follow the individual evolutionary paths of galaxies we aim at selecting galaxies at different cosmic times based on the same parameters and compare them with respect to other properties of interest.

Since galaxies are a diverse class of objects, various parameters, such as their morphology, their color or luminosity qualify for this selection. It is important to notice, however, that broadly speaking the classification of galaxies in the local universe turns out to be remarkably simple, placing individual objects either onto a relatively tight red sequence of mostly massive sources or a somewhat broader distribution (the so-called blue cloud) in the plane spanned by visual broad-band color and luminosity or stellar mass content (e.g. Baldry et al. 2004). Interestingly, the perhaps most intuitive feature of galaxies – namely their appearance (also known as morphology) – is also related to this color-magnitude distribution (e.g. Strateva et al. 2001). Red sequence objects are predominantly elliptically shaped, i.e. of earlier Hubble types, while those that reside in the blue cloud cover later types observed as spiral galaxies. Spiral galaxies are often also referred to as disks due to their flat profiles when seen edge-on. Physically, they are rotationally supported systems while elliptical galaxies are pressure supported.

Clearly, there are intermediate objects and complex phenomena but for the moment they shall be of minor interest for our global picture. For this thesis two observations are of highest importance: First, the red sequence objects are generally dominated by older stellar populations. They show little ongoing star formation activity and must hence have formed their substantial amount of stars at earlier times. Star forming galaxies, in turn, are found among the bluer objects. Indeed, galaxies show specific colors because their broad-band spectral energy distributions (SEDs) are dictated by the composition of their dominant stellar populations. Stellar population synthesis modeling (e.g. Bruzual and Charlot 2003) is hence a road to assemble the spectral footprints of galaxies allowing even for rough morphological information solely based on photometric observations.

Interestingly (and this is the second point of interest for this work), even at much higher redshifts (e.g. Bell et al. 2004; Kriek et al. 2006; Williams et al. 2009; Marchesini et al. 2010) and hence earlier cosmic times the apparent color bimodality is observed to persist, raising questions of how the populations of blue and red galaxies are connected and whether there

[10] Cosmic variance leads to different number counts and hence results for, e.g., luminosity functions of galaxies for different survey fields that underscore the scales needed to trace overdensities and voids in a representative fashion.

[11] For an overview on the observing programs see Chapter 4.2. Table 1 in Ilbert et al. (2009) lists the sensitivities achieved in the ultraviolet to mid-infrared bands.

are evolutionary paths from one family to the other.[12] Since we already pointed out that red elliptical galaxies are found to be massive[13] the most appealing evolutionary direction is from the star forming blue cloud to the quiescent red sequence. It is hence vital to compare the number densities of color-selected galaxies as a function of their luminosity or total stellar mass at different epochs in order to compare their differential evolution as well as the evolution of the integrated luminosity or mass density.[14] These are the diagnostics that advanced our constantly growing understanding of galaxy formation and evolution. Different evolutionary channels from the blue cloud to the red sequence have been proposed from evolutionary luminosity function studies, all involving a shutdown of star formation (known as star formation quenching) at some point (e.g. Faber et al. 2007). Empirically, Peng et al. (2010) recently suggested alternative pathways to when and under which conditions quenching occurs. We will cover these findings at a later stage in this thesis when contextually appropriate. It should be noted that the question of what physical processes cause galaxies to quench their star formation has not been definitely answered to-date.

In addition to drawing inferences from the number density distributions of galaxies it is the direct observation of the mass build-up through recent star formation at different times which is of highest priority to constrain the evolution of galaxies. This is the subject to be covered in this thesis. In the following we will first discuss the essential background motivating the immediate goals of this thesis before we proceed to a brief outline of how we actually measure star formation rates.

Clearly, there is much more to know about the population of galaxies, their properties and their shapes etc. which cannot be covered in this introduction. For a profound and comprehensive overview on galaxies and their evolution we refer the reader therefore to the literature (in particular to the comprehensive textbook by Mo et al. 2010).

1.3.1. The growth of stellar mass through star formation

From the observational measurement of star formation rates (SFRs) in galaxies at various cosmic epochs over the past 15 years the picture has emerged that the global star formation activity in the universe is a rapidly evolving quantity. Lilly et al. (1996) as well as Madau et al. (1996) first presented evolutionary measurements of the total and comoving volume-normalized SFR, a quantity referred to as an SFR density (SFRD) in the following.[15] They

[12] As one caveat to the simple color division in blue and red sources it should not be forgotten that galaxies can also be reddened by dust extinction. Potentially, even those systems with substantial star formation activity are covered by larger amounts of dust. The color-based selection of galaxies hence needs to be efficient in selecting intrinsically red objects because of older stellar populations. This can be achieved by color-color techniques (e.g. Williams et al. 2009) or by selection via intrinsic colors inferred from fitting stellar population synthesis models to the observed SED under the assumption of a reddening law (e.g. as used by Ilbert et al. 2010, for the selection major parts of this thesis are based on).

[13] The stellar mass content of galaxies is measured from the stellar mass-to-light ratio. In practice, this can either be approximately determined from broad-band colors (Bell and de Jong 2001) or, as done in this thesis, from stellar population modeling if a simple analytic form for the star formation history of the galaxy as well as a dust extinction law (e.g. Calzetti et al. 1994, 2000; Charlot and Fall 2000) is assumed. Either way the stellar mass estimates depend on the explicit assumption of the initial mass distribution function of stars (the stellar IMF).

[14] More information on luminosity and mass functions – in particular with respect to their visualization – is found in Appendix B.3.

[15] see Appendix B.1 for a definition and explanation on comoving distance measures.

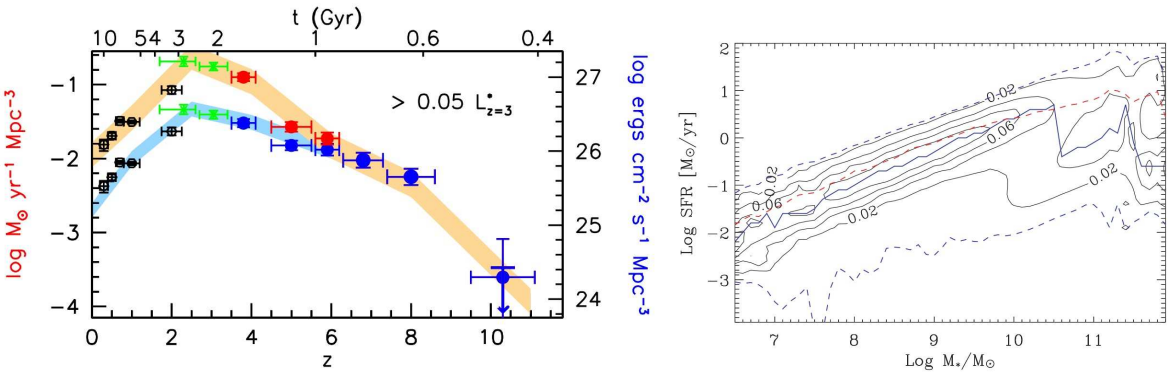

Figure 1.4. – The cosmic star formation history (CSFH) and the relation between star formation rate and stellar mass in the local universe. *Left:* A recent measurement of the evolution of the comoving SFR density (SFRD) over time which is based on ultraviolet emission. The literature data span the redshift ranges $z < 2$ (black open squares; Schiminovich et al. 2005), $2 \lesssim z \lesssim 3$ (green crosses; Reddy and Steidel 2009) as well as $3 \lesssim z \lesssim 10$ (filled circles; Bouwens et al. 2009, 2011b,a). The upper set of points with underlying orange shaded region are the data after dust extinction corrections have been applied while the shaded blue region shows the uncorrected trends. The steep decline of the SFRD since $z \sim 1$ is observationally well established. The CSFH at earlier epochs, in particular the continuous increase since the highest redshifts is less well constrained to-date. Particularly, the minor importance of dust-obscured star formation shown here is under debate. *Right:* The tight relation between SFR and stellar mass as inferred from emission line diagnostics for galaxies without contribution of an active galactic nucleus that reside in the local universe. The red dashed curve depicts the average trend along with likelihood contours. The data shown are from the Sloan Digital Sky Survey. IMAGES TAKEN FROM Bouwens et al. (2011b) AND Brinchmann et al. (2004).

and a constantly growing number of other authors (see Hopkins and Beacom 2006, for a compilation) concluded that the SFRD undergoes a rapid decline over the last ~ 8 billion years (corresponding to a redshift of $z \sim 1$). The SFRD at even earlier cosmic times is less well established. The currently preferred scenario from the observers' side is that the cosmic star formation activity reaches a maximum around $1 < z < 3$ and steeply declines to higher redshifts (see Figure 1.4).

Most evidence for this scenario comes from SFRD measurements that are based on ultraviolet (UV) emission. To be precise, the UV luminosity function has been constrained at various epochs even out to $z \sim 10$ (see in particular Bouwens et al. 2011b, for recent results) and the resulting, integrated UV luminosity densities has been converted into SFRDs at the corresponding cosmic times. In the presence of interstellar dust surrounding the emitting stars the UV light is absorbed (see Appendix B.5) so that empirically derived dust extinction corrections have to be applied. These corrections are found to be substantial as shown in Figure 1.4 at redshifts of $z \ll 4$ highlighting the critical need for alternative dust-unbiased measurements of the SFRD at these epochs.

Dust extinction can be inferred from the UV continuum properties of galaxies (e.g. Charlot and Fall 2000). At the high redshifts probed by, e.g., Bouwens et al. (2011b) the observed near-infrared data trace the rest-frame UV continuum of the objects. Based on such diagnostics they infer that star forming galaxies at the highest redshifts observed to-date are essentially dust-free. Hence they conclude that the uncorrected UV emission of such distant galaxies provides an unbiased measure of the SFRD in the early universe. Already

at $z \sim 4$ dust-obscured star formation appears to cease its importance in this scenario. This stark contrast between the resulting dust correction factors applied to the global cosmic star formation activity from early to late times raises numerous questions that are of high relevance for our understanding of the total stellar mass growth in the universe and hence galaxy evolution as a whole. It is hence clear that sensitive and dust-unbiased star formation estimates at high redshifts are critical (see also below).

With growing knowledge about the global cosmic star formation history (CSFH) questions on the main drivers of its rapid evolution have been and are still raised. One insightful finding was revealed by comparing SFRs of galaxies that are differently massive. In the local universe it was found that star forming sources form a tight sequence in the SFR/stellar mass plane (see Figure 1.4; and e.g. Brinchmann et al. 2004) while quiescent galaxy – unsurprisingly – fall significantly below this trend at the high-mass end. Also at higher redshift (see, e.g., Elbaz et al. 2007, for results at $z \sim 1$) evidence for the existence of such a 'main sequence' of star forming galaxies exists while average SFRs follow the global trend and substantially increase as we go back in time. These results are surprising in that the mass that is contained in stars should intuitively have little effect on the stellar mass growth. As Dutton et al. (2010) and Noeske et al. (2007a) argue it is the net rate of cold gas accretion onto the dark matter halo which might shape the SFR-sequence at any epoch since this quantity shows a similar evolution as the SFR-sequence. Hence in the SFR-sequence the total stellar mass might act as a proxy for dark matter halo mass as the one rises monotonically with respect to the other (e.g. Moster et al. 2010). Hence secular processes are supposed to be responsible for supplying galaxies with molecular gas through the gravitational interaction of baryonic gas and dark matter, providing a vital example for the interplay between the baryonic and the dark universe.

It is, however, critical to obtain detailed observational insights into the evolutionary properties of this SFR-sequence. It has been argued that star formation in galaxies is supposed to 'downsize' (e.g. Cowie et al. 1996) which has been interpreted as a shift of the main contribution to the global star formation activity from more to less massive galaxies over time. The question if this is indeed the case and how it would affect the shape of the SFR-sequence at different epochs is of high relevance.

Particularly SFR measurements from dust-unaffected tracers are needed as well as a statistically representative galaxy sample even at comparatively low stellar masses out to substantial redshifts. It is an important motivation for this thesis to accurately measure the average evolutionary trends of differently massive galaxies and to determine the characteristic mass scales of galaxies in which star formation predominantly occurs.

1.3.2. The role of starbursts in galaxy evolution and observational cosmology

The merging of galaxies is an alternative channel for the gas-supply of galaxies. Large amounts of gas accumulate in galaxy interactions of similarly massive galaxies (so-called major mergers) which typically leads to a starburst, i.e. a significant excess in star formation activity compared to normal star forming galaxies. In turn, starbursts are supposed to be predominantly driven by galaxy interactions. It is established that local starbursts, sources also known as (ultra-)luminous infrared galaxies ((U)LIRGs) due to their high luminosities of $> 10^{11}$ $(> 10^{12})$ $L_{\odot}$ at infrared wavelengths, are interacting systems (e.g.

Sanders et al. 1988)[16]. Also infrared-luminous starbursts at higher redshifts, so-called sub-millimeter galaxies (SMGs) have been found to be mostly driven by major galaxy interactions (e.g. Engel et al. 2010).

This poses the question whether (merger-driven) starburst activity contributes a significant fraction to the global star formation rate at different cosmic epochs. As mentioned before, the existence of a tight star forming main sequence of galaxies favors secular trends in which galaxies accrete their gas predominantly in a less stochastic way. A number of recent studies revealed indeed that major mergers are of minor importance for the global star formation activity at redshifts of $z < 1$ (e.g. Robaina et al. 2009). Other recent studies (e.g. Elbaz et al. 2011; Rodighiero et al. 2011; Williams et al. 2011), using different diagnostics, also support a picture in which starbursts might contribute at most ~ 10 % to the total cosmic star formation at any epoch out to $z \sim 2$.

It might appear tempting to extrapolate the minor importance of extreme star formation out to higher redshifts. As we go back in cosmic time it is, however, reasonable to challenge this paradigm. In a hierarchically forming and expanding universe that was substantially denser at early epochs the seeds of the largest present-day overdensities are thought to have been sown early on and should, in principle, be observable already at high redshift. It is likely to find sites of extreme star formation in these denser environments (called proto-clusters) where the starburst activity might be powered by gas-rich (major) galaxy mergers. In turn, finding extreme starbursts at $z > 4$ is a road to reveal overdense regions within only 1.5 Gyr after the Big Bang. Cosmological simulations predict the existence of these proto-clusters at high redshifts, a paradigm that needs to be tested against observations. This is why the search for massive starbursts at very high redshifts is critical to constrain models of cosmological structure formation.

In the COSMOS field one proto-cluster at $z = 5.3$ could be recently revealed around a massive starburst thereby constraining its baryonic mass content (Figure, 1.5; Capak et al. 2011). Also in the GOODS-North field one proto-cluster structure at $z \sim 4$ could be identified after the serendipitous carbon monoxide (CO) detection of three extreme starbursts (Daddi et al. 2009b,a).

The search for extreme starbursts at such high redshifts is also motivated by the observation of massive and no longer star forming galaxies lying on the red sequence even beyond $z \sim 2$ (e.g. Kriek et al. 2006, 2008a; Williams et al. 2009; Marchesini et al. 2010). Given the comparatively short formation timescales at such high redshifts, it is likely that a substantial fraction of their mass has been rapidly build up (e.g. Kriek et al. 2008b). Massive starbursts at even higher redshifts, triggered by major mergers and thereby shaping their elliptical morphologies are hence likely the progenitors of the earliest massive quiescent galaxies observed to-date. It is, however, an open question if the number densities of both populations match (e.g. Coppin et al. 2009).

It is furthermore important to constrain the number density of $z > 4$ massive starbursts since their individually high SFRs of typically several hundreds of solar masses per year (e.g. Michałowski et al. 2010) might give rise to a significant contribution to the global

[16] The same study suggests also a link between mergers and nuclear activity. This scenario has recently been challenged by Cisternas et al. (2011) who found no significant statistical enhancement in black hole growth through major mergers at redshifts $0.3 < z < 1$. In parts of this thesis we will be dealing with active galactic nuclei (AGN). We refer to the excellent reviews by Antonucci (1993) and Urry and Padovani (1995) for essential background information on different types of AGN, their unification and their properties.

SFRD at these early times. Given their large dust reservoirs (e.g. Michałowski et al. 2010) there might hence be more dust-obscured star formation activity in the early universe than currently assumed (see Figure 1.4). It should be noted that it is another challenge to explain how the large amounts of interstellar dust observed in these extreme starbursts have been produced at such early times (e.g. Michałowski et al. 2010; Dwek et al. 2011).

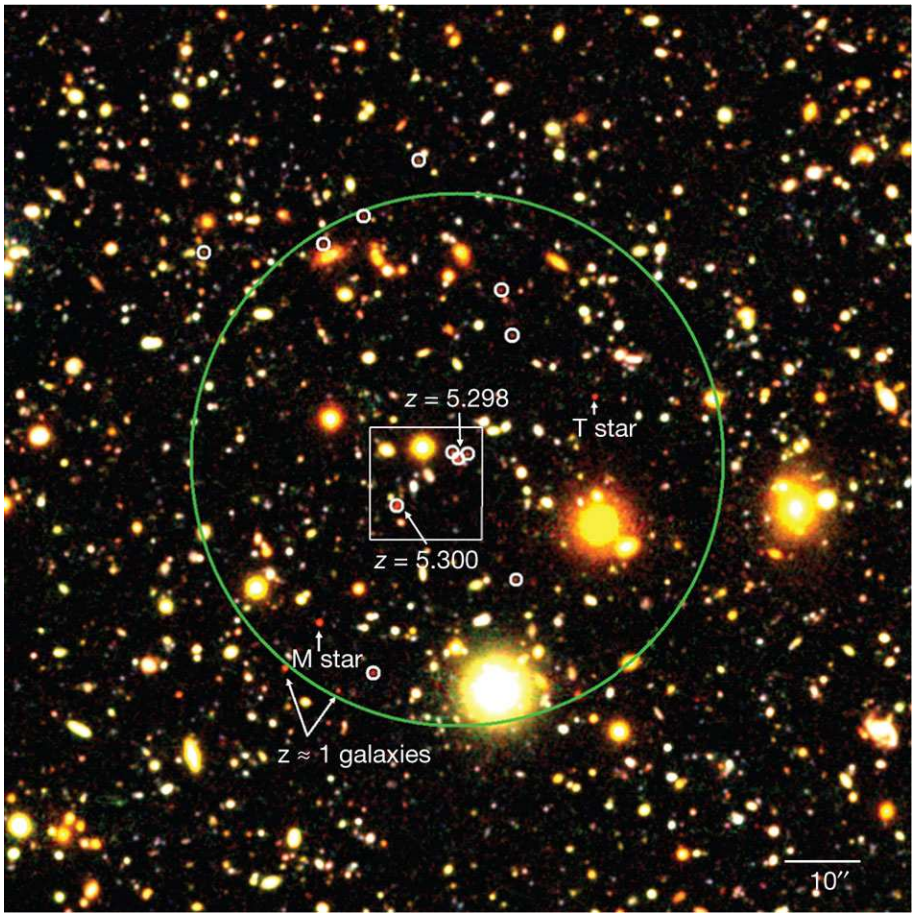

Figure 1.5. – Optical composite image of a confirmed high-redshift proto-cluster core that hosts an extreme starburst. This area corresponds to a $2' \times 2'$ region around the (sub-)millimeter source AzTEC-3 (its optical counterpart is labeled with $z = 5.3$), a massive starburst that resides at a redshift of $z = 5.3$ in the COSMOS field. Broad-band dropout sources likely residing at a similar redshift are denoted by white circles. A 2 Mpc comoving radius is indicated with a green circle. Arrows point to foreground stars and to objects with spectroscopic redshifts (labeled by their redshift values) including confirmed proto-cluster members as well as red objects at much lower z. This example shows that massive starbursts at $z > 4$ qualify to reveal mass-overdensities at early times thereby paving the way to observationally map cosmic structure formation. Image taken from Capak et al. (2011).

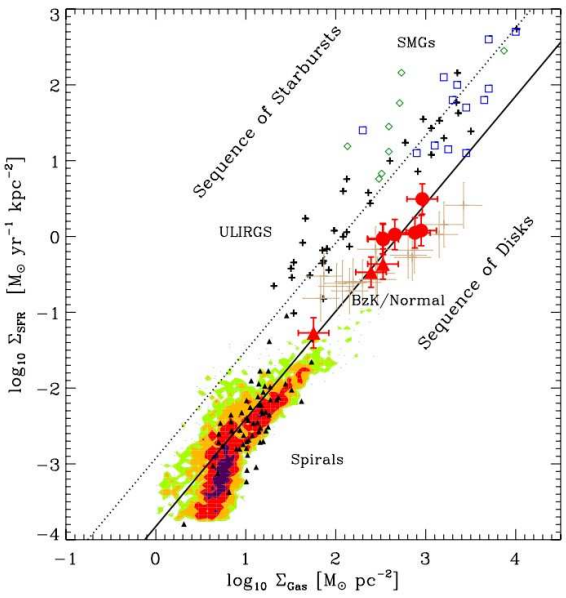

Figure 1.6 – Modern view on the relation of the surface densities of molecular gas and star formation rate in galaxies. Shown are regions of local spiral galaxies (shaded; Bigiel et al. 2008), local spiral (crosses) and ultra-luminous infrared galaxies (ULIRGs; filled triangles; Kennicutt 1998b), normal star forming galaxies out to a redshift of $z \sim 1.5$ (Daddi et al. 2010b; Tacconi et al. 2010; red filled circles/triangles, brown crosses) as well as distant massive starbursts (sub-millimeter galaxies, SMGs; light green; Bouché et al. 2007; Bothwell et al. 2010). The current data suggest that throughout cosmic time there is a bimodality in the star formation law between starbursts and average star forming systems resembling the properties of local ULIRGs and local disk galaxies respectively. IMAGE TAKEN FROM Daddi et al. (2010b).

1.4. Essentials for this work: star formation on galaxy scales and its measurement at long wavelengths

How individual stars form is a matter of vast complexity and far from being fully understood today. In short, (hot) baryonic gas around a galaxy is supposed to cool on cosmologically short timescales, to reach the center of the galaxy, to subsequently become denser and cooler and to finally collapse resulting in clouds of dense and cold gas. It is an observationally supported and generally accepted scenario that stars form in dense clouds of molecular gas as there is a tight empirical correlation between the surface density of molecular gas and that of star formation (Figure 1.7; see e.g. Schmidt 1959; Kennicutt 1998b; Leroy et al. 2008). Hence, molecular gas is supposed to be the material out of which stars form.[17] This relation is typically described by a power-law as already suggested in the seminal work by Schmidt (1959). Observationally supported values for its power-law index are found between $N \sim 1$ (Bigiel et al. 2008) and $N \sim 1.4$ (Kennicutt 1998b). Theoretical work discussing different possible underlying physical reasons for this empirical star formation law is presented by Krumholz et al. (2009) and Dib (2011). The ratio of gas surface density to star formation rate surface density is commonly used as a gas consumption timescale.

It has been suggested (see Daddi et al. 2010b; Genzel et al. 2010, for recent results) that this star formation law comes in two flavors (see Figure 1.7). Star forming galaxies show an apparent bimodality in the observed star formation surface density versus neutral gas surface density suggesting that most galaxies (i.e. the constituents of the SFR-sequence) have typical gas depletion timescales of a few billion years that are significantly larger than those determined for starbursts. It is speculated that galaxy major mergers are the main cause for this observed bimodality as during the merging process the available gas is very efficiently compressed and subsequently transformed into stars explaining the higher star

[17] Note that recent simulations (Glover and Clark 2011) challenged this logically appearing and commonly accepted paradigm in that they showed that essentially atomic gas suffices to form stars. They point out that only the physical conditions found in dense molecular clouds – in particular a sufficient shielding from the interstellar radiation field – might be required for star formation.

formation efficiency observed in starbursts (e.g. Bournaud et al. 2010). This bimodality is supposed to persist out to high redshift while especially for average star forming objects currently only limited data exist at $z > 1$.[18]

Since this thesis is not directly concerned with the theoretical framework behind star formation numerous question remain open in this introduction. We therefore refer the interested reader to the excellent reviews by Mac Low and Klessen (2004) and McKee and Ostriker (2007).

1.4.1. Measuring star formation rates of galaxies from their (far-)infrared emission

In this work we measure SFRs from far-IR and radio continuum emission. Both have advantages compared to other prominent SFR tracers (see, e.g., Kennicutt 1998a, for a review on SFR tracers). Both are unaffected by the effects of dust obscuration while the far-IR emission even demands the presence of interstellar dust. Provided there is dust in a galaxy especially the ultraviolet (UV) light of massive (young) stars is absorbed and thermally re-emitted at far-infrared (far-IR) wavelengths. Therefore the far-IR emission alone is a good tracer of the star formation rate provided that all UV photons are thermally processed.

As Kennicutt (1998a) points out, far-IR emission is best tracing the SFR in dense (local) starbursts which offer the ideal conditions for an almost calorimetric measurement due to young stars dominating the radiation field and the presence of large amounts of (opaque) dust. While it is not clear a priori that extreme starbursts at high redshift provide the same dense interstellar environments as their local cousins the presence of large dust reservoirs and predominantly young stellar populations is a valid working assumption. We therefore use the integrated far-IR luminosity for our best estimate of the SFR in an extreme starburst at $z = 4.622$.[19]

Essentially no tracer provides a perfect measure of the SFR under all possible conditions. Also the far-IR emission ceases its near-perfection if environments much different from those found in starbursts are concerned. If the dust is not entirely optically thick or if it is also significantly heated by the visible light emitted by older stars the far-IR emission becomes probably a less reliable SFR tracer (see, e.g., Kennicutt 1998a, and references therein for a discussion).

No matter which SFR tracer is used the calibration from the observed luminosity in a given spectral range is converted into an SFR with the help of stellar population synthesis models. This furthermore requires an assumption of the initial mass function (IMF) of stars. For the influence of different choices of IMFs on various SFR tracers in an extragalactic context we refer the reader to Wilkins et al. (2008).

1.4.2. The (far-)IR/radio correlation in star forming galaxies

The origin of radio emission from star forming galaxies will be outlined in more detail at a later stage (see Section 4.1). For a general profound and comprehensive introduction into radio emission from galaxies we refer the reader to the excellent review by Condon (1992).

[18] Information on how the molecular gas content in (distant) galaxies is measured is provided in Appendix. B.4.
[19] The measurement of IR luminosities from dust emission at far-IR wavelengths is outlined in Appendix B.5.

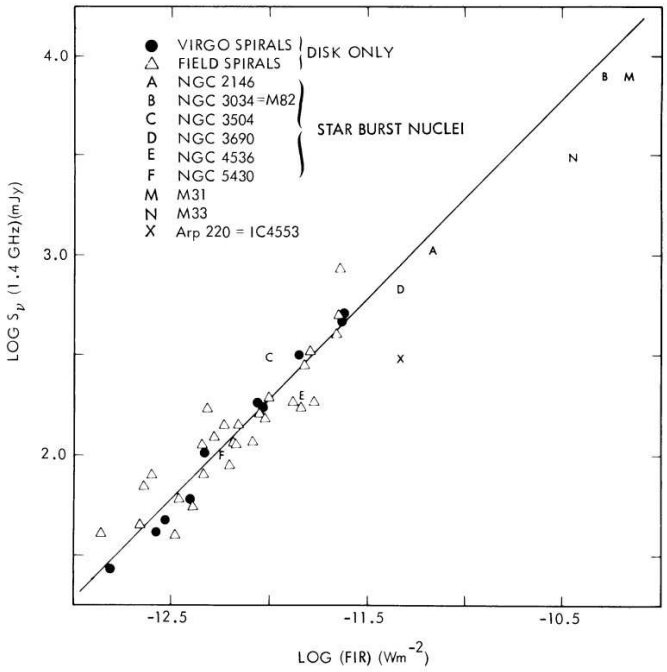

Figure 1.7 – Early results on the relation between (far-)infrared and radio continuum emission in nearby galaxies with extended emission detected at 1.4 GHz that reside either in the Virgo cluster (circles) or the field (triangles). Nearby starbursts are shown as well and follow the general trend. IMAGE TAKEN FROM Helou et al. (1985).

Here we want to recap the underlying observational paradigms allowing for estimates of SFRs from radio continuum emission.

Radio continuum emission at frequencies up to a few gigahertz is predominantly of non-thermal nature (e.g. Condon 1992). Its spectrum can be well described by a power-law $F_\nu \propto \nu^{\alpha_{\rm rc}}$. In case of an ensemble of relativistic electrons spiraling in a static and homogeneous magnetic field such a power-law synchrotron spectrum is produced if the electron energy distribution also follows a power-law. Thermal free-free emission from HII regions contributes to the radio emission but clearly underscores the non-thermal emission in the low GHz regime.

Surprisingly, it is empirically well established that the radio emission (not solely) in star forming galaxies is tightly correlated with their thermal emission at far-IR wavelengths (e.g. Helou et al. 1985; Condon 1992; Yun et al. 2001; Bell 2003a). Physically, this relation raises a number of questions that largely remain open to-date. Most important for our work is that this relation leads to an alternative radio-based way of estimating SFRs based on well-known calibrations and that this seems to hold true grossly over the redshift range probed in this thesis (e.g. Sargent et al. 2010a,b).

The intrinsic dispersion of this relation in the local universe is very low (< 0.3 dex) and places it among the tightest relations in observational astrophysics. The relations holds over several orders of magnitude in luminosity, hence being valid also over a wide range of SFRs.

It is suggestive to infer that this tight relation points to a common origin of both IR and radio emission within galaxies while it is an ongoing effort to constrain the physical origin of this relation and to trace the regimes where it might break down. Insightful suggestions have been made to explain its physical drivers by a calorimeter model (e.g. Lisenfeld et al. 1996; Voelk 1989) or by postulating a conspiracy (Bell 2003a). The far-IR/radio relation has been challenged on sub-kpc scales in nearby spiral galaxies (e.g. Dumas et al. 2011) which revealed that it is not uniform across the disk and deviated from a linear behavior in

Figure 1.8. – The IRAM 30 m telescope located near the city of Granada on Pico Veleta in the Spanish Sierra Nevada. The left picture shows the 30 m dish during a pooled observing run in the evening hours in November 2008 during which sources discussed by Martínez-Sansigre et al. (2009) were observed. The right picture was taken at the Mirador San Nicolás in the old Arabic quarter of Granada facing towards Pico Veleta. The trained eye will recognize the telescope as a tiny white point in the foreground of the cloud's shadow (at the lower central part of the shadow in the image center). If the picture extended more to the right, the Alhambra would be seen.

certain regions. A detailed model is provided by Lacki et al. (2010) and useful implications for higher redshift applications are discussed by Lacki and Thompson (2010).

The far-IR/radio correlation has typically been calibrated based on 1.4 GHz radio continuum data. In order to apply the calibrations that have been established in the local universe (e.g. Condon 1992; Yun et al. 2001; Bell 2003a) at higher redshifts one needs to scale the radio-continuum luminosity appropriately under the assumption of a spectral index value for the radio continuum. How this should be done for distant objects is derived in Appendix B.2.

1.5. Observatories and instruments

While data from multiple observing instruments are used in this thesis, three facilities are of special importance for our radio-focussed work.

The *Very Large Array* (VLA; Thompson et al. 1980, for an early review), operated by the National Radio Astronomy Observatory (NRAO) is a Y-shaped radio interferometer located in New Mexico/USA near the town of Magdalena. Its 27 antennas (each dish has a diameter of 25 m) can be arranged in four different configurations from the most extended (A-array) to the most compact one (D-array) thereby covering baselines between more than 35 km and 35 m. Here we use L-band continuum data at an observed frequency of 1.4 GHz (an effective wavelength of 20 cm) obtained in A and C configuration observed in the VLA-COSMOS project (Schinnerer et al. 2007, 2010).

The *30 m telescope* (Mauersberger 2003, for an overview) is located on the Pico Veleta mountain in the Spanish Sierra Nevada at an altitude of 2850 m (see Figure 1.8). It is

operated by the Instituto de Radioastronomía Milimétrica (IRAM).[20] Until recently it was equipped with the second generation MAx-Planck Millimeter BOlometer camera (MAMBO-II; Kreysa et al. 1998), a 117 pixels array observing at a frequency of 250 GHz (an effective wavelength of 1.2 mm). Data from this camera are used in this thesis. The same holds true for the privately funded 128 element Goddard-IRAM Superconducting 2-Millimeter Observer (GISMO; Staguhn et al. 2008) that is currently installed at the 30 m telescope. It features next generation superconducting Transition Edge Sensor (TES) based bolometer technology and observes at a frequency of 150 GHz (an effective wavelength of 2 mm).

The Plateau de Bure Interferometer (PdBI; Guilloteau et al. 1992) is also operated by the IRAM consortium. This interferometer array consists of six 15 m antennas and is located in the French Hautes-Alpes to the south of the city of Grenoble on the Plateau de Bure at an elevation of 2550 m. It can be arranged in four different configurations (A, B, C, D) with baselines up to 760 m in the most extended A configuration. In this thesis we present emission line and continuum data observed in the 3 mm band using the B, C and D configurations.

[20] IRAM is sponsored by the Spanish Instituto Geográfico Nacional, the German Max-Planck-Gesellschaft and the French Centre National de la Recherche Scientifique (CNRS). Its headquarters are located in Saint-Martin-d'Hères suburb of Grenoble/France. The French, English and German translations of the institute's name are chosen to match the IRAM acronym.

2. Overview

In the following this thesis is structured as follows. Each Chapter starts with a context outline which is followed by a detailed introduction into the technical or scientific matter.

Chapter 3 provides methodological background. The image stacking technique that is extensively used in this work is introduced (Sections 3.1 and 3.2) and its implementation into a newly developed software during this thesis is detailed (Section 3.3). The ongoing development (Section 3.3.3) and scientific applications (also those not further presented in this thesis; Section 3.3.4) of this software are discussed. Statistical background is provided in the Appendices A.1 and A.2.

Chapter 4 describes the stellar-mass based selection and evaluation of an extensive panchromatic galaxy sample (Section 4.2) that is used as input to the imaging stacking routine in order to perform stacks at radio continuum wavelengths (Section 4.3) in bins of stellar mass and photometric redshift. A newly developed method to assess the statistical representativeness of these sub-samples is described in Appendix A.3. The resulting radio-based evolution of the average (specific) star formation rate of galaxies at redshifts $0.2 < z < 3$ as a function of stellar mass is discussed and compared to literature work from a variety of star formation rate tracers in Section 4.4. The influence of sample selection parameters on the results for star forming sources is discussed in Section 4.5.

Chapter 5 builds on the results presented in Chapter 4 and literature measurements of the evolution of the stellar mass distribution function for star forming galaxies. These ingredients enable the study of the global evolution of the cosmic star formation rate with respect to the relative importance of differently massive galaxies (Section 5.2). The results are compared to literature measurements that use multiple star formation diagnostics (Section 5.3). Appendix B.3 provides mathematical background on the visualization of luminosity functions and related quantities.

Chapter 6 takes the step from average levels of star formation to highly elevated ones and bridges the gap to even earlier cosmic times. To this end a single extreme starburst at $z = 4.622$ is studied in detail with respect to its star forming properties, molecular gas content and its hidden nuclear activity (Section 6.3) using a variety of diagnostics including optical spectroscopy and millimeter interferometry (Section 6.2). The star formation process at such early times is finally compared to that in objects with highly elevated star formation activity at later times (Section 6.4).

Chapter 7 provides a detailed summary of the other Chapters with a focus on the most important findings. Prospects for future work as well as ongoing projects are also discussed in this Chapter

Fundamental background information on the ^{12}CO line as well as dust continuum emission properties in a high redshift context are given in the Appendices B.4 and B.5, respectively. Appendix B.4 also provides information on convenient units used in the context of

^{12}CO line emission and hence also in this thesis. More fundamental constants, units and conversions used in this thesis are found in Appendix C.

During this PhD work the author of this thesis contributed to other studies that are not presented here but that are of special value for the scientific Chapters of this thesis. Among those is a publication on the millimeter properties of obscured quasars (Martínez-Sansigre et al. 2009) which provides fundamental results for the content of Chapter 6. The work of Capak et al. (2011) yields important insights into why extreme starbursts like the one presented in Chapter 6 are of high relevance to constrain and actually observationally map cosmic structure formation in the early universe. The work of Dwek et al. (2011) thereby provides valuable insights into the estimation of star formation rates in such objects and the process of dust production at early times. Further (ongoing) projects are highlighted where contextually appropriate.

3. Seeing through the noise: Pushing observational limits via image stacking

This Chapter introduces an IDL-based multi-purpose image stacking algorithm that has been successfully applied at radio wavelengths in order to produce the scientific results presented in the next Chapters. It has been fully designed and implemented throughout the course of this thesis and currently finds applications at radio and various other (shorter) wavelengths to address a variety of scientific questions in the context of galaxy evolution. Parts of this Chapter are published in

A. Karim, E. Schinnerer, A. Martínez-Sansigre, M. T. Sargent, A. van der Wel, H.-W. Rix, O. Ilbert, V. Smolčić, C. Carilli, M. Pannella, A. M. Koekemoer, E. F. Bell & M. Salvato, 2011, ApJ, 730, 61, *The star formation history of mass-selected galaxies in the COSMOS field*

3.1. Introduction

Multi-wavelength deep field look-back surveys – providing large data-sets of galaxies – are the key element for studying cosmic evolution. Typically, the number of galaxies a survey finds depends on the wavelength and hence varies – for a given survey – from catalog to catalog resulting from observations with individual instruments in various bands. This effect would occur even if the sensitivities were chosen to be the same in all bands observed because, clearly, the spectral energy distribution of a galaxy does not follow a flat distribution across the electromagnetic spectrum. In other words, for the observed differential flux density of a galaxy as a function of observed frequency generally holds $S_{\nu}^{\rm obs}(\nu_{\rm obs}) \neq {\rm const}$. The effect of surface-brightness dimming generally[1] causes a galaxy to fade with increasing distance/redshift, eventually pushing it below a given sensitivity limit. Moreover, the spectral shapes of galaxies vary with galaxy type and potentially with redshift due to evolutionary effects. These might not only be changes in the stellar populations a given galaxy type hosts at different cosmic times but also an evolving composition of the interstellar medium leading to different (wavelength-dependent) dust-extinction laws and different dust-emission properties at infrared wavelengths.

In reality it is observationally unfeasible to design a multi-wavelength survey in such a way that the sensitivities in *a*ll bands are matched to the lowest possible flux level expected across all galaxy types and a substantial redshift range due to the unrealistically long observing times required. For a given band a survey therefore generally remains *flux-limited*. Often open questions in the field of galaxy evolution deal with relations between two distinct (global) galaxy properties or calibrations between two quantities derived from observables. In such cases deriving average trends has the highest priority.

[1] Unless (under certain circumstances) observed at (sub-)mm wavelengths (see Appendix B.2).

These, however, can already be studied if a given galaxy population is represented in a statistically complete sense only with respect to one observable or derived galaxy property. While then many or even most of the galaxies detected in one band (A) do not have a significant counterpart in the other band (B), co-adding postage stamp cutout images of the survey-map obtained in band B at the positions of sources in the sample resulting from band A it is possible to estimate the typical properties for a specific galaxy population with respect to band B. Usually referred to as stacking, this technique has proven to be a powerful tool to estimate the typical flux density of galaxies with respect to a given galaxy property, not only in the radio (e.g. White et al. 2007; Carilli et al. 2008; Dunne et al. 2009; Pannella et al. 2009; Garn and Alexander 2009; Bourne et al. 2010; Messias et al. 2010) but also in the mid-IR (e.g. Zheng et al. 2006, 2007a,b; Martin et al. 2007a; Bourne et al. 2010), far-IR (e.g. Lee et al. 2010; Rodighiero et al. 2010a; Bourne et al. 2010) as well as sub-mm (e.g. Greve et al. 2010; Martínez-Sansigre et al. 2009). The list can be extended to other wavebands always requiring a galaxy sample in the other band representative for the underlying population.

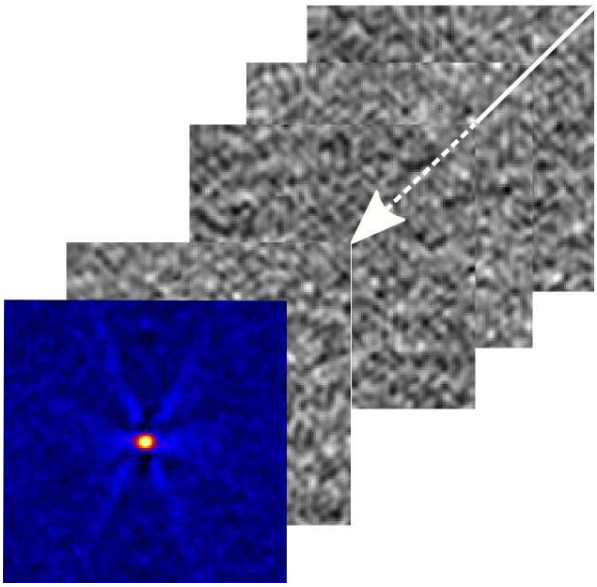

Figure 3.1. – Illustration of an image stacking experiment. First, individual cutout images (gray scale), centered at the positions of catalog sources detected at a different wavelength, are retrieved from a survey image. Subsequently, the individual cutouts are stacked, i.e. a single co-added map (colored foreground image) is produced by averaging over all pixels that are located at the same position in each cutout. This illustration, also shown on the cover page of this thesis, is based on a test stacking experiment at 1.4 GHz of $\sim 11,000$ massive galaxies at redshifts of $z > 1$ in the COSMOS field which results in a $\sim 40\sigma$ detection from median statistics. Despite the extraordinarily deep radio imaging used the vast majority of objects is individually undetected at 1.4 GHz. The input galaxy sample is culled from the mass-selected galaxy catalog presented in Ilbert et al. (2010) and the 1.4 GHz VLA-COSMOS map (Schinnerer et al. 2007, 2010) used has a resolution of $1.5'' \times 1.4''$. The images shown here have sizes of $40'' \times 40''$ (i.e. (115×115) pixels). The stacked map resembles well the synthesized beam (comparable to a point spread function) of the VLA-COSMOS image.

A major limitation of the image stacking approach is that deeper insights into intrinsic properties of a given relation, such as its dispersion, remain largely unexplored. Via a bootstrapping approach this limitation might be partially circumvented but only at the expense of largely unprobed assumptions about the intrinsic shape of the flux density distribution of the galaxies at the wavelength stacked. In short, the image stacking technique provides a highly important tool for modern galaxy evolution studies while it cannot be regarded as a substitute for newer observing instruments enabling even deeper observations.

3.2. Image stacking techniques

There are several ways to perform an image stack and not all involve the stacking of actual images but instead rely on averaging of a single pixel column (e.g. Dunne et al. 2009; Bourne et al. 2010). In order to retrieve the full average photometric information for a given galaxy population stacked, the retrieval of postage stamp cutout images each centered on the position of a catalog source, however, is a prerequisite. A full stacking routine should therefore be capable of processing the input imaging in two ways. Either the cutout images are readily available and need to be processed by the algorithm or the routine itself should be able to retrieve the individual cutout images from a full survey image. Given typical pixel scales and image dimensions of deep field surveys the latter should be regarded as a common option because mostly standard computer memory suffices to temporarily load these full images. Specific scientific problems often require to process many input samples at a time and it is therefore desirable for the user to be left only with the task to produce the individual catalogs as input for the stacking algorithm.

An important question regards the statistical method to estimate the typical flux density of an input sample at the wavelength stacked. More precisely, stacking means averaging over pixels located at the same position in each postage stamp in a statistically appropriate way. This problem can be approached by computing either the mean or the median of the mentioned set of pixels. Ideally, the resulting stamp then shows the spatial distribution of the average emission for the sample studied. For an input sample of N galaxies its background noise level should correspond to $\sim 1/\sqrt{N}$ of the noise measured in a single radio stamp. Non-uniform noise properties within the input map can be addressed by applying a weighted scheme to compute the mean but also the median (see Appendix A.1).

Any sample of galaxies likely contains also a fraction of sources with detections at the wavelength stacked. Even if this fraction is small, the mean is sensitive to the large excess in flux density compared to the average emission of the individual non-detections. On the other hand, setting a threshold and excluding detections from the stack artificially changes the sample and the results, hence, depend on the threshold applied. In addition, foreground objects and other extended bright features need to be handled with care and might be a source of contamination affecting the noise in the final stamp but also potentially the signal itself. It is therefore beneficial to exclude stamps showing these features from a mean stack. By resorting to the median, the stacking technique becomes more robust against outliers allowing the use of the entire input sample. While it is often argued that there is no straight-forward way of interpreting the sample median compared to the sample mean, White et al. (2007) showed that the median is a well-defined estimator of the mean of the underlying population in the presence of a dominant noise background, a typical situation, e.g., at radio wavelengths.

The key capabilities an image stacking routine should have can be summarized as follows:

- Efficient handling of cutout postage stamps and their direct retrieval from an input image based on user-defined coordinates.

- Multiple options of average estimators including median and mean statistics also in a noise-weighted fashion.

- Optional (automated or manual) rejection of cutout stamps showing bright and extended noise features or being heavily contaminated by foreground interlopers.

3.3. Full implementation of an image stacking algorithm

The development of a new multi-purpose image stacking routine is a major achievement of this thesis. Originally designed for a specific scientific purpose (the radio-based and mass-dependent cosmic star formation history) and implemented along the guidelines described above it has been improved several times for extended and more flexible use. The resulting IDL-package StackAttack provides a multi-functional and computationally efficient stacking environment whose various options are steered by a simple input ASCII file.

3.3.1. Workflow and performance

The elements in the workflow of StackAttack are:

1. Processing of the user-defined input parameters.

2. Evaluating the imaging input (pre-extracted cutout stamps or an input image).
   In case an entire survey image is used:

   a) Creating a basic FITS-header by extracting only the relevant information out of the FITS-header of the input survey map. Processing of the input coordinate list (StackAttack is capable of processing both, an ASCII coordinate list[2] as well as an array of structures written to a FITS table).

   b) Extracting cutout images centered at a given input catalog position with cutout dimensions specified by the user and correct FITS-header information.

3. Building a data cube from the individual cutouts with parallel storage of their individual FITS-headers.

4. Estimation and storage of the background noise level in each cutout stamp for weighted stacking methods and to monitor the noise-decrease during a stacking experiment. Additional transformations of individual cutout stamps are optionally available (e.g. subtracting a local sky background or rotations about a random multiple of π in case of large-scale noise distortions in the input image). Optionally, quality checks on individual cutouts can be performed and individual cutouts can be subsequently flagged automatically if not already manually flagged by the user.

5. Averaging over all pixel columns located at the same position in each cutout according to the user-defined statistic of choice and storage of the final stacked map.

6. Updating the astrometric information in the FITS-header such that the central pixel in the stacked map acts as the new reference pixel (defining at the same time the new origin in coordinate space such that positions in pixel space correspond to relative offsets to the central position). This eases later visual inspection of the stacked map.

[2] StackAttack processes decimal coordinate formates in degrees (J2000).

7. Measuring the background noise level as well as the peak signal in the stacked map and estimating its uncertainty via a bootstrapping technique (see Appendix A.1). Including these measurements in the new FITS-header via dedicated keywords.

8. Writing the stacked map along with the new FITS-header and other (optional) output to disk. File names are chosen to resemble that of the input sample. Optional outputs includes the full data cube of cutouts including all corresponding FITS-headers in order to enable later visual inspection of individual input sample members.

9. Optionally, keeping the input survey map in the computer memory if multiple stacks on the same image should be performed.

As outlined above, it was necessary to achieve flexible input image processing including correct astrometric operations. Therefore the final stacking routine needs to retrieve the essential FITS-header information of a given input survey image and extract the astrometric parameters. Often FITS-headers carry extensive additional information that is not required for the stacking experiment, including imaging and data acquisition as well as reduction history information. One has to be aware that the footprint data reduction pipelines leave in a FITS-header might cause memory problems if many cutout images with individual FITS-headers are extracted at a time. As the example of the VLA-COSMOS image shows, the assembly of a data cube of cutouts would be restricted to sample sizes smaller than usually needed for a stacking experiment even if the computer memory is comparatively large. StackAttack therefore builds a basic FITS-header from the survey map input including only the essential keywords containing, e.g., astrometry parameters as well as physical units, scalings and observing facility information. Some of the FITS image and header processing is handled using external routines provided within the IDL Astronomy Library[3].

Even though StackAttack is implemented in IDL, the user is free to chose the preferred working environment with respect to sample selection and to embedding StackAttack in the own workflow. The ASCII file containing the user defined input parameters can be prepared by the user using any text editor or, e.g., shell-based text manipulation thereby also setting the output path. The entire stacking package can be compiled at once such that a single call suffices to start StackAttack from shell as a background process, requiring only an IDL installation and license as well as a local copy of the IDL Astronomy Library. As a result, the way StackAttack is implemented eases the handling of large numbers of input samples and different survey images and can be smoothly embedded in any environment of choice. This is a prerequisite, e.g., for extensive stacking simulations carried out currently in a hybrid workflow of StackAttack, PERL and shell-scripting (Sargent, Karim et al. in prep.). Extensive stacking experiments in which multiple large data sets need to be processed furthermore require a high computational efficiency. The StackAttack algorithm is optimized to assure fast computation. Even if the input image is large ($\gg 1$ gigabyte) and a standard workstation[4] is used, the routine processes an input sample of $\sim 10,000$ galaxies in less than two minutes. It thereby produces a mean and a median stacked map in parallel

[3] We thank Wayne Landsman and the NASA Goddard Space Flight Center for making the library publicly available at http://idlastro.gsfc.nasa.gov.

[4] The term standard refers to the processor power of a modern but usual personal workstation. The computer should, however, posses enough memory reserves. As a rule of thumb, the random access memory should correspond to the input image size plus 1 gigabyte and for extraordinarily large sample sizes it should be as large as twice the image size.

including error estimation for both statistics via bootstrapping (see Section A.2).

Given its flexibility with respect to input image processing StackAttack is a wavelength-independent, i.e. a pan-chromatic, image stacking tool. It still offers dedicated options that are useful only for specific wavelengths.

3.3.2. Measurement of flux densities and error estimation

Along the way from the input sample to the final average result the measurement of total flux densities and an estimation of the errors is certainly critical. How to best measure a flux density, however, depends on the input imaging and, generally, cannot not be automated. It is hence up to the user to perform the final image processing part in a stacking experiment. For the most general case of flux measurement via aperture photometry StackAttack offers build-in capabilities that only need to be adjusted to the needs at the wavelength of choice. For example, aperture photometry and unit conversions have been pre-implemented for the processing of Spitzer/MIPS images according to the MIPS user manual[5]. This example shows that imaging obtained with a given instrument needs specific treatment even in the simple approach of measuring flux densities via aperture photometry.

Perhaps the most non-trivial flux density measurement needs to be performed if (radio) interferometric imaging is used. Flux density units at radio continuum wavelengths are typically reported in Janskys per beam. The total flux density of a point source can therefore be measured by retrieving solely the flux density at the brightest pixel. However, especially if the interferometric imaging has a high angular resolution, the point source limit turns out to be an oversimplification in a stacking experiment of extragalactic sources even if they are intrinsically point-like as detailed in the next Chapter (see Section 4.3.2). Extensive and well-tested software to treat radio interferometric imaging is publicly available and should be used in the workflow. As outlined above, a major advantage of StackAttack is that it is optimized to process large numbers of input samples and that it can be embedded smoothly in different computing environment. In order to assure this flexibility up to the final step from the input to the resulting flux density even in the photometrically exotic case of radio interferometric imaging we implemented an external shell-based routine that uses the AIPS[6] pipeline. Another dedicated and newly implemented external shell-based routine is finally used to translate the extensive human-readable AIPS output into a machine-readable ASCII table. Both routines drastically improve the efficiency of the workflow in extensive radio stacking experiments. The individual steps to be performed in case of radio input imaging and the parameters typically used are detailed in Section 4.3.2.

While flux density measurement depends on the input imaging used the same, in principle, holds true for the estimation of measurement errors. In other words, if standard photometric techniques are used also error estimation can be performed in a standard way when dealing with a stacked map. However, in a stacking experiment not only the pure measurement uncertainty is of interest but also the effects caused by the intrinsic flux dispersion of the input sample. How large this dispersion is depends on the homogeneity of

[5] The manual and other image processing as well as calibration requirements for Spitzer/MIPS data are found at http://irsa.ipac.caltech.edu/data/SPITZER/docs/mips/.

[6] AIPS is available from the National Radio Astronomy Observatory (NRAO) at http://www.aips.nrao.edu/ and copyrighted by Associated Universities, Inc. using the GNU copright form.

the pre-selected galaxy population but also on the quality of the sample selection methods which often depends on properties that themselves are affected by measurement errors (e.g. colors). The user should be free to select the input sample so that restrictions of any kind would neither be useful nor helpful since also very homogeneously selected samples will show a minimum flux dispersion. It should rather be the aim to find a most objective way to incorporate sample-dependent uncertainties in the final error estimation.

StackAttack therefore uses a bootstrapping approach (see Appendix A.2) that handles both median and mean statistics as well as noise-weighted estimators (see Appendix A.1). Our method is a simplification in that it uses the central pixel in each cutout stamp and hence assumes that the dispersion of the peak signal is trivially related to that of the total signal[7]. A total flux measurement for each individual object and subsequently bootstrapping the set of total flux densities is, however, typically unfeasible since the bulk of objects is undetected in a stacking experiment. It might be performed only if standard aperture photometry with a single aperture extent is used but it is out of reach for more complicated situations, e.g., in a (radio) interferometric stacking experiment as discussed above. Overall our approach is a fair and efficient compromise that yields realistic insights in the dispersion of the input sample. Generally, it might not be straight forward to incorporate this intrinsic sample dispersion in the total error budget of the integrated flux density. Exemplarily we discuss a way to treat the most important case for this thesis of radio continuum stacking in the next Chapter (see Section 4.3.2).

3.3.3. Additional software features and prospects

Especially in case of mean-stacking experiments, concepts of outlier rejection are worth to explore. This affects direct detections within a sample at the wavelength stacked as well as noise distortions due to imaging artifacts and (extended) foreground structures. Not all of these problems are actually related and hence different solution strategies are needed.

Perhaps simplest is the handling of spatially well separated direct detections at the wavelength stacked. If those are catalogued, a cross-match between input sample and survey catalog suffices to exclude the detections from the stack. In order to arrive at a representative signal for the input sample, however, the contribution of both, detections and non-detections, needs to be accounted for. A useful way of combining stacked signal and individual detections is to average them in a way that accounts for the typically very different numbers of sources on both sides of the detection threshold.[8] A noise-weighted average is an appropriate choice since the decrease in background-noise in a correct stacking experiment is proportional to the inverse square-root of the number of sources stacked. By definition the noise-weight is thus directly proportional to the number of undetected sources.

As a caveat, the handling of direct detections based on a source catalog will always

[7] Another assumption is that the astrometry is well behaved in the sense that the position in the input sample neither has a systematic offset to the corresponding position of an object in the stacked map nor that the flux in the two bands intrinsically peaks at distinct positions. Since the sources are generally unresolved the latter point is of minor importance while the former point was tested for the radio imaging used to obtain the results presented in this thesis (see Section 4.3.1 in the next Chapter).

[8] While typically the bulk of the sources will be undetected at the wavelength stacked the signal contributed by the rare detections is substantially larger which leads to an imbalance of flux contribution if not accounted for by a number-weighted averaging scheme.

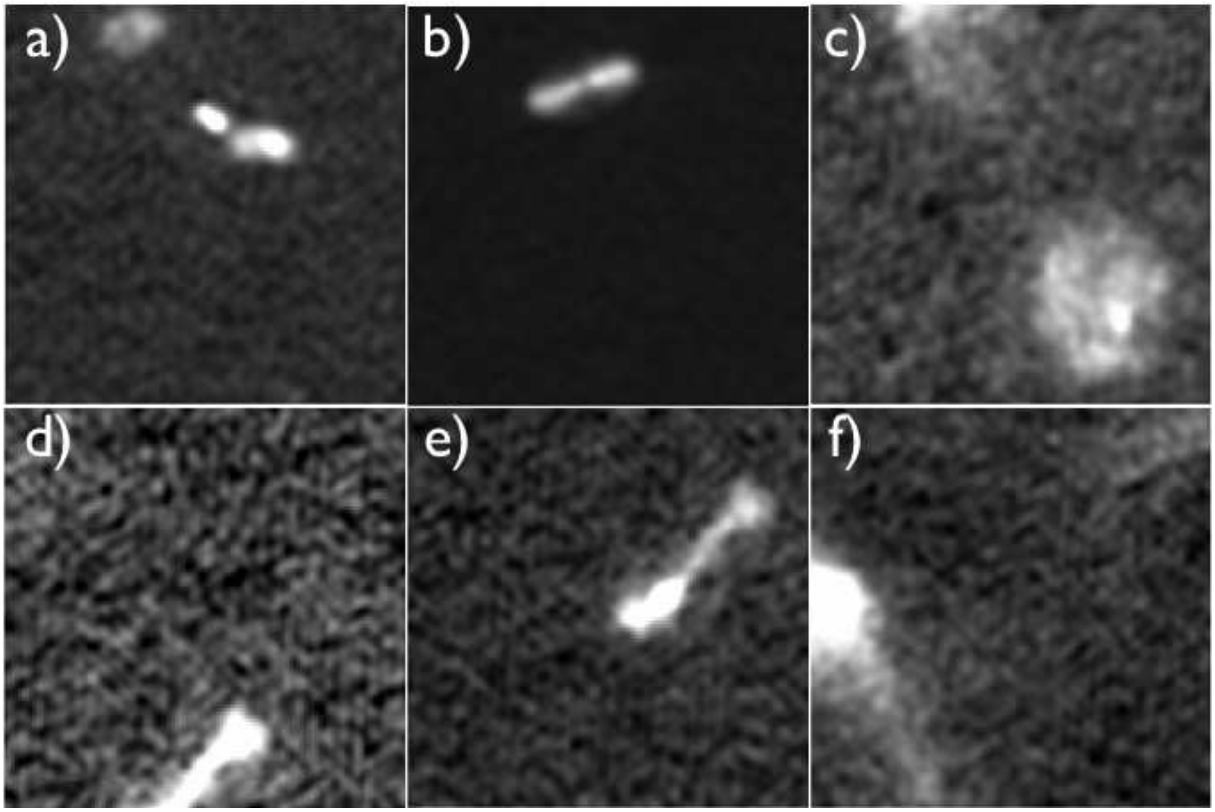

Figure 3.2. – Cutout images affected by noise distortions, e.g., through foreground objects. The examples shown here are taken from the test radio stacking experiment presented in Figure 3.1. Mostly seen are lobes from bright radio galaxies at different foreground distances. Examples *a)* and *b)* will barely affect the stacked signal measured at the center but enhance the background noise level which complicates the total flux measurement. Other examples (especially *e)* but also *c)*) artificially add signal at the image center which significantly affects a mean stacking experiment even given the fact that foreground distortions – as shown here – are generally rare in the stacking experiments presented in this thesis.

be biased to some extent due to the detection threshold chosen for the catalog and the user might want to test the robustness of the stacking experiment against the choice of different thresholds. StackAttack provides the functionality to identify sources above a user-defined detection threshold and to store the corresponding cutouts in an alternative data cube that can be processed later by the user. In order to avoid the identification of pure noise-peaks, the routine measures the average signal-to-noise ratio over 3×3 pixel apertures within the central region of each cutout after determining if adequately bright pixels exist within the same region. This part of the implementation has been developed independently of the stacking algorithm for efficient and successful 1.4 GHz counterpart search to distant star forming galaxies (see Chapter 6). It should be noted that testing of this software feature was so-far restricted to the radio regime and that evaluation of its performance at different wavelength is an ongoing effort.

The source finding capabilities of StackAttack can also be used to detect extended foreground structures in a given cutout stamp that might contribute to the signal in its central region (see Figure 3.2). In a stacking experiment at radio wavelengths such structures

could be lobes of radio galaxies that are clearly not related to the actual source stacked. These typically very bright structures might only affect the off-center regions of a cutout in which case they leave a footprint in a final mean-stacked map, leading hence to significant background distortions, artificially boosted noise levels and often even to an apparent loss of information (e.g. Garn and Alexander 2009). Rejecting also cutouts that show off-central bright structures might hence be beneficial but this needs to be evaluated separately for different wavelength regimes and cannot be generalized. This is hence not an automatic feature of StackAttack. In case of radio stacking, however, significantly less than $1\ \%$ of objects in a sample are rejected on average and the effect of this artificial cut on the sample thus is negligible.

Finally, direct detections might cause another important complication in case of a high projected source density. If a source in the survey image happens to be close enough to a source in the input sample signal confusion occurs. Depending on the input sample it might even happen that two or more of its constituents might be blended into one in the survey image, thereby counting the total signal twice in the stack. While crowded fields are generally problematic, the situation degrades especially in combination with large beam sizes. It is hence fair to say that a stacking experiment suffers from low angular resolution as well as from increasing survey sensitivity.

Various strategies have been proposed to address these issues mainly at infrared (e.g. Bourne et al. 2010; Chary and Pope 2010) and sub-mm (e.g. Greve et al. 2010) wavelengths, typically starting from subtracting detected sources above a given threshold from the survey image and hence working with a residual map. Chary and Pope (2010) sort the sources in the selection band by decreasing flux and retrieve cutouts centered at the catalog positions. In parallel they mask out all pixels in the survey map that are within a source aperture centered at the position of a catalog source. A subsequent cutout that includes this area will hence include no signal contribution from the masked pixels. The size of the source aperture thereby is the same as used for extracting the photometry in the stacked map. While there are several risks going along with such an image manipulation, a main problem of this approach is the assumption of a strong correlation between source intensity in the selection band and at the wavelength stacked. It might not be the case for every stacking experiment that brighter sources in one band are always brighter in the other. Moreover, this method is restricted to stacking the entire galaxy population in the selection band at once, hence not allowing to cull sub-populations based on other galaxy properties. This is caused by the fact that only sources that are actually contained in the input sample will be masked out while other objects might still lead to source confusion. To account for all objects in a given selection band a complicated deblending strategy has been applied by Greve et al. (2010) that involves the identification of a chain of neighbors when considering the relative distances of sources in an input sample in relation to the beam size of the survey map. This chain leads to a system of equations connecting measured (i.e. blended) and intrinsic fluxes of all sources contained in the chain to be solved for the intrinsic signal of the source of interest. Based on stacking simulations it has been shown by Kurczynski and Gawiser (2010) that such a deblending strategy indeed provides a vast improvement over other methods if the survey map resolution is so coarse that source blending becomes the dominant source of errors (e.g. at (sub-)mm wavelengths). An alternative strategy is to exploit the knowledge about the source clustering properties of the input sample (e.g. Bourne et al. 2010). This involves an autocorrelation analysis of the positions in the input sam-

ple and leads to an estimate of the average flux excess expected in a stacking experiment as detailed by Bourne et al. (2010). The limitations of this approach are the assumption that source clustering follows the same laws in both the selection and the stacking band as well as the fact that only a global (i.e. common) correction factor for subsequent stacks of sub-samples can be obtained.

It is certain that not all methods discussed above apply equally well to *any* stacking experiment since their limitations prohibit to use them in a general context. Any artificial source rejection from an input sample as well as any deblending strategy hence needs to be chosen with care and applied wisely depending not only on resolution and sensitivity but also on the choice of input sample as well as the stacking method. It is also noteworthy that radio interferometric imaging offers practically ideal conditions for image stacking experiments. The high angular resolution of radio images fruitfully combines with the comparatively low detection rate even deep radio surveys show. Source confusion issues are hence marginalized and constitute a negligible source of uncertainty for the results of a radio stacking experiment.

Clearly, further stacking simulations that involve artificial sources placed into residual maps at various wavelengths are needed to explore further the potential biases of stacking experiments with respect to the various parameters mentioned. Thanks to its efficient implementation StackAttack qualifies well for extensive simulations that are currently underway (Sargent, Karim et al. in prep.).

3.3.4. Panchromatic applications of the image stacking routine

The newly implemented image stacking routine StackAttack has been used in the 1.4 GHz band of the VLA-COSMOS survey for an extensive radio continuum stacking study of stellar mass-selected galaxies in the COSMOS field to reveal their average star formation properties (Karim et al. 2011a). Further details on stacking and flux measurements at radio wavelengths as well as the scientific results are presented in the upcoming Chapters of this thesis.

At radio wavelengths the routine is currently also used in a very different scientific context (Smolčić, Karim et al. in prep.) constraining the evolution of the 1.4 GHz luminosity function for massive quiescent galaxies, the main hosts of active galactic nuclei (AGN) with substantial radio emission (radio-AGN) since $z \sim 3$ (Figure 3.3). The luminosity functions are used to observationally constrain the total mechanical energy output of radio-AGN (Figure 3.4) that sets the rate by which radio-AGN heat their surrounding interstellar media thereby preventing further star formation (a process called 'radio-mode feedback'). These results extend the initial findings by Smolčić et al. (2009b) and can be directly compared to theoretical predictions (e.g. Croton et al. 2006). Further radio continuum stacking studies are under-way: Selecting galaxies based on their rest-frame ultraviolet continuum properties (the so-called UV-slope) enables insights into the evolution of the average dust-extinction. Moreover, comparing the average UV-derived star formation rates with radio-stacking based ones at various redshifts the appropriate dust extinction correction factors can be evaluated in a stellar-mass dependent way.

StackAttack is also extensively utilized at infrared wavelengths using Spitzer/MIPS and Herschel/PACS maps of the COSMOS field (Sargent, Karim et al. in prep.). The goals of this study are twofold. On the one hand thorough numerical as well as stacking simulations

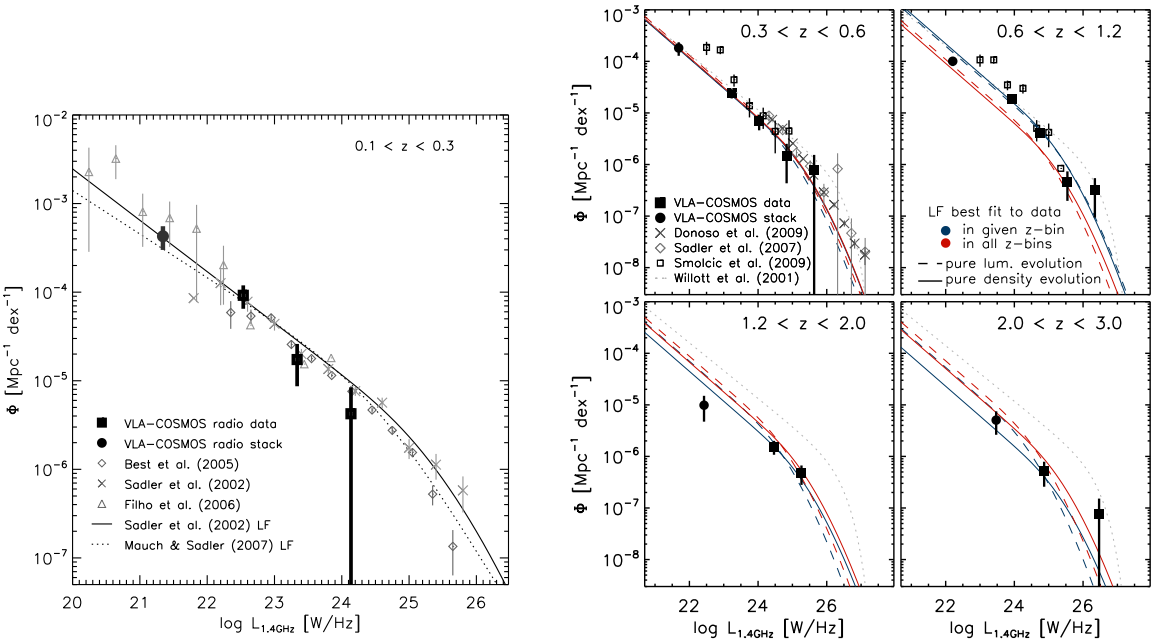

Figure 3.3. – Evolution of the radio luminosity function (LF) for quiescent galaxies with stellar masses $M_* \gtrsim 3 \times 10^{10}\ M_\odot$ in the COSMOS field. These results by Smolčić, Karim et al. (in prep.), to be submitted to The Astrophysical Journal, have been constrained with the help of StackAttack at low radio luminosities.
Left: Local ($0.1 < z < 0.3$) LF (open thick symbols). Volume densities that have been derived based on a volume limited radio detected sample are denoted by black open squares, while the volume density that is based on stacked data is shown by an open black circle. The LFs derived based on literature data (SDSS, 2dF, NGC catalog; Sadler et al. 2002; Best et al. 2005; Filho et al. 2006; Mauch and Sadler 2007) are also shown, and labeled in the panel. Two analytic LFs (Sadler et al. 2002; Mauch and Sadler 2007; S02, M07) are also displayed.
Right: Evolution of the LF in four redshift bins out to $z = 3$. Here stacked data are indicated as filled black circles. In the $0.3 < z < 0.6$ redshift range we show literature results (Sadler et al. 2007; Donoso et al. 2009). The displayed lines show the best fit evolution to the COSMOS data using the S02 LF (full dark-grey curve: pure luminosity evolution; full light-gray curve: pure density evolution), and the M07 LF (black dashed curve: pure luminosity evolution). For comparison we also show the assumed evolution of the low-power radio AGN by Willott et al. (2001) as a light-gray dash-dotted curve.

of artificial sources are carried out in order to investigate potential stacking biases and especially how stacking-derived flux ratios (such as colors) are affected. A second aim is to explore the evolution of the radio/infrared relation at faint (low-mass) levels based on the galaxy samples used in Karim et al. (2011a) in order to extend previous studies of galaxies detected in the COSMOS field (Sargent et al. 2010a,b).

At millimeter wavelengths StackAttack is used to explore the cold dust emission properties at the faint end of the star forming galaxy population on an initial 2 mm deep field image taken in the GOODS-North field (Walter et al. in prep.). This map was recently obtained with the privately funded Goddard-IRAM Superconducting 2-Millimeter Observer (GISMO), a next generation bolometer array camera currently operated at the IRAM 30 m telescope.

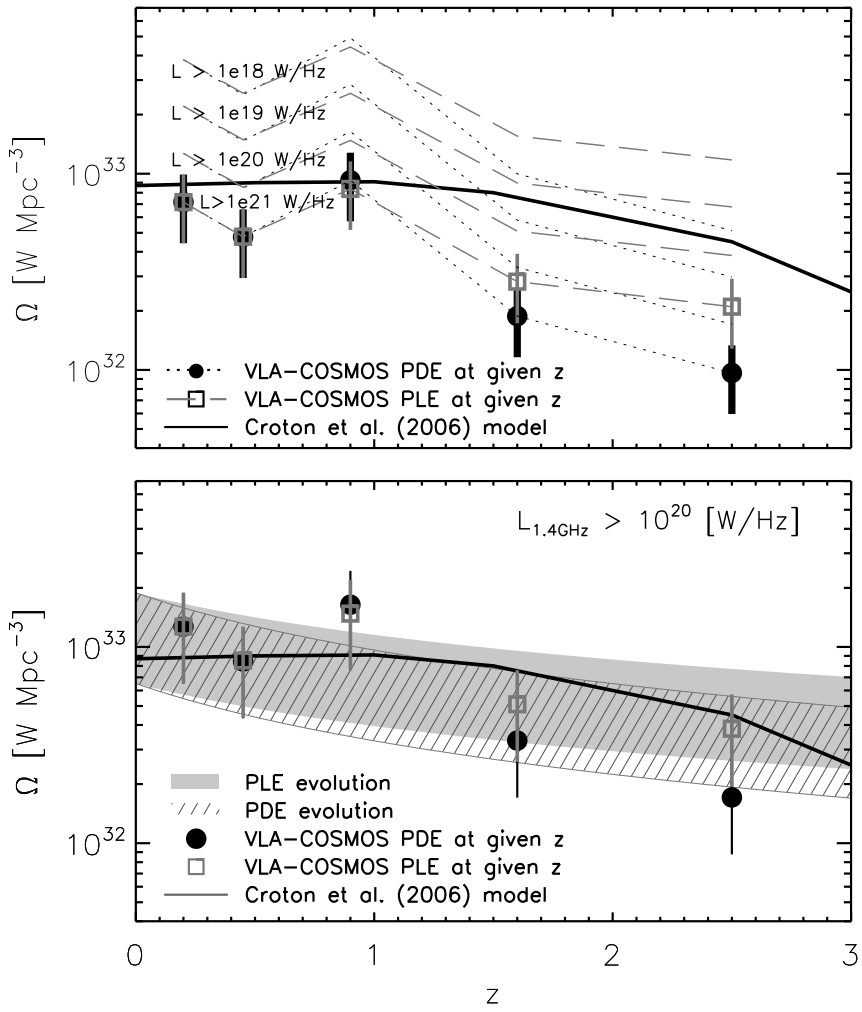

Figure 3.4. – Comoving volume averaged heating rate (Ω) done by quiescent massive galaxies in the COSMOS field as a function of redshift. These results by Smolčić, Karim et al. (in prep.), to be submitted to The Astrophysical Journal, have been constrained with the help of StackAttack in order to observationally constrain the effect of 'radio-mode feedback' to galaxy evolution. Ω was derived by first converting the luminosity functions shown in Figure 3.3 into kinetic energy density functions and then integrating the latter over radio luminosity (see Bîrzan et al. 2008 and Smolčić et al. 2009b for details). Both panels show the COSMOS data points derived by assuming pure density (PDE; filled circles), and pure luminosity (PLE; open squares) evolution that best fit the data in a given redshift bin. The (dotted and dashed) lines in the top panel illustrate the discrepancy in Ω if various lower boundary integral values are assumed (indicated in the panel). The thick solid line shows the 'radio-mode feedback' heating rate drawn from the Croton et al. (2006) cosmological model, and required to reproduce observed galaxy properties.

3.4. Summary

A major time invest during the course of this thesis was the development and implementation of an IDL-based multi-purpose image stacking routine. The resulting software package StackAttack is an efficient, flexible and portable image stacking tool capable of processing arbitrary survey imaging and input samples using various statistical estimators.

StackAttack has been intensively tested and applied at radio continuum wavelengths while it is already used to produce scientific results also at infrared and millimeter wavelengths. Clearly, not all features of this software have been fully developed and exploited in a panchromatic fashion given the vast diversity of requirements demanded by different input samples at different wavelengths. Especially the implementation of deblending strategies is an ongoing effort as well as the exploration of biases introduced in a stacking experiment via numerical and stacking simulations.

4. Star formation at $0.2 < z < 3$ in mass-selected galaxies in the COSMOS field

In this chapter the newly developed image stacking routine introduced above is used at radio continuum wavelengths to study the average (specific) star formation rate ((S)SFR) of $> 10^5$ stellar mass-selected galaxies in the 2 deg^2 COSMOS field. We separately consider the total sample and a subset of galaxies that shows evidence for substantive recent star formation in the rest-frame optical spectral energy distributions. At redshifts $0.2 < z < 3$ both populations show a strong and mass-independent decrease in their SSFR towards the present epoch. It is best described by a power- law $(1 + z)^n$, where $n \sim 4.3$ for all galaxies and $n \sim 3.5$ for star forming (SF) sources. The decrease appears to have started at $z > 2$, at least for high-mass ($M_* \gtrsim 4 \times 10^{10}\ M_\odot$) systems where our conclusions are most robust. Our data show that there is a tight correlation with power-law dependence, $\mathrm{SSFR} \propto {M_*}^\beta$, between SSFR and stellar mass at all epochs. The relation tends to flatten below $M_* \approx 10^{10}\ M_\odot$ if quiescent galaxies are included; if they are excluded from the analysis a shallow index $\beta_{\mathrm{SFG}} \approx -0.4$ fits the correlation. On average, higher mass objects always have lower SSFRs, also among SF galaxies. At $z > 1.5$ there is tentative evidence for an upper threshold in SSFR that an average galaxy cannot exceed, possibly due to gravitationally limited molecular gas accretion. It is suggested by a flattening of the SSFR-M_* relation (also for SF sources), but affects massive ($> 10^{10}\ M_\odot$) galaxies only at the highest redshifts. Since $z = 1.5$ there thus is no direct evidence that galaxies of higher mass experience a more rapid waning of their SSFR than lower mass SF systems. In this sense, the data rule out any strong 'downsizing' in the SSFR. This chapter is part of the publication

A. Karim, E. Schinnerer, A. Martínez-Sansigre, M. T. Sargent, A. van der Wel, H.-W. Rix, O. Ilbert, V. Smolčić, C. Carilli, M. Pannella, A. M. Koekemoer, E. F. Bell & M. Salvato, 2011, ApJ, 730, 61, *The star formation history of mass-selected galaxies in the COSMOS field*

4.1. Introduction

Over the last years multi-waveband surveys of various wide fields have lead to estimates of star formation rates (hereafter SFRs) and stellar masses for large numbers of galaxies out to high redshifts. Both quantities are crucial for understanding galaxy evolution. On the one hand an evolution of the observed number density of galaxies as a function of stellar mass, i.e. the mass function, reveals how the stars are distributed among galaxies at different cosmic epochs. If, on the other hand, an increase in stellar mass of any population of galaxies can solely be explained by the rate at which new stars are formed within these systems or if other mechanisms are dominant can only be discussed if the corresponding

SFRs themselves are known.

A number of studies (e.g. Lilly et al. 1996; Madau et al. 1996; Chary and Elbaz 2001; LeFloc'h et al. 2005; Smolčić et al. 2009a; Dunne et al. 2009; Rodighiero et al. 2010b; Gruppioni et al. 2010; Bouwens et al. 2011b; Rujopakarn et al. 2010 and for a compilation Hopkins 2004 and Hopkins and Beacom 2006) revealed that the star formation rate density (hereafter SFRD), i.e. the SFR per unit comoving volume, rapidly declines over the last ~ 10 Gyr following the purported maximum of star formation activity in the universe. The question of whether the stellar mass content of galaxies could be a major driver for this decline has gained significant interest after the discovery of a tight correlation of SFR and stellar mass for star forming (hereafter SF) galaxies with an intrinsic scatter of only about 0.3 dex (e.g. Brinchmann et al. 2004; Noeske et al. 2007b; Elbaz et al. 2007). This relation was studied in the local universe (Brinchmann et al. 2004; Salim et al. 2007) suggesting an apparent bimodality in the SFR-M_* plane if all galaxies are taken into account. It was also found to exist for SF galaxies at $z \lesssim 1.2$ (e.g. Noeske et al. 2007b; Elbaz et al. 2007; Bell et al. 2007; Walcher et al. 2008) and further out to $z \approx 2.5$ (Daddi et al. 2007; Pannella et al. 2009).[1] Consequently the stellar mass normalized SFR (hereafter specific SFR or SSFR), i.e. the SFR at a given epoch divided by the stellar mass the galaxy possesses at the same cosmic epoch, shows a tight (anti-)correlation.

By studying the SSFR galaxies of different stellar masses can be directly compared. The SSFR itself defines a typical timescale that can be interpreted as a current efficiency of star formation within a galaxy compared to its past average star formation activity. The compilation of the studies mentioned (e.g. Pannella et al. 2009; González et al. 2010; Dutton et al. 2010), not using a common tracer for star formation nor selection technique for separating the SF galaxy fraction and data originating from various wide fields, suggests a steep evolution of the normalization of the SSFR-M$_*$ relation[2] for *SF* galaxies. Studies, covering a broad dynamical range in stellar mass, have been carried out for *all* galaxies and confirmed the SSFR, as a function of redshift, to be even more rapidly increasing from $z = 0$ to $z \approx 1$ (e.g. Feulner et al. 2005b; Zheng et al. 2007a; Damen et al. 2009b, 2010) as well as throughout an even wider range in redshift (e.g. Feulner et al. 2005a; Pérez-González et al. 2008; Dunne et al. 2009; Damen et al. 2009a). It has been claimed that the steepness of the SSFR-increase with redshift might be a challenge for a cold dark matter concordance model (ΛCDM) suggested by comparisons to predictions from semi-analytical models (SAMs) (see Santini et al. 2009; Damen et al. 2009a; Firmani et al. 2010 and, e.g., Guo and White 2008, for theoretical results based on a SAM).

It was recently discussed by Stark et al. (2009) and González et al. (2010), at least for moderately massive SF galaxies ($M_* \sim 5 \times 10^9\ M_\odot$), that the rapidly evolving SSFR might turn constant in the early universe. Their data show constant SSFRs up to the highest redshift ranges ($z \approx 7 - 8$) probed so far. This significant deviation of the SSFR-evolution from a power-law ($\mathrm{SSFR} \propto (1+z)^n$), fitting well the data below $z \approx 2$, could be a hint for different physical mechanisms regulating star formation in the early universe (González et al. 2010). However, this deviation could also be a result of observational data significantly underestimating the SSFRs at these high redshifts (Dutton et al. 2010) caused by selection

[1] It needs to be mentioned that at $z \sim 2$ Erb et al. (2006) only found a weak correlation between SFR and stellar mass. However, their galaxy sample selection at ultraviolet wavelengths preferentially traces SFR rather than stellar mass, thus potentially biasing their results towards a flatter SFR-M_* relation.

[2] In the following we will refer to this relation for SF galaxies as the SSFR-sequence.

biases [3]. Recent theoretical models propose an enhanced merger rate (Khochfar and Silk 2010) at high z in order to account for the purported constancy of the SSFR. This is in contrast to pure steady cold-mode gas accretion above a limiting dark matter halo mass (the so-called 'mass floor' of $M_{\rm DM} \sim 10^{11}\ M_{\odot}$; Bouché et al. 2010) reproducing well the observed slope of the SSFR-sequence at all redshifts $z < 2$.

It was generally found that at $z < 2$ *all* galaxies show a significant (negative) slope of the SSFR-M_* relation leading to lower SSFRs in more massive galaxies. *Star forming* galaxies also seem to show this behavior but the trend tends to be significantly weaker especially at $z > 1$ where, based on the sBzK selection technique, the slope was found to be practically vanishing (Daddi et al. 2007; Pannella et al. 2009). It therefore is an ongoing debate if this phenomenon of a decreasing slope of the SFR-M_* relation for SF galaxies with redshift is real or just an artifact (for an introduction and a summary of the conflicting observational results see, e.g., Fontanot et al. 2009). This effect is commonly interpreted as star formation efficiency being shifted from higher mass objects in the cosmic past to lower mass objects in the present and sometimes referred to as 'cosmic downsizing' (Cowie et al. 1996). Most recently, based on first Herschel/PACS far-infrared data, even the opposite effect, the so-called SSFR-upsizing at $z \gtrsim 1.5$, has been proposed (Rodighiero et al. 2010a).[4]

More measurements are needed to understand the relation of SFR and stellar mass and its evolution with redshift. This holds especially true for the population of SF galaxies. An accurate measurement of the (S)SFR-sequence at all epochs is key for a better understanding of galaxy evolution. As it was claimed (e.g. Noeske et al. 2007b) a tight correlation of SFR and stellar mass disfavors star formation histories (SFHs) of individual normal galaxies that are mainly driven by stochastic processes, such as mergers. Quite contrarily it favors smooth SFHs in such a way that the SFH at any cosmic epoch of a galaxy is solely determined by its stellar mass content measured at the corresponding redshift unless the galaxy becomes subject to quenching of star formation. In this sense the SFR-M_* relation at a given redshift is regarded an isochrone for galaxy evolution in the same manner the Hertzsprung-Russel-Diagram is an isochrone for the evolution of a stellar population at a given age.[5] It should be mentioned, however, that Cowie and Barger (2008) disagree with this conclusion which underlines the importance of future studies that use a sufficiently deep direct SFR tracer to study the intrinsic dispersion of the SSFRs .[6]

Several tracers across the electromagnetic spectrum are used to estimate the star formation rate of a normal galaxy[7]. While rest-frame ultraviolet (UV) light originates mainly from massive stars and thus directly traces young stellar populations it will be strongly at-

[3] Note the very small number of galaxies currently studied in the extreme high redshift regime. Also note the highly discrepant SSFR-estimates presented by Yabe et al. (2009) and Schaerer and de Barros (2010) at the most extreme redshifts as summarized by Bouché et al. (2010) in their Figure 13.

[4] This trend is weakly supported by the earlier findings of Oliver et al. (2010).

[5] The (S)SFR-mass relation is therefore also sometimes referred to as 'the galaxy main sequence' (Noeske et al. 2007b) that is, for an individual galaxy of stellar mass M_*, connected by evolutionary tracks (e.g. the so-called tau-model discussed in Noeske et al. 2007a) at distinct cosmic epochs (see also Noeske 2009, for a summary).

[6] Cowie and Barger (2008) cannot confirm the low level of intrinsic dispersion in the SSFR-M_* plane found by Noeske et al. (2007b) and they discuss other hints they find supporting SFHs to be rather dominated by episodic bursts. We emphasize that the larger dispersion of SSFRs might be caused by the relatively broad bins in redshift used by Cowie and Barger (2008) given the steep increase with redshift of SSFRs at $z < 1.5$ while studying *all* massive galaxies.

[7] 'Normal' galaxies are defined as systems that do not host an active galactic nucleus.

tenuated by dust. The absorbed UV emission is thermally reprocessed by heating the dust which in turn reemits at infrared (IR) wavelengths. Star formation also leads to emission in the radio continuum since charged cosmic particles are accelerated in shocks within the remnants of supernovae (SNR) leading to non-thermal synchrotron radiation (e.g. Bell 1978a and e.g. Muxlow et al. 1994, for observations of individual SNRs). Thermal free-free emission (*Bremsstrahlung*) in general contributes only weakly to the 1.4 GHz signal (see e.g. Condon 1992) but might become dominant in low-mass systems where the synchrotron emission was empirically found to be strongly suppressed (Bell 2003a). Also empirically the phenomenon of radio emission triggered by star formation results in its well known strong correlation with the far-IR output of a given SF galaxy (e.g. Helou et al. 1985; Condon 1992; Yun et al. 2001; Bell 2003a) that appears to persist out to high ($z > 2$) redshifts in a non-evolving fashion (e.g. Sargent et al. 2010a,b).

A major advantage of radio emission as a tracer for star formation is its obvious independence of any correction for dust attenuation. Due to well known underlying physical processes the spectral energy distribution of a normal galaxy in the low ($\lesssim 5$) GHz regime shows a $F_\nu \propto \nu^{\alpha_{\rm rc}}$ shape (e.g. Bell 1978a). While $\alpha_{\rm rc} = -0.8$ is found to be a typical value for the radio spectral index (e.g. Condon 1992; Bell 2003a, for a summary but also, e.g., Scheuer and Williams 1968; Bell 1978b, for early results) no further spectral features are expected in this frequency range thus leading to a robust K-correction up to high ($z \lesssim 3$) redshifts.[8] Both advantages directly confront the rather uncertain dust attenuation coefficient for UV light and the presence of polycyclic aromatic hydrocarbon (PAH) emission features redshifted (at $z \gtrsim 0.8$) into the 24 μm band commonly used as an estimator for the total infrared (TIR) emission. Also the combination of UV and mid-IR emission tracing star formation is limited since it is typically tested in moderately SF systems at low redshift (for a summary see Calzetti and Kennicutt 2009) which might not resemble high redshift galaxies with higher SFRs and larger dust content. Finally, even at a resolution of $\sim 5''$ achieved by current UV and IR telescopes blending of sources becomes a severe issue for the faint end of the sources (see, e.g., Zheng et al. 2007b). Current radio interferometers such as the (E)VLA and (e)Merlin achieve resolutions of $\lesssim 2''$ that are needed to unambiguously identify optical counterparts. This unambiguity is particularly important in a stacking experiment as otherwise flux density from nearby sources might contribute to the emission of an individual object. A drawback of using radio emission to trace star formation is the generally low sensitivity to the normal galaxy population even in the deepest radio surveys to-date which usually limits the analysis to a stacking approach. Therefore, current radio surveys allow one to study average SFR properties while they cannot shed light on the intrinsic dispersion of individual sources. This situation will improve with future EVLA surveys.

Studying the stellar-mass dependence of the SFH requires a mass-complete sample in order to prevent inferred evolutionary trends from being mimicked by sample incompleteness. Early type galaxies containing predominantly older stellar populations and showing therefore a prominent 4000 Å break (see e.g. Gorgas et al. 1999) are likely to be excluded in optical surveys above $z \sim 1$ even at deep limiting magnitudes as the break is redshifted into the selection band. Optical selection, thus, potentially limits any study of a stellar mass-complete sample to the bright (i.e. high-mass) end or is effectively rather a selection

[8] Unless radiative losses, e.g. inverse Compton scattering against the cosmic microwave background, steepen the spectral index to values ∼-1.3.

by unobscured SFR than by stellar mass if the full sample is considered for the analysis.

Channel 1 of the IRAC instrument onboard the Spitzer Space Telescope provides us with the $3.6\ \mu\mathrm{m}$ waveband that samples the rest-frame K-band at $z \sim 0.5$ to the rest-frame z-band at $z \sim 3$. It is therefore ideal in probing mainly the light from old low-mass stars while not being severely affected by dust. For the analysis presented here, hence, a deep and rich ($\sim 100,000$ sources at $z \leq 3$) $3.6\ \mu\mathrm{m}$ galaxy sample in combination with accurate photometric redshifts and stellar-mass estimates has been used (Ilbert et al. 2010). With a sky coverage of $2\ \mathrm{deg}^2$ the Cosmic Evolution Survey[9] (COSMOS) provides the largest cosmological deep field to-date (see Scoville et al. 2007d, for an overview). The uniquely large COSMOS $3.6\ \mu\mathrm{m}$ galaxy sample offers uniform high-quality pan-chromatic data for *all* sources enabling us to study the SSFR in small bins in both stellar mass and redshift. Additionally the evolution of the stellar mass-functions has been studied already based on the same sample and its SF sub-population (Ilbert et al. 2010). As it was argued (e.g. in Daddi et al. 2010a) the combination of the individual evolutions of the mass function and the (S)SFR-sequence might be the most important observational constraints for understanding the stellar mass build-up on cosmic scales jointly resulting in a potentially peaking and declining SFRD. We will discuss further implications in the next Chapter.

This Chapter is organized as follows. In Section 4.2 we present our principle and ancillary COSMOS data sets and the selection of our sample. Sec 4.3 contains a detailed description of the application of our stacking algorithm at radio wavelengths and the derivation of average SFRs from 1.4 GHz image stacks. Additional methodological considerations pertaining to both sample selection and flux density estimation by image stacking are to be found in the Appendices. Readers who wish to directly proceed to our results and their interpretations can find those regarding the relation of SSFR and stellar mass in Section 4.4.

Throughout this and the following Chapter all observed magnitudes are given in the AB system. We assume a standard cosmology with $H_0 = 70$ (km/s)/Mpc, $\Omega_M = 0.3$ and $\Omega_\Lambda = 0.7$ consistent with the latest WMAP results (Komatsu et al. 2009) as well as a radio spectral index of $\alpha_{\mathrm{rc}} = -0.8$ in the notation given above if not explicitly stated otherwise. A Chabrier (2003) initial mass function (IMF) is used for all stellar mass and SFR calculations in this Chapter. Results from previous studies in the literature have been converted accordingly.[10]

4.2. The pan-chromatic COSMOS data used

In order to study the redshift evolution of galaxies in general, and the evolution of their SFRs in particular, a complete and large sample of normal galaxies is needed as it not only provides representative but also statistically significant insights.

The large area of $2\ \mathrm{deg}^2$ covered by the COSMOS survey, fully imaged at optical wavelengths by the Hubble Space Telescope (HST; Scoville et al. 2007a; Koekemoer et al. 2007), is necessary to minimize the effect of cosmic variance. Deep UV GALEX (Zamojski et al. 2007) to ground-based optical and near-infrared (NIR) (Taniguchi et al. 2007; Capak et al. 2007) imaging of the equatorial field[11] yielded accurate photometric data products for

[9] http://cosmos.astro.caltech.edu

[10] Logarithmic masses and SFRs based on a Salpeter (1955) IMF, a Kroupa (2001) IMF and a Baldry and Glazebrook (2003) IMF are converted to the Chabrier scale by adding -0.24 dex, 0 dex and 0.02 dex, respectively.

[11] The COSMOS field is centered at RA $= 10:00:28.6$ and Dec $= +02:12:21.0$ (J2000)

$\sim 1 \times 10^6$ galaxies down to 26.5th magnitude in the i-band (Ilbert et al. 2009; Capak et al. 2007). Thanks to extensive spectroscopic efforts at optical wavelentghs using VLT/VIMOS and Magellan/IMACS (Lilly et al. 2007; Trump et al. 2007) the estimation of photometric redshifts for all these sources could be accurately calibrated. Ongoing deep Keck/DEIMOS campaigns (PIs Scoville, Capak, Salvato, Sanders and Karteltepe) extent the spectroscopically observed wavelength regime to the NIR which is critical to improve the photometric calibration for faint sources at high redshifts. In addition to observations of the whole or parts of the COSMOS field in the X-ray (Hasinger et al. 2007; Elvis et al. 2009) and millimeter (Bertoldi et al. 2007; Scott et al. 2008), imaging by Spitzer in the mid- to far-IR (Sanders et al. 2007) as well as interferometric radio data (Schinnerer et al. 2004, 2007, 2010) covering the full $2\ \mathrm{deg}^2$ have been obtained.

4.2.1. VLA-COSMOS radio data

Radio observations of the full ($2\ \mathrm{deg}^2$) COSMOS field were carried out with the Very Large Array (VLA) at 1.4 GHz (20 cm) in several campaigns between 2004 and 2006. The entire field was observed in A- and C-configuration (Schinnerer et al. 2007) where the 23 individual pointings were arranged in a hexagonal pattern. Additional observations of the central seven pointings in the most extended A-configuration (Schinnerer et al. 2010) were obtained in order to achieve a higher 1.4 GHz sensitivity in the area overlapping with the COSMOS MAMBO millimeter observations (Bertoldi et al. 2007). In both cases the data reduction was done using standard procedures from the Astronomical Imaging Processing System (AIPS; see Schinnerer et al. 2007, for details). At a resolution of $1.5'' \times 1.4''$ the final map has a mean rms of ~ 8 μJy/beam in the central $30' \times 30'$ and ~ 12 μJy/beam over the full area, respectively. Using the SAD algorithm within AIPS, a total of 2,865 sources were identified at more than 5σ significance in the final VLA-COSMOS mosaic (Schinnerer et al. 2010). As the outermost parts of the map are not covered by multiple pointings the noise increases rapidly towards the edges. In this study we therefore exclude these peripheral regions resulting in a final useable area of $1.72\ \mathrm{deg}^2$.

4.2.2. A 3.6 μm selected galaxy sample within the COSMOS photometric (redshift) catalogs

Deep Spitzer IRAC data mapping the entire COSMOS field in all four channels have been obtained during the S-COSMOS observations (Sanders et al. 2007). The data reduction yielding images and associated uncertainty maps for all the four channels is described in Ilbert et al. (2010) (I10 hereafter). For the $3.6\ \mu$m channel a source catalog has been obtained by O. Ilbert and M. Salvato (private communication) using the SExtractor package (Bertin and Arnouts 1996). Given the point spread function (PSF) of 1.7" a Mexican hat filtering of the $3.6\ \mu$m image within SExtractor was used in order to assure careful deblending of the sources.

The resulting sample of $3.6\ \mu$m sources down to a limiting magnitude of $m_{\mathrm{AB}}(3.6\ \mu\mathrm{m}) = 23.9$ in the 2.3 deg^2 field, not considering the masked areas around bright sources ($K_s < 12$), areas of poor image quality and the field boundaries, consists of 306,000 sources.[12]

[12] As a stacking analysis depends on the input sample prior masked areas consequently reduce further the effective area for this study. All space densities reported in this work are therefore computed for an effective

As detailed in I10 photometric redshifts (hereafter photo-z's) were assigned to all 3.6 μm detected sources. The vast majority of sources is also detected at optical wavelengths and therefore contained in the COSMOS photo-z catalog[13] (Ilbert et al. 2009) so that in general photometric information from 31 narrow-, intermediate and broad-band FUV-to-mid-IR filterbands was available.[14] Within the remaining 4 % (i.e. a total of 8507) of the 3.6 μm sources 2714 are also contained in the COSMOS $K-$band selected galaxy sample (McCracken et al. 2010) and are also regarded as real sources. I10 assigned photo-z's to these extremely faint objects using the available NIR-to-IRAC photometry.

The quality of the photo-z's was estimated (for details see I10) by using spectroscopic redshifts for a total of 4,148 sources at $m_{AB}(i^+) < 22.5$ from the zCOSMOS survey (Lilly et al. 2009). At a rate of < 1 % of outliers the accuracy was found to be $\sigma_{(z_{\rm phot}-z_{\rm spec})/(1+z_{\rm spec})} = 0.0075$ down to the magnitude limit of the spectroscopic sample. For all objects within the 3.6 μm selected catalog – regardless of i-band magnitude the accuracy was derived by using the 1σ uncertainty on the photo-z's from the probability distribution function which yields a conservative estimate of the photo-z uncertainty as detailed in Ilbert et al. (2009). At $1.25 < z < 2$ the relative photo-z uncertainty is 0.08 and thus higher by a factor of four compared to the median value for the full ($m_{\rm AB}(3.6\ \mu{\rm m}) \geq 23.9$) sample.[15] We account for this when binning the data in redshift by choosing increasing bin widths with increasing redshift.[16] It is worth noting that the photo-z accuracy is degraded at magnitudes fainter than $m_{AB}(i^+) = 25.5$ (See Figure 12 in Ilbert et al. (2009)). Our choice of lower stellar mass limits (see Section 4.2.6) and our stellar mass binning-scheme (see Section 4.2.6) automatically ensures a low fraction (< 15 %) of these optically very faint objects within the lowest mass-bin above our mass limit at any redshift. The fraction of such faint objects effectively vanishes towards higher masses as also pointed out by I10.[17]

4.2.3. Estimation of stellar masses

Stellar masses for all objects within the 3.6 μm selected parent sample have been computed by I10. Here, we briefly summarize the method and the important findings. For the estimation of stellar masses based on a Chabrier IMF stellar population synthesis models generated with the package provided by Bruzual and Charlot (2003) (BC03) have been used. Furthermore an exponentially declining SFH and a Calzetti et al. (2000) dust extinction law have been assumed. Spitzer MIPS 24μm flux densities (from LeFloc'h et al. 2009) have been included in the SED template fitting as an additional constraint on the stellar mass.

field size of 1.49 deg^2.

[13] This optically deep sample has a limiting magnitude of 26.2 in the i^+ selection band (see Table 1 in Salvato et al. (2009)).

[14] As described in detail by I10 all photo-z's used in our study were obtained using a χ^2 template-fitting procedure implemented in the code *Le Phare* (Arnouts et al. 2002; Ilbert et al. 2006) and a library of 21 templates. Additional stellar templates were used to reject stars (i.e. sources with a lower χ^2 values for the stellar compared to the galaxy templates) from the final galaxy sample.

[15] For a color-selected sub-set of galaxies for which spectroscopic redshifts from the zCOSMOS-faint survey (Lilly et al., in prep.) were available the photo-z accuracy was directly tested at $1.5 < z < 3$. This yields an accuracy of $\sigma_{\Delta z/(1+z)} = 0.04$ with 10% of catastrophic failures.

[16] It should be mentioned, however, that the projected-pair analysis by Quadri and Williams (2009) independently shows that photo-z's from data sets with broad- and intermediate band photometry like the COSMOS catalog are not expected to have very different photo-z errors at $z > 1.5$ than at lower redshifts.

[17] I10 use comparable mass limits and their Figure 8 shows the strong decline of the fraction of optically faint objects with mass at all z.

Systematic uncertainties on the stellar masses, caused by the use of photo-z's, the choice of the dust extinction law and library of stellar population synthesis models, have been investigated. No systematic effect due to the use of photo-z's is apparent. Stellar masses derived from the BC03 templates are systematically higher by 0.13-0.15 dex compared to the newer Charlot & Bruzual (2007) versions (Bruzual 2007) that have an improved treatment of thermally pulsing asymptotical giant branch (TP-AGB) stars. As BC03 models are commonly used in the literature, both studies, I10 and this work, are based on BC03 mass estimates.

4.2.4. Spectral classification

A number of studies suggest the existence of a bimodality in the SSFR-M_* plane (e.g. Salim et al. 2007; Elbaz et al. 2007; Santini et al. 2009; Rodighiero et al. 2010a) leading to a tight SSFR-sequence to be in place only for SF galaxies. Therefore a deselection of quiescent, i.e. non SF, objects is needed.

Following I10 we classify galaxies with a best-fit BC03 template that has an intrinsic (i.e. dust unextincted) rest-frame color redder than $(\mathrm{NUV} - r^+)_{\mathrm{temp}} = 3.5$ as quiescent. Several authors (e.g. Wyder et al. 2007; Martin et al. 2007b; Arnouts et al. 2007) suggest this color to be an excellent indicator for the recent over past average SFR as it directly traces the ratio of young (light-weighted average age of $\sim 10^8$ yr) and old ($\geq 10^9$ yr) stellar populations. Seeking for a color bimodality that discriminates galaxies with currently high from those with low star formation activity the $\mathrm{NUV}-r$ color appears therefore to be superior to purely optical rest-frame colors such as $U - V$ (e.g. Bell et al. 2004).

Using a dust uncorrected $\mathrm{NUV} - r^+$ versus $r^+ - J$ rest-frame color-color diagram[18] I10 showed that in the range $0 \leq z \leq 2$ for $(\mathrm{NUV}-r^+)_{\mathrm{temp}} > 3.5$ quiescent galaxies are well separated from the parent sample without severe contamination by dust-obscured SF galaxies. This quiescent population is therefore comparable to the one classified by Williams et al. (2009) based on a $U - V$ versus $V - J$ rest-frame color-color diagram.

Furthermore our quiescent population shows a clear separation from the parent sample with respect to galaxy morphology. I10 visually classified a subset of 1,500 isolated and bright galaxies from the $3.6\ \mu$m parent sample using HST/ACS images and found the quiescent population among those to be clearly dominated by elliptical (E/S0) systems. A further cut ($(\mathrm{NUV} - r^+)_{\mathrm{temp}} < 1.2$) was shown to efficiently separate late type spiral and irregular galaxies from early type spirals as well as the remaining tail of elliptical systems. As any such color cut effectively is a cut in star formation activity we discuss the spectral pre-classification of SF systems in more detail in Section 4.5.

4.2.5. AGN contamination

A major concern arising in the context of using radio emission to trace star formation is contaminating flux from active galactic nuclei (AGN). For some galaxies the total radio signal might even be dominated by an AGN. For our study, ideally, we should therefore remove all galaxies hosting an AGN from our sample.

[18] Here the absolute magnitudes were inferred from the observed magnitudes not accounting for dust reddening.

Cross-matching the most recent XMM-COSMOS photo-z catalog (Salvato et al. 2009; Brusa et al. 2010) with the 3.6 μm selected parent sample delivered a total of 1,711 (i.e. ~ 1 %) X-ray detected objects. Most of these sources exhibit best-fit composite AGN/galaxy SEDs[19] while a minor fraction is well fitted by an SED showing no AGN contribution. However, here all X-ray detections are treated as potential AGN contaminants and thus removed from our sample.[20]

Studies of the radio luminosity function (e.g. Sadler et al. 2002; Condon et al. 2002) agree that radio-AGN contribute half of the radio light in the local universe at radio luminosities slightly below $L_{1.4\ \mathrm{GHz}} \sim 10^{23}$ W/Hz and outnumber SF galaxies above $\sim 2 \times 10^{23}$ W/Hz. Detailed multi-wavelength studies (Hickox et al. 2009; Griffith and Stern 2010) yield that radio-AGN are hosted by red galaxies. The evolution out to $z \approx 1.3$ of the radio-AGN fraction for luminous (i.e. $L_{1.4\ \mathrm{GHz}} > 4 \times 10^{23}$ W/Hz) radio-AGN as a function of stellar mass has been presented by Smolčić et al. (2009b) who selected a parent sample of red galaxies with rest-frame $\mathrm{U-B}$ colors in a range close to our quiescent galaxy fraction. The derived AGN-fractions at a given stellar mass within the red galaxy population are therefore applicable to our sample.

According to Smolčić et al. (2009b) (see their Figure 11) the luminous radio-AGN fraction at $0.7 < z < 1.3$ is well below 25 % at all $\log(M_*[M_\odot]) < 11.5$ where it drops quickly to ~ 1 % at $\log(M_*[M_\odot]) = 11$ and continuously to lower levels as stellar mass decreases. At masses lower than $\log(M_*[M_\odot]) = 11$ the radio-AGN fractions are subject to non-negligible evolution between $0 < z < 1$ while the fractions at higher masses increase only mildly. However, given that the radio-AGN fractions are well below 1 % in the former (i.e. low) mass range out to $z \sim 1.3$ it is unlikely that they rise above 10 % at $z \gg 1$. The evolution of the radio-AGN fraction at the high-mass end is much slower but the fractions are high already in the local universe. We therefore set an arbitrary but reasonable threshold and exclude all quiescent objects above $\log(M_*[M_\odot]) = 11.6$, where the expected radio-AGN fraction exceeds 50 %, from our stacking analysis. As the radio-AGN fraction sharply drops below this limit the remainder of our full galaxy sample should be generally free from radio-AGN contamination. Within the highest mass bin probed here ($M_* > 10^{11}\ M_\odot$; see Figure 4.2), however, the average fraction of radio AGN among the quiescent galaxies could still be ~ 25 % at $z > 1$. This fraction appears high but among the entire galaxy population (quiescent and SF sources) the percentage drops to at most 10 % within our highest mass-bin at $z \sim 1$. As shown by I10 globally, but in particular at $M_* > 10^{11}\ M_\odot$ the fraction of quiescent galaxies among the entire sample decreases strongly towards higher redshifts (see also Taylor et al. 2009).[21] An upper bound of 10 % to the potential fraction of radio-AGN within our highest mass-bin hence is a well justified number at $z > 1$.

Due to prominent spectral features we regard the SED-fits for quiescent objects as most

[19] Based on the Salvato et al. (2009) classification that uses an enhanced set of AGN/galaxy templates in order to fit the FUV-to-mid-IR SED and that includes further priors (e.g. variability information) in the fitting procedure while delivering accurate photometric redshifts for all these sources.

[20] Note that Hickox et al. (2009) and Griffith and Stern (2010) yield strong evidence that X-ray and radio selected AGN are mutually distinct populations such that it is actually questionable to remove X-ray selected objects from our samples. We confirmed that our results do not change significantly when including those objects and urge caution to remove more objects if deeper X-ray data compared to the XMM imaging used here is at hand.

[21] The global stellar mass density of quiescent galaxies at $z = 1.5$ is about an order of magnitude lower than the SF one.

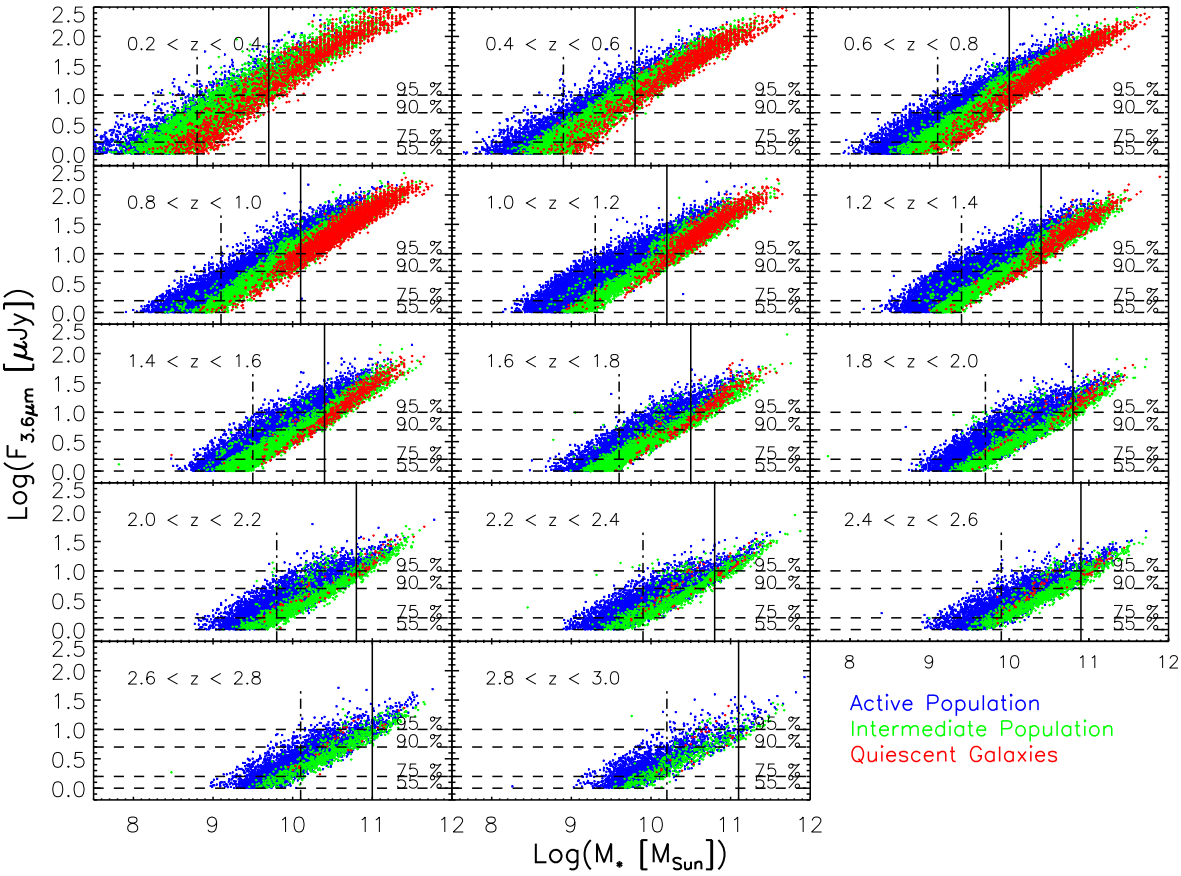

Figure 4.1. – Observed 3.6 μm flux versus stellar mass from SED fits. The 12 panels show photometric redshift bins, as $0.2 \leq z_{\rm phot} \leq 3$ indicated in the upper left part of each panel. Flux densities relate to AB-magnitudes via $m_{\rm AB}(3.6\ \mu{\rm m}) = -2.5\log_{10}(F_{3.6\ \mu{\rm m}}\ [\mu{\rm Jy}]) + 23.9$ (23.9 is the magnitude limit of the catalog). Blue points denote highly active SF systems, with intrinsic rest-frame template colors $({\rm NUV} - r^+)_{\rm temp} < 1.2$; red points denote quiescent (low star formation activity) galaxies with $({\rm NUV} - r^+)_{\rm temp} > 3.5$. Green points are objects of intermediate intrinsic rest-frame color (and hence star formation activity). Horizontal dashed lines mark the levels of the detection completeness, estimated through Monte Carlo simulations of artificial sources (see Section 4.2.6). The vertical dashed-dotted line in each panel denotes the lower mass limit, to which the sample of SF systems (i.e. the union of all blue and green points) is representative of the underlying SF population and the SFR is not affected by the intrinsic catalog incompleteness. The solid vertical line in each panel denotes the mass limit to which the *entire* sample is regarded as representative.

trustworthy such that also the SED-derived SFRs are expected to be accurate for individual objects. These SFRs therefore serve as a prior for revealing potential radio-AGN among the radio-detections in our sample. Hence we correlated our sample with the latest version of the VLA-COSMOS catalog (Schinnerer et al. 2010) and excluded those objects showing radio-derived SFRs more than twice as large as the SED-derived values. We find that the overall number of objects excluded in each sample to be stacked is negligible. The same holds for very luminous ($L_{1.4\ \mathrm{GHz}} > 10^{25}$ W/Hz) radio sources among the radio-detections that are most likely high-power radio-AGN. We therefore excluded also these objects relying on individual photo-z's in order to estimate the radio luminosity. The total fraction of galaxies among all objects in a given bin that we exclude by these two criteria amounts – on average – to less than 0.3 % such that only a fraction of radio detections is rejected. We stress the smallness of this percentage as the advantage of our radio-approach is its insensitivity to dust obscuration which might be challenged by relying on individual optical best-fit SEDs as we partially do when removing some of the radio-detected objects. It should be noted that the high-power radio-AGN candidates are exclusively hosted by red galaxies within our sample. Hence, X-ray detected sources are the only objects that have been removed from our SF samples.

As the radio-based SFR-results presented in this chapter (see Section 4.4) are based on a median stacking approach (see Chapter 3) a minor fraction of contaminating outliers such as AGN is even tolerable. We conclude that contamination of the stacked radio flux densities caused by AGN emission at radio frequencies is not a siginifcant source of uncertainty in the context of this study and that our conclusions would not change if we included the radio-AGN candidates in our analysis.

4.2.6. Completeness considerations

In the following we will discuss the completeness of our (sub-)samples. It is important to distinguish between two kinds of effects. While the full 3.6 μm-selected source catalog (1) is subject to a flux density-dependent level of detection incompleteness we are interested in (2) how representative for the underlying population a given subset of galaxies is at a given mass. Our lower mass limits hence need to be chosen such that the objects at hand remain sufficiently representative.

I10 evaluated the efficiency of the source extraction procedure (and hence the detection completeness) with Monte Carlo simulations of mock point-sources inserted into the 3.6 μm mosaic. At the flux density cut of 1 μJy ($m_{\mathrm{AB}}(3.6\ \mu\mathrm{m}) = 23.9$) the catalog was found to be 55 % complete; 90 % completeness is reached at $F_{3.6\ \mu\mathrm{m}} \approx 5$ μJy ($m_{\mathrm{AB}}(3.6\ \mu\mathrm{m}) = 22.15$). This rather shallow decline in detection completeness towards the magnitude limit is due to source confusion.

Figure 4.1 shows the distribution of 3.6 μm flux density with stellar mass in narrow redshift slices for our source catalog, color coded by the spectral type of the galaxies (see Section 4.2.4). The Monte Carlo detection completeness levels of the catalog are indicated by horizontal dashed black lines starting from the flux density limit at the bottom to the 95 % completeness limit at the top in each panel. Each sub-population shows a clear correlation between 3.6 μm flux density and stellar mass, and the quiescent population residing at the high-mass end at all flux densities. While SF sources (the union of all blue and green data points) span the entire range of 3.6 μm flux densities at all redshifts, hardly any qui-

escent objects with low flux densities are observed at intermediate and high redshifts. We consequently find fewer and fewer low-mass quiescent objects as redshift increases. This is certainly the combined effect of a general absence of such sources at higher redshifts plus the loss of these objects at low flux densities due to the global detection incompleteness of our catalog.

Detection incompleteness affects all sources at a given 3.6 μm flux density, regardless of their spectral type. However, the different distribution of quiescent and SF sources with respect to 3.6 μm flux density necessitates that a different lower mass limit ('*representativeness limit*', hereafter) be adopted, depending on whether we consider the redshift evolution of SF galaxies or that of the entire galaxy population. We now discuss how the limiting mass is set for these two samples:

- In the case of the *entire galaxy population*, it is important to be working with a sample in which the fractional contribution of quiescent and SF sources reflects the true population fractions as closely as possible. The probability that this is the case becomes larger, the better the underlying population is sampled; i.e. it rises with increasing detection completeness. We therefore require an intrinsic catalog completeness of 90 % (corresponding $m_{\rm AB}(3.6\ \mu{\rm m}) = 22.15$) at all masses considered. This is an arbitrary but reasonable threshold as the intrinsic catalog completeness rises rapidly towards higher flux densities.
  In order to evaluate the actual mass representativeness limit we need to define yet another type of completeness level, which we shall refer to as *statistical completeness*. By applying the analytical scheme described in detail in Appendix A.3 we ensure that the statistical completeness of our sample always reaches at least 95 %. This value sets the actual level of representativeness of a given sub-sample. In the following we will also present results for sub-samples below the evaluated mass-limits which will be indicated separately. Those results represent strict upper limits in (S)SFR.

- For studying the *SF population* we need not be as conservative because we are dealing with a *single* sub-population that is subject to less internal variation of SF activity as a (bimodal) sample including both quiescent and SF systems. We thus consider sources down to the limiting flux density of the 3.6 μm catalog when we compute the mass limits at a given redshift. Since this implies that at low stellar masses the flux distribution is sharply cut due to the magnitude limit of our catalog, we still need to use the scheme presented in Appendix A.3 to identify stellar mass limits that provide a representative flux density distribution for SF galaxies. As visible in all panels of Figure 4.1, the lowest mass bin always contains objects over the full range of detection completeness, from 55 % to 100%. One might expect – and the SED fits confirm this – that among galaxies of a given mass, those with the fainter fluxes have lower SSFRs. Failure to include them (due to detection incompleteness) would thus yield average radio-derived SSFRs that are biased towards higher values. We wish to emphasize, however, that our choice of the statistical completeness level ensures that this bias is small above our mass limit and that our samples hence are 'representative' in the sense that they can be expected to render a meaningful measurement of, e.g., the average SSFR of the underlying population.

The stellar mass representativeness limits for the whole sample and the SF systems are marked in Figure 4.1 as vertical lines for each redshift bin in the range $0.2 < z_{\rm phot} < 3$ and

Table 4.1. Stellar mass limits for all/SF galaxies

z	All galaxies $\log(M_*\ [M_\odot])_{\rm lim}$	SF systems $\log(M_*\ [M_\odot])_{\rm lim}$
0.3	9.7	8.8
0.5	9.8	8.9
0.7	10.0	9.1
0.9	10.1	9.1
1.1	10.2	9.3
1.3	10.4	9.4
1.5	10.4	9.5
1.7	10.5	9.6
1.9	10.8	9.7
2.1	10.8	9.8
2.3	10.8	9.9
2.5	10.9	9.9
2.7	11.0	10.1
2.9	11.1	10.2

Note. — The lower stellar mass limits above which our samples are regarded representative. Those limits are as shown in Figure 4.1 and A.1 and have been derived based on the scheme that is detailed in Appendix A.3.

listed in Table 4.1. Note that they increase with redshift. As a consequence, our results will be based on fewer mass bins at high redshift and the aforementioned bias in the lowest mass bin may therefore have a larger impact on fitting trends. Very conservatively speaking, our results for SF objects presented in the following should generally be regarded as most robust at $z \lesssim 1.5$ while evolutionary trends inferred at the high mass end are robust out to our redshift limit of $z = 3$. We will also show results for SF galaxies obtained at masses lower than the individual mass limits and treat them as not entirely representative. Such measurements will be indicated with different symbols in our plots and we will discuss any further implications in Section 4.4.4.

The final sample of galaxies with $m_{\rm AB}(3.6\ \mu{\rm m}) = 23.9$ and $z_{\rm phot} < 3$ consists of 165,213 sources over an effective area of ~ 1.5 deg^2. Figure 3 in I10 shows the redshift distribution with a median of $z_{\rm phot} \sim 1.1$. After adopting a lower redshift limit of $z_{\rm phot} = 0.2$ in order to account for the small local volume sampled by our effective area and our binning scheme 113,610 sources[22] (90,957 SF galaxies) enter our analysis. This is by far the largest galaxy sample used for studying the dependence between SFR and stellar mass throughout cosmic time. Figure 4.2 shows the adopted binning scheme and the number of galaxies contained in each stellar mass and photo-z bin.

[22]This number already considers the upper limiting mass for quiescent galaxies as discussed in Section 4.2.5 and excludes further 328 sources (i.e. 0.3 %) classified as radio-AGN.

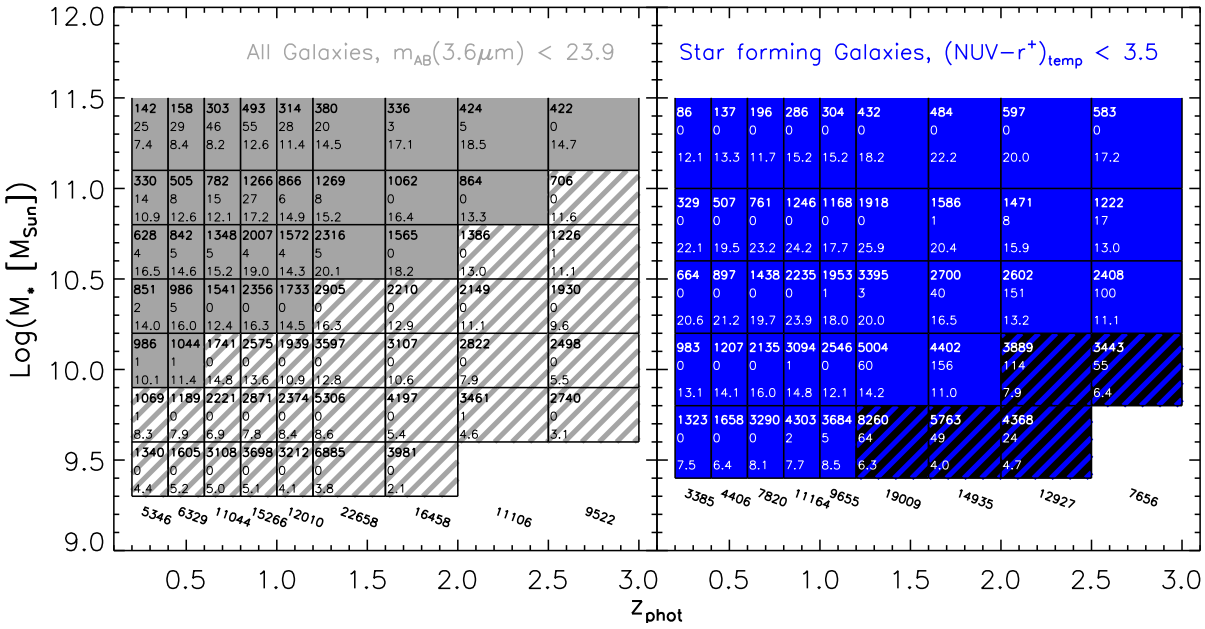

Figure 4.2. – Binning scheme in stellar mass and photometric redshift for the entire (left) and the SF (right) sample. Hatched bins lie below the corresponding limits denoted in Figure 4.1 and are hence regarded representative of the underlying galaxy population. The top number in each box is the total number of galaxies used in the radio stack; the bottom number shows the signal to noise ratio achieved in the radio stack. In the left panel, the middle number is the amount of potential radio-AGN (not detected in the X-ray) that has been excluded from the stack. In the right panel this number gives the amount of optically very faint sources only detected redwards from the K-band. No radio-AGN candidate has been found among the radio-detected sources in the SF sample and only X-ray detected objects have been removed. The total number of galaxies per redshift bin is given below the panels.

4.3. Image stacking at radio continuum wavelengths

The bulk of objects in our $3.6\ \mu$m selected sample is not individually detected in the 1.4 GHz continuum. An estimation of the SFR based on the radio flux density for *every* object in the sample is therefore impossible. On the other hand, studying only radio-detected galaxies in this sample yields effectively a selection by SFR and not by stellar mass since only radio-bright, i.e. highly active star forming, normal galaxies remain.[23] As outlined in the previous chapter similar situations occur frequently in modern galaxy evolution research and are ideally addressed by an image stacking approach.

4.3.1. Median stacking and error estimates

We use the input imaging processing options of our stacking routine to retrieve cutouts with sizes of $40'' \times 40''$, centered on the position of the optical counterpart. Since the COSMOS astrometric reference system was provided by the VLA-COSMOS observations

[23] The currently deepest radio surveys (e.g. Owen and Morrison 2008, with $\mathrm{rms}_{1.4\ \mathrm{GHz}} \sim 3\ \mu$Jy) individually detect galaxies with SFRs $\gtrsim 50\ M_\odot/\mathrm{yr}$ at a redshift of $z = 1$.

the positional accuracy between radio and optical sources should be well within the errors of both datasets. As detailed in Schinnerer et al. (2007) the relative and absolute astrometry of the VLA data are 130 and < 55 mas, respectively. In other words the average distribution of radio flux follows the one at optical wavelengths and the central pixel in any stacked image was always the brightest one. Averaging over pixels located at the same position in each stamp hence is an astrometrically well-defined problem.

In this study median stacking is our method of choice. As outlined in the previous chapter compared to the mean the stacking experiment becomes more robust against outliers allowing the use of the entire input sample.[24]. Non-uniform noise properties within the radio map can also be addressed by applying a weighted scheme to compute the median (see Appendix A.1). White et al. (2007) showed that the median is a well-defined estimator of the mean of the underlying population in the presence of a dominant noise background.

Although, strictly speaking, these arguments only apply to the case of pure point sources, the condition of a dominant noise background is given in our study. One has to be aware of the fact that there is in principle no possibility to access the intrinsic distribution of radio peak fluxes of the underlying population as a whole. The observed distribution merely is the intrinsic one as smeared out by the gaussian noise background. However, it still contains information that needs to be used in order to find proper confidence limits for any statistic applied. Based on the above arguments, we expect the broadened distribution to be not only shifted but also skewed towards positive flux density values. As a result, the uncertainty for the obtained peak flux density is poorly estimated by the background noise in the final stamp. Using a bootstrapping technique (see Appendix A.2) allows us to obtain more realistic, asymmetric error bars for our measured peak flux densities.

4.3.2. Integrated flux densities, luminosities and SFRs from stacked radio images

So far we considered only the average peak flux density which, to first order, would not require to stack individual cutouts but only their central pixel. However, the typical galaxy of a given sample might exhibit extended radio emission. In that case the peak flux density is no longer equivalent to the total source flux but underestimates the typical radio flux density and hence all other quantities derived from it.

The effect of bandwidth smearing (BWS), chromatic aberration caused by the finite bandwidth used during the VLA-COSMOS observations leads to a spatial broadening of a source even if it is intrinsically point-like. Within a single pointing the BWS increases with increasing radial distance from the pointing center and the effect is analytically well determined (e.g. Bondi et al. 2008). For a mosaic like the VLA-COSMOS map that consists of many overlapping pointings the effect becomes analytically unpredictable due to the varying uncertainties introduced by the calibration and observing conditions.

[24] We applied the different stacking techniques discussed above to some of our sub-samples. We found the median flux densities obtained to be within $\lesssim 7$ % of those obtained when using a mean stacking technique that excludes radio-stamps including extended foreground features. For the mean stack we co-added objects in a given sub-sample that are not individually detected in the radio imaging and the flux density of the detected sources has been added to the flux density obtained from the stack in a noise-weighted fashion. This ensures that those objects that are not individually radio-detected – i.e. the bulk of our sources – are most strongly weighted

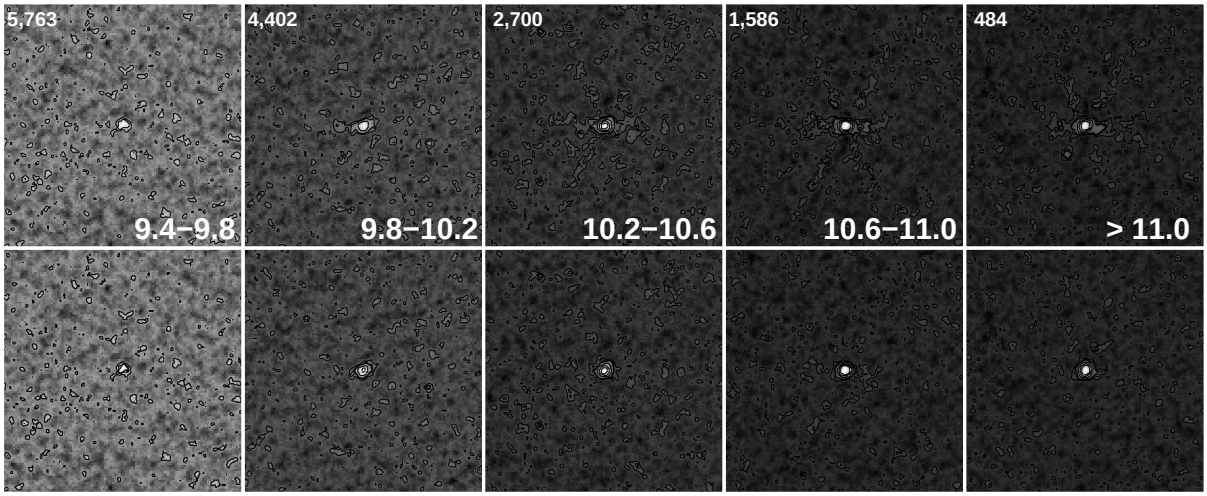

Figure 4.3. – Examples for $40'' \times 40''$ (i.e. (115×115) pixels) 1.4 GHz postage stamp images obtained via median stacking of star forming galaxies (see Section 4.2.4) in the redshift bin between $1.6 < z < 2$. The number of galaxies for which individual radio cutout images from the VLA-COSMOS map (resolution of $1.5'' \times 1.4''$) have been co-added is given at the upper left of each stamp in the top row while the number at the lower right denotes the bin extent in $\log(M_* \ [M_\odot])$. Due to the high signal-to-noise ratios (SNRs) achieved, generally, a clear (dirty) beam pattern is visible. The bottom row shows the corresponding CLEANed stamps (see Section 4.3.2, for details). Contour levels are at 2, 4, $5\sigma_{\rm bg}$ and followed by steps of $5\sigma_{\rm bg}$. (The individual SNRs are given in Figure 4.2 and flux densities measured as well as the background noise levels reached are listed in Table 4.3).

For all our samples we constructed median co-added cutout images (Figure 6.7) and determined accurate RMS-noise estimates (hereafter $\sigma_{\rm Stack}$) for the image stacks by averaging over adequate off-centure aperture tiles. These (115×115) pixel^2 dirty maps were processed within AIPS.[25]

We used the task PADIM to make the stacked images equal in size to a (512×512) pixel^2 image of the VLA-COSMOS synthesized (dirty) beam by filling the outer image frame with additional pixels of constant value The task APCLN with a circular CLEAN box of radius of seven pixels (i.e. $2.45''$) around the central component was then used to CLEAN each dirty map down to a flux density threshold of $2.5 \times \sigma_{\rm Stack}$[26].

Integrated flux densities, as well as source dimensions and position angles after deconvolution with the CLEAN beam were obtained by fitting a single-component Gaussian elliptical model to the CLEAN image within a quadratic box of (15×15) pixel^2 around the central pixel using the task JMFIT. Errors on the integrated flux densities have been estimated according to Hopkins et al. (2003) and rely on the combined information on the best-fit source model

[25] Note that only bright (> 45 μJy) radio sources have been CLEANed in the individual pointings prior to the assembly of the final mosaic. Hence, a stack of fainter sources will display a clear beam pattern as seen in Figure 6.7 which must be deconvolved.

[26] This is a conservative threshold. We confirmed that this choice does not lead to systematic biases by CLEANing individual stacked images down to $1 \times \sigma_{\rm Stack}$. Integrated flux densities obtained from both approaches do not differ by more than 3 % and do not lead to mass-dependent effects. The mentioned fluctuations are well within the error margins.

and the bootstrapping results from the image stacking:

$$\frac{\sigma_{\mathrm{Total}}}{\langle F_{\mathrm{Total}}\rangle} = \sqrt{\left(\frac{\sigma_{\mathrm{data}}}{\langle F_{\mathrm{Total}}\rangle}\right)^2 + \left(\frac{\sigma_{\mathrm{fit}}}{\langle F_{\mathrm{Total}}\rangle}\right)^2}, \tag{4.1}$$

where (Windhorst et al. 1984; Condon 1997 and also the explanations in Schinnerer et al. 2004, 2010)

$$\frac{\sigma_{\mathrm{data}}}{\langle F_{\mathrm{Total}}\rangle} = \sqrt{\left(\frac{S}{N}\right)^{-2} + \left(\frac{1}{100}\right)^2} \tag{4.2}$$

$$\frac{\sigma_{\mathrm{fit}}}{\langle F_{\mathrm{Total}}\rangle} = \sqrt{\frac{2}{\rho_S} + \left(\frac{\theta_{\mathrm{B}}\theta_{\mathrm{b}}}{\theta_{\mathrm{M}}\,\theta_{\mathrm{m}}}\right)\left(\frac{2}{\rho_\psi^2} + \frac{2}{\rho_\phi^2}\right)}. \tag{4.3}$$

$\theta_{\mathrm{M}} = 1.5''$ is the major axis and $\theta_{\mathrm{m}} = 1.4''$ the minor axis of the beam while θ_{M} and θ_{m} are the major and minor axis of the measured (hence convolved) flux density distribution. In order to include the bootstrapping error estimates we set $S/N = \langle F_{\mathrm{peak}}\rangle/\sigma_{\mathrm{bs}}$, i.e. the ratio of the peak flux density in the stacked dirty map and the 68 % confidence interval resulting from the bootstrapping. The same applies to the parameter-dependent estimators of the fit entering equation (4.3) that are given by:

$$\rho_X^2 = \frac{\theta_{\mathrm{M}}\,\theta_{\mathrm{m}}}{4\,\theta_{\mathrm{B}}\theta_{\mathrm{b}}}\left(1 + \frac{\theta_{\mathrm{B}}}{\theta_{\mathrm{M}}}\right)^a \left(1 + \frac{\theta_{\mathrm{b}}}{\theta_{\mathrm{m}}}\right)^b \left(\frac{S}{N}\right)^2 \tag{4.4}$$

and $a = b = 1.5$ for ρ_F, $a = 2.5$ and $b = 0.5$ for ρ_{M} as well as $a = 0.5$ and $b = 2.5$ for ρ_{m}.

For a given sub-sample centered at a given median redshift $\langle z_{\mathrm{phot}}\rangle$ the average (median stacking based) integrated flux density $\langle F_{\mathrm{Total}}\rangle$ observed at 1.4 GHz can be directly converted into a rest-frame 1.4 GHz luminosity using a K-correction that depends on the radio spectral index α_{rc} (here $\alpha_{\mathrm{rc}} = -0.8$, e.g. Condon 1992):

$$\begin{aligned}\langle L_{1.4\ \mathrm{GHz}}\rangle\ [\mathrm{W/Hz}] &= 9.52 \times 10^{12}\,\langle F_{\mathrm{Total}}\rangle\ [\mu\mathrm{Jy}] \\ &\times \left(D_L\ [\mathrm{Mpc}]\right)^2 4\pi \left(1 + \langle z_{\mathrm{phot}}\rangle\right)^{-(1+\alpha_{\mathrm{rc}})}\end{aligned} \tag{4.5}$$

with D_L the luminosity distance at this median photo-z of all objects inside the bin.

It was pointed out by Dunne et al. (2009) that the median redshift might not be appropriate for estimating the radio luminosity if the peak of the radio flux density distribution does not coincide with the median of the photo-z distribution. They overcame this problem by deriving (and subsequently effectively stacking) luminosities according to Eq. (4.5) for all objects relying both on the individual photo-z's and peak flux density measurements at the pixel corresponding to the position in the input catalog. At $z > 0.2$ they afterwards applied a common (i.e. redshift independent) factor to the median of all obtained luminosities to correct for the difference between peak and total flux density as well as for the effect of BWS. A similar approach was recently also used by Bourne et al. (2010). The method by Dunne et al. (2009) is justified given their data as they find for $z > 0.2$ that the ratio of total to peak flux density does not change significantly, in particular not as a function of K-band magnitude. However, our data does not yield such a uniform behavior with respect to mass in the correction factor as Figure 4.4 shows. Indeed, if we were to state an average peak to total flux density conversion it would be a function of mass.

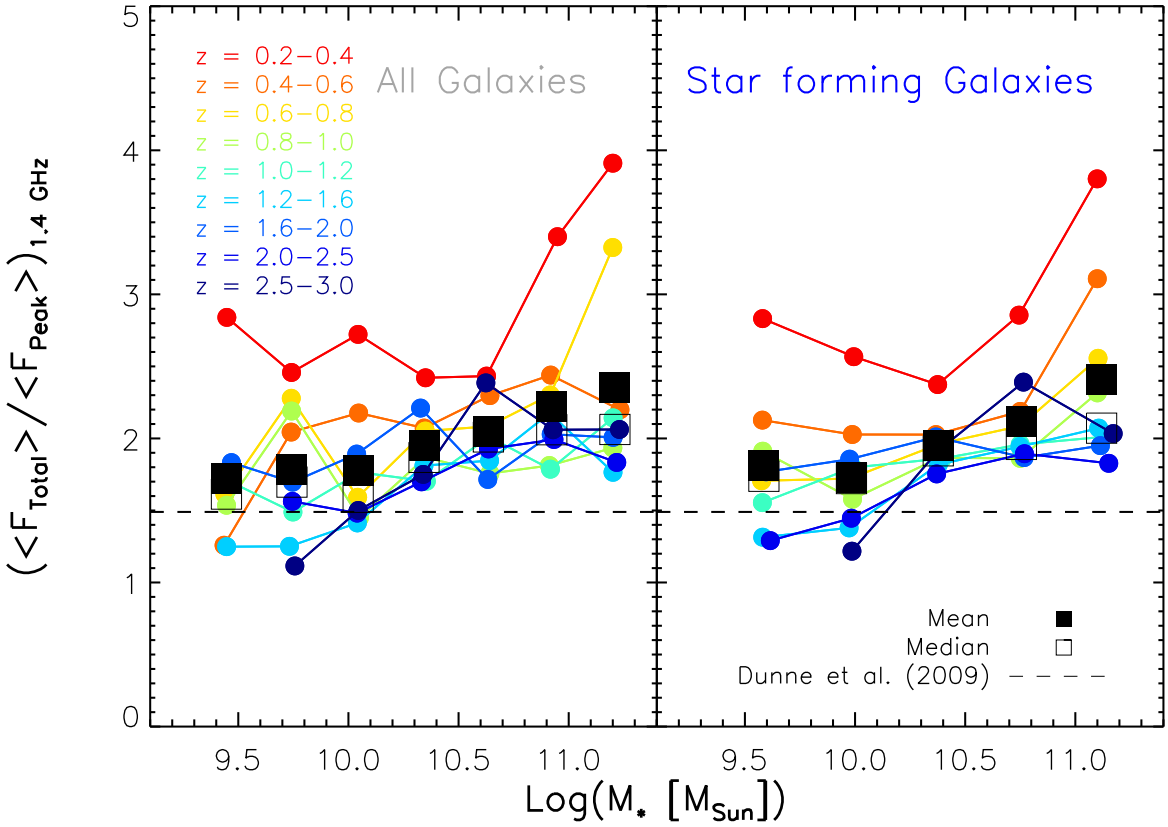

Figure 4.4. – Ratio of integrated to peak flux density at 1.4 GHz of the stacked radio images for different sample sub-sets. The left panel shows results for the entire sample, the right panel the sub-set of blue (SF) galaxies. The data is color-coded by redshift and the dashed black line depicts the uniform correction factor used in the radio stacking study by Dunne et al. (2009). It is evident that the extent of radio emission is not uniform across our samples because our radio imaging has a higher angular resolution compared to the VLA map used by Dunne et al. (2009). All measured data points are listed in Table 4.2 and 4.3.

An explanation for the discrepancy of our findings compared to Dunne et al. (2009) can be found in the use of higher resolved A-array data in our case compared to the B-array data constituting their radio continuum imaging. Hence, both results are correct given the respective data used and show that higher resolution radio data needs to be treated differently. The spread in conversion factors within our sub-samples is large and lower redshift objects show a significantly larger $\langle F_{\rm Total}\rangle/\langle F_{\rm Peak}\rangle$ ratio[27] (see Figure 4.4). Moreover, further variations might arise depending on the galaxy population studied. Hence, if high-resolution data is used, results are more robust when first total flux densities are individually derived for any radio stacking experiment before computing radio luminosities. As it is apparent from the Dunne et al. (2009) results their method should be considered, how-

[27]Note that a larger conversion factor is equivalent to a larger source extent. Since it is unlikely that the varying number counts in our sub-samples are responsible for mass- or redshift-dependent source sizes we infer that higher mass objects are intrinsically more extended at all redshifts compared to their lower mass siblings. The larger correction factors at lower z can be explained by the increasing angular diameter distance towards higher z.

ever, if stacking is used to infer the average radio luminosity of an entire galaxy population with a broad redshift distribution ($\Delta z \gtrsim 1$). As our broadest bins in redshift have $\Delta z = 0.5$ – and this only at $z \gg 1$ where they span a much smaller range in time – it is indeed more accurate to rely on our approach given our radio imaging.

In order to convert the derived average 1.4 GHz luminosities into average SFRs we use the calibration of the radio-FIR correlation by Bell (2003a) scaled to a Chabrier IMF[28]:

$$\langle \mathrm{SFR} \rangle \; [M_\odot/yr] = \begin{cases} 3.18 \times 10^{-22}\, L & , \; L > L_c \\ \frac{3.18 \times 10^{-22}\, L}{0.1 + 0.9\,(L/L_c)^{0.3}} & , L \leq L_c \end{cases} \tag{4.6}$$

where $L = \langle L_{1.4\ \mathrm{GHz}} \rangle$ is the average radio luminosity derived from the median stack according to Eq. (4.5) and $L_c = 6.4 \times 10^{21}$ W/Hz is the radio luminosity of an L_*-like galaxy. As Bell (2003a) empirically argues the low-luminosity population needs to be treated separately from higher values of radio luminosities since non-thermal radio emission might be significantly suppressed in these galaxies. Even though our work exploits the radio-faint regime our derived average 1.4 GHz luminosities lie generally above this threshold. Only at the lowest masses and $z \lesssim 0.8$ we find $\langle L_{1.4\ \mathrm{GHz}} \rangle < L_c$ (see Table 4.2 and 4.3). Any study relying on the calibration by Yun et al. (2001) is, consequently, directly comparable to our results as Yun et al. (2001) used a uniform normalization very similar to the case $L > L_c$ in Eq. (4.6).[29] According to Bell (2003a) individual objects scatter about the average calibration by about a factor of two. It is not necessary to include this dispersion in the estimation of the final uncertainty on the SFR computed from the stack since the latter involves a sufficiently large number of sources to ensure that the average relation is representative. We do not attempt to take the differences of the derived SFRs caused by the discrepancy of the mentioned calibrations into consideration for the error estimates of our results. We also neglect any uncertainty on the median photo-z so that all errors on the derived SFRs result from propagation of the errors derived using equation (4.1).[30]

Finally, for a given sample, specific SFRs are computed as the ratio of the SFR and the median stellar mass. Based on the same arguments as before we neither take into account an uncertainty in the median mass for the error estimates of our derived SSFRs. As we exclusively deal with average quantities in this work we omit the $\langle\rangle$-notation in the following.

4.4. The Specific SFR (SSFR) of mass-selected galaxies over cosmic time from radio stacking

In the remaining parts of this chapter we present our measurements of the SSFR-M_* relation (this Section) and discuss their implications for the evolution of the cosmic SFR density (see Section 5.1).

[28] Bell (2003a) adopts a Salpeter initial mass function with IMF $\propto M^{-2.35}$ in the mass range from 0.1 to 100 $M_\odot$ so that we divide his normalization by 1.74.

[29] A radio luminosity independent calibration has also been presented by Condon (1992). We refer to Dunne et al. (2009) who present all their results using both the Bell (2003a) and Condon (1992) calibration.

[30] This is justified as this error scales with the number of objects as $1/\sqrt{N}$ where $N \gg 10^2$ given our binning scheme.

Table 4.2. Radio stacking results for *the entire mass-selected sample*

$\Delta \log(M_*)$ M_* [$M_\odot$]	$\langle \log(M_*) \rangle$ M_* [$M_\odot$]	$\Delta z_{\rm phot}$	$\langle z_{\rm phot} \rangle$	$\langle F_{\rm Peak} \rangle$ [μJy/beam]	$\langle F_{\rm Total} \rangle$ [μJy]	rms [μJy/beam]	$\langle L_{1.4\ \rm GHz} \rangle / L_c$ $L_c = 6.4 \times 10^{21}$ W/Hz	$\langle$SFR$\rangle$ [$M_\odot$/yr]
9.3-9.6	9.45†	0.2-0.4	0.27	$1.7^{+0.3}_{-0.4}$	$4.9^{+1.4}_{-2.2}$	$0.399^{+0.015}_{-0.002}$	$0.2^{+0.0}_{-0.1}$	$0.6^{+0.1}_{-0.2}$
	9.44†	0.4-0.6	0.49	$2.0^{+0.4}_{-0.3}$	$2.5^{+1.1}_{-1.0}$	$0.388^{+0.006}_{-0.006}$	$0.3^{+0.1}_{-0.1}$	$0.9^{+0.3}_{-0.3}$
	9.44†	0.6-0.8	0.69	$1.4^{+0.2}_{-0.3}$	$2.2^{+1.2}_{-1.9}$	$0.276^{+0.004}_{-0.006}$	$0.6^{+0.4}_{-0.6}$	$1.5^{+0.6}_{-1.0}$
	9.45†	0.8-1.0	0.89	$1.3^{+0.2}_{-0.3}$	$1.9^{+0.5}_{-0.9}$	$0.246^{+0.007}_{-0.013}$	$1.0^{+0.3}_{-0.5}$	$2.1^{+0.5}_{-1.0}$
	9.44†	1.0-1.2	1.11	$1.1^{+0.3}_{-0.2}$	$1.9^{+1.6}_{-1.2}$	$0.275^{+0.005}_{-0.010}$	$1.7^{+1.4}_{-1.1}$	$3.5^{+2.8}_{-2.3}$
	9.45†	1.2-1.6	1.40	$0.7^{+0.2}_{-0.1}$	$0.9^{+0.5}_{-0.4}$	$0.179^{+0.001}_{-0.003}$	$1.4^{+0.9}_{-0.6}$	$2.8^{+1.8}_{-1.2}$
	9.47†	1.6-2.0	1.78	$0.5^{+0.2}_{-0.3}$	$0.9^{+0.8}_{-1.0}$	$0.243^{+0.004}_{-0.006}$	$2.6^{+2.3}_{-2.8}$	$5.2^{+4.6}_{-5.7}$
9.6-9.9	9.74†	0.2-0.4	0.27	$3.9^{+0.6}_{-0.2}$	$9.6^{+2.5}_{-1.0}$	$0.469^{+0.017}_{-0.033}$	$0.3^{+0.1}_{-0.0}$	$0.9^{+0.2}_{-0.1}$
	9.74†	0.4-0.6	0.49	$3.6^{+0.3}_{-0.4}$	$7.4^{+1.3}_{-1.9}$	$0.455^{+0.010}_{-0.004}$	$1.0^{+0.2}_{-0.2}$	$2.0^{+0.3}_{-0.4}$
	9.74†	0.6-0.8	0.69	$2.4^{+0.2}_{-0.3}$	$5.4^{+0.9}_{-1.3}$	$0.341^{+0.028}_{-0.002}$	$1.6^{+0.3}_{-0.4}$	$3.2^{+0.6}_{-0.8}$
	9.74†	0.8-1.0	0.89	$2.1^{+0.3}_{-0.2}$	$4.5^{+1.4}_{-0.9}$	$0.265^{+0.002}_{-0.010}$	$2.4^{+0.8}_{-0.5}$	$4.9^{+1.6}_{-0.9}$
	9.75†	1.0-1.2	1.10	$2.7^{+0.3}_{-0.3}$	$4.0^{+1.4}_{-1.3}$	$0.320^{+0.022}_{-0.005}$	$3.5^{+1.3}_{-1.2}$	$7.2^{+2.6}_{-2.4}$
	9.73†	1.2-1.6	1.41	$1.9^{+0.2}_{-0.3}$	$2.3^{+1.1}_{-1.4}$	$0.216^{+0.006}_{-0.007}$	$3.7^{+1.8}_{-2.3}$	$7.6^{+3.6}_{-4.7}$
	9.75†	1.6-2.0	1.82	$1.3^{+0.2}_{-0.2}$	$2.1^{+1.0}_{-1.0}$	$0.232^{+0.003}_{-0.015}$	$6.2^{+3.0}_{-3.1}$	$12.7^{+6.0}_{-6.2}$
	9.75†	2.0-2.5	2.21	$1.3^{+0.2}_{-0.3}$	$2.0^{+0.7}_{-0.8}$	$0.271^{+0.015}_{-0.008}$	$8.9^{+3.0}_{-3.8}$	$18.2^{+6.1}_{-7.6}$
	9.76†	2.5-3.0	2.65	$0.9^{+0.2}_{-0.3}$	$1.0^{+0.5}_{-0.6}$	$0.293^{+0.005}_{-0.005}$	$6.9^{+3.3}_{-4.2}$	$14.1^{+6.6}_{-8.6}$
9.9-10.2	10.04*	0.2-0.4	0.27	$5.1^{+0.6}_{-0.5}$	$13.8^{+2.9}_{-2.4}$	$0.504^{+0.014}_{-0.008}$	$0.5^{+0.1}_{-0.1}$	$1.2^{+0.2}_{-0.2}$
	10.05*	0.4-0.6	0.49	$5.4^{+0.5}_{-0.5}$	$11.8^{+2.1}_{-2.2}$	$0.472^{+0.016}_{-0.022}$	$1.5^{+0.3}_{-0.3}$	$3.1^{+0.6}_{-0.6}$
	10.04†	0.6-0.8	0.68	$5.3^{+0.2}_{-0.5}$	$8.5^{+0.7}_{-1.7}$	$0.360^{+0.011}_{-0.013}$	$2.4^{+0.2}_{-0.5}$	$5.0^{+0.4}_{-1.0}$
	10.05†	0.8-1.0	0.89	$3.9^{+0.2}_{-0.4}$	$5.7^{+0.8}_{-1.5}$	$0.288^{+0.005}_{-0.009}$	$3.1^{+0.4}_{-0.8}$	$6.3^{+0.9}_{-1.7}$
	10.05†	1.0-1.2	1.09	$4.0^{+0.3}_{-0.4}$	$7.0^{+1.4}_{-1.6}$	$0.364^{+0.002}_{-0.004}$	$6.1^{+1.2}_{-1.4}$	$12.5^{+2.5}_{-2.9}$
	10.04†	1.2-1.6	1.39	$3.3^{+0.2}_{-0.2}$	$4.7^{+1.0}_{-1.0}$	$0.260^{+0.003}_{-0.006}$	$7.3^{+1.6}_{-1.5}$	$14.8^{+3.2}_{-3.0}$
	10.04†	1.6-2.0	1.87	$2.9^{+0.2}_{-0.2}$	$5.5^{+0.8}_{-0.8}$	$0.274^{+0.005}_{-0.003}$	$17.0^{+2.6}_{-2.4}$	$34.6^{+5.2}_{-4.9}$
	10.04†	2.0-2.5	2.28	$2.2^{+0.2}_{-0.3}$	$3.2^{+0.9}_{-1.1}$	$0.277^{+0.006}_{-0.003}$	$15.9^{+4.3}_{-5.5}$	$32.4^{+8.8}_{-11.2}$
	10.04†	2.5-3.0	2.73	$1.7^{+0.3}_{-0.3}$	$2.5^{+1.3}_{-1.2}$	$0.308^{+0.004}_{-0.007}$	$18.8^{+9.3}_{-8.8}$	$38.2^{+18.9}_{-17.9}$
10.2-10.5	10.35	0.2-0.4	0.29	$7.5^{+0.5}_{-0.4}$	$18.1^{+2.4}_{-1.7}$	$0.534^{+0.016}_{-0.005}$	$0.7^{+0.1}_{-0.1}$	$1.6^{+0.2}_{-0.1}$
	10.34	0.4-0.6	0.49	$7.9^{+0.4}_{-0.4}$	$16.4^{+1.9}_{-1.8}$	$0.495^{+0.010}_{-0.018}$	$2.1^{+0.2}_{-0.2}$	$4.3^{+0.5}_{-0.5}$
	10.35*	0.6-0.8	0.68	$4.8^{+0.5}_{-0.5}$	$9.8^{+2.2}_{-2.1}$	$0.386^{+0.025}_{-0.009}$	$2.8^{+0.6}_{-0.6}$	$5.7^{+1.3}_{-1.2}$
	10.35*	0.8-1.0	0.89	$5.1^{+0.4}_{-0.4}$	$9.5^{+1.7}_{-1.6}$	$0.311^{+0.005}_{-0.006}$	$5.1^{+0.9}_{-0.9}$	$10.5^{+1.9}_{-1.8}$
	10.35*	1.0-1.2	1.09	$5.4^{+0.3}_{-0.3}$	$9.2^{+1.3}_{-1.2}$	$0.375^{+0.020}_{-0.009}$	$8.1^{+1.1}_{-1.0}$	$16.6^{+2.3}_{-2.1}$
	10.34†	1.2-1.6	1.38	$4.6^{+0.4}_{-0.3}$	$8.3^{+1.5}_{-1.4}$	$0.279^{+0.001}_{-0.012}$	$12.5^{+2.3}_{-2.1}$	$25.4^{+4.7}_{-4.2}$
	10.33†	1.6-2.0	1.81	$4.2^{+0.4}_{-0.2}$	$9.3^{+1.7}_{-1.0}$	$0.325^{+0.008}_{-0.009}$	$26.8^{+4.8}_{-2.9}$	$54.5^{+9.7}_{-5.9}$
	10.33†	2.0-2.5	2.36	$3.7^{+0.4}_{-0.4}$	$6.2^{+1.5}_{-1.5}$	$0.330^{+0.025}_{-0.006}$	$33.0^{+8.1}_{-7.8}$	$67.1^{+16.4}_{-15.9}$
	10.34†	2.5-3.0	2.81	$3.3^{+0.3}_{-0.6}$	$5.8^{+1.2}_{-2.3}$	$0.343^{+0.009}_{-0.005}$	$45.5^{+9.4}_{-18.5}$	$92.6^{+19.2}_{-37.6}$
10.5-10.8	10.63	0.2-0.4	0.28	$9.8^{+0.7}_{-0.7}$	$23.9^{+3.1}_{-2.9}$	$0.594^{+0.027}_{-0.019}$	$0.9^{+0.1}_{-0.1}$	$1.8^{+0.2}_{-0.2}$
	10.64	0.4-0.6	0.48	$8.1^{+0.8}_{-0.4}$	$18.6^{+3.4}_{-2.0}$	$0.555^{+0.010}_{-0.026}$	$2.4^{+0.4}_{-0.2}$	$4.8^{+0.9}_{-0.5}$
	10.63	0.6-0.8	0.69	$6.4^{+0.4}_{-0.6}$	$13.3^{+1.6}_{-2.7}$	$0.420^{+0.006}_{-0.020}$	$3.9^{+0.5}_{-0.8}$	$7.9^{+0.9}_{-1.6}$
	10.64	0.8-1.0	0.89	$6.3^{+0.4}_{-0.5}$	$11.1^{+1.5}_{-2.0}$	$0.331^{+0.002}_{-0.010}$	$6.0^{+0.8}_{-1.1}$	$12.2^{+1.6}_{-2.2}$
	10.64	1.0-1.2	1.09	$5.6^{+0.4}_{-0.4}$	$11.3^{+1.7}_{-1.7}$	$0.391^{+0.013}_{-0.016}$	$9.8^{+1.5}_{-1.5}$	$20.0^{+3.0}_{-3.0}$
	10.64*	1.2-1.6	1.37	$6.2^{+0.5}_{-0.4}$	$11.4^{+2.0}_{-1.9}$	$0.308^{+0.004}_{-0.004}$	$17.1^{+3.0}_{-2.8}$	$34.7^{+6.1}_{-5.7}$
	10.63*	1.6-2.0	1.78	$6.9^{+0.4}_{-0.3}$	$11.8^{+1.6}_{-1.1}$	$0.378^{+0.017}_{-0.009}$	$32.6^{+4.4}_{-3.0}$	$66.3^{+9.0}_{-6.1}$
	10.64†	2.0-2.5	2.27	$5.2^{+0.3}_{-0.3}$	$10.0^{+1.2}_{-1.4}$	$0.400^{+0.008}_{-0.008}$	$48.3^{+6.0}_{-6.6}$	$98.3^{+12.3}_{-13.4}$
	10.62†	2.5-3.0	2.76	$4.9^{+0.5}_{-0.6}$	$11.6^{+2.6}_{-2.6}$	$0.437^{+0.003}_{-0.012}$	$88.4^{+19.6}_{-20.0}$	$179.7^{+39.8}_{-40.6}$
10.8-11.1	10.95	0.2-0.4	0.27	$9.6^{+1.0}_{-1.0}$	$32.7^{+5.4}_{-5.1}$	$0.882^{+0.009}_{-0.007}$	$1.1^{+0.2}_{-0.2}$	$2.2^{+0.4}_{-0.4}$
	10.92	0.4-0.6	0.48	$9.2^{+0.6}_{-0.4}$	$22.5^{+2.6}_{-2.0}$	$0.733^{+0.030}_{-0.009}$	$2.8^{+0.3}_{-0.2}$	$5.7^{+0.7}_{-0.5}$
	10.92	0.6-0.8	0.69	$6.7^{+0.7}_{-0.7}$	$15.5^{+3.2}_{-3.0}$	$0.556^{+0.034}_{-0.013}$	$4.5^{+0.9}_{-0.9}$	$9.2^{+1.9}_{-1.8}$
	10.91	0.8-1.0	0.90	$7.1^{+0.5}_{-0.3}$	$12.8^{+1.8}_{-1.1}$	$0.412^{+0.025}_{-0.014}$	$7.0^{+1.0}_{-0.6}$	$14.3^{+2.0}_{-1.3}$
	10.92	1.0-1.2	1.10	$7.6^{+0.5}_{-0.4}$	$13.6^{+1.8}_{-1.6}$	$0.509^{+0.008}_{-0.011}$	$12.1^{+1.6}_{-1.5}$	$24.6^{+3.2}_{-3.0}$
	10.91	1.2-1.6	1.36	$6.3^{+0.6}_{-0.6}$	$13.7^{+2.5}_{-2.5}$	$0.417^{+0.010}_{-0.008}$	$20.2^{+3.7}_{-3.7}$	$41.0^{+7.4}_{-7.5}$
	10.92	1.6-2.0	1.79	$7.8^{+0.3}_{-0.3}$	$15.9^{+1.4}_{-1.2}$	$0.479^{+0.003}_{-0.005}$	$44.5^{+3.9}_{-3.4}$	$90.5^{+7.8}_{-6.8}$
	10.93*	2.0-2.5	2.21	$6.9^{+0.5}_{-0.4}$	$13.8^{+2.0}_{-1.6}$	$0.523^{+0.012}_{-0.009}$	$63.1^{+8.9}_{-7.4}$	$128.4^{+18.1}_{-15.1}$
	10.93†	2.5-3.0	2.72	$6.8^{+0.5}_{-0.7}$	$14.0^{+2.0}_{-3.0}$	$0.583^{+0.013}_{-0.036}$	$102.3^{+14.6}_{-21.7}$	$207.9^{+29.6}_{-44.1}$
> 11.1	11.20	0.2-0.4	0.27	$9.2^{+0.9}_{-1.9}$	$36.0^{+5.5}_{-10.8}$	$1.250^{+0.047}_{-0.038}$	$1.2^{+0.2}_{-0.4}$	$2.5^{+0.4}_{-0.8}$
	11.23	0.4-0.6	0.48	$10.3^{+2.0}_{-3.2}$	$22.6^{+8.4}_{-13.0}$	$1.227^{+0.008}_{-0.025}$	$2.8^{+1.0}_{-1.6}$	$5.7^{+2.1}_{-3.3}$
	11.20	0.6-0.8	0.69	$7.3^{+1.2}_{-1.2}$	$24.4^{+6.1}_{-6.5}$	$0.897^{+0.010}_{-0.007}$	$7.1^{+1.8}_{-1.9}$	$14.4^{+3.6}_{-3.8}$
	11.20	0.8-1.0	0.90	$8.6^{+0.9}_{-1.0}$	$16.6^{+3.6}_{-4.0}$	$0.681^{+0.013}_{-0.009}$	$9.2^{+2.0}_{-2.2}$	$18.7^{+4.0}_{-4.5}$
	11.20	1.0-1.2	1.10	$10.1^{+0.7}_{-0.8}$	$21.6^{+2.8}_{-3.1}$	$0.881^{+0.018}_{-0.013}$	$19.3^{+2.5}_{-2.8}$	$39.2^{+5.1}_{-5.7}$
	11.20	1.2-1.6	1.35	$11.1^{+0.9}_{-1.1}$	$19.6^{+3.5}_{-4.3}$	$0.762^{+0.012}_{-0.022}$	$28.2^{+5.1}_{-6.2}$	$57.4^{+10.3}_{-12.5}$
	11.20	1.6-2.0	1.78	$14.3^{+0.7}_{-1.0}$	$28.7^{+3.0}_{-4.0}$	$0.835^{+0.022}_{-0.009}$	$79.7^{+8.4}_{-11.0}$	$162.0^{+17.1}_{-22.4}$
	11.22	2.0-2.5	2.22	$13.7^{+1.1}_{-0.9}$	$25.0^{+4.1}_{-3.6}$	$0.737^{+0.023}_{-0.025}$	$115.3^{+18.9}_{-16.5}$	$234.4^{+38.5}_{-33.6}$
	11.23*	2.5-3.0	2.71	$11.3^{+0.9}_{-0.8}$	$23.2^{+3.8}_{-3.5}$	$0.767^{+0.021}_{-0.030}$	$169.4^{+27.8}_{-25.7}$	$344.4^{+56.5}_{-52.3}$

Note. — Median stacking-based average 1.4 GHz radio flux densities and derived average quantities for all our bins in mass and redshift for *the entire mass-selected sample*. A Chabrier (2003) IMF is assumed. Radio luminosities are stated in units of L_c, the threshold luminosity below which Bell (2003a) empirically found the non-thermal radio emission to be suppressed (see Eq. (4.6)). Resulting SFRs from bins with lower radio luminosity are hence boosted compared to, e.g., the calibration of the radio-IR relation by Yun et al. (2001). The median stellar mass and median z for any given bin are also stated.

† Mass bin contains data below the limit of mass representativeness and yields an upper limit to the average SFR (see Section 4.2.6 for further details.)

* First mass bin above the limit of representativeness (see Section 4.2.6) which contains a low fraction (< 15 %) of optically faint objects with $m_{AB}(i^+) \geq 25.5$ for which the photo-z accuracy is degraded (see Section 4.2.2 for further details).

Table 4.3. Radio stacking results for *star forming systems*

$\Delta\log(M_*)$ M_* [$M_\odot$]	$\langle\log(M_*)\rangle$ M_* [$M_\odot$]	$\Delta z_{\rm phot}$	$\langle z_{\rm phot}\rangle$	$\langle F_{\rm Peak}\rangle$ [μJy/beam]	$\langle F_{\rm Total}\rangle$ [μJy]	rms [μJy/beam]	$\langle L_{1.4\ \rm GHz}\rangle/L_c$ $L_c = 6.4\times10^{21}$ W/Hz	$\langle$SFR$\rangle$ [$M_\odot$/yr]
9.4-9.8	9.58	0.2-0.4	0.28	$3.1^{+0.5}_{-0.5}$	$8.7^{+2.3}_{-2.2}$	$0.408^{+0.001}_{-0.002}$	$0.3^{+0.1}_{-0.1}$	$0.9^{+0.2}_{-0.2}$
	9.58	0.4-0.6	0.49	$2.4^{+0.2}_{-0.4}$	$5.1^{+1.4}_{-2.0}$	$0.372^{+0.016}_{-0.033}$	$0.7^{+0.2}_{-0.3}$	$1.5^{+0.3}_{-0.5}$
	9.58	0.6-0.8	0.69	$2.1^{+0.3}_{-0.2}$	$3.6^{+1.2}_{-0.7}$	$0.258^{+0.009}_{-0.002}$	$1.0^{+0.3}_{-0.2}$	$2.1^{+0.7}_{-0.4}$
	9.58	0.8-1.0	0.89	$1.7^{+0.2}_{-0.2}$	$3.2^{+0.7}_{-1.0}$	$0.219^{+0.004}_{-0.006}$	$1.7^{+0.4}_{-0.5}$	$3.6^{+0.8}_{-1.1}$
	9.58*	1.0-1.2	1.10	$2.1^{+0.3}_{-0.2}$	$3.2^{+1.0}_{-0.7}$	$0.246^{+0.006}_{-0.009}$	$2.9^{+0.9}_{-0.6}$	$5.9^{+1.9}_{-1.2}$
	9.58†	1.2-1.6	1.40	$1.1^{+0.2}_{-0.2}$	$1.4^{+0.5}_{-0.5}$	$0.169^{+0.001}_{-0.004}$	$2.2^{+0.8}_{-0.8}$	$4.5^{+1.7}_{-1.7}$
	9.60†	1.6-2.0	1.79	$0.8^{+0.2}_{-0.2}$	$1.5^{+0.9}_{-1.3}$	$0.210^{+0.004}_{-0.004}$	$4.2^{+2.6}_{-3.7}$	$8.5^{+5.4}_{-7.4}$
	9.62†	2.0-2.5	2.17	$1.1^{+0.2}_{-0.2}$	$1.4^{+0.6}_{-0.7}$	$0.237^{+0.001}_{-0.000}$	$6.3^{+2.5}_{-2.9}$	$12.7^{+5.1}_{-5.9}$
9.8-10.2	9.99	0.2-0.4	0.28	$6.9^{+0.4}_{-0.8}$	$17.7^{+2.0}_{-3.5}$	$0.523^{+0.019}_{-0.011}$	$0.6^{+0.1}_{-0.1}$	$1.5^{+0.1}_{-0.2}$
	9.99	0.4-0.6	0.49	$6.2^{+0.5}_{-0.5}$	$12.6^{+2.0}_{-1.9}$	$0.441^{+0.011}_{-0.016}$	$1.7^{+0.3}_{-0.3}$	$3.4^{+0.5}_{-0.5}$
	9.98	0.6-0.8	0.68	$5.4^{+0.3}_{-0.6}$	$9.3^{+1.2}_{-2.2}$	$0.336^{+0.022}_{-0.029}$	$2.7^{+0.3}_{-0.6}$	$5.4^{+0.7}_{-1.3}$
	9.99	0.8-1.0	0.89	$3.9^{+0.2}_{-0.4}$	$6.2^{+0.9}_{-1.5}$	$0.264^{+0.002}_{-0.005}$	$3.4^{+0.5}_{-0.8}$	$6.8^{+1.0}_{-1.6}$
	9.99	1.0-1.2	1.09	$3.7^{+0.3}_{-0.3}$	$6.6^{+1.4}_{-1.3}$	$0.305^{+0.010}_{-0.006}$	$5.8^{+1.2}_{-1.1}$	$11.9^{+2.4}_{-2.2}$
	9.97*	1.2-1.6	1.39	$3.2^{+0.2}_{-0.2}$	$4.4^{+1.0}_{-1.0}$	$0.225^{+0.014}_{-0.001}$	$6.8^{+1.5}_{-1.5}$	$13.9^{+3.1}_{-3.1}$
	9.98*	1.6-2.0	1.85	$2.5^{+0.2}_{-0.2}$	$4.6^{+1.0}_{-0.8}$	$0.228^{+0.006}_{-0.004}$	$14.0^{+3.0}_{-2.6}$	$28.5^{+6.2}_{-5.2}$
	9.98†	2.0-2.5	2.25	$2.0^{+0.2}_{-0.1}$	$2.8^{+1.0}_{-0.5}$	$0.248^{+0.012}_{-0.002}$	$13.6^{+4.8}_{-2.6}$	$27.6^{+9.8}_{-5.2}$
	9.99†	2.5-3.0	2.71	$1.6^{+0.2}_{-0.2}$	$2.0^{+1.4}_{-1.5}$	$0.256^{+0.001}_{-0.001}$	$14.5^{+10.1}_{-11.2}$	$29.5^{+20.6}_{-22.7}$
10.2-10.6	10.37	0.2-0.4	0.29	$12.2^{+0.8}_{-0.3}$	$29.0^{+3.5}_{-1.4}$	$0.592^{+0.014}_{-0.014}$	$1.2^{+0.1}_{-0.1}$	$2.4^{+0.3}_{-0.1}$
	10.37	0.4-0.6	0.49	$11.5^{+1.1}_{-0.6}$	$23.3^{+4.4}_{-2.6}$	$0.542^{+0.007}_{-0.011}$	$3.0^{+0.6}_{-0.3}$	$6.2^{+1.2}_{-0.7}$
	10.39	0.6-0.8	0.68	$8.2^{+0.3}_{-0.3}$	$16.0^{+1.4}_{-1.3}$	$0.415^{+0.026}_{-0.009}$	$4.6^{+0.4}_{-0.4}$	$9.4^{+0.8}_{-0.7}$
	10.38	0.8-1.0	0.89	$7.8^{+0.3}_{-0.4}$	$14.5^{+1.4}_{-1.5}$	$0.324^{+0.006}_{-0.002}$	$7.9^{+0.8}_{-0.8}$	$16.0^{+1.5}_{-1.6}$
	10.40	1.0-1.2	1.10	$6.5^{+0.3}_{-0.3}$	$12.0^{+1.3}_{-1.1}$	$0.358^{+0.013}_{-0.004}$	$10.6^{+1.1}_{-1.0}$	$21.5^{+2.3}_{-2.0}$
	10.38	1.2-1.6	1.38	$5.3^{+0.2}_{-0.2}$	$9.7^{+0.9}_{-0.8}$	$0.267^{+0.005}_{-0.004}$	$14.7^{+1.3}_{-1.2}$	$29.9^{+2.7}_{-2.5}$
	10.37	1.6-2.0	1.81	$4.9^{+0.3}_{-0.3}$	$9.8^{+1.1}_{-1.3}$	$0.298^{+0.007}_{-0.000}$	$28.2^{+3.2}_{-3.7}$	$57.3^{+6.5}_{-7.5}$
	10.37*	2.0-2.5	2.32	$4.0^{+0.2}_{-0.3}$	$7.0^{+0.7}_{-1.1}$	$0.302^{+0.010}_{-0.001}$	$35.6^{+3.5}_{-5.8}$	$72.5^{+7.0}_{-11.7}$
	10.38*	2.5-3.0	2.78	$3.5^{+0.3}_{-0.3}$	$6.6^{+1.2}_{-1.3}$	$0.311^{+0.010}_{-0.009}$	$50.9^{+8.9}_{-10.2}$	$103.5^{+18.1}_{-20.8}$
10.6-11.0	10.74	0.2-0.4	0.28	$18.8^{+1.3}_{-1.7}$	$53.8^{+6.4}_{-8.3}$	$0.851^{+0.017}_{-0.014}$	$2.0^{+0.2}_{-0.3}$	$4.0^{+0.5}_{-0.6}$
	10.75	0.4-0.6	0.48	$13.8^{+1.2}_{-1.3}$	$30.2^{+5.0}_{-5.4}$	$0.707^{+0.012}_{-0.015}$	$3.9^{+0.6}_{-0.7}$	$7.9^{+1.3}_{-1.4}$
	10.75	0.6-0.8	0.69	$13.3^{+1.1}_{-0.6}$	$27.7^{+4.4}_{-2.5}$	$0.573^{+0.035}_{-0.023}$	$8.1^{+1.3}_{-0.7}$	$16.4^{+2.6}_{-1.5}$
	10.75	0.8-1.0	0.89	$10.5^{+0.6}_{-0.5}$	$19.5^{+2.6}_{-2.2}$	$0.433^{+0.009}_{-0.001}$	$10.5^{+1.4}_{-1.2}$	$21.3^{+2.8}_{-2.4}$
	10.75	1.0-1.2	1.10	$8.1^{+0.3}_{-0.4}$	$15.8^{+1.2}_{-1.7}$	$0.454^{+0.005}_{-0.018}$	$14.1^{+1.0}_{-1.5}$	$28.7^{+2.1}_{-3.1}$
	10.75	1.2-1.6	1.37	$8.6^{+0.4}_{-0.4}$	$16.8^{+1.6}_{-1.8}$	$0.333^{+0.002}_{-0.003}$	$25.0^{+2.3}_{-2.7}$	$50.9^{+4.7}_{-5.4}$
	10.77	1.6-2.0	1.79	$7.9^{+0.4}_{-0.3}$	$14.8^{+1.7}_{-1.1}$	$0.387^{+0.011}_{-0.009}$	$41.3^{+4.9}_{-3.0}$	$83.9^{+9.9}_{-6.1}$
	10.77	2.0-2.5	2.22	$6.3^{+0.7}_{-0.5}$	$11.9^{+2.6}_{-1.9}$	$0.397^{+0.002}_{-0.004}$	$55.2^{+11.9}_{-8.7}$	$112.3^{+24.2}_{-17.7}$
	10.76	2.5-3.0	2.72	$5.6^{+0.3}_{-0.4}$	$13.3^{+1.2}_{-1.6}$	$0.428^{+0.005}_{-0.020}$	$97.6^{+9.0}_{-11.9}$	$198.4^{+18.2}_{-24.2}$
> 11.0	11.10	0.2-0.4	0.29	$19.8^{+3.7}_{-4.1}$	$75.4^{+20.8}_{-23.1}$	$1.640^{+0.084}_{-0.100}$	$2.9^{+0.8}_{-0.9}$	$5.9^{+1.6}_{-1.8}$
	11.10	0.4-0.6	0.48	$18.1^{+1.2}_{-1.8}$	$56.3^{+6.2}_{-9.3}$	$1.364^{+0.071}_{-0.048}$	$6.9^{+0.8}_{-1.2}$	$14.1^{+1.6}_{-2.3}$
	11.10	0.6-0.8	0.69	$12.7^{+1.1}_{-1.4}$	$32.6^{+5.1}_{-6.4}$	$1.086^{+0.040}_{-0.011}$	$9.6^{+1.5}_{-1.9}$	$19.5^{+3.1}_{-3.8}$
	11.10	0.8-1.0	0.89	$13.8^{+1.4}_{-1.7}$	$32.0^{+5.6}_{-6.7}$	$0.907^{+0.039}_{-0.007}$	$17.1^{+3.0}_{-3.6}$	$34.9^{+6.1}_{-7.3}$
	11.13	1.0-1.2	1.10	$13.4^{+1.5}_{-1.3}$	$26.9^{+5.6}_{-4.9}$	$0.881^{+0.013}_{-0.009}$	$24.2^{+5.0}_{-4.4}$	$49.2^{+10.2}_{-9.0}$
	11.11	1.2-1.6	1.36	$13.4^{+1.0}_{-0.8}$	$27.7^{+4.1}_{-3.1}$	$0.734^{+0.023}_{-0.027}$	$40.5^{+6.0}_{-4.5}$	$82.3^{+12.2}_{-9.2}$
	11.11	1.6-2.0	1.80	$15.6^{+1.1}_{-1.6}$	$30.3^{+4.3}_{-6.3}$	$0.701^{+0.013}_{-0.014}$	$85.9^{+12.1}_{-17.9}$	$174.6^{+24.6}_{-36.4}$
	11.15	2.0-2.5	2.22	$11.9^{+0.6}_{-0.5}$	$21.8^{+2.3}_{-1.8}$	$0.594^{+0.023}_{-0.044}$	$100.1^{+10.6}_{-8.5}$	$203.5^{+21.6}_{-17.2}$
	11.17	2.5-3.0	2.71	$11.1^{+0.7}_{-1.1}$	$22.5^{+2.9}_{-4.6}$	$0.645^{+0.007}_{-0.004}$	$164.5^{+20.8}_{-33.7}$	$334.4^{+42.4}_{-68.5}$

Note. — Median stacking-based average 1.4 GHz radio flux densities and derived average quantities for all our bins in mass and redshift for *star forming systems within our mass-selected sample*. For details see caption of Table 4.2.

† Mass bin contains data below the limit of mass representativeness and yields an upper limit to the average SFR (see Section 4.2.6 for further details.)
* First mass bin above the limit of representativeness (see Section 4.2.6) which contains a low fraction (< 15 %) of optically faint objects with $m_{AB}(i^+) \geq 25.5$ for which the photo-z accuracy is degraded (see Section 4.2.2 for further details). The average SFR measured in this bin might be slightly overestimated towards higher values (see Section 4.2.6).

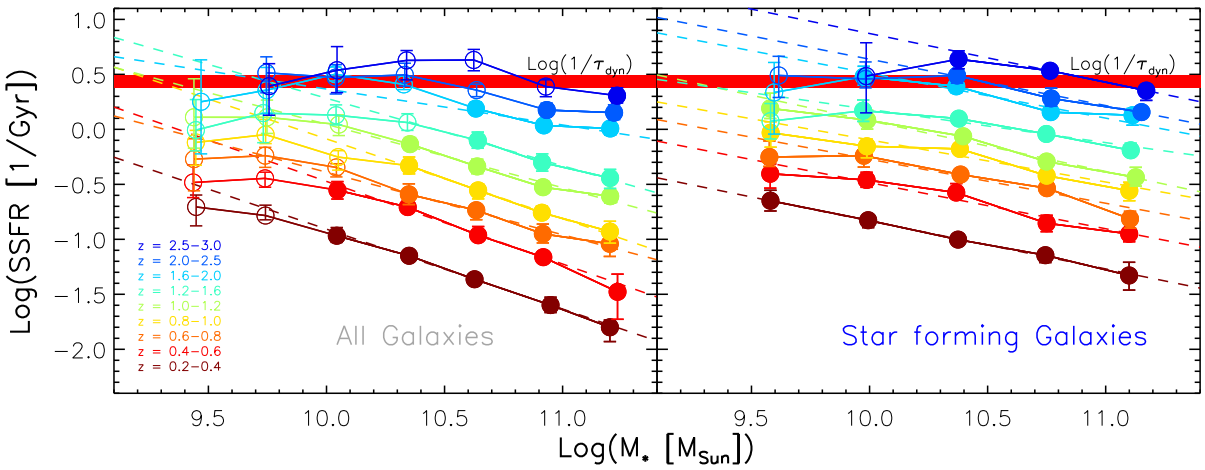

Figure 4.5. – Radio stacking based measurement of the SSFR as a function of stellar mass at $0.2 < z < 3.0$ for our entire galaxy sample (left) and SF systems (right). Open symbols depict samples containing galaxies less massive than the individual limits denoted in Figure 4.1 and are regarded as not representative for the underlying galaxy population and rather represent upper SSFR limits. Dashed lines are two-parameter fits of the form $c \times M_*^{\beta}$ to the mass-representative data depicted by filled symbols (see Table 4.4). The horizontal red band sketches the inverse dynamical time of (370 ± 50) Myr measured in local disk galaxies (Kennicutt 1998b) and also found in massive disk galaxies at $z \sim 1.5$ (Daddi et al. 2010b). Galaxies with such high levels of SSFR effectively double their mass within a dynamical time. As detailed in Section 4.4.1 this might represent an upper bound to the average SSFR. All measured data points are listed in Table 4.2 and 4.3. The derivation of error bars involves a bootstrapping analysis combined with the uncertainties to the best-fit model of each stacking-derived average radio source (see App. A.2 and Section 4.3.2; for further details). We do not account for uncertainties associated with the SFR-calibration, the photometric redshift and stellar mass estimates as the large number of objects stacked for each data point ensures that even the joint error budget is statistically reduced to a low level that would not substantially enhance our uncertainty ranges.

4.4.1. The relation between SSFR and stellar mass

We first consider the whole sample including all galaxies and show the redshift dependent radio-based SSFRs that are distributed in the logarithmic SSFR-M_* plane as seen in the left panel of Figure 4.5. It is clear that the SSFR for a given stellar mass increases with redshift and that it generally decreases with increasing stellar mass.

The data at the high-mass end (above $\log(M_*) \approx 10.5$) within all considered redshift slices suggest power-law relations between SSFR and stellar mass of the form

$$\mathrm{SSFR}(M_*, z) = c(z) \times {M_*}^{\beta(z)}. \tag{4.7}$$

In the following we will refer to the index β also as slope since the relation is commonly shown in $\log$-space. The dashed lines in Figure 4.5 depict the best fit to the data in the mass-representative regime (see Section 4.2.6) and indicate that only the normalization evolves while the power-law index β_{ALL} of the individually fitted relations shows minor fluctuations but no clear evolutionary trend. Only at $z \gtrsim 1.5$ there is tentative evidence for a somewhat shallower slope. However, at the highest redshifts probed too few mass-representative data points exist to perform the linear fit. Our evidence is solely supported by the offset between

the SSFR of the most massive galaxies and those of intermediate mass remaining the same as at $z \sim 1.8$. Based on our data it therefore is justified to consider the index $\beta_{\rm ALL}$ in Eq. (4.7) a constant at least for all $z < 1.5$ and $\log(M_*) \gtrsim 10.5$.

At $\log(M_*) < 10 - 10.5$ we see at practically all epochs that the measured SSFRs significantly deviate from the relation fitted to the high-mass end. The extrapolation towards lower masses over-predicts the measurement. In Section 4.2.6 we argued that all these data points – lying below the mass representativeness limits – likely represent upper limits. We hence believe this is a genuine deviation that is reminiscent of the bimodality (whereby quiescent galaxies preferentially populate the high-mass end) in the SSFR-M_* plane confirmed at various redshifts for galaxy samples with individually measured SFRs (e.g. Brinchmann et al. 2004; Salim et al. 2007; Elbaz et al. 2007; Santini et al. 2009; Rodighiero et al. 2010a).

Using our spectral classification scheme we separately study the SF galaxy population in order to break the afore mentioned bimodality. The right panel in Figure 4.5 shows that a power-law relation according to Eq. (4.7) holds over the entire mass range probed, once quiescent galaxies are excluded. Linear fits exclusively to the mass-representative regime show that, at $z \lesssim 1.5$: (i) SSFR declines towards higher mass, and that (ii) the slope β_{SFG} is constant, as it was the case for the entire galaxy population. Compared to the entire sample, the slope is significantly shallower.[31] All theses conclusions also hold at all other epochs probed but are supported by fewer data points significantly above the mass-representativeness limits that enter the fits. Hence we regard our conclusions as most robust at $z < 1.5$.

Above $z \sim 1.4$ and below $\log(M_*) \approx 9.5 - 10$, we again find that measurements in the regime not regarded as mass-representative lie significantly below the linear fits. Since quiescent galaxies are even less frequent at these redshifts[32], the bimodality argument is obviously insufficient to explain this observed trend. A possible explanation is that the magnitude limit of our catalog leads to a loss of dust-dominated systems with low masses but high star formation activity. If this were the case our previous statement that SSFRs in the under-represented mass-regime are upper limits would not necessarily hold. However, we do not expect a sufficiently high number density of low-mass dusty starbursts to make this scenario plausible. Another explanation could lie in the dynamical considerations presented in Section 4.4.2.

4.4.2. A potential upper limit to the average SSFR of normal galaxies

The fact that the aforementioned deviations from the linear fits at low masses steadily grow with redshift hints at a solid upper limit to the average SSFR. Local spiral galaxies have on average a dynamical timescale – i.e. the rotation timescale at the outer radius of a disk galaxy – of $\tau_{\rm dyn} \sim 0.37$ Gyr (Kennicutt 1998b). Daddi et al. (2010b) show that this still holds at $z \sim 1.5$. The inverse of this dynamical timescale, $1/\tau_{\rm dyn} \sim 2.7$ Gyr^{-1}, is similar to the threshold that seems to prevent our average SSFRs from rising continuously with decreasing mass. Note also that this dynamical timescale approximately equals the free-

[31] At high masses, the radio-derived SSFRs for SF galaxies lie significantly above those for all galaxies demonstrating that the SED-based pre-selection is efficient.

[32] Also at high z there is evidence for the existence of quiescent systems that are predominantly massive (e.g. Cimatti et al. 2004; Kriek et al. 2006, 2008b; Brammer et al. 2009). However, as our spectral classification of SF systems is efficient to exclude passive galaxies (see I10) and as these systems are also rare we do not expect them to cause the observed trend.

Table 4.4. Two parameter fits to the mass dependence of the SSFR

	All galaxies			SF systems		
Δz	$\log(c_{\rm ALL}$ [1/Gyr])	$\beta_{\rm ALL}$	χ^2/d.o.f	$\log(c_{\rm SFG}$ [1/Gyr])	$\beta_{\rm SFG}$	χ^2/d.o.f
0.2-0.4	-1.63 ± 0.04	-0.73 ± 0.03	0.11	-1.27 ± 0.03	-0.44 ± 0.03	0.03
0.4-0.6	-1.22 ± 0.04	-0.75 ± 0.04	0.24	-0.90 ± 0.03	-0.42 ± 0.03	0.78
0.6-0.8	-0.96 ± 0.08	-0.57 ± 0.08	0.17	-0.67 ± 0.03	-0.40 ± 0.03	1.37
0.8-1.0	-0.81 ± 0.07	-0.73 ± 0.06	0.07	-0.48 ± 0.03	-0.38 ± 0.03	1.42
1.0-1.2	-0.53 ± 0.05	-0.58 ± 0.05	0.64	-0.38 ± 0.03	-0.46 ± 0.03	0.61
1.2-1.6	-0.33 ± 0.13	-0.61 ± 0.12	0.12	-0.12 ± 0.03	-0.30 ± 0.03	1.08
1.6-2.0	0.04 ± 0.08	-0.33 ± 0.07	1.47	0.10 ± 0.07	-0.41 ± 0.07	2.21
2.0-2.5				0.22 ± 0.06	-0.42 ± 0.05	0.19
2.5-3.0				0.43 ± 0.16	-0.44 ± 0.15	0.81
	$\langle\beta_{\rm ALL}\rangle =$	-0.67 ± 0.02	$^{+0.34}_{-0.08}$	$\langle\beta_{\rm SFG}\rangle =$	-0.40 ± 0.01	$^{+0.10}_{-0.06}$

Note. — A power-law fit of the form $c \times (M_*/10^{11}\ M_\odot)^\beta$ (Eq. (4.7)) was applied to the radio stacking-based SSFRs as a function of mass within any redshift slice. Fits have only been applied if more than two data points remained above the mass limit where the individual sample is regarded mass-representative. The results for all galaxies are shown in the left half of the table while those for star forming systems (see Section 4.2.4) are given in the right half. The weighted average power-law index (over all accessible redshifts) found for each population is stated at the bottom along with the formal standard error and the scatter range yielding a more realistic uncertainty estimate.

fall time (Genzel et al. 2010) which is commonly used to relate SFR volume density with gas volume density (e.g. Schmidt 1959; Kennicutt 1998b; Krumholz and McKee 2005; Krumholz et al. 2009; Leroy et al. 2008).

As indicated in Figure 4.5 the population of $z > 1.5$ galaxies reaches average levels of star formation that enable these normal SF systems to double their mass within a dynamical time scale. Generally, star formation is thought to be limited by the rate at which cold gas is accreted onto the galaxy (e.g. Dutton et al. 2010; Bouché et al. 2010 and also e.g. Kereš et al. 2005; Macciò et al. 2006, where simulations actually show the cold gas inflow) while the efficiency of star formation does not appear to change out to the highest redshifts accessible to molecular gas studies in normal disk galaxies to-date (Daddi et al. 2010a; Tacconi et al. 2010). Consequently, even the highly elevated gas fractions – i.e. the amount of gas available for star formation over the sum of gas and stellar mass – compared to local disk systems (e.g. Daddi et al. 2010a, who find up to 60 % at $z = 1.5$) might not suffice to sustain a star formation activity that proceeds faster than gravity permits. As average galaxies reach inverse SSFRs comparable to their inverse dynamical – and, most importantly, free fall – time it is hence likely that an effective gas accretion threshold is reached. Hence the SSFR should stop its growth with redshift at some point. Lower mass galaxies reach this threshold at lower redshifts than the more massive systems leading to the flattening of the relation we observe at the lower mass end. We will henceforth refer to the transition from an inclined to a flat SSFR-sequence as *'crossing mass'*.

It is clear that carbon monoxide ALMA-studies at $z > 1.5$ of typical SF systems with $M_* \leq 10^{10}\ M_\odot$ are required to understand their molecular gas properties and to test the star formation law of this population.

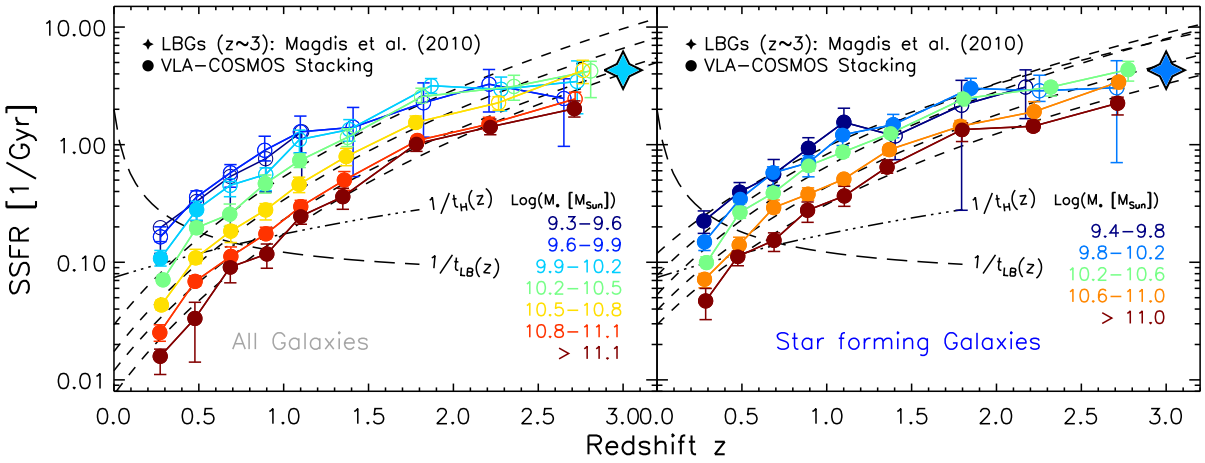

Figure 4.6. – Redshift evolution of the SSFRs for all galaxies (left) and SF systems (right) in logarithmic stellar mass bins. Two-parameter fits of the form $C \times (1+z)^n$ are applied only to data points derived from samples regarded as representative for the given underlying galaxy population which are depicted by filled symbols (see Table 4.5). The black long-dashed line gives the mass-doubling limit above which galaxies are able to double their mass until $z = 0$ assuming a constant SFR and it therefore equals the inverse lookback-time. The black dashed-dotted line depicts the inverse age of the universe at any given redshift and hence makes measured SSFRs comparable to the past average star formation activity. The SED-derived measurement of Magdis et al. (2010) for LBGs at $z \sim 3$ with $\log(M_*) \sim 10$ is shown as a filled star. All data results are listed in Table 4.2 and 4.3.

4.4.3. The redshift evolution of SSFRs as a function of mass

The redshift evolution of our data is shown in Figure 4.6 for all galaxies and for the SF population. Both panels suggest a co-evolution of the considered mass-bins at least out to $z \sim 1.5$; while all measured SSFRs increase with redshift, the high-mass end does not evolve faster compared to lower masses and it always has the lowest SSFRs. An offset between the typical SSFRs of different mass bins is also evident for SF galaxies but it is smaller than for the entire galaxy population which shows a wider spread of SSFRs at fixed mass. Clearly, all these aspects are the direct result of our previous findings:

- A constant slope β of the SSFR-M_* relation is observed for all galaxies (at the high-mass end) as well as for SF galaxies alone at least out to $z \sim 1.5$.
- The slope $\beta_{\rm SFG}$ is shallower for SF systems.

In Figure 4.6 we also plot the mass doubling line[33] (long dashed line) and the inverse age of the universe at any given redshift (dashed-dotted line). Our measurement clearly shows that virtually all SF galaxies display a higher star formation activity than is required if their entire mass had been build up at a constant rate over the whole age of the universe.[34] All galaxies, generally, cross the dashed-dotted line sooner or later depending on their stellar

[33] At a given redshift, the mass-doubling threshold is given by the inverse lookback time. A SSFR in excess of this limit is hence a mass-independent indicator for the potential of a galaxy to double its mass by $z = 0$ if it were to maintain its current SFR.

[34] This does not necessarily imply that an individual galaxy maintains a high level of star formation activity. All statements we make here refer to an average galaxy of a given mass and cosmic epoch having a well-defined

Table 4.5. Two parameter fits to the redshift evolution of the SSFR

All galaxies				SF systems			
$\Delta\log(M_*)$ M_* $[M_\odot]$	$\log(C_{\rm ALL})$ $C_{\rm ALL}$ [Gyr^{-1}]	$n_{\rm ALL}$	χ^2/d.o.f	$\Delta\log(M_*)$ M_* $[M_\odot]$	$\log(C_{\rm SFG})$ $C_{\rm SFG}$ [Gyr^{-1}]	$n_{\rm SFG}$	χ^2/d.o.f
				9.4-9.8	-0.92 ± 0.45	3.02 ± 0.15	0.65
10.2-10.5	-1.53 ± 0.56	4.18 ± 0.05	3.05	9.8-10.2	-0.92 ± 0.33	3.42 ± 0.07	1.63
10.5-10.8	-1.76 ± 0.93	4.28 ± 0.05	1.48	10.2-10.6	-1.11 ± 0.28	3.62 ± 0.04	5.24
10.8-11.1	-1.92 ± 1.48	4.27 ± 0.05	1.75	10.6-11.0	-1.28 ± 0.47	3.48 ± 0.04	1.73
> 11.1	-2.12 ± 3.93	4.53 ± 0.07	2.37	> 11.0	-1.41 ± 0.82	3.40 ± 0.06	1.52
	$\langle n_{\rm ALL} \rangle =$	4.29 ± 0.03	$^{+0.24}_{-0.11}$		$\langle n_{\rm SFG} \rangle =$	3.50 ± 0.02	$^{+0.12}_{-0.48}$

Note. — A power-law fit of the form $C \times (1+z)^n$ was applied to the radio stacking-based SSFRs as a function of redshift within any mass bin. Fits have only been performed if more than two data points remained above the mass limit where the individual sample is regarded mass-representative. The results for all galaxies are shown in the left half of the table while those for star forming systems (see Section 4.2.4) are given in the right half. The weighted average power-law index (over all accessible masses) found for each population is stated at the bottom along with the formal standard error and the scatter range yielding a more realistic uncertainty estimate.

mass. The most massive systems enter the stage of sub-average star formation activity already at $z \sim 0.8$.

At the high-mass end ($\log(M_*) \gtrsim 11$) the SSFR for SF galaxies increases by almost a factor of 50 and is about twice as much for all galaxies within $0.2 \leq z \leq 3$. For a given mass-bin the redshift evolution is well described by a power law $g(z) \propto (1+z)^n$ as depicted by the dashed lines in Figure 4.6.[35] For the most massive SF galaxies this relation holds out to the highest redshifts probed, thus no flattening is observed. However, towards lower masses and $z \gtrsim 2$ significant deviation of the data from the best-fit relation with lower SSFR towards lower masses is apparent. Again the argument of an upper SSFR limit due to dynamical reasons might explain such a deviation. For reference we also show the recent SED-based measurement by Magdis et al. (2010) for a Lyman Break Galaxy (LBG) sample at $z \approx 3$. Their study probes $M_* \approx 10^{10}\ M_\odot$ and we see that their SSFR-measurement is significantly below the extrapolation given by our evolutionary fit in the same mass-regime even for SF galaxies. Basically, their data point is extending our measured data at the low-mass end if evolution were to stop at about $z \approx 1.5$ (a scenario suggested by the data of Stark et al. 2009 and González et al. 2010).

Summarizing our findings a separable function of the form

$$\mathrm{SSFR}(M_*, z) \propto f(M_*) \times g(z) = M_*^{\beta} \times (1+z)^n \tag{4.8}$$

describes well the mass-dependent evolution of the SSFR given our data within the restrictions discussed. For SF galaxies we find $\beta_{\rm SFG} \approx -0.4$ and $n_{\rm SFG} \approx 3.5$. We emphasize again that the dynamical arguments discussed in Section 4.4.2 would give rise to a value

SSFR thanks to the SSFR-M_* relation. Star formation might still be subsequently quenched in an individual system so that its evolutionary track does not need to coincide with those shown in Figure 4.6.

[35] We fitted only data in the representative mass range.

of $\beta_{\rm SFG} = 0$ below the crossing mass of the average SSFR and the upper limiting SSFR. The results of the individual fits to our data yielding the parameters β and n for all and SF galaxies are presented in Tables 4.4 and 4.5.

It is worth noting that at $z > 1$ – where angular diameter distance is approximately constant – the evolutionary trend we find is very close to the redshift dependence of the radio luminosity of about $(1+z)^{3.8}$ (see Section 4.3.2). As the SSFR is proportional to the radio luminosity this is yet another argument to support that our inferences are not challenged by systematic errors to the median redshift even in our broader bins at $z > 1$ (see also the corresponding discussion in Section 4.3.2).

In order to alternatively probe our inferences in the redshift range below $z = 1.5$ where our data yields the most robust results we also stacked the same bins in redshift and mass into the Spitzer 24 and 70 μm COSMOS maps. We inferred SFRs from the total (8-1000 μm) IR luminosity predicted by the best-fitting IR SED (Chary and Elbaz 2001) given the joint flux density information. The results do not deviate significantly from those derived from the radio emission so that all our conclusions remain robust also when derived from the IR data. All these and further results will be presented and discussed in detail in a separate publication (Sargent et al., in prep.).

4.4.4. Comparison to other studies

In this Section we compare our findings with results in the literature, with a particular focus on those least dependent on extinction corrections because they use either radio stacking or stacking of IR imaging by Spitzer and, most recently, Herschel. Literature data we show in the Figures belonging to this Section are based on a Salpeter IMF and have been converted to the Chabrier scale.

The evolutionary power law we derived for *all* mass-selected galaxies is in excellent agreement with the results presented by Damen et al. (2009a), both in terms of the evolutionary exponent and the normalization of the trend. We hence concur, in particular, with those findings of Damen et al. (2009a) resulting from a detailed comparison of their results with predictions from the semi-analytical model of Guo and White (2008). The study of Damen et al. (2009a), which is based on SFRs from 24 μm and UV detections in conjunction with deep K-band observation in the Chandra Deep Field South, is also in broad agreement with the 24 μm stacking analysis of Zheng et al. (2007a) at $z < 1$ in the same field. Consistent findings have also been presented recently in the Spitzer/MIPS stacking analysis at 70 and 160 μm by Oliver et al. (2010) whose data covers the largest on-sky area of all aforementioned surveys, albeit at a reduced depth of $F_{3.6\ \mu{\rm m}} = 10\ \mu$Jy (an order of magnitude shallower compared to our sample) which prevents them from reliably constraining the evolution beyond $z \sim 1$. Based on a deep rest-frame NIR bolometric flux density selected galaxy sample in the northern Great Observatories Origins Deep Survey (GOODS Giavalisco et al. 2004) field Cowie and Barger (2008) measure extinction corrected UV-based SSFRs for all individual objects out to $z = 1.5$. Their average trends with mass agree well with our results for all galaxies in the comparable redshift ranges and also on absolute scales both studies are consistent at all masses.

Radio-based measurements of the SSFR-M_* relation have been presented by Dunne et al. (2009). In terms of the evolution of the SSFR-sequence both their and our study show a good agreement. The findings by Dunne et al. (2009) differ from ours (see Figure 4.7) as

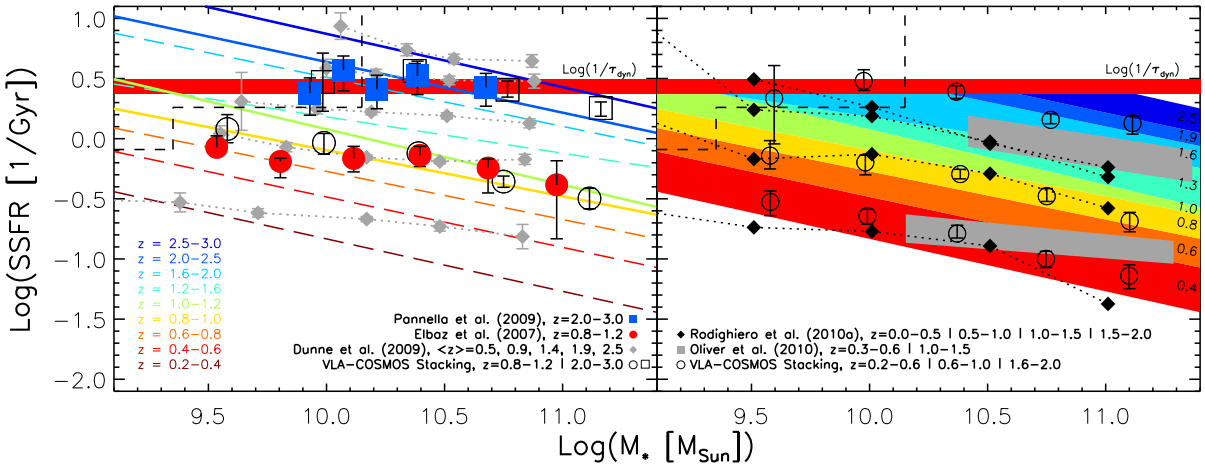

Figure 4.7. – **Left Panel:** Comparison of our results (dashed and solid lines of different color) of the mass dependence of the SSFR for SF systems at different redshifts to Dunne et al. (2009); grey diamonds, Elbaz et al. (2007); red circles at $z \sim 1$, as well as Pannella et al. (2009); blue squares at $z \sim 2$. The mass limits above which our sample is representative are denoted as black dashed lines in the upper left. **Right Panel:** The corresponding measurements by Oliver et al. (2010); grey shaded bands and Rodighiero et al. (2010a); black diamonds at various redshifts along with our results (color bands with mean redshift scale at the right hand side). The Herschel/PACS based SSFR-sequence (Rodighiero et al. 2010a) suggests a mild 'upsizing' trend and appears to stop its evolution at $z > 1.5$ where the only (apparent) deviation from our data occurs. See Section 4.4.4 and Appendix 4.5 for a discussion of effects introduced by selection biases. For immediate comparison our data are shown as open symbols in both panels, rebinned in z in order to cover the same range in redshift as each referenced study. The inverse horizontal red band sketches the inverse dynamical time as detailed in Section 4.4.1.

well as from most other studies not restricted to SF galaxies only in that they report an almost non-existent slope $\beta_{\rm ALL}$ at all reliably probed epochs. Their analysis and ours share some methodological similarities (e.g. the use of a mass- (in their case: K-) selected sample[36] and a radio stacking approach) and should therefore be directly comparable. Despite the technical differences in the exact implementation of the image stacking as already discussed (see Section 4.3.2) it seems unlikely that an explanation for the different trends can be found in the radio data used. It appears more likely that the derivation of individual stellar masses causes the differences as Dunne et al. (2009) use a direct conversion from the rest-frame K-band magnitudes as measured from the best-fitting SED templates to stellar mass which exclusively depends on redshift. Such a conversion should not only be different for SF and quiescent sources (Arnouts et al. 2007) but even ceases to be applicable towards lower mass SF sources as discussed in App. D of I10. It is hence likely that low-mass SF sources with higher SSFRs have migrated to higher masses producing artificially elevated SSFRs at the high-mass end. This explanation is consistent with the generally higher deviations from our results at higher masses (see Figure 4.7). Since neither we nor Dunne et al. (2009) find a significant evolution of the slope $\beta_{\rm ALL}$ in the SSFR-M_* plane the pure evolutionary behavior reported in both studies is largely consistent.

[36] It is, however, worth noting that our number statistics are larger by about a factor of four.

The SSFR-M_* relation for sBzK – and hence SF K-band selected – galaxies in the COSMOS field was derived by Pannella et al. (2009) based on radio stacks from the same VLA image. Our results for SF galaxies are (necessarily) in good agreement with their findings at $z \approx 2$ (left panel of Figure 4.7) where they do not probe the highest mass-range presented here. A main conclusion of Pannella et al. (2009) is, however, a mass-independent SSFR at $z > 1.5$ which is mainly inferred from a measurement on their entire SF sample (not further divided by redshift) and a measurement at $z \approx 1.6$ both covering the same mass-range as considered here. A similar tendency at $z \sim 2$ has previously also been reported by Daddi et al. (2007) in a study carried out in the GOODS fields. Their work is based on 24 μm detected galaxies down to $\log(M_*) \approx 9.5$ but also based on radio stacks of their K-band selected sample. As galaxies at $1.3 < z < 1.5$ substantially contribute to the photometric redshift distribution of the Pannella et al. (2009) sample, it is likely that the sBzK criterion no longer selects *all* SF objects at these low redshifts. In this context we also refer to Section 4.5 where the upper left panel in Figure 4.9 shows that the sBzK criterion by construction fails to select *all* SF sources at $z < 1.5$. As we already pointed out, our SSFR-M_* relation for our SF sample tends to flatten towards lower M_*. When considering only low to intermediate masses, all measurements based on stacking into the VLA-COSMOS 1.4 GHz map are thus in good agreement. The steeper slope $\beta_{\rm SFG}$ of the SSFR-M_* relation for SF galaxies found in this study is thus a consequence of the fact that we span a larger mass range at $z \approx 2$.

The left panel of Figure 4.7 also shows the results at $z \approx 1$ presented by Elbaz et al. (2007) based on 24 μm detection resulting from deep Spitzer/MIPS observations of the GOODS fields and UV-corrected SFRs. Although this study too infers a nearly constant relation between SSFR and mass, the figure shows that the radio-derived results agree with the mid-IR measurements remarkably well. This illustrates that measurements of the slope $\beta_{\rm SFG}$ of the SSFR-M_* for SF galaxies are quite sensitive to deviations at the edges of the mass range even if measurements at individual masses do not significantly differ between different studies. Finally, it is also worth noting that, towards lower redshifts, our slope $\beta_{\rm SFG}$ agrees well with the measurements by Noeske et al. (2007b) which are based on SFRs from emission lines, UV as well as 24 μm imaging for a K-band selected sample of the DEEP2 spectroscopic survey. Also in the local universe GALEX/UV-based values around $\beta = -0.35$, consistent with our study, have been reported for galaxies taken from the Sloan Digital Sky Survey (SDSS) (Salim et al. 2007; Schiminovich et al. 2007). It should be mentioned that, based on the SDSS emission lines study of Brinchmann et al. (2004), Elbaz et al. (2007) found a slightly shallower slope $\beta_{\rm SFG} = -0.23$ for SF galaxies in the local universe.

Image stacking results using Herschel/PACS data at 160 μm have been presented by Rodighiero et al. (2010a). Their GOODS-North Spitzer/IRAC data is only slightly shallower compared to our COSMOS imaging. As the right panel of Figure 4.7 shows, individual measurements by Rodighiero et al. (2010a) at $z < 1$ are in good agreement with our findings. (The one exception being their lowest redshift which extends to $z = 0$, explaining the overall slightly lower SSFRs.) At $z > 1.5$ the Rodighiero et al. (2010a) results suggest that SSFRs cease to grow further at the high-mass end. While in this redshift range our radio-derived SSFRs agree with the far-IR based ones at the lowest masses probed, the radio measurement yields about 0.4 dex (i.e. significantly) higher SSFRs at the high-mass end as they do not show a different redshift trend than at lower z. As our highest redshift bin is centered at a slightly higher z compared to the corresponding one of Rodighiero et al. (2010a) the

difference might be slightly lower if the bins were perfectly matched and given the high-mass SSFR-evolution for SF galaxies is continuing at $z > 1.5$. We therefore see no clear evidence for strong discrepancies of radio- and far-IR stacking derived SSFRs at high z as speculated by Rodighiero et al. (2010a) when comparing their results to those of Pannella et al. (2009) and especially those of Dunne et al. (2009). We emphasize, however, that future far-IR studies could test potential mass-dependent changes in the radio-IR correlation at $z > 1.5$ responsible for the slight differences reported here.[37] Based on power-law fits to their data Rodighiero et al. (2010a) infer a steepening of $\beta_{\rm SFG}$ towards higher z, an effect they consequently term 'upsizing'. Note, however, that our measurements of $\beta_{\rm SFG}$ agree with those of Rodighiero et al. (2010a) within the uncertainties. Tentative evidence for upsizing is also reported by Oliver et al. (2010) who use Spitzer/MIPS stacking of late-type galaxies at 70 and 160 μm (see right panel of Figure 4.7). In the following Section we show that we can mimic an upsizing trend, as well as the somewhat flatter evolution of the SSFR out to $z \approx 2$ reported by, e.g., Rodighiero et al. (2010a) if we restrict our SF sample to those sources with the most active star formation.

4.5. A note on the selection of star forming galaxies

Because we cannot measure radio-based SSFRs for individual galaxies, selecting the SF population directly in the SSFR-M_* plane is impossible. In Section 4.2.4 we argue that the intrinsic (dust-extinction corrected) rest-frame NUV-r color is a reliable way to select SF galaxies (see also I10). In this section, we test our color selection in two ways in order to demonstrate its fidelity and to assess how our findings relate to previous measurements in the literature: we (1) choose a bluer color-cut to study the ensuing changes in the evolution of the SSFR-M_* relation, and we (2) compare both – the bluer and the previously used – color cuts to the BzK-selection of SF galaxies at high redshifts (Daddi et al. 2004).

4.5.1. Highly active star forming galaxies

I10 have shown that the color selection criterion $(\mathrm{NUV} - r^+)_{\rm temp} < 1.2$ leads to a morphologically clean sample of late-type spiral and irregular galaxies with template SED-based SSFRs that are clearly separated from the passive population (see Section 4.2.4). This color threshold is somewhat arbitrary (as it is less well motivated than the cut we applied to select SF systems) but by virtue of being substantially bluer than our original choice it minimizes contamination by passive galaxies.

We derived SSFRs as a function of redshift and mass in the same way as before for galaxies with $(\mathrm{NUV} - r^+)_{\rm temp} < 1.2$. Although the exclusion of systems with intermediate star forming activity has reduced the sample size considerably, it was still possible to cover the same dynamic ranges. Only the binning scheme has been slightly modified for this strongly star formation population (see Figure 4.8). Its SSFRs usually are significantly higher compared to our original choice of SF galaxies, the slope β of the SSFR-M_* relation

[37] Herschel/PACS observations of the GOODS-North field (Elbaz et al. 2010) revealed that in the same redshift regime the total ($8 - 1000$ μm) IR luminosity appears to be overestimated when the IR template-SED fit is constrained by a single 24 μm measurement. The deviation starts at $L_{\rm IR} \sim 10^{12}$ $L_\odot$ and grows with increasing $L_{\rm IR}$, SFR and consequently mass as these quantities are correlated. It is therefore necessary to test the radio-IR correlation in the proposed way using far-IR data.

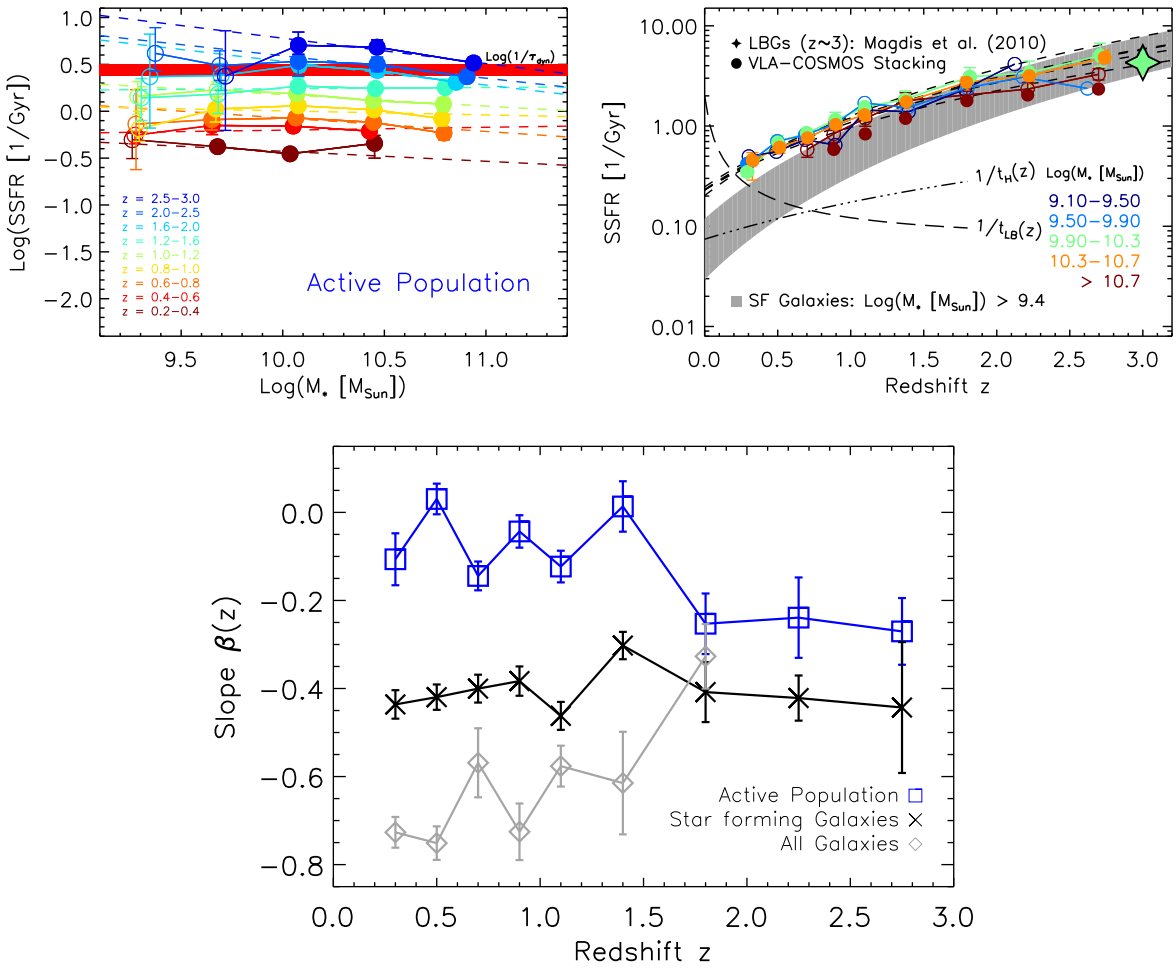

Figure 4.8. – The SSFR-M_* relation (upper left) and time evolution of SSFRs in various mass-bins (upper right) for galaxies with high star formation activity ((NUV-r$^+$)$_{\rm temp} < 1.2$). Dashed lines (color coded by redshift) denote two-parameter fits of the form $c \times M_*^{\beta}$ to the mass complete data (filled circles). The dynamical ranges are the same as in Figure 4.5 and 4.6, where the other quantities shown are explained. The color threshold is substantially bluer and rather arbitrary compared to the one used for the selection of SF systems. Compared to the results of the entire SF sample the radio stacks yield a flatter SSFR-sequence out to $z \sim 1.5$ ($\beta \approx -0.08 \pm 0.05$) and a mild 'upsizing' trend (lower panel) while overall a shallower evolution of the SSFR $\propto (1+z)^{2.3\pm0.3}$ is found for this sample of most vigorously SF galaxies (upper right, where fits to the mass-complete data in the different mass bins are depicted as dashed black lines). All these trends seen for highly active SF galaxies are hence a result of a simple selection effect. The inverse horizontal red band sketches the inverse dynamical time as detailed in Section 4.4.1.

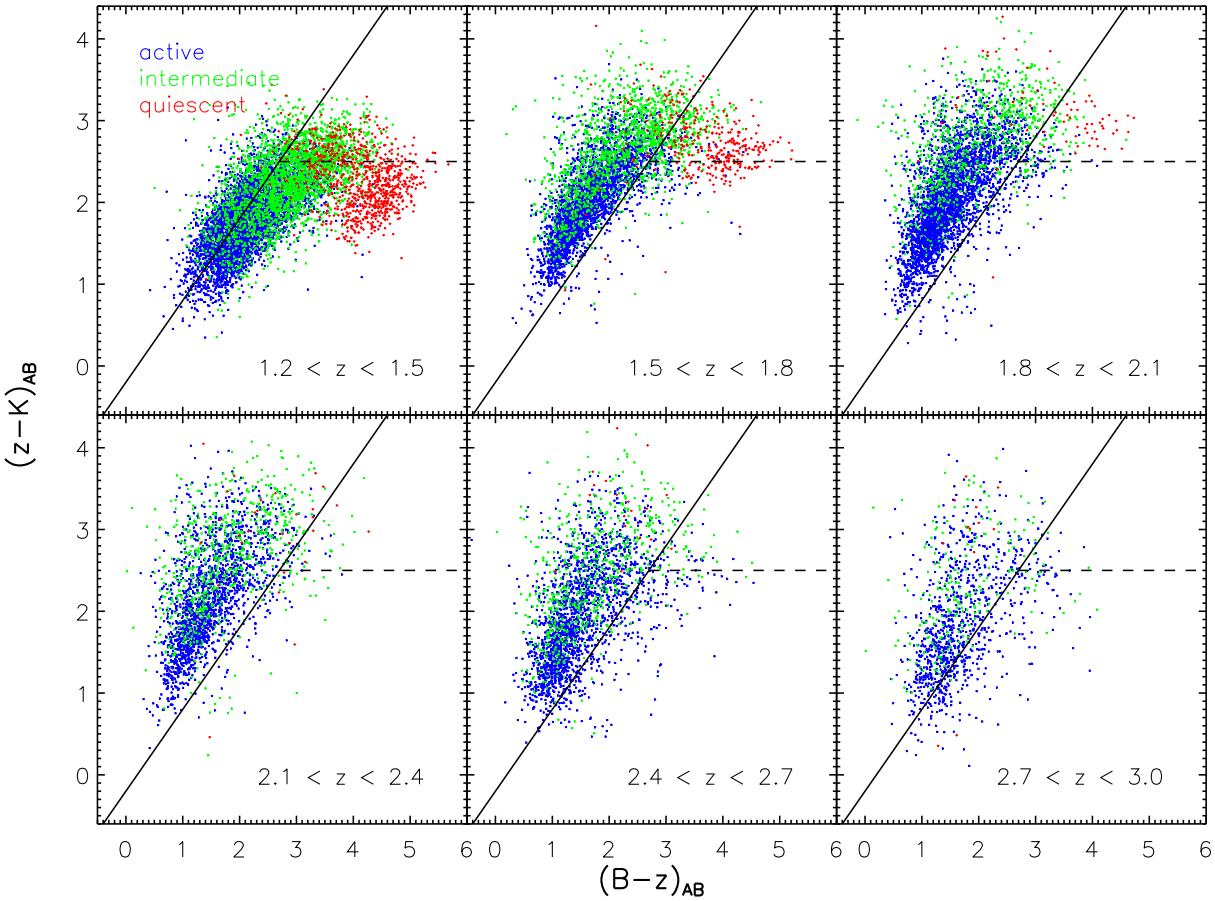

Figure 4.9. – BzK diagram of our sample in various redshift bins. The color coding refers to our choice of the $(\mathrm{NUV} - r^{+})_{\mathrm{temp}}$ color threshold in order to predefine systems with high (blue), intermediate (green) and negligible (red) star formation activity. In the lowest redshift panel the original (Daddi et al. 2004) sBzK criterion (diagonal line) does not appear to be efficient enough in selecting *all* SF galaxies and is particularly missing the systems with intermediate levels of star formation. At higher redshifts our SF sample (all green and blue sources) overlaps very well with the sBzK population so that our color selection for the purpose of radio stacking is appropriate to select normal SF systems at $z > 1.5$.

is shallower at low to intermediate redshifts and thus in excellent agreement with those literature results for SF galaxies discussed in Section 4.4.4 that report an almost flat SSFR-sequence. At the high-z end we see a steepening of the slope β (i.e. an 'upsizing' trend), similar or even more evident to what was found by Rodighiero et al. (2010a) and, at lower significance, also by Oliver et al. (2010). The evolutionary exponent n is consistent with previous measurements as well (see e.g. Pannella et al. 2009).

The bluer color threshold hence is able to reproduce most literature findings albeit with SSFRs that tend to be comparativey high, especially at low redshift. However, it has yet to be confirmed that the galaxy population selected in this way is representative of the *entire* SF population.

4.5.2. (s)BzK galaxies at $z \sim 2$

We cross-matched our 3.6 μm selected catalog with the K band selected catalog for the COSMOS field (McCracken et al. 2010) and thus obtain a magnitude calibration in the crucial wavebands that allows us to apply the BzK selection criterion of Daddi et al. (2004). Figure 4.9 shows the BzK diagram for our sample, with galaxies in six redshift slices color coded according to their $(\mathrm{NUV} - r^+)_{\mathrm{temp}}$ color as described in Section 4.2.4. Our 'star forming' sample is the union of all galaxies plotted in blue *and* green.

At $z > 1.5$, the sBzK criterion (all galaxies to the left of the diagonal line in each panel) is established to efficiently select normal SF systems. Figure 4.9 illustrates that the selection window for sBzK galaxies is populated by *both* the most actively star formation sources (blue dots) and the majority of the sources with intermediate star forming rates (plotted in green; i.e. the rest of the SF sample used throughout this Chapter). Only a small number of objects with moderate SF activity fall into the passive BzK region in the upper right of each panel. This is the reason for the aforementioned excellent agreement of our results with Pannella et al. (2009) at $z \approx 2.1$; their and our sample are virtually indistinguishable and both studies rely on the same radio data. More importantly, however, the BzK diagram strongly supports our original selection of SF objects in the crucial redshift regime $z > 1.5$, where we have just shown that previously reported changes in the slope β can be mimicked by simply selecting only very blue objects, hence, most actively forming systems.

4.6. Summary and conclusion

Based on an unprecedentedly rich sample of galaxies selected at 3.6 μm with panchromatic (FUV to mid-IR) ancillary data and mapped in 1.4 GHz radio continuum emission in the COSMOS field we have measured stellar mass-dependent average (specific) star formation rates ((S)SFR) in the redshift range $0.2 < z < 3$. These were obtained using a median image stacking technique that is best applied in the radio regime where the angular resolution is high and the fraction of direct detections is comparatively low such that blending of sources is negligible.

We individually measured integrated radio flux densities in each stacked image and showed that a uniform (i.e. mass-independent) correction factor is inappropriate to convert between peak and total flux density when high angular resolution radio continuum data is used. Furthermore, we applied various criteria in order to minimize the impact of contaminating radio flux density from active galactic nuclei and discussed to which lower mass limit at a given redshift our sample remains representative with respect to the star formation properties of the underlying population. We emphasize that all our findings are to be regarded as most robust at $z < 1.5$ while our data place valuable constraints on evolutionary trends at the highest masses as far as $z = 3$.

Using the template-based, rest-frame $(\mathrm{NUV} - r^+)_{\mathrm{temp}}$ color from SED-fits in the NUV-mid-IR, we separate SF galaxies from quiescent systems in order to study the average mass dependence of their SSFR at all epochs considered. We also discussed potential effects introduced by such a color threshold, such as mimicking a potential upturn of the SSFR-M_* relation.

Our findings are summarized as follows:

1. The massive end of our global sample of mass-selected galaxies (including quiescent and SF systems) shows a power-law relation between SSFR and stellar mass ($\mathrm{SSFR} \propto M_*^{\beta}$) with an index of roughly $-0.7 \lesssim \beta_{\mathrm{ALL}} \lesssim -0.6$ and a trend towards shallower indices with increasing redshift. Towards lower masses the relation appears to flatten, probably because quiescent galaxies with low SSFRs preferentially occupy the massive end of the normal galaxy population.

2. For a given stellar mass we report a strong increase of the SSFR with redshift that is best parametrized by a power-law $\propto (1+z)^{4.3}$.

3. The relation between SSFR and mass for star forming (SF) systems only (referred to as the SSFR-sequence) evolves as $(1+z)^{3.5}$ and shows a shallower power-law index of $\beta_{\mathrm{SFG}} \approx -0.4$ because quiescent galaxies do not lower the observed average SSFRs at the high-mass end anymore. The parameter β_{SFG} does not significantly change with cosmic time so that the average SSFR is best described by a separable function in mass and redshift (Eq. 4.8 in Section 4.4.3).

4. Towards lower masses and $z > 1.5$ also the SSFR-sequence itself tends to flatten which might be explained by an upper limiting threshold where average SF systems already reach levels of star formation that qualify them to double their mass within a dynamical time. It is plausible that the SSFR at a given time does not continue to increase till the regime of dwarf galaxies at the rate predicted by our power-law index. We, however, cannot rule out that low-mass systems with high star formation activity but also very high dust content are missed given the limiting magnitude in our selection band.

We firmly conclude that, out to $z \sim 1.5$, our results hence neither support the so-called 'SSFR-downsizing' nor '-upsizing' scenarios proposed by some earlier work while they do confirm the downsizing scenario in the following take:

The SFR declines strongly but in a mass-independent fashion while the most massive galaxies always show the least star formation activity and are hence the first to fall below their past-average star formation activity.

5. A constant characteristic mass for star forming galaxies since $z \sim 3$ in the COSMOS field

In this Chapter the results of the previous Chapter are used to obtain a deeper insight into the mass-dependent cosmic star formation history. First we combine our results with recent measurements of the galaxy (stellar) mass function in order to determine the characteristic mass of a star forming galaxy at a given epoch: we find that since $z \sim 3$ two thirds of all new stars were always formed in galaxies of $M_* > 10^{9.75}\ M_\odot$ with a constant peak around $M_* = 10^{10.6 \pm 0.4}\ M_\odot$. This constancy of the characteristic mass is surprising as it challenges the often stressed 'downsizing paradigms' in which the characteristic mass is supposed to shift towards smaller values over time. Finally, our analysis constitutes the most extensive SFR density determination with a single technique out to $z = 3$. This chapter is part of the publication

A. Karim, E. Schinnerer, A. Martínez-Sansigre, M. T. Sargent, A. van der Wel, H.-W. Rix, O. Ilbert, V. Smolčić, C. Carilli, M. Pannella, A. M. Koekemoer, E. F. Bell & M. Salvato, 2011, ApJ, 730, 61, *The star formation history of mass-selected galaxies in the COSMOS field*

5.1. Introduction

Over the past 15 years one of the most important quantities in observational cosmology has been the star formation rate density (hereafter SFRD), the star formation rate (SFR) per unit comoving volume. Describing the global rate of star formation in the universe at a given cosmic epoch, it has attracted so much interest since already initial studies revealed its rapidly evolving character (Lilly et al. 1996; Madau et al. 1996). It substantially declines since ~ 10 Gyr ago following the purported maximum of star formation activity in the universe (see also Hopkins and Beacom 2006, for a compilation). After the initial findings many results are found in the literature that support this picture of the cosmic star formation history (CSFH) based on ever-growing galaxy samples leading to an improving accuracy (e.g. Chary and Elbaz 2001; Hopkins 2004; LeFloc'h et al. 2005; Smolčić et al. 2009a; Dunne et al. 2009; Rodighiero et al. 2010b; Gruppioni et al. 2010; Bouwens et al. 2011b; Rujopakarn et al. 2010).

The literature results cover a vast diversity of SFR tracers including ultraviolet (UV) light, emission line diagnostics, (far-)infrared (IR) emission as well as synchrotron emission from supernova remnants detected at radio continuum wavelengths. How much of the *total* SFRD, i.e. the contribution of *all* star forming (SF) galaxies, can be observed clearly depends on the depth of the data used. All studies therefore rely on extrapolations to account for the contribution of faint (low-mass) systems.

The results of the previous chapter allow us to accurately constrain the CSFH even in a

mass-dependent fashion, a previously barely explored parameter. Based on our measurement of radio-derived SFRs as a function of mass we directly derive SFRDs for *SF galaxies* above the limiting mass at $z < 1.5$ and further constrain the CSFH out to $z = 3$. We will also introduce two alternative extrapolations to low-mass objects that we do not directly observe. Because of our generally low mass limit, the impact of the extrapolation – especially out to $z = 1.5$ – to these faint galaxies is small compared to most other studies.

5.2. The mass distribution function of the SFRD at fixed redshift

At a given redshift and stellar mass, the SFRD is computed as the product of (i) the comoving number density as inferred directly from the number of galaxies in the relevant mass bin and (ii) their average SFR as measured in our stacking analysis.

As already pointed out, our SFRs likely represent an upper limit at the smallest masses where the sampling of the underlying population is no longer representative. Consequently, SFRDs at low masses are upper bounds, as we can correct the number counts in a given low-mass bin for the lost objects. This is done by computing the expected number from the observed mass functions derived for the same sample of SF galaxies that is used for this study (for further details see Ilbert et al. 2010, I10 in the following). We account for the slightly smaller portion of the COSMOS-field accessible to the radio-stack compared to the area used for the derivation of the mass-functions. The correction for the expected number counts is always small so that corrected and uncorrected values of SFRD(M_*, z) agree within the errors. Since it is a systematic correction it still needs to be taken into account.

All number-count corrected and uncorrected data points for the SFRD(M_*, z) are shown in Figure 5.1. There appears to be a characteristic mass of $M_* = 10^{10.6\pm0.4}\ M_\odot$ that contributes most to the total SFRD at a given redshift. Up to $z \sim 1.8$ our data points sample below this characteristic mass and the peak is well constrained. At higher redshifts this is no longer the case.

We want to motivate now that the underlying functional form for the distribution of data points in the SFRD-M_* plane is actually known because of two facts:

1. There is a (possibly broken) power-law relation between (S)SFR and stellar mass for SF galaxies at all $z < 3$ as measured in this study.

2. The functional form of the mass function for SF objects in the same redshift range is well determined.

Regarding the second point, the mass function of SF galaxies is commonly (e.g. Lilly et al. 1995; Bell et al. 2003, 2007; Zucca et al. 2006; Arnouts et al. 2007; Pozzetti et al. 2009; Ilbert et al. 2005, 2010) found to be well parametrized by a power law with an exponential cutoff at a characteristic mass M^* as introduced by Schechter (1976) of the form

$$\begin{aligned} \Phi_{\rm SFG}(M_*)dM_* &= \Phi^*_{\rm SFG}\,(M_*/M^*_{\rm SFG})^{\alpha_{\rm SFG}} \\ &\times \exp\left(-M_*/M^*_{\rm SFG}\right) d(M_*/M^*_{\rm SFG}). \end{aligned} \tag{5.1}$$

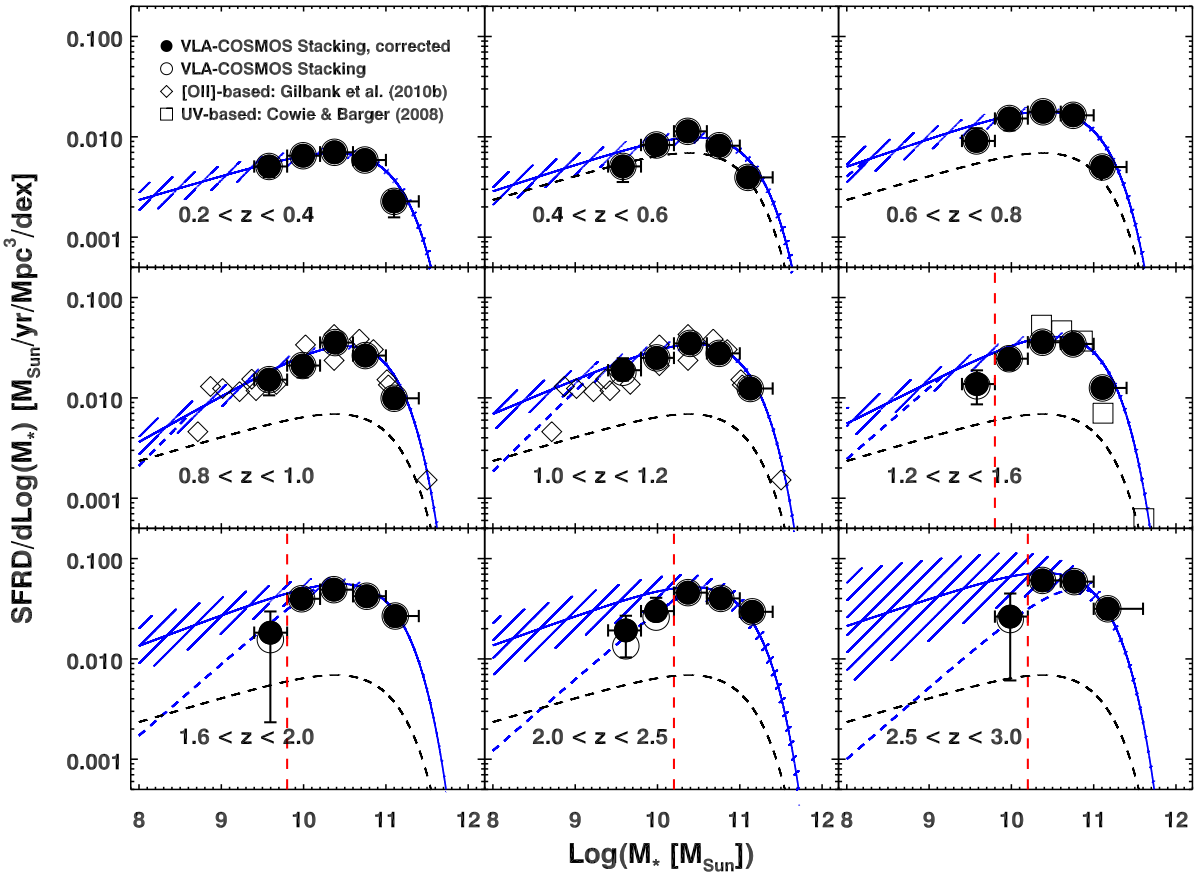

Figure 5.1. – The distribution of the SFR density (SFRD) with respect to stellar mass, as measured at various epochs out to $z \sim 3$. In each panel the data points have been derived by multiplying the observed number densities of SF galaxies with the average (stacking-based) radio SFRs. Below the limit where our data is regarded mass-representative (see Section 4.2.6 and Appendix A.3) – depicted by red dashed vertical lines – number densities have been corrected using the mass functions (Ilbert et al. 2010). The uncorrected data are shown for comparison as open circles suggesting that these corrections are generally small and no corrections are needed at $z < 1.5$. For $0.8 < z < 1.2$, the [OII]λ3727-derived SFRDs (from Gilbank et al. 2010b); open diamonds, rescaled by a constant factor of two to match our data agree well with the trends in our data. The same holds true for the UV-based results by Cowie and Barger (2008) depicted at $1.2 < z < 1.6$ for which no rescaling was necessary. Note that their data was derived over a broader range in redshift down to $z = 0.9$. As our data suggest globally only a mild evolution between $0.9 < z < 1.4$ the comparison depicted is justified. In each panel we overplot the Schechter function that results from multiplying the best-fit radio derived SSFR-sequence at a given epoch with the corresponding mass function for SF galaxies. The uncertainty range is obtained by choosing the two sets of Schechter parameters within their error margins that maximize/minimize the integral. Dashed blue lines show the distribution obtained if an upper limit to the average SSFR at lower masses (see Section 4.4.2 for details) is assumed (referred to as 'case B' in Section 5.2). All literature data plotted here have been converted to our Chabrier IMF.

Table 5.1. Schechter parameters for the stellar mass function of *star forming galaxies*

$\Delta z_{\rm phot}$	$\alpha_{\rm SFG}$	$\log(M^*_{\rm SFG})$ M_* $[M_\odot]$	$\Phi^*_{\rm SFG}$ $[10^{-3}$ Mpc^{-3} dex$^{-1}]$
0.2-0.4	$-1.32^{+0.01}_{-0.01}$	$11.00^{+0.03}_{-0.03}$	$1.15^{+0.08}_{-0.07}$
0.4-0.6	$-1.32^{+0.01}_{-0.01}$	$11.04^{+0.03}_{-0.03}$	$0.70^{+0.05}_{-0.04}$
0.6-0.8	$-1.32^{+0.01}_{-0.01}$	$10.95^{+0.02}_{-0.02}$	$0.86^{+0.05}_{-0.05}$
0.8-1.0	$-1.16^{+0.01}_{-0.01}$	$10.86^{+0.02}_{-0.02}$	$1.38^{+0.06}_{-0.06}$
1.0-1.2	$-1.19^{+0.02}_{-0.02}$	$10.92^{+0.02}_{-0.02}$	$0.94^{+0.05}_{-0.05}$
1.2-1.5	$-1.28^{+0.02}_{-0.02}$	$10.91^{+0.02}_{-0.02}$	$0.68^{+0.03}_{-0.03}$
1.5-2.0	$-1.29^{+0.02}_{-0.02}$	$10.96^{+0.02}_{-0.02}$	$0.46^{+0.02}_{-0.02}$
2.0-2.5	$-1.29^{+0.03}_{-0.03}$	$10.95^{+0.03}_{-0.03}$	$0.32^{+0.06}_{-0.06}$
2.5-3.0	$-1.29^{+0.03}_{-0.03}$	$10.95^{+0.03}_{-0.03}$	$0.27^{+0.05}_{-0.05}$

Note. — At $z < 2$ all parameters have been derived by I10. At $z > 2$ we assume a non-evolving shape so that $\alpha_{\rm SFG}$ and $M^*_{\rm SFG}$ are taken to be the average of the respective lower z values. $\Phi^*_{\rm SFG}$ was then derived by matching the number densities to those observed in the mass-representative regime of our data.

This Schechter function has recently been qualitatively as well as quantitatively been modeled to be the natural consequence of essentially two types of cessation of star formation (Peng et al. 2010).[1]

Multiplying $\Phi_{\rm SFG}(M_*)$ by the SFR-sequence, i.e. another power-law in mass, again produces a Schechter function. Hence we can write

$$\mathrm{SFRD}(M_*, z) dM_* = \Phi_{\rm SFRD}\left(\Phi^*_{\rm SFRD}, \tilde{\alpha}, M^*\right) dM_*, \tag{5.2}$$

i.e. a distribution (SFRD function hereafter) of the same functional form as Eq. (5.1) with the three parameters $\Phi^*_{\rm SFRD}$, $\tilde{\alpha}$ and M^*. While the exponential cutoff mass M^* is the same as the one in the mass function (defined above as $M^*_{\rm SFG}$), $\tilde{\alpha} = \alpha_{\rm SFG} + \tilde{\beta}_{\rm SFG}$ is the sum of the low-mass slope of the mass function of SF galaxies and the slope[2] of the SFR-sequence (see also Santini et al. 2009, for a similar parameterization). The parameter $\Phi^*_{\rm SFRD}$ acts as a normalization and its role in the global evolutionary picture will be discussed in Section 5.3.

The index $\alpha_{\rm SFG}$ and also the cutoff mass M^* for SF galaxies are constant in the redshift regime considered (e.g. Bell et al. 2003, 2007; Arnouts et al. 2007; Pérez-González et al.

[1] Peng et al. (2010) refer to these two processes as 'environment-' and 'mass-quenching'. The former one is likely to be explained by star formation being shut off in satellite systems as soon as galaxies fall into larger dark matter halos while the latter one is a continuous process stopping star formation within galaxies above the characteristic mass $M^*_{\rm SFG}$ at a rate proportional to their SFR. In the following we will make use of evolutionary constraints on the mass function parameters $\alpha_{\rm SFG}$, $\Phi^*_{\rm SFG}$ and $M^*_{\rm SFG}$ for SF galaxies in particular. Their trends are not only supported by recent literature (see the further discussion in this Section) but also naturally contained in the empirical Peng et al. (2010) model.

[2] Please note that $\tilde{\beta}_{\rm SFG}$ denotes the slope of the SFR-M_* relation for SF galaxies which is connected to the slope $\beta_{\rm SFG}$ of the SSFR-sequence (see Section 4.4.1 and Table 4.4) by $\tilde{\beta}_{\rm SFG} = \beta_{\rm SFG} + 1$.

2008; Pozzetti et al. 2009 as well as Table 5.1 which is based on the results of Ilbert et al. 2010). We assume here that $\alpha_{\rm SFG}$ and $M^*_{\rm SFG}$ stay constant also at $z > 2$. These assumptions are tentatively supported by the few observational constraints reported for these high redshifts as detailed in Section 5.3. As detailed in Section 4.4.1, the power-law index $\beta_{\rm SFG}$ – that enters the parameter $\tilde{\alpha} = \alpha_{\rm SFG} + \beta_{\rm SFG} + 1$ in Eq. 5.2 – is also found to be a constant. However, we explained in Section 4.4.2 that at masses lower than the crossing mass between the SSFR-sequence and a possible SSFR-threshold $\beta_{\rm SFG} = 0$ should be assumed. In the following we will hence consider two possible scenarios below the suggested crossing mass at a given redshift:

$$\textbf{Case A}: \quad \tilde{\alpha} = \alpha_{\rm SFG} + \beta_{\rm SFG} + 1$$
$$\textbf{Case B}: \quad \tilde{\alpha} = \alpha_{\rm SFG} + 1.$$

Figure 5.1 shows that at $z < 1.5$ the parameterization of the SFRD function in Eq. (5.2) can reproduce our data at all masses sampled and irrespective of the exact value of $\tilde{\alpha}$. For this redshift range Figure 5.1 also includes results of two other studies that rely on different SFR tracers. At $z \sim 1$ the dependence of the SFRD on stellar mass has recently been measured using the [OII]λ3727 line to trace star formation (Gilbank et al. 2010b). We over-plot these data points in the corresponding redshift bins in Figure 5.1 and find that our SFRD function accurately fits these measurements as well.[3] The same holds for the UV-derived results based on a Salpeter IMF by Cowie and Barger (2008) in the GOODS-North field at $0.9 < z < 1.5$. Given our results, the global evolution of the SFRD-function between $0.9 < z < 1.4$ is mild such that we can plot these data in Figure 5.1 in the bin $1.2 < z < 1.6$. It is worth noting that the Cowie and Barger (2008) measurements at $z < 0.9$ equally support our finding that the peak of the SFRD does not shift with redshift to higher values.

Below the limiting stellar mass (dashed red lines in Figure 5.1) our data points are lower than the prediction of Eq. 5.2 if we assume case A for $\tilde{\alpha}$ (even though we have applied a number density correction). Moreover, we remind the reader that – in keeping with our previous discussion – these data points are likely upper limits. Given the comparatively large uncertainties of our SFRD functions at high z these deviations are not highly significant but the trend is systematic and suggests a steepening of the low-mass slope of the SFRD function. It is directly related to the fact that the corresponding data points deviate from the best-fit (S)SFR-M_* relation at lower mass. In Section 4.4.2 we proposed an upper limit to the average SSFR due to dynamical reasons as a possible explanation for the trends. Taking into account this limit of $\mathrm{SSFR} = 1/\tau_{\rm dyn} \sim 2.7$ Gyr^{-1} yields an index $\beta_{\rm SFG} = 0$ below the mass at which our fitted high-mass SSFR-M_* relation crosses the supposed SSFR limit at a given epoch. We plot the SFRD function for $\tilde{\alpha} = \alpha_{\rm SFG} + 1$ as dashed blue lines in Figure 5.1. As the crossing mass increases with redshift and lies below the mass-representativeness threshold at $z < 1$ it has little impact on the mass-integrated SFRD. The reason is that the mass-dependent SFRD has declined already by at least an order of magnitude from the

[3] These data are based on a Baldry & Glazebrook IMF and have been converted to the Chabrier scale. An additional rescaling by a constant factor of two was necessary in order to match our calibration. This is in agreement with the results by Gilbank et al. (2010b) that show SFRs based on practically all probed alternative tracers to be in excess of the [OII]-derived ones. They discuss possible explanations for this deviation. Given the well known global uncertainty in the absolute calibration of SFR tracers this deviation is, however, not significant.

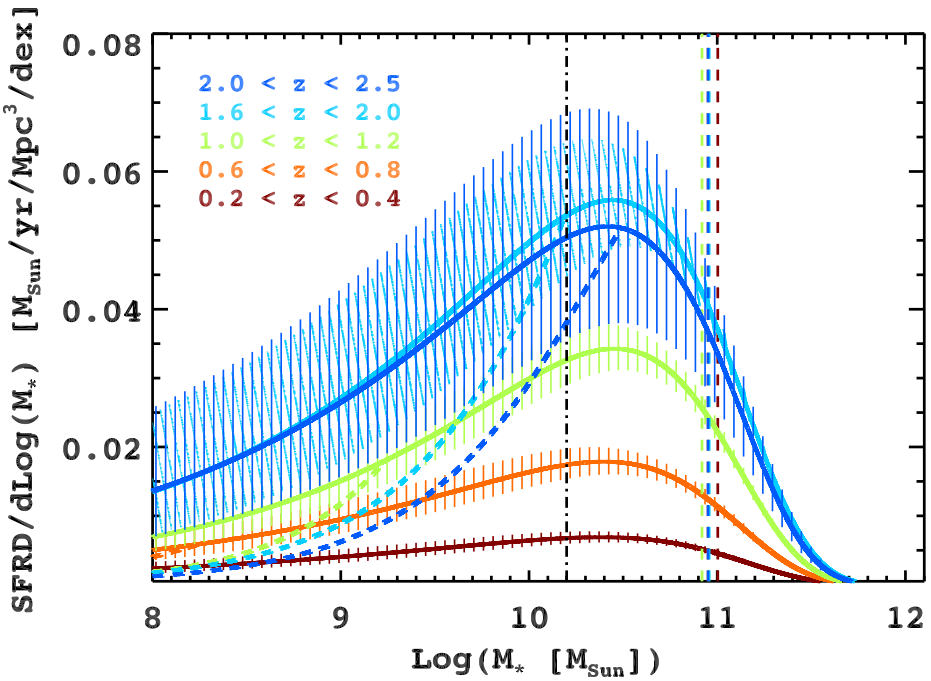

Figure 5.2. – The Schechter-function description of the SFRD (referred to as SFRD function) for $z < 2.5$, with color denoting the redshift range. This plot combines the information in the preceding Figure, now displayed with a linear scaling of the y-axis. The dashed vertical lines of different colors show the Schechter parameter $M^*_{\rm SFG}$ (from Ilbert et al. 2010) for different redshifts. It is found to be nearly redshift-independent for SF galaxies. The representativeness limit of our SF sample is below $M^*_{\rm SFG}$ at all epochs as indicated for the highest redshift bin ($2 < z < 2.5$; dash-dotted vertical line). Thick dashed lines of different colors depict the modified low-mass end trends for our SFRD functions (referred to as 'case B') that result from assuming an upper limit to the average SSFR of ${\rm SSFR} \sim 1/\tau_{\rm dyn}$. Here, $\tau_{\rm dyn} \sim 0.37$ Gyr is the dynamical timescale for normal SF galaxies (see Section 4.4.2 for details). This plot clearly shows that the characteristic mass of SF galaxies – which always lies below $M^*_{\rm SFG}$ – does not evolve over time. This conclusion holds regardless of the exact shape of the SSFR-sequence at lower masses. Therefore, our data exclude a scenario in which the peak of the SFRD function has shifted to lower masses at later epochs.

peak value before reaching the crossing mass. The changes are largest at $z > 1.8$ where the dashed SFRD function (case B) drops quickly towards lower masses right after the peak and, in doing so, traces our data points better than before for $\tilde{\alpha} = \alpha_{\rm SFG} + \beta_{\rm SFG}$ (case A). However, we emphasize that our data cannot clearly favor case A or B proposed given the large uncertainties of the Schechter parameters and the lack of representativeness of our data at such low masses at high z. Any scenario suggested, hence, awaits confirmation based on deeper data in the selection band once they are available. We robustly conclude that a single Schechter function is a good model for the SFRD-function over all masses at least out to $z \sim 1$ and that the distribution of SFRDs peaks in the same mass-range at all z probed in both case A and B.

Figure 5.2 shows the time evolution of our above constructed SFRD function. This non-logarithmic plot clearly illustrates the existence of a characteristic mass of star formation at all epochs although it should be kept in mind that our results are most robust at $z < 1.5$.

Our findings exclude an evolution of this characteristic mass towards lower values with cosmic time. At $z < 1.5$ this important result is supported by independent observations at different wavelengths (Cowie and Barger 2008; Gilbank et al. 2010a,b) and, towards $z \approx 2$, also by empirical arguments (Peng et al. 2010) while the recent model of Boissier et al. (2010) predicts a mild evolution of this characteristic mass by about 0.3 dex. In Figure 5.2 again dashed lines of corresponding color denote the low-mass trends of the SFRD functions once we assume the SSFR-limit discussed. As pointed out above, within the important mass-range above $10^{10}\ M_{\odot}$ – at which the SFRD function peaks at any epoch – a mass-independent proportional increase is apparent even out to $z > 2$. In contrast to that, the mass-dependent SFRD appears to evolve mildly below $10^{9}\ M_{\odot}$. As a result galaxies in the stellar mass range between $10^{10} - 10^{11}\ M_{\odot}$ contribute most to the global – i.e. mass-integrated – SFRD at any epoch but low-mass systems gain more relative importance towards low redshifts. Evidently, low-mass systems show the same evolutionary trends as those of higher mass if case A is assumed.

Earlier observational findings appear to be at odds with the existence of a characteristic stellar mass for star formation we measure. While they are all based on shallower survey data compared to our COSMOS imaging, the limiting magnitude of these samples is not necessarily the reason for the different conclusions. Juneau et al. (2005) – using a mass-independent extinction correction and hence a linear conversion from [OII] luminosity to SFR – report that out to $z \sim 2$ the contribution to the increase of the global SFRD is more rapid, the more massive the galaxies are. While this is a similar trend we find if we assume an upper limit in SSFR (case B), their lowest stellar mass-bin – centered at $10^{9.6}\ M_{\odot}$ – always appears to contribute most to the SFRD integrated over all masses. Hence, there is no clear evidence for a peak in the SFRD mass-distribution function and certainly not in the higher mass-range our data supports. However, based on their findings in the local universe (Gilbank et al. 2010a), Gilbank et al. (2010b) empirically showed that a mass-dependent calibration between [OII] luminosity and SFR is more appropriate. If true, this would modify the low the low-mass dominance in the derived SFRDs of Juneau et al. (2005) to correspond more closely to our result.[4]

Independently, also the radio-stacking based study by Pannella et al. (2009) suggests a strong dependence of the dust-attenuation correction on stellar mass at higher ($z > 1.5$) redshifts. Similarly to Juneau et al. (2005), Bauer et al. (2005) derive their [OII]-based (S)SFRs from a mass-independent calibration albeit neglecting extinction corrections.[5] Finally, Bundy et al. (2006), who favor a shift of the characteristic mass towards lower values with cosmic time, entirely base their conclusion on the stellar mass functions they derive for SF galaxies (selected by rest-frame (U-B) color and [OII] equivalent line width) within the DEEP2 survey sample. At $z \lesssim 1.4$ these mass functions do not show an evolution of the faint-end slope, but the Schechter parameter M^{*}_{SFG} appears to decrease with cosmic time, in contrast to the already discussed broad agreement in the more recent literature according to which neither α_{SFG} nor M^{*}_{SFG} change in this redshift range.

To conclude, we summarize our findings as follows.

[4] Indeed, as Gilbank et al. (2010b) point out, the mass-dependence here is not only introduced by dust extinction but results from an interplay of various additional factors, e.g. the metallicity or the ionisation parameter.

[5] In the context of mass-dependent evolutionary effects not considering any extinction correction is equivalent to considering a mass-uniform one.

1. Up to normalization, the mass distribution function of the SFRD at $z < 1$ is a universal Schechter function with possible deviations only below $10^8\ M_\odot$.

2. We explain this surprising constancy in shape of this SFRD-function by the non-evolving slope of the SFR-sequence and the constant shape of the mass function for SF galaxies.

3. Our data at $z < 1.5$ clearly disfavors a strong 'downsizing' scenario in which the characteristic mass of SF galaxies that contribute most to the overall SFRD – integrated over all masses at a given time – shifts towards lower values over cosmic time. The situation does not appear to change even at $z > 1.5$ where, however, deeper data is needed to confirm our results. The characteristic mass is $M_* = 10^{10.6\pm0.4}\ M_\odot$.

4. If we assume an upper limit to the average SSFR of the order of the inverse dynamical scale ($\tau_{\rm dyn} \sim 0.37$ Gyr) the SFRD of galaxies less massive than $10^9\ M_\odot$ evolves less rapidly than the one of the dominant higher mass range above $10^{10}\ M_\odot$.

5.3. The evolution of the SFRD

As all introduced parameters show this remarkable constancy throughout the redshift range probed (at least out to $z \approx 1$) the redshift dependence of Eq. (5.2) is entirely contained in the normalization $\Phi^*_{\rm SFRD}$. Eq. (5.2) becomes a separable function so that we rewrite:

$$\mathrm{SFRD}(M_*, z) dM_* = \Phi^*_{\rm SFRD}(z)\, \varphi\left(\tilde{\alpha}, M^*\right) dM_*, \tag{5.3}$$

where mass-dependence consequently is solely contained in the universal SFRD function φ. The global SFRD at a given redshift, integrated over all masses, is simply given by

$$\mathrm{SFRD}(z) = \Phi^*_{\rm SFRD}(z) \int \varphi\left(\tilde{\alpha}, M^*\right) dM_*. \tag{5.4}$$

In the following we will motivate that the evolution of the integrated SFRD follows a simple power-law of the form

$$\Phi^*_{\rm SFRD}(z)\left[M_\odot/\mathrm{yr}/\mathrm{Mpc}^3\right] \propto (1+z)^{n_{\Phi^*_{\rm SFG}} + n_{\rm SSFR}}, \tag{5.5}$$

where the two power-law indices result from the change in stellar mass density contained in SF galaxies and the increase of the (S)SFR-sequence with redshift.

As detailed in I10 and previously also found by other studies (e.g. Bell et al. 2003, 2007; Arnouts et al. 2007; Pozzetti et al. 2009) the stellar mass density of SF galaxies grows after the Big Bang only until $z \sim 1$. At lower redshifts it stays constant. Consequently, as the shape of the mass functions does not evolve, also the Schechter parameter $\Phi^*_{\rm SFG}$ in the mass function is constant in this redshift regime, apart from fluctuations due to large scale density fluctuations. As shown in Figure 5.3, these fluctuations are consistent with cosmic variance as estimated by Scoville et al. (2007c) and detailed in I10.[6] It is clear that cosmic variance effects are strongest at low redshifts as the effective volume sampled in a redshift bin with $\Delta z = 0.2$ increases with redshift. In the interest of simplicity and to avoid systematic errors caused by cosmic sampling variance we adopt a constant $\Phi^*_{\rm SFG}$ at $z < 1$.

[6] For a detailed discussion on cosmic variance in the COSMOS field we refer to Meneux et al. (2009).

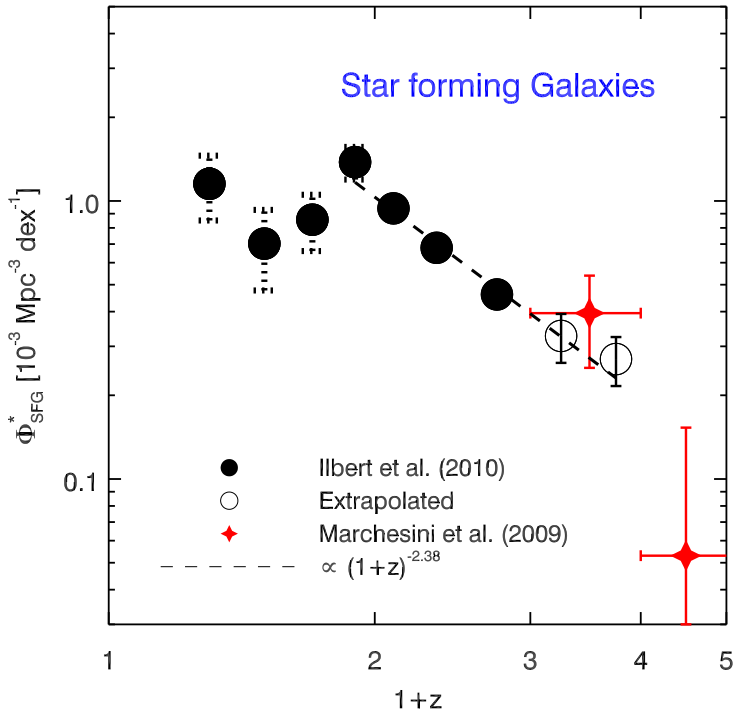

Figure 5.3. – The redshift dependence of the Schechter parameter $\Phi^*_{\rm SFG}$ of the mass functions for SF galaxies as derived in the COSMOS field (I10). At $z < 1$ the normalization $\Phi^*_{\rm SFG}$ behaves like the other Schechter parameters and stays constant except for fluctuations very likely caused by cosmic variance. An estimate of the cosmic variance error (see Scoville et al. 2007c, for further details) is added in quadrature to the error of the Schechter fit at these redshifts, as indicated by dotted error bars. At earlier epochs the mass build-up is reasonably well characterized by a power law in $(1 + z)$. This trend is consequently also seen in the evolution of the stellar mass density of SF galaxies (I10). The two highest redshift points (open symbols) were obtained under the assumption that the mass functions keep their shapes also at earlier cosmic times by matching the normalization to the numbers of galaxies observed in our mass-representative bins at the high-mass end. This assumption is supported by the direct observational constraint of $\Phi^*_{\rm ALL}$ from the best-fit Schechter-parameterization of the total mass-function measured by Marchesini et al. (2009) which – at these high redshifts – should be representative for the SF population; red diamonds.

If we therefore set $n_{\Phi^*_{\rm SFG}}(z < 1) = 0$ in Eq. (5.5) the evolution of the integrated SFRD in the range $0 < z < 1$ is entirely described by the global, i.e. mass-uniform, decline of the average SFR of SF galaxies with cosmic time. It is important to emphasize once again that this strong decline is definitely not caused by a decreasing number of SF galaxies, in particular not at all at the high-mass end. As the efficiency of star formation within SF systems appears not to change over cosmic time (Daddi et al. 2010a; Tacconi et al. 2010), we conclude that below $z \sim 1$ the strongly evolving integrated SFRD must be exclusively caused by a strongly declining mass density of cold molecular gas available for star formation towards the local universe. Recent theoretical model predictions (Obreschkow and Rawlings 2009; Dutton et al. 2010) indeed support such an evolutionary behavior of the cosmic mass density of molecular hydrogen. As we already explained in Section 4.4.3, systematic redshift uncertainties will not influence our conclusions either as they would only be propagated along the redshift trend inferred.

At earlier epochs (i.e. $z > 1$) we monitor the redshift dependence of the parameter $\Phi^*_{\rm SFG}$ as measured by I10 (Table 5.1). Figure 5.3 shows that the above choice of a power law at $z > 1$ is a reasonable assumption and we find $n_{\Phi^*_{\rm SFG}}(z > 1) = -2.38 \pm 0.02$ from a fit to our COSMOS data points at $1 < z < 3$. It should be mentioned that the two highest redshift points in Figure 5.3 (open circles) were obtained by assuming that $\alpha_{\rm SFG}$ and $M^*_{\rm SFG}$ stay constant also at $z > 2$ where I10 did not directly measure the mass function. The normalization $\Phi^*_{\rm SFG}(z > 2)$ was therefore obtained by matching the number densities to those observed in the mass-complete regime of our data when fixing the parameters $\alpha_{\rm SFG}$ and $M^*_{\rm SFG}$ to their average values at $z < 2$. This extrapolation is supported by the total mass function at $z > 2$ measured by Marchesini et al. (2009). At these high redshifts we assume the total mass function to be representative for the SF population as quiescent galaxies are not expected to significantly contribute to the number density. The study by Marchesini et al. (2009) was carried out based on data taken in various survey fields for which deep NIR imaging is available allowing them to estimate Schechter parameters for the total mass function also in two high-z bins in the ranges $2 < z < 3$ and $3 < z < 4$. Within the errors all our extrapolated Schechter parameters at $2 < z < 3$ are in good agreement with their results. In particular the exponential cutoff mass at $2 < z < 3$, $M^*_{\rm ALL} \equiv M^*_{\rm SFG} = 10^{10.96}$, they find[7] agrees remarkably well with our assumption (see Table 5.1). Their normalization $\Phi^*_{\rm ALL} \equiv \Phi^*_{\rm SFG}$ does not deviate significantly from our prediction and the evolutionary trend we suggest is also supported by their data (see Figure 5.3). It is clear, however, that future measurements of the stellar mass function at $z > 1.5$ – based on deeper NIR or mid-IR data – are critical to confirm the validity of our assumptions. Based on the currently available data we conclude that the stellar mass build-up in the SF galaxy population inevitably leads to a shallower decline of the integrated SFRD between $3 > z > 1$ compared to the steep decline between $1 > z > 0$.

In order to validate our parameterization of the evolution of the integrated SFRD we proceed as follows. First, we simply add up all SFRDs measured in different mass bins in a given redshift bin (all data points shown in the corresponding panels in Figure 5.1) obtaining a lower limit to the integrated SFRD at that epoch. Second, in order to account for the contribution of the low-mass ($\log(M_*) < 9.5$) SF population that we cannot directly measure, we integrate Eq. (5.2) from our mass-limit down to $10^5\ M_\odot$. As we discuss in Section 5.2 a single value of the index $\tilde{\alpha}$ in Eq. (5.2) might not be valid over the entire low-mass range as the SSFR-M_* relation might flatten as soon as an upper limiting SSFR is reached. The upper left panel in Figure 5.4 hence shows the two alternative extrapolations and all obtained data are given in Table 5.2. The contribution of the integral generally lifts the SFRD at a given redshift by a linear factor of ~ 1.4 if we assume an SSFR-limit (red filled circles) and ~ 1.7 if a single low-mass end slope $\tilde{\alpha}$ is used (red open circles), suggesting the stacking analysis missed ~ 30 % or ~ 40 % respectively of the integrated SFRD. The differences between both extrapolations are largest at $z > 1$ below which either method yields practically the same results. As pointed out in Section 5.2 our data cannot clearly rule out any of the two alternative low-mass Schechter functions proposed. Consequently, our extrapolations overlap within their individual uncertainty ranges at all redshifts. In the following we favor, however, the extrapolation that includes the SSFR-limit as it assures a more conservative approach compared to the generally larger values the alternative extrapolation yields.

[7] As Marchesini et al. (2009) estimate the mass function based on a Kroupa IMF, masses are directly comparable to ours.

Table 5.2. The total SFR density as a function of redshift (cosmic star formation history)

z	$\mathrm{SFRD}_{\mathrm{obs}}(z)$ $[M_\odot\,\mathrm{yr}^{-1}\,\mathrm{Mpc}^{-3}]$		$\mathrm{SFRD}_{\mathrm{int}}(z)$ $[M_\odot\,\mathrm{yr}^{-1}\,\mathrm{Mpc}^{-3}]$	
0.30	0.011	$(0.011)^{+0.001}_{-0.001}$	$0.018^{+0.002}_{-0.006}$	$\left(0.019^{+0.004}_{-0.007}\right)$
0.50	0.015	$(0.015)^{+0.001}_{-0.001}$	$0.023^{+0.002}_{-0.006}$	$\left(0.025^{+0.004}_{-0.008}\right)$
0.70	0.025	$(0.025)^{+0.002}_{-0.002}$	$0.039^{+0.003}_{-0.009}$	$\left(0.043^{+0.007}_{-0.015}\right)$
0.90	0.043	$(0.043)^{+0.003}_{-0.003}$	$0.055^{+0.002}_{-0.008}$	$\left(0.058^{+0.005}_{-0.010}\right)$
1.10	0.048	$(0.047)^{+0.004}_{-0.003}$	$0.061^{+0.003}_{-0.005}$	$\left(0.073^{+0.010}_{-0.016}\right)$
1.40	0.048	$(0.048)^{+0.004}_{-0.004}$	$0.063^{+0.004}_{-0.007}$	$\left(0.070^{+0.008}_{-0.018}\right)$
1.80	0.070	$(0.069)^{+0.007}_{-0.008}$	$0.095^{+0.014}_{-0.014}$	$\left(0.119^{+0.040}_{-0.048}\right)$
2.25	0.066	$(0.062)^{+0.007}_{-0.006}$	$0.098^{+0.011}_{-0.009}$	$\left(0.115^{+0.043}_{-0.046}\right)$
2.75	0.077	$(0.077)^{+0.009}_{-0.011}$	$0.121^{+0.017}_{-0.017}$	$\left(0.175^{+0.236}_{-0.099}\right)$

Note. — The central column states the number density corrected (raw) sum over all mass bins at a given redshift of the product of the average SFR and the total number of galaxies contained in the corresponding bin down to the redshift-dependent limiting masses of this study. It is hence the sum of the data points within each panel of Figure 5.1 and – at least out to $z = 1.5$ a robust direct measurement of the total dust unbiased SFRD for galaxies more massive than $\sim 3.2 \times 10^9\ M_\odot$. The values in the right column additionally take into account the not directly measured low-mass end where we integrate over the SFRD-function at a given redshift as introduced in Section 5.2 while we assume a potential upper SSFR limit (see Section 4.4.1 for details). The values in brackets result from deriving the low-mass end contribution by integrating the single Schechter-models of the SFRD-functions and hence assuming no upper limit in SSFR. Like all other results presented in this work all values are based on a Chabrier (2003) IMF.

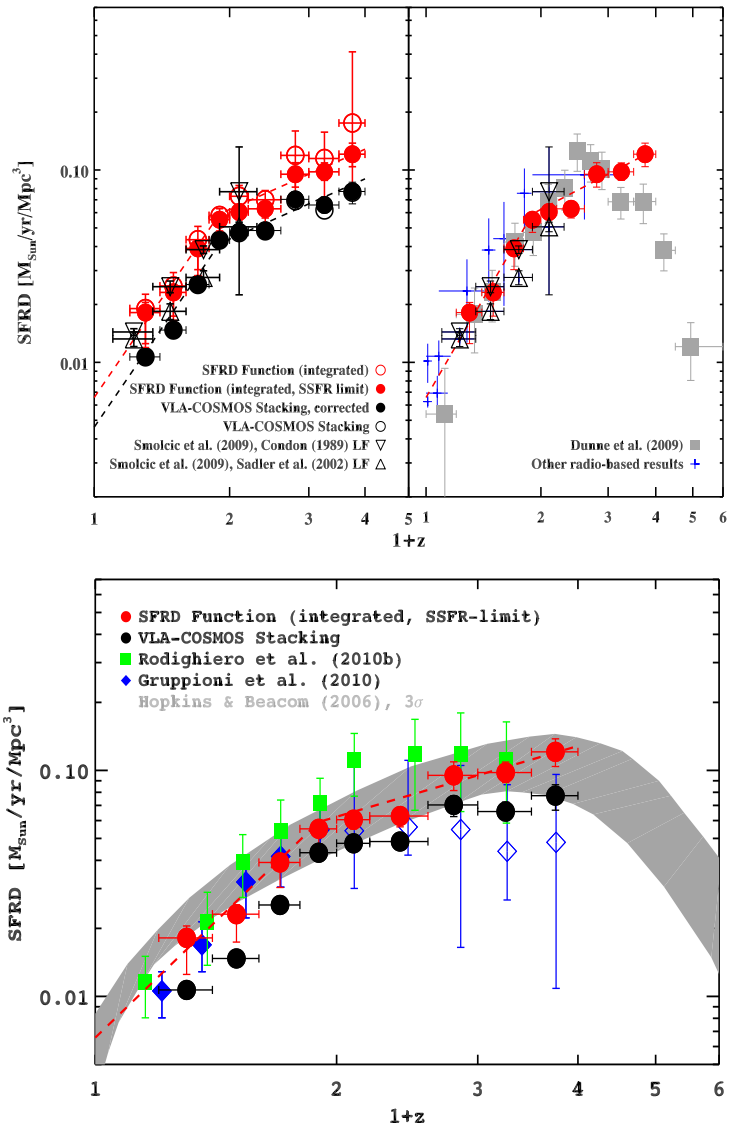

Figure 5.4. – **Upper left:** The cosmic star formation history (CSFH) out to $z = 3$ from the VLA-COSMOS survey. Black circles (raw and number density-corrected) represent the sum of the data points in all redshift-bin panels of Figure 5.1 and hence a direct – stacking-based – measurement of the SFRD down to the limiting mass at each epoch. Evidently, the number density corrections are always small and no corrections are necessary at $z < 1.5$ where our results are most robust. Red filled circles correspond to the 'total' SFRD at each epoch, obtained by integrating the Schechter-function fit (Figure 5.1) down to $M_* = 10^5\ M_\odot$ and assuming an upper limit to the average SSFR (case B in Section 5.2; see also Section 4.4.1 for details). Red open circles are obtained by the same method assuming no upper SSFR-limit (case A in Section 5.2). The redshift evolution can be described by a broken power-law (dashed lines) that results from the joint (non-)evolution of the SF stellar mass density and the evolution of the (S)SFR-sequence. Down- and upward-facing triangles depict the results by Smolčić et al. (2009a) based on VLA-COSMOS radio detections extrapolated by two distinct radio luminosity functions (LF). **Upper right:** Compilation of radio-based literature estimates of the integrated CSFH between $0 < z < 4$, compared to our results. The radio-stacking based results by Dunne et al. (2009) are depicted in grey and suggest a clear peak of the CSFH at $z \sim 1.5$ (see Section 5.3 for a full list of references and discussion). **Bottom:** Mid- to far-IR measurements of SFRDs between $0 < z < 2.5$ along with our data and the 3σ envelope from the Hopkins and Beacom (2006) compilation. The Herschel/PACS-based results (Gruppioni et al. 2010) are lower limits at $z \gtrsim 1.2$ and should be compared to our non integrated measurements (filled black circles). Note the remarkable agreement of the IR- and radio-based data at all z.

It is evident that the number density corrections at our low-mass end discussed in Section 5.2 have almost no impact on our direct measurements (depicted as black open circles in the upper left panel of Figure 5.4) of the SFRDs. Even more, at $z < 1.5$ practically no corrections were necessary which highlights again that our inferences are most robust at these redshifts. It is therefore justified to regard the corrected values (depicted as black filled circles in the upper left and lower panel of Figure 5.4) as a direct and dust unaffected average measurement of the SFRD for SF galaxies to a lower mass limit of $M_* \sim 3.2 \times 10^9\ M_\odot$. The evolutionary power-law, scaled to our data points and with the indices in the two redshift regimes, matches well the observed cosmic star formation history (CSFH) with respect to our measured data points presenting lower limits as well as to the integrated ones. This may seem surprising as our evolutionary model does not take into account differential effects with mass as introduced by assuming an SSFR limit (case B in Section 5.2). However, since the bulk of the mass-integrated SFRD is contained in our direct stacking based measurements even at high z – which show a mass-independent evolution – the model represents a good approximation.

In Figure 5.4 we also compare[8] our data to the CSFH derived from confirmed SF radio sources within the COSMOS field in conjunction with extrapolations based on two distinct evolved local radio luminosity functions (see Smolčić et al. 2009a, for details). This comparison shows how good a deep radio survey constrains the CSFH and leads us to slightly favor the extrapolations based on the Condon (1989) radio luminosity function in the Smolčić et al. (2009a) study as already our mass-limited, direct, stacking-based measurements of the SFRD on their own already reach the values which they inferred using the Sadler et al. (2002) radio luminosity function at any $z < 1$.

The upper right panel of Figure 5.4 shows our data along with other radio-based measurements (Haarsma et al. 2000; Machalski and Godlowski 2000; Condon et al. 2002; Sadler et al. 2002; Serjeant et al. 2002; Smolčić et al. 2009a) and the radio-stacking derived CSFH by Dunne et al. (2009). Since the referenced measurements based on radio detections have been extensively discussed in Smolčić et al. (2009a), we will focus our comparison on the study of Dunne et al. (2009) as it is methodologically closest to our study. Here the extrapolations towards faint sources are based on the evolving K-band luminosity function with the fixed faint-end slope presented by Cirasuolo et al. (2010). As we previously pointed out, the evolutionary trends Dunne et al. (2009) find are in good agreement with our results. Also on absolute scales the results of both studies are basically indistinguishable with significant[9] deviations only at the highest redshifts probed in our study. However, at $z > 1.5$ the trends observed tend to suggest different conclusions as Dunne et al. (2009) find a clear peak of the CSFH around $z = 1.5 - 2$ followed by a strong decline of the SFRD with redshift. Indeed, at the highest redshifts probed in our study the SFRD extrapolated by Dunne et al. (2009) does not exceed our direct measurement (without extrapolations, see the top left panel in Figure 5.4). Hence, one would have to assume that galaxies below $\sim 10^{10}\ M_\odot$ do

[8] All literature data mentioned within the remainder of this Section are based on a Salpeter IMF and have been converted to the Chabrier scale.

[9] The error bars to the data points shown here – for which we assume an upper SSFR limit – are smaller at high redshifts compared to those of the corresponding ones if no limit is assumed. We might have underestimated the uncertainty introduced by the extrapolations in the former case because of the assumed error to the dynamical timescale (370 ± 50 Myr) which is the purported limit to the inverse SSFR. However, it should be noted that Dunne et al. (2009) do not include any uncertainty caused by their extrapolation into their error budget.

not contribute at all to the mass-integrated SFRD at $z > 2$ in order to support this peak based on our data.

Especially when compared to dust extinction corrected UV-based studies the existence and location of the CSFH peak as measured by a dust-unbiased star formation tracer is important. Recent UV-based measurements (Reddy and Steidel 2009; Bouwens et al. 2011b) suggest a peak of the CSFH at around $z = 2 - 2.5$ and assume that the dust obscuration for the bulk of SF galaxies does not dramatically change out to $z \sim 4$ (as shown by e.g. Bouwens et al. 2009; Finkelstein et al. 2009; McLure et al. 2010; Wilkins et al. 2010). Our rising SFRD at $z > 2$ suggest that SF galaxies at these redshifts have a somewhat higher dust content or obey a different reddening law than the corresponding sources at lower redshifts. Whether dust-obscured sources at $z > 2$ are lost in optical/UV based measurements of the CSFH cannot be definitely answered given the mentioned large error bars our data show. Future Herschel studies of the total IR luminosity evolution at $z > 2$ should reveal potentially larger dust reservoirs in these systems. The even more rapid decline of the radio-based SFRD as derived by Dunne et al. (2009) appears to support the picture drawn by e.g. Bouwens et al. (2011b) that obscured star formation does not significantly contribute to the global SFRD at $z \gg 4$. Such conclusions should, however, be treated with caution as it is highly unclear at such early cosmic times what extrapolation to the directly measured radio derived SFRDs are needed given the high stellar mass limits (see also Gallerani et al. 2010).

Our integrated CSFH is also supported by recent studies carried out at mid-IR (Rodighiero et al. 2010b) and far-IR (Gruppioni et al. 2010) wavelengths. The latter study is based on $\sim 210-240$ Herschel/PACS detections at 100 and 160 μm in 150 arcmin^2 within the GOODS-N field and provides us with a deep view of the dust-unbiased CSFH. The lower panel in Figure 5.4 shows that the agreement of the Herschel-based results presented by Gruppioni et al. (2010) with our radio-stacking derived mass-integrated CSFH is striking. Out to $z \sim 1$ we also find a broad agreement with the measurements of Rodighiero et al. (2010b). While Gruppioni et al. (2010) show only lower limits at $z \gtrsim 1$ below this redshift both studies measure an evolution of $(1+z)^n$ with $n = 3.8 \pm 0.3$ (0.4). A recent 24 μm based study by Rujopakarn et al. (2010) confirms this result measuring $n = 3.4 \pm 0.2$. All these values are in remarkable agreement with our average measured evolution of the SSFR-sequence of $\langle n_{\rm SFG} \rangle = 3.5 \pm 0.02$ (see Section 4.4 and Table 4.5)[10] and hence a strong support for both our measurement as well as our parameterization given in Eq. (5.5), especially out to $z = 1$. It is, however, worth mentioning that our work, compared to the other studies mentioned, draws on a far larger sample.

Finally we want to stress the fact that any shallower high redshift trend in the evolution of the SSFR-sequence also at the high-mass end would indeed lead to a decline in the evolution of the SFRD as Eq. (5.5) suggests. This scenario cannot be ruled out given our data as the SSFR at the low-mass end of our sample tends to flatten and the high-mass end might follow at slightly higher redshifts based on the dynamical time arguments presented in Section 4.4.2 that result in a global upper limit to the average SSFR. Hence, again, a deeper mid-IR selected sample of SF galaxies is needed to accurately probe the regime above $z = 1.5$ where the CSFH is supposed to peak.

[10] Note that the scatter of the individual measurements at different redshifts of $\beta_{\rm SFG}$ stated in Table 4.5 is actually a more realistic uncertainty range than the formal error to their weighted mean.

5.4. Summary and conclusion

Building on the results of the previous chapter we explored the cosmic star formation history (CSFH) in a mass-dependent fashion. By taking advantage of the simple functional form of both the (S)SFR-sequence and the mass function of SF galaxies in the redshift range we study we have shown that

- the mass distribution function of the comoving SFR density (SFRD) at any redshift below $z = 1$ is well parameterized by a single Schechter function with a possible low-mass modification at higher z.
- the typical mass of a SF galaxy contributing most to the total (stellar mass integrated) SFRD is $10^{10.6\pm0.4}\ M_{\odot}$, with no evidence for evolution out to $z = 3$.

Out to $z \approx 1$ the evolution of the integrated SFRD, in turn, is entirely controlled by the mass-uniform evolution of the SSFR-sequence as the number of SF galaxies in a given comoving volume does not change anymore. A strong and global decline in the mass density of molecular gas, i.e. the reservoir out of which stars are formed, appears therefore to be the only driver of the observed decrease of the integrated SFRD with cosmic time. The rate at which the SFRD declines is in excellent agreement with the most recent other studies that use mid- to far-IR emission as an alternative dust-unbiased tracer for star formation. Towards earlier epochs this steep trend becomes shallower as the comoving stellar mass density of SF systems decreases. In other words, there are simply less (SF) galaxies at $z > 1$ while their individual SFRs further increase with redshift. This statement is certainly valid for galaxies more massive than $10^{10}\ M_{\odot}$ which dominate the CSFH at all epochs out to $z = 3$. Our results do not suggest any change of this trend towards the highest redshifts probed but it should be emphasized again that our data cannot constrain the situation as strongly as at $z < 1.5$. Hence, we do not rule out that the CSFH peaks in this redshift range. Indeed, the constancy of the SSFR at $z \gg 2$ suggested by other studies and motivated by the dynamical time threshold we discuss would give rise to a decline of the global SFRD at such high redshifts.

6. Extreme star formation within 1.5 Gyr after the Big Bang: a case study

Only recently, i.e. around the start of this PhD thesis, spectroscopic observations of millimeter (mm) sources revealed that objects with extreme star formation activity exist already in the very early universe (at redshifts $z > 4$). The star formation rates (SFRs) measured in these few sources known to-date reach the equivalent of at least several hundreds of solar masses per year. This gives rise to refer to them as the most vigorously star forming environments in the universe. Previously, similar SFRs have only been measured in the rare high redshift hosts of bright quasi stellar objects (QSOs) while the newly discovered massive starbursts are typically selected as (optically faint) star forming sources.

Massive starbursts at such early times bear the potential to substantially boost our understanding of cosmological structure formation and the build-up of the massive end of the $z \gtrsim 2$ galaxy population. It is likely that the high star formation rates are triggered by (major) galaxy mergers within early mass overdensities (so-called proto-clusters) predicted by cosmological simulations. Extreme starbursts can therefore be regarded as the lighthouses of proto-clusters which – in a hierarchical universe – are the seeds of the most massive galaxy clusters observed to-date. Recent observational results confirm this to be a promising road and highlight the special importance of high redshift massive starbursts for constraining models of cosmic structure formation. Only eight extreme starbursts at $z > 4$ have been detected in carbon monoxide (^{12}CO) emission, two of which are gravitationally lensed. These observations reveal large reservoirs of molecular gas which – combined with the high star formation rates – suffice to build up very massive galaxies in short time. There is growing observational evidence that massive quiescent galaxies (i.e. objects with little ongoing star formation) exist already at $z > 2$ and the $z > 4$ extreme starbursts are hence good candidates to be their progenitors. Moreover, the elliptical morphologies of the quiescent sources have likely been shaped by major mergers.

The connection to the earliest quiescent galaxies is not the only motivation to assemble a representative sample of these early massive starbursts. It is also important to shed light on the importance of extreme star formation for the global cosmic star formation activity at the highest redshifts. The massive starbursts unveiled to-date are known to be dust-rich and might hence represent an important fraction of dust-obscured star formation in the early universe. While ultra-deep surveys suggest that dust-enshrouded star formation drastically ceases its importance at redshifts beyond $z \sim 4$, they might underscore the massive end due to the small area covered and a potentially incomplete selection strategy for high redshift star forming sources.

It is an ongoing effort (see Section 7.4.2) of this PhD project to construct a comprehensive sample of $z > 4$ extreme starbursts based on the identification of radio continuum counterparts to distant Lyman-break galaxies (LBGs), i.e. star forming systems which are selected via the broad-band dropout technique in the B or V band. With its deep (in par-

ticular at radio wavelengths) and extensive observational coverage and large contiguous area, the COSMOS field is the ideal celestial area for this effort. The discovery of three spectroscopically confirmed $z > 4$ massive starbursts during this thesis has proven the success of our radio-based approach. Based on time-consuming follow-up observations at mm-wavelengths in continuum and spectroscopy one of these new sources could already be studied in detail as presented in this Chapter. This analysis reveals an interesting composite nature of the $z \sim 4.62$ massive and gas-rich starbursts Vd-17871, making it to-date the most distant host of an obscured active galactic nucleus. This exceptional source yields important insights into the diversity of the high redshift starburst population representing yet another motivation for a detailed and representative ensemble study. This Chapter is about to be submitted to The Astrophysical Journal for publication as

A. Karim, E. Schinnerer, P. L. Capak, V. Smolčić, M. T. Sargent, M. Aravena, E. Le Floc'h, H. Aussel, A. Martínez-Sansigre, F. Bertoldi, C. L. Carilli, E. Dwek, O. Ilbert, E. van Kampen, A. M. Koekemoer, H. J. McCracken, M. Michałowski, H.-W. Rix, M. Salvato, I. Smail & J. Staguhn, *A dark knight rises: a hidden quasar in the $z \sim 4.62$ molecular gas-rich starburst system Vd-17871*

6.1. Introduction

One of the key questions in modern observational cosmology regards the importance of galaxies showing highly elevated star formation activity (starbursts) for the total comoving volume-averaged star formation rate (SFR) density (SFRD) and whether it changes over cosmic time. While at low and intermediate redshifts ($z < 2$) the picture emerged that (merger-driven) starburst galaxies contribute very little to the global star formation (e.g. Robaina et al. 2009; Elbaz et al. 2011; Rodighiero et al. 2011) the situation might be drastically different at very high redshifts $z > 4$. At these earlier cosmic times – when the universe was denser – it is plausible that stars mainly formed in galaxies residing in more clustered environments where major mergers trigger a substantial amount of the starburst activity.

Indeed, massive starbursts have been found in the rare galaxy overdensities known at $z > 4$ (Daddi et al. 2009b,a; Capak et al. 2011) with growing evidence that star forming sources at these redshifts tend to cluster around individual extreme starbursts (Capak et al. in prep.).[1] This is suggestive that extreme star formation may contribute significantly to the cosmic SFRD in the very early universe.

Given their extreme SFRs of several hundreds to more than a thousand $M_\odot$/yr massive starbursts at $z > 4$ are ultra luminous infrared (IR) galaxies (ULIRGs) with IR luminosities $L_{\rm IR} \gg 10^{12}\ L_\odot$ and expected cold dust temperatures of $T_D \sim 35$ K similar to starbursts at $z \sim 2$ (e.g. Kovács et al. 2006). While the expected monochromatic flux densities at millimeter (mm) wavelengths are detectable with modern bolometer cameras the large beam-sizes of $\gtrsim 10''$ of single-dish telescopes often lead to major problems in the association with the correct counterparts at much shorter wavelengths. The unambiguous counterpart identification and accurate spectroscopic redshifts are, however, a prerequisite for observations

[1] Observational evidence for galaxy overdensities at such high redshifts (so-called proto-clusters) has been reported earlier (e.g. Overzier et al. 2006, 2008). Those proto-clusters have been searched for in the environments of massive high redshift radio galaxies selected as ultra steep spectrum (USS) radio sources (see De Breuck et al. 2002, for details on the massive nature of USS radio sources and their selection).

of rotational transitions of the ^{12}CO molecule within the relatively narrow bandwidths mm-telescopes provide.[2] Measuring the ^{12}CO emission, in turn, is critical for key insights into the state and distribution of the potentially large reservoirs of molecular gas fueling the star formation activity in these objects. Blind searches for ^{12}CO-line emission – without pre-determination of spectroscopic redshifts – have been extremely time consuming and feasible to-date for only two $z \gtrsim 4$ sources with highly boosted flux levels due to gravitational lensing (Lestrade et al. 2010; Cox et al. 2011).

As a result, single-dish blank-sky mm-surveys alone might not be the most promising road to assemble a comprehensive sample of massive starbursts in the very early universe. Pointed interferometric continuum observations of the brightest objects (e.g. Younger et al. 2007) help to increase the success rate (Capak et al. 2011; Smolčić et al. 2011) but they are restricted to individual sources pre-selected solely by their emission at mm-wavelengths. Consequently, to-date ^{12}CO emission has only been detected in six unlensed $z > 4$ sources residing in a number of prominent deep-fields with highly different ancillary data (Schinnerer et al. 2008; Daddi et al. 2009b,a; Coppin et al. 2010; Riechers et al. 2010; Carilli et al. 2010). Due to those often serendipitous detections in different environments important questions remain open. Especially their relation to the better-studied population of $z \sim 2$ starbursts (e.g. Chapman et al. 2005; Greve et al. 2005), typically found among the so-called sub-millimeter galaxies (SMGs), their intrinsic diversity and nature are unclear. A representative census of extreme star formation within the first 1.5 Gyr is, however, critical to provide tight constraints for cosmological models (e.g. Baugh et al. 2005; Coppin et al. 2009).

Optical data in combination with radio data provide a promising road to reveal extreme starbursts at $z > 4$ in their full diversity based on mm-follow-up observations (Capak et al. 2008; Schinnerer et al. 2008) and to be confirmed here.[3] Modern cosmological deep field surveys – particularly the 2 deg^2 Cosmic Evolution Survey (COSMOS; see Scoville et al. 2007d, for an overview) – reach not only an adequate celestial area but also depth of their panchromatic data to provide a comprehensive view on the $z > 4$ starburst population, superior to the smaller areas and single waveband selection window current mm-surveys provide.

At redshifts $z > 4$ massive star forming environments and molecular gas reservoirs have been found also around optically luminous – typically broad line-selected – quasars (e.g. Omont et al. 1996; Carilli et al. 2002; Walter et al. 2003; Riechers et al. 2006, 2008). At all $z > 2$ the star formation properties of such quasars have not been found to differ significantly from those derived for massive starbursts (Riechers 2011; Daddi et al. 2010b). Yet, tentative evidence for different gas excitation and spatial distribution properties might point to an evolutionary merger sequence from an initial starburst to a far-IR bright quasar (Riechers et al. 2010). Such an evolutionary link has been suggested also for $z \sim 2$ sources by Coppin et al. (2008) similar to the scenario proposed for a link between local ULIRGs

[2] Note, however, that the Atacama Large Millimeter Array (ALMA) in full operation will drastically improve the current situation both with respect to counterpart identification as well as to bandwidth restrictions in blind searches for ^{12}CO line emission.

[3] Note that also the $z = 4.76$ starburst J033229.4-275619 (Coppin et al. 2009) found in the LABOCA Survey of the Extended Chadra Deep Field-South (LESS; Weiß et al. 2009b) nominally is an optical broad-band dropout galaxy with a weak radio continuum counterpart. A deep mm-survey accompanying a panchromatic deep field therefore provides valuable ancillary data while the actual selection function is based on much different wavelength data.

and quasars by Sanders et al. (1988). Regardless of the validity of such an evolutionary sequence, it is clear that intrinsically different objects comprise the population of extreme starbursts at high redshift and it is desirable to explore the full diversity of this population.

A population largely ignored so far in this picture are (radio-quiet to radio-intermediate) obscured quasars[4] which might contain similarly large molecular gas reservoirs and reach comparable far-IR luminosities as the massive star forming sources at high-z (Martínez-Sansigre et al. 2009). Obscured active galactic nuclei (AGN) are supposed to contribute a substantial fraction to the unresolved (hard) X-ray background at energies above 1 keV (see Comastri 2004, for a review). Globally, they might be more abundant than unobscured quasars (e.g. Martínez-Sansigre et al. 2005, 2008) while at higher X-ray luminosities at least a 1:1 ratio is expected (e.g. Ueda et al. 2003; Treister and Urry 2005). While obscured AGN are found in deep hard X-ray surveys (e.g. Alexander et al. 2003) they merely trace the lower luminosity end (i.e. Seyfert -2 objects; Martínez-Sansigre et al. 2006b). Mid-IR selection has proven to be a vital strategy for finding the intrinsically more luminous obscured sources (e.g. Martínez-Sansigre et al. 2005). Provided deep enough optical data is available obscured quasars could also be found in apparently star forming galaxies selected at rest-frame optical wavelengths where the host galaxy dominates the emission over the heavily obscured AGN. Detailed radio continuum studies of obscured AGN (Martínez-Sansigre et al. 2006a; Klöckner et al. 2009) suggest that they resemble radio quiet rather than radio-loud AGN while typically exhibiting higher radio luminosities compared to the radio quiet population. Therefore these sources are expected to be detectable even beyond $z = 4$ in deep radio continuum surveys.

In this Chapter we report on the detection of molecular gas emission as traced by the redshifted ^{12}CO($J = 5 \rightarrow 4$) rotational transition (CO(5-4) in the following) in the $z = 4.622$ starburst system Vd-17871 using the Plateau de Bure Interferometer (PdBI). Residing in the COSMOS field for which high-quality and deep multi-wavelength (hard X-rays to radio continuum) photometric data exist, this source has been selected as a V-band dropout – and hence Lyman Break Galaxy (LBG) – with a weak 1.4 GHz counterpart. As we will show, in addition to a large reservoir of molecular gas this source harbors an obscured radio-intermediate AGN. This confirms that the optical selection of (normal) star forming galaxies is capable of revealing extreme starbursts but also obscured composite sources at very high redshifts. As this AGN is hidden it manifests its presence mainly through substantial heating of the dust continuum at rest-frame mid-IR wavelengths.

Throughout this Chapter all observed magnitudes are given in the AB system. We assume a standard cosmology with $H_0 = 70$ (km/s)/Mpc, $\Omega_M = 0.3$ and $\Omega_\Lambda = 0.7$ consistent with the latest WMAP results (Komatsu et al. 2009) as well as a radio spectral index of $\alpha_{\rm rc} = -0.8$ (e.g. Condon 1992). A Chabrier (2003) initial mass function (IMF) is used for all stellar mass and SFR calculations in this Chapter.

[4] For an introduction and review on different types of active galactic nuclei and their unification see Antonucci (1993); Urry and Padovani (1995).

6.2. Target selection and observations

From a sample of 15,000 V-band dropout galaxies (see Steidel et al. 1995, 1996, for an introduction into the broad-band dropout selection method and initial results) in the COSMOS field we selected Vd-17871 as one of six objects with weak counterparts in the deep VLA 1.4 GHz imaging (Schinnerer et al. 2010). The similarly selected source J1000+0234 had been previously revealed to be a $z \sim 4.5$ extreme starburst with a large molecular gas content and evidence for an on-going major merger (Capak et al. 2008; Schinnerer et al. 2008). In the following we describe key features of Vd-17871 and our follow-up observations.

6.2.1. Panchromatic COSMOS data and selection criteria

Ground-based imaging of the COSMOS field has been obtained in 23 optical to near-IR bands at the Subaru, UKIRT and CFHT telescopes (Capak et al. 2007; Ilbert et al. 2009; McCracken et al. 2010). The field has been surveyed by the Very Large Array (Schinnerer et al. 2007, 2010), the Hubble and Spitzer Space Telescopes (Scoville et al. 2007b; Sanders et al. 2007) and the XMM-Newton as well as Chandra X-ray telescopes (Hasinger et al. 2007; Elvis et al. 2009). At far-IR and sub-mm wavelengths the COSMOS field has been observed by Herschel/PACS (Poglitsch et al. 2010) as part of the PACS Evolutionary Probe (PEP) survey (Lutz et al. 2011) and by Herschel/SPIRE (Griffith and Stern 2010) as part of the Herschel Multi-tiered Extra-galactic Survey (HerMES; Oliver et al. in prep.).

Vd-17871 is part of the V-band dropout sample – star forming sources at $z > 4$ – culled from the latest release of the COSMOS photometric catalog. This sample has been selected based on the broad-band color criteria described in Iwata et al. (2007) among objects with a signal-to-noise ratio (SNR) of more than 2σ in the Subaru z^+ band: $V - i^+ > 1.55$, $i^+ - z^+ > -1$, $V - i^+ > 7(i^+ - z^+) + 0.15$.

LBGs at $z \sim 3$ typically have radio-derived star formation rates (SFRs) of ~ 30 $M_\odot$/yr (Carilli et al. 2008) while for massive (Spitzer/IRAC detected) LBGs in the GOODS-North field Magdis et al. (2010) find ~ 100 $M_\odot$/yr based on their radio and IR-emission. For an individual source at a typical V-band dropout redshift of $z = 4.5$ to be detected at a $> 3.5\sigma$ level in the deep imaging of the VLA-COSMOS field (12 μJy average rms; Schinnerer et al. 2010) an SFR of > 2000 $M_\odot$/yr is required if the local calibration of the far-infrared/radio relation by Bell (2003b) is used. As this clearly would be an extreme SFR enhancement compared to the average LBG, we searched for weak radio continuum emission in the near vicinity of all V-band dropouts in order to find extreme starbursts.

Vd-17871 is indeed associated with a 7.2σ source in the deep VLA-COSMOS image at 2.5" resolution. Given the high significance of the radio counterpart the above calculation suggests a tremendous SFR of ~ 4000 $M_\odot$/yr in this object. Hence, even if only 10 % of the total radio emission were powered by star formation, Vd-17871 would still show a significantly elevated stellar mass growth compared to the global population of massive LBGs.

6.2.2. Keck/DEIMOS observations

Spectroscopic observations of Vd-17871 with the Deep Imaging Multi-Object Spectrograph (DEIMOS; Faber et al. 2003) on Keck-II have been carried out in February 2009 under clear conditions ($\sim 1''$ seeing). The total observing time of 4 hr was split into blocks of 30 min

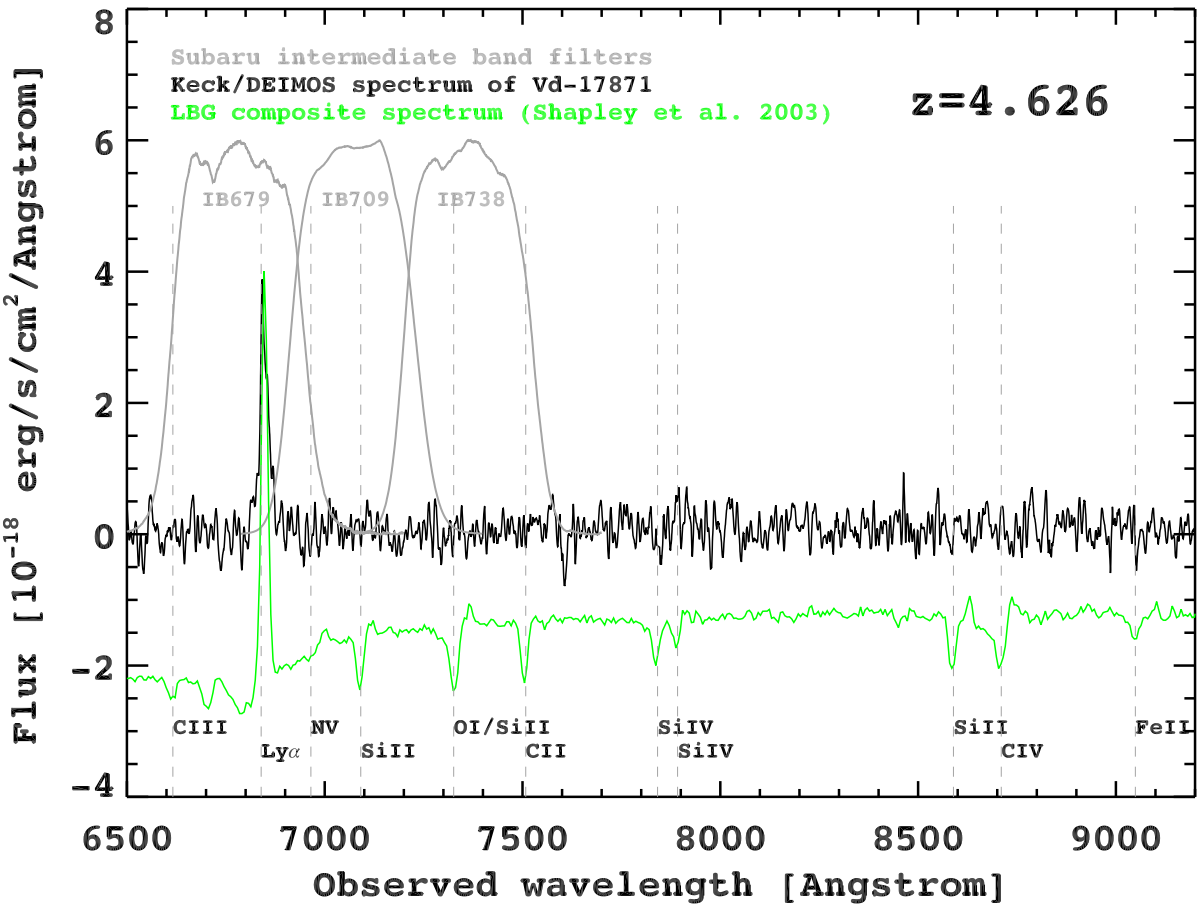

Figure 6.1. – Smoothed Keck/DEIMOS spectrum for Vd-17871 (black) showing a significant single emission line detection but no underlying continuum. The line shape suggests it to be Lyman-α at a redshift of $z = 4.626$. Tentatively, the line is double-peaked placing a lower limit to the velocity dispersion of $\gtrsim 1000$ km/s and at most ~ 2170 km/s (see Section 6.3.3 for details). Both values are compatible with line widths typical for the narrow-line region in the vicinity of an AGN. We also show the average empirical Lyman Break Galaxy template (green) by Shapley et al. (2003) indicating prominent absorption lines typically seen in high redshift star forming systems by vertical dashed lines. The transmission curves for three Subaru intermediate band filters are indicated in grey showing that filter IB679 covers the Lyman-α line explaining the flux elevation seen in the optical to near-IR spectral energy distribution (see Figure 6.3).

and the 830l/mm grating tilted to 7900 Å as well as the OG550 blocker were used while ghosting was removed by dithering the targets by $\pm 3''$ along the slit.

For data reduction we used the modified DEEP2 DEIMOS pipeline (see Capak et al. 2008) and we determined the total instrumental throughput using the standard stars HZ-44 and GD-71. Using bright stars in the mask we estimated the amount of wavelength-dependent slit losses from dispersion as well as extinction in the atmosphere and corrected for the A, B, and water absorption bands.

The 1D-spectrum is shown in Figure 6.1. One emission line is clearly detected. Its strength and shape strongly suggest it to be Lyman-α emission redshifted to $z = 4.626 \pm 0.001$. We detect no underlying continuum emission, not surprising given the faintness of the source at observed optical magnitudes ($i^+ \sim 25.5$). Due to the same reason absorp-

tion lines typically seen in star forming sources at high z (e.g. Shapley et al. 2003) remain invisible. No potential spectral line emission from an active galactic nucleus (AGN) are seen.

6.2.3. Millimeter continuum and CO-line observations

We observed Vd-17871 with the 117 element array bolometer camera MAMBO-II (Kreysa et al. 1998) operating at 1.2 mm (250 GHz) during pooled observations in March 2009 at the IRAM 30 m telescope. Pointing accuray was checked every 20-40 minutes using the nearby sources J0948+004 and J1058+016. Regularly, gain calibration was performed and focus was checked using mm-bright sources such as Saturn. Fluxes and foci have been always found to be accurate and stable. MAMBO-II was used in on-off mode with one scan consisting of two off-source positions in between two on-source position and an integration time of one minute per position resulting in a total of four minutes per scan. The azimuthal wobbler throw – i.e. the on-sky angle between the off-source positions covered by the periodic movement of the secondary mirror – was chosen to be between 32 and 45 degrees. Individual scans were obtained at different times of the day resulting in different physical off-source positions, thereby minimizing the risk of the sky position being accidentally coincident with another astronomical source. The source elevation during the observations was never below 45 degrees. The total integration time (using the most sensitive pixel number 20) was 2.6 hours and resulted in a significant detection of $S_{1.2\ mm} = 2.5 \pm 0.5$ mJy/beam under a low sky-noise level (typically $\lesssim 50$ mJy/beam). The atmospheric opacity was always below $\tau_{230\ GHz} \leq 0.3$. We used the MOPSIC data reduction package (R. Zylka, IRAM) to obtain the flux measurement given above and in Table 6.1.

At the IRAM Plateau de Bure Interferometer (PdBI) Vd-17871 was observed between October 2010 and March 2011 in B, C and D configuration at 3 mm with the wide-band correlator WideX (3.6 GHz of total bandwidth in dual polarization mode) tuned to 102.4476 GHz, i.e. the redshifted frequency of the ^{12}CO(5-4) transition. Usually all six antennas were available during the observations. The nearby quasar J0948+003 was used for atmospheric amplitude and phase calibration of all observing tracks. Given the slight polarization of this source long tracks were manually split in two parts in order to obtain similar fits to the phase variations in both polarizations, hence improving the phase calibration compared to the results of the automatic pipeline reduction. For tracks with sufficient SNR, bandpass calibration was performed using the same source, J0948+003. This way the effect of 'parasites', i.e. signal peaks in individual spectral channels artificially produced by the electronics of the PdBI, could be reduced to a minimum. J0948+003 shows some spectral slope, i.e. an increase in flux density with frequency in the lowest frequency quarter of the wide-band. This slope does not affect the channels expected to cover the line emission but might partially lower the continuum flux level in the off-line channels at the high velocity end. A continuum level estimated from all off-line channels will, however, not significantly suffer from this flux reduction due to the large bandwidth available. For two out of five tracks used to obtain the final results the stronger quasars 3C84 or J1055+018 were used as bandpass calibrators in order to obtain a sufficient signal and, hence, accuracy in the correction. This leads to a single clearly identifiable 'parasite' not associated with any physical line emission. We consequently flagged the associated spectral channels for our analysis. We reduced the data with the routines CLIC and MAPPING contained in the latest

version[5] of the GILDAS software (Guilloteau and Lucas 2000). Using natural weighting, a velocity-integrated map of the CO(5-4) emission with a restoring beam of $3.87'' \times 2.36''$ was obtained, the resolution for the off-line continuum emission is $3.75'' \times 2.25''$. The net on-source integration time of 13 hours gave an rms of 0.42 mJy/beam in a single 50 km/s (i.e. 17 MHz) wide channel and 0.03 mJy/beam in the 3.3 GHz wide line-free continuum. Using the MAPPING task UV_AVERAGE we averaged over the channels covering the line emission (i.e. 850 km/s; see below) and, independently, over the same number of off-line channels. We subsequently subtracted the latter average from the former via the task UV_SUBTRACT in order to image the net line emission. We also used the task UV_AVERAGE for imaging the continuum emission using all off-line channels. Finally, we separately imaged the line and the continuum emission with a cell size of 0.4"/pixel and used the CLEAN task to obtain beam-deconvolved maps. For both images CLEANing was performed down to 1σ within a box around the source. Using a threshold of 2σ does not alter the results. The resulting maps are shown in Figure 6.7.

6.3. Source properties of Vd-17871

6.3.1. The molecular gas reservoir

We detect spatially unresolved CO(5-4) line emission toward Vd-17871 at a significance of 5.8σ. The MAPPING task UV_FIT was used to confirm that the emission is unresolved. A Gaussian fit to the line profile (Figure 6.2) yields a peak line strength of (1.3 ± 0.2) mJy/beam and a full width at half maximum (FWHM) of (397 ± 82) km s^{-1}. This results in a velocity-integrated line intensity of (0.56 ± 0.15) Jy km s^{-1}. The line is centered at (102.508 ± 0.009) GHz (i.e. $z_{\rm CO} = 4.622 \pm 0.001$) and hence blue-shifted by (279 ± 33) km/s with respect to the Ly-α emission, a typical offset commonly found in $z \gg 1$ starbursts (e.g. Greve et al. 2005). We marginally detect the 3 mm dust continuum emission in Vd-17871 at a 4.3σ level (0.13 mJy/beam) in the line-free channels.

Following Solomon and Vanden Bout (2005) we derive a line luminosity of $L'_{\rm CO(5-4)} = (1.8 \pm 0.4) \times 10^{10}$ K km s^{-1} pc^{-2} ($L_{\rm CO(5-4)} = (1.1 \pm 0.3) \times 10^8\ L_\odot$) from the velocity-integrated CO(5-4) line-flux. To convert this luminosity into a total molecular gas mass we assume – in absence of lower-J CO observations – that a single molecular gas phase is thermalized up to the $J = 5$ level. In this case $L'_{\rm CO(5-4)} = L'_{\rm CO(1-0)}$ and a typical conversion factor of $\alpha_{\rm CO} = 0.8$ found for local ULIRGs (Downes and Solomon 1998) and commonly used for high-z starbursts (Solomon and Vanden Bout 2005) leads to a total molecular (H_2+He) gas mass of $(1.4 \pm 0.4) \times 10^{10}\ M_\odot$.

6.3.2. Panchromatic morphology and ultraviolet to mid-IR photometry

The rest-frame ultraviolet (UV) morphology of Vd-17871 is fairly complex with two main emission knots being separated by 1.5" (i.e. ~ 10 kpc at $z = 4.662$) with a position angle of ~ 45 degrees (east of north; Figure 6.7). A priori it is not clear if both knots belong to the same astronomical system. As the Keck/DEIMOS observations only targeted the northern knot (source A in the following) with an east-west slit orientation no spectroscopic redshift

[5] We used the GILDAS release from April 2011, the latest public version available at the time of data calibration and reduction.

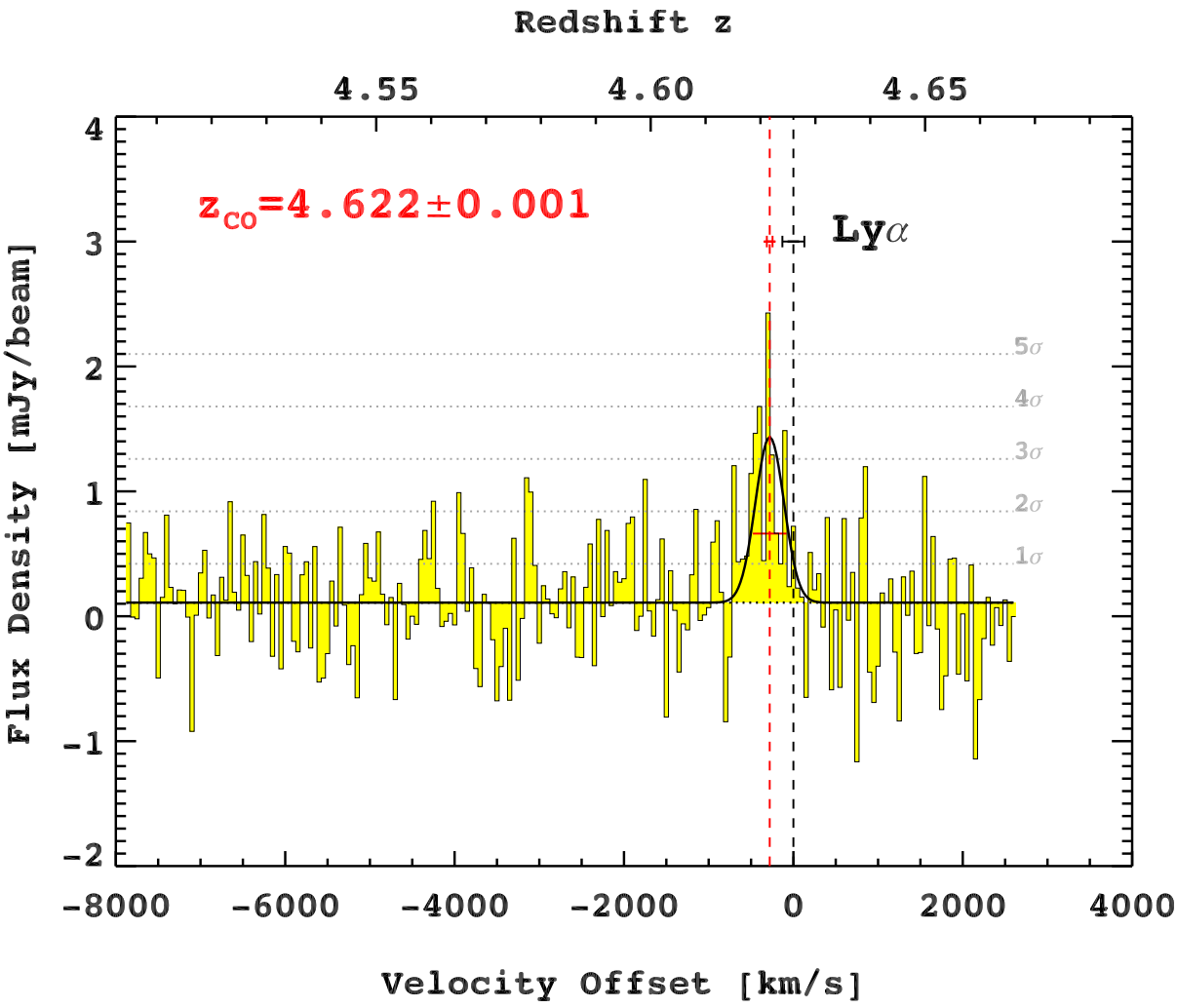

Figure 6.2. – Redshifted ^{12}CO(5-4) spectrum from IRAM/Plateau de Bure Interferometer observations towards Vd-17871 in the 3 mm atmospheric window. The full 3.6 GHz bandwidth provided by the WideX correlator translates into a 10,000 km s^{-1} velocity coverage. We significantly detect the ~ 400 km s^{-1} wide (FWHM) ^{12}CO(5-4) line blue-shifted by (280 ± 34) km s^{-1} with respect to the Lyman-α line as indicated by the vertical dashed lines resulting in a redshift of $z_{\rm CO} = 4.622$. The spectrum has been re-binned to a velocity resolution of 50 km s^{-1} and the line profile has been fit by a single Gaussian. The channel rms is indicated by gray horizontal lines in steps of 1σ. The underlying 102 GHz continuum is detected at a $\sim 4\,\sigma$ level in the combined off-line channels.

information has been retrieved for the southern one (source B). We therefore separately extracted the photometry at both positions, as verified and described in detail by Smolčić et al. (in prep.). As the sources are separated by 1.5”, which is smaller than the aperture used to extract the photometry a deblending strategy was required in the bands where both sources are detected. At optical wavelengths, where the sources are well separated we have simply subtracted the interfering source from the image, while in the IRAC (3.6 and 4.5 μm) bands we have modeled the interfering source as a point source before subtraction. In Figure 6.3 we show the spectral energy distributions (SEDs) of both sources which appear very similar. The observed optical photometry therefore indeed supports a

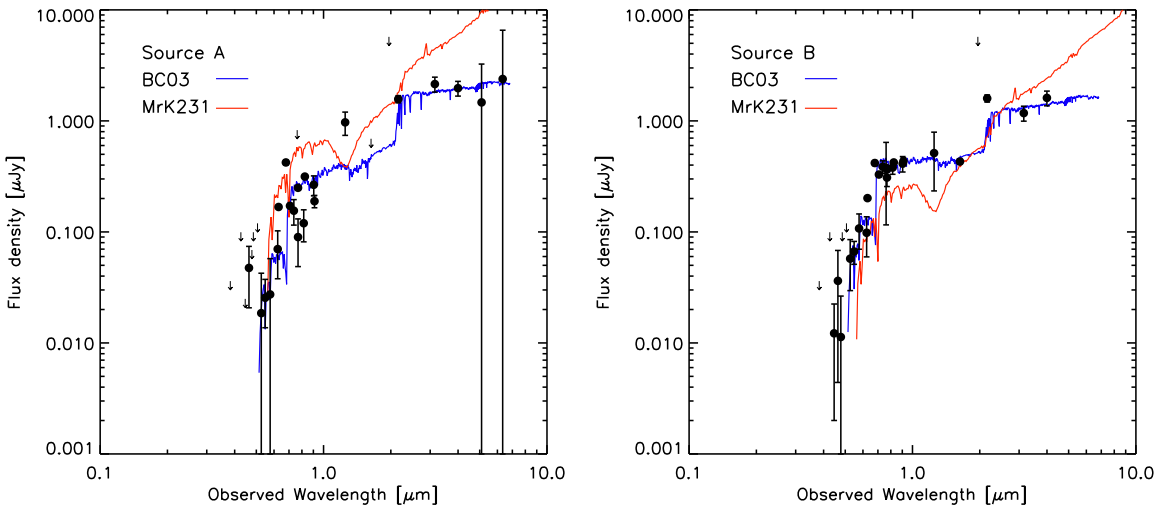

Figure 6.3. – The rest-frame UV-to-near-IR spectral energy distributions (SEDs) of both components that are likely part of the system Vd-17871 (see Figure 6.7). The photometric data (black filled circles) are obtained from ground- and space-based observations in 37 broad and intermediate bands in the COSMOS field. We used a deblending strategy (see descriptions in the text) in order to separately extract the photometry at the positions of the rest-frame UV sources A (left panel) and B (right panel) seen in the ACS imaging (Figure 6.7). While only the redshift of source A has been determined spectroscopically (see Figure 6.1), both sources are optically faint and appear photometrically very similar, suggesting both to reside at a similar (high) redshift. The best fit Bruzual and Charlot (2003) templates (BCO3, blue solid curves) to the photometry of both sources suggest the emission to be of stellar origin in each case (the best fit parameters are stated in the text). In contrast, the AGN-dominated (power-law) spectrum of the local ULIRG/Seyfert-1 Mrk 231 (red solid curves;Polletta et al. 2007) – using the scaling to the far-IR emission for source A (see Figure 6.5) – poorly fits the observed data. Also source B is not well fit by this template (see Section 6.3.3 for details and further implications). Source A shows a flux elevation in the intermediate band centered at 0.679 μm due to Lyman-α emission (see Figure 6.1) which is strongest at the position of this source.

high redshift nature of source B. Using the latest version of the publicly available HYPER-Z code (Bolzonella et al. 2000) and a library of observed and synthetic templates we fit the observed stellar SEDs separately for both sources while fixing the redshift to the spectroscopically measured value. All 37 filters available have been used in both cases. In the models used we force the derived galaxy age to be less than the difference between the age of the universe at a given redshift and a fixed formation redshift of $z = 8$. We assumed a constant and, alternatively, exponentially declining star formation histories (SFHs) $\propto \exp -t/\tau_*$ with $\tau_* = (0.1, 0.2, 0.3, 0.6, 2, 5, 15)$ Gyr. Furthermore assuming a Calzetti et al. (2000) extinction law we varied A_V from 0-4 in steps of 0.2. Both sources are best fit with templates from the Bruzual and Charlot (2003) stellar population synthesis library, exponentially declining SFHs ($\tau_*(A) = 0.1$, $\tau_*(B) = 0.3$ Gyr) and $A_V = 0$. While both sources are found to be young the fits suggest a somewhat lower age of 0.45 Gyr for source A compared to the 0.72 Gyr found for source B. Indeed, the parameters found for source A are reminiscent of a starburst or single burst model. Within the error margins the individual stellar masses for both sources are very similar with $M_*(A) = 10^{10.45\pm0.2}$ $M_\odot$ and $M_*(B) = 10^{10.35\pm0.2}$ $M_\odot$

leading to a total stellar mass content of $\sim 5 \times 10^{10}\ M_{\odot}$ in this system. Nominally, the total baryonic mass budget in the system Vd-17871 (source A *and* B) is dominated by stars by 80 % and by 66 % if we underestimated the gas mass by 50 % (see below). If we consider only the spectroscopically confirmed source A, however, and assume that all the gas is concentrated in this source, the molecular gas fraction is between one third to one half of all baryons.

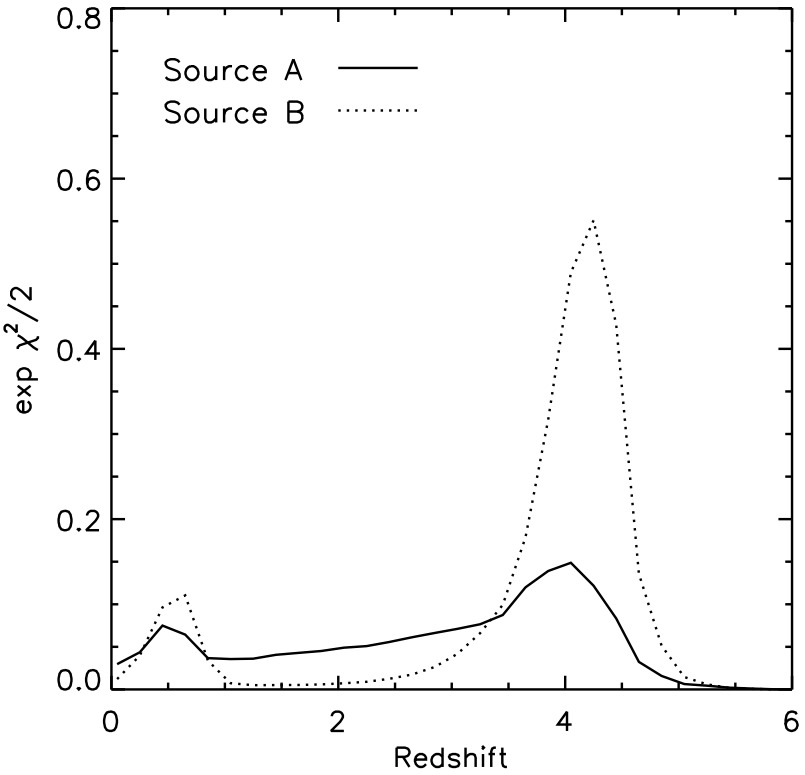

Figure 6.4. – Redshift probability distribution functions for the two neighboring sources seen in the ACS imaging (see Figure 6.7). The photometric redshift (photo-z) estimation is based on the observed, deblended photometry for both sources (see Figure 6.3) using a variety of template libraries, star formation histories and dust extinction parameters and the HYPER-Z code provided by Bolzonella et al. (2000) (see text for details). Source B shows a clear probability maximum at $z \sim 4.2$ while for source A a similarly high redshift is favored. Within the uncertainties both values are consistent with the spectroscopic redshift determination of source A (see Figure 6.1).

The absolute V-band magnitudes found from the best-fit templates are equally faint for both sources ($\mathrm{M_V(A)} = -23.05$, $\mathrm{M_V(B)} = -22.66$) and compatible with the purported high redshift nature. Moreover, if we treat the redshift as a a free parameter in our fits we obtain very similar photometric redshifts of ∼4.1 (∼4.2) for source A (B), close to the spectroscopic determination (see Figure 6.4). Moreover, in the deep $\mathrm{K_S}$-band imaging of the COSMOS field from the UltraVISTA survey (McCracken et al. in prep.) source A is detected at a level consistent with the rest-frame U-band emission expected for a high redshift galaxy while there is no evidence for a foreground object at the position of source B or elsewhere. Instead, at the position of source B only a tentative detection is found in the UltraVISTA $\mathrm{K_S}$-band image. An interesting photometric feature is clearly seen in source A where the flux in

the Subaru intermediate band IB679 is substantially boosted as it covers the Ly-α line at the observed redshift (see Figure 6.1). The emission in the intermediate band filter is overall diffuse and extends towards source B. Moreover, in the two-dimensional Keck/DEIMOS spectrum the Ly-α line shows multiple components both spatially and in redshift.

Within the positional uncertainty both the CO and the dust continuum emission are centered at the position of source A while the radio continuum – detected at higher significance compared to the mm-data – peaks right between both UV emission knots at a distance of 0.6" (corresponding to 4 kpc at $z = 4.662$). The comparatively strong Spitzer/IRAC 3.6 μm emission is centered at the position of source A, suggesting substantial flux contribution from the redshifted Hα line compatible with the massive star forming nature of this object. Higher signal-to-noise mm-data are required to clarify whether all interferometric data spatially coincide at the 1.4 GHz position or if rather the radio continuum is offset to all other emission sources including the Ly-α and Hα lines.

We conclude that both emission knots seen in the ACS imaging are most likely part of the same astrophysical system while the bulk of star formation activity is probably concentrated in the northern part (A). This source geometry and the spectral information is overall reminiscent of an early-stage major galaxy merger and very similar to the previously spectroscopically confirmed source J1000+0234 (Capak et al. 2008) that has been selected using the exact same criteria.

6.3.3. The thermal dust to radio continuum emission properties and indications for nuclear activity

Space-based mid- to far-IR data (from Spitzer/MIPS, Herschel/PACS&SPIRE) are available for Vd-17871. These are complemented by the continuum photometry obtained at 1.2 mm and 3 mm to provide insights into the amount, temperature and state of its dust emission.

A single modified black body (gray body; e.g. Beelen et al. 2006) with a dust temperature $T_{\rm D} = (42 \pm 1)$ K at an emissivity of $\beta = 1.5 \pm 0.1$ provides a good description of the far-IR emission, particularly tracing well the cool dust peak in Vd-17871. Trying to fit all IR data with the prototypical starburst IR-SED by Elbaz et al. (2011) significantly fails to reproduce the mid- to far-IR emission observed if scaled to match the single dish and interferometric cool dust continuum data (Figure 6.5). This template would likewise overpredict the mm-emission and the SPIRE photometry if scaled to the MIPS datum unless we were to significantly vary its cool dust emission properties. At the redshift of the source the 24 μm band falls right between the prominent rest-frame 3.3 μm and 6.6 μm polycyclic aromatic hydrocarbon (PAH) features which hence cannot have boosted the mid-IR emission observed. The global IR-emission in Vd-17871 is in better agreement with the redshifted and properly scaled IR SED of the local composite starburst and Seyfert-1 ULIRG Mrk 231 (Polletta et al. 2007), leading to a total $(8 - 1000)$ μm far-IR luminosity of $\sim 8 \times 10^{12}$ $L_{\odot}$ for Vd-17871 that would hence be partially powered by an AGN. On the other hand, the optical spectrum and the deep Chandra imaging do not yield evidence for the presence of an AGN in Vd-17871. No prominent spectral lines (such as CIV λ1540) and no X-ray emission are detected but the absence of such features could also point to a high level of obscuration in our line of sight. While the slit orientation might have prevented us from observing further spectral line emission the Lyman-α line width of $\lesssim 50$ Å (i.e. $\lesssim 2170$ km/s) suggests that the slit covers the central (narrow-line) region since it is broad compared to typical values

found in pure star forming sources.[6] Yet, it is too narrow for being consistent with line emission originating from the broad-line region. This suggests that the AGN in our line of sight is covered by a central dust screen, compatible with the obscuring torus scenario around the accreting black hole suggested for type-2 AGN sources (e.g. Urry and Padovani 1995). Consequently, the host galaxy dominates the rest-frame UV-optical emission.

This explains why a normal galaxy template provides the best fit to the rest-frame UV-to-optical SED of Vd-17871. This holds true in particular in comparison to the Mrk 231 template. In Figure 6.3 we show the redshifted UV-to-near-IR part of the Mrk 231 template in addition to the best-fit stellar population synthesis models. Since the 3 mm dust continuum appears to coincide with source A (as well as the CO emission; see Figure 6.7) we chose for this source the same scaling of the template as used at far-IR wavelengths (see Figure 6.5). The short wavelength SED of source B is shown along with the redshifted Mrk 231 template where no scaling is applied in order to reflect the purported lower contribution of this source. Figure 6.3 shows that the so-scaled Mrk 231 template is clearly disfavored for source A and it is also ruled out for source B at optical wavelengths. If we rescaled the Mrk 231 template – assuming that both source A and source B contribute to the far-IR emission in equal parts – it would provide a better but still poor match to the observed photometry, significantly over-predicting the near-IR data of both sources.

The obscured AGN hypothesis is favored further because the Mrk 231 template also significantly under-predicts the 160 μm emission observed that is marginally detected at a $\sim 3\ \sigma$ level. It hence under-predicts the total IR luminosity. It is unlikely that redshifted strong AGN ionization lines (mainly [O IV] and [Si III]; Weedman et al. 2005) are responsible for this substantial flux elevation as the inferred line-widths would be unusually broad. As Martínez-Sansigre et al. (2009) point out, a typical obscured quasar has a composite mid-to-far-IR SED consisting of a dominant cool dust component at far-IR wavelengths as well as deep silicate absorption in the mid-IR (see also Martínez-Sansigre et al. 2008, for results on the mid-IR spectra of obscured quasars at high-z). They show that clumpy torus models (Nenkova et al. 2008a,b, e.g.) do not provide a reasonable fit of the global dust emission unless additional extinction from cool dust – distributed on kpc scales within the host galaxy – is assumed. Martínez-Sansigre et al. (2009) suggest two distinct gray bodies to represent the far-IR emission of a typical obscured quasar. The cool dust emission we find is thereby in reasonable agreement with the warmer gray body option ($T_{\rm D} = 47$ K, $\beta = 1.6$). The differences are, however, marginal given that our single component gray body fit yields an emissivity value consistent with that of the Martínez-Sansigre et al. (2009) component fit. While our data do not constrain the rest-frame mid-IR portion covered by the Martínez-Sansigre et al. (2009) SED it is reasonable to adopt this model for our data given the strong indications for an obscured AGN in our source.

We still need to bridge the spectral gap blueward of the cool dust emission peak. While emission from a (clumpy) dust torus is typically represented by a continuum of hot gray bodies (e.g. Nenkova et al. 2008a,b) the best approach in our case of sparse data coverage

[6] Since the Lyman-α emission appears to be extended (see Section 6.3.2) it might at least partially originate from distances larger than the extent of the narrow-line region. Given the tentative evidence for two distinct line components at the spectral resolution available it is challenging to determine the line profile and hence to derive an accurate width of the Lyman-α line. We therefore assume a single component and take its FWHM as an upper limit to the line width. Note, however, that half the full width – in case of two line components – would suggest a velocity dispersion of $\gtrsim 1000$ km/s, still compatible with that expected in the narrow-line region.

is a simpler model. We therefore follow the descriptions in Weiß et al. (2007); Aravena et al. (2008) and fit an alternative two-component gray body spectrum to the IR data points excluding the observed 24 μm datum and assuming that the dust emission can be optically thick with an optical depth $\tau_\nu > 1$:

$$S_\nu = \frac{\Omega}{(1+z)^3}\left[B_\nu(T_{\rm D}) - B_\nu(T_{\rm BG})\right](1-e^{-\tau_\nu}), \tag{6.1}$$

thereby introducing the Planck function $B_\nu(T)$, the redshifted cosmic microwave background temperature $T_{\rm BG}$ ($T_{\rm BG} = 2.73 \times (1+z)$ K) and the source's apparent solid angle Ω (assuming a source extent of 1"). We adopt an emissivity index $\beta = 2.0$ and $\kappa_0 = 0.4$ cm^2 g^{-1} at $\nu_0 = 250$ GHz (Kruegel and Siebenmorgen 1994) in the frequency-dependent description for the dust absorption coefficient $\kappa(\nu) = \kappa_0(\nu/\nu_0)^\beta$.

This fit yields a cool component with a temperature of $T_{\rm D}^{\rm C} = 42$ K – as found for the single component gray body – and mass $M_{\rm D}^{\rm C} = 3.98 \times 10^8\ M_\odot$ dominating the total dust-mass budget against the $M_{\rm D}^{\rm H} = 1.56{\times}10^6\ M_\odot$ contribution of the bolometrically dominant hot-dust component found at a temperature of $T_{\rm D}^{\rm H} = 102$ K. Overall, these dust characteristics are reminiscent of those found in unobscured mm-bright (typically broad-line selected) $z \sim 2$ QSOs such as the Cloverleaf (Beelen et al. 2006) or the mm-bright X-ray absorbed broad-line QSO J100038+020822 in the COSMOS field (Aravena et al. 2008). However, it should be noted again that Vd-17871 does not belong to this class of objects but corresponds best to the mid-IR selected radio-intermediate obscured quasars at $z \sim 2$ presented by Martínez-Sansigre et al. (2009). The inferred total $(8-1000)$ μm luminosity of the two components is $1.48 \times 10^{13}\ L_\odot$ to which the cool component contributes ~ 30 %. From the average result of our single and double component fits we conclude that the cool dust luminosity amounts to $(4.75 \pm 0.75) \times 10^{12}\ L_\odot$ which - if powered solely by star formation – suggests an SFR of $(475 \pm 75)\ M_\odot{\rm yr}^{-1}$. Note that AGN heating of the dust might also occur on the larger (kpc) scales the cool dust is expected to occupy (e.g. Martínez-Sansigre et al. 2009, and references therein). Therefore, strictly, also the cool dust derived SFR should be considered an upper limit. Overall, our double gray body model in combination with the mean obscured quasar SED from Martínez-Sansigre et al. (2009) at rest-frame mid-IR wavelengths and a normal galaxy template (Bruzual and Charlot 2003; see above) provides a good fit to the entire SED of Vd-17871.

The radio continuum emission yields further evidence for an AGN in Vd-17871. The total 1.4 GHz flux density of $(79 \pm 11)\ \mu{\rm Jy\,beam}^{-1}$ suggests a 1.4 GHz luminosity[7] of $(1.2 \pm 0.2) \times 10^{25}$ W Hz^{-1} at the CO-redshift of the source which is well below the limit for a Fanaroff and Riley (1974) class II (FRII) source[8] of $L_{1.4\,\rm GHz} \sim 5 \times 10^{25}$ W Hz^{-1} but nominally at the edge to be considered a radio-loud object (see Urry and Padovani 1995, for a review on the classification of AGN).[9] This flux density is consistent with the total flux density derived if the higher resolution (1.5×1.4") VLA-COSMOS image is used. Also the position of the

[7] We assume a radio continuum spectrum $F_\nu \propto \nu^{\alpha_{\rm rc}}$ with $\alpha_{\rm rc} = -0.8$ (e.g. Condon 1992).

[8] The FRI/FRII break occurs at $L_{0.178\,\rm GHz} = 2.5 \times 10^{26}$ W Hz^{-1} which we scale to a 1.4 GHz luminosity limit assuming again a radio continuum spectral index of $\alpha_{\rm rc} = -0.8$.

[9] Due to its clearly composite nature this source is, however, likely more similar to the radio-quiet population in the typical quasar terminology. The bulk of the sources in the obscured quasar sample of Martínez-Sansigre et al. (2006a) shows the same intermediate radio luminosity as Vd-17871 and a detailed high resolution radio interferometric follow-up study by Klöckner et al. (2009) suggests that these sources are geometrically reminiscent of the radio-quiet population.

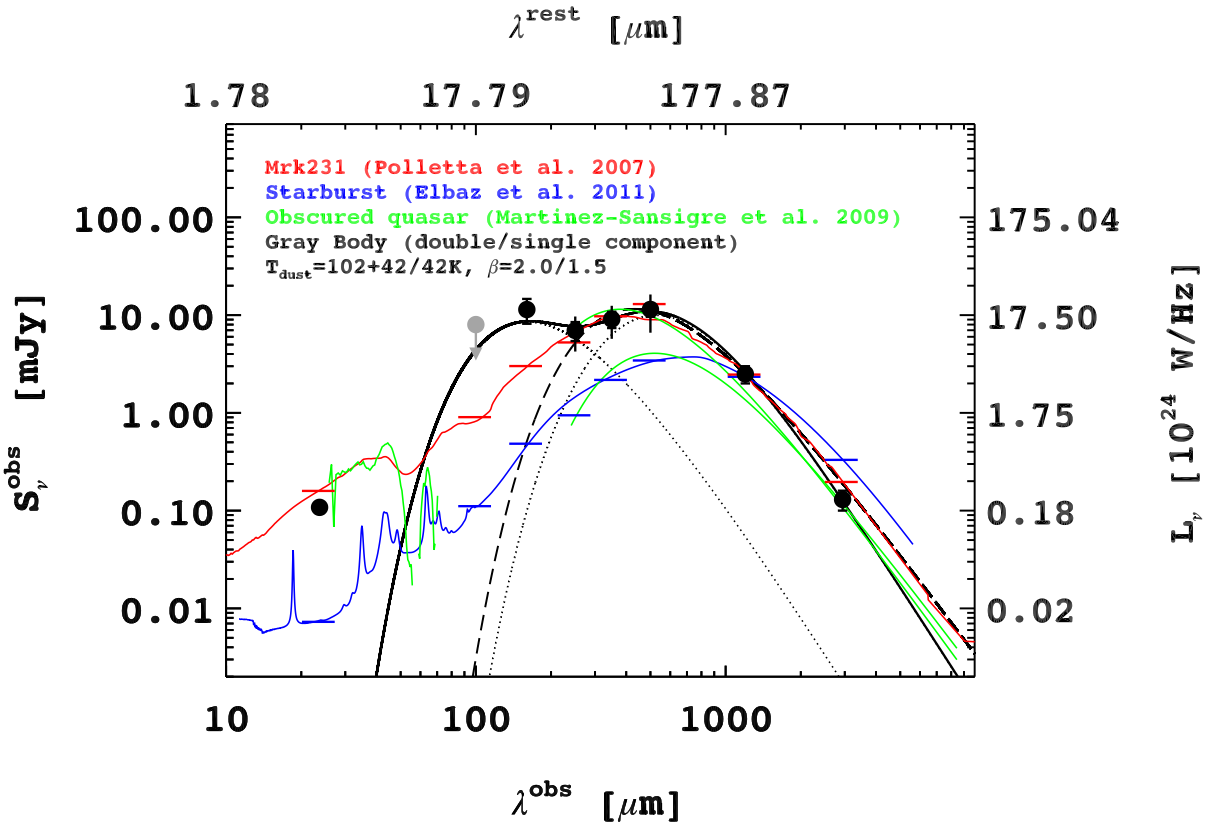

Figure 6.5. – The rest-frame near-to-far-IR spectral energy distribution (SED) of Vd-17871 observed at mid-IR (SPITZER/MIPS), far-IR(Herschel/PACS & SPIRE) as well as mm (MAMBO-II & PdBI) wavelengths (black filled circles). A clear peak in the cool dust continuum is seen around 500 μm (rest-frame $\sim$ 90 μm). The redshifted templates of the local composite Seyfert-1 ULIRG Mrk 231 (red; Polletta et al. 2007) and of the prototypical starburst SED (blue) suggested by Elbaz et al. (2011) are overplotted as scaled to the observed photometry. The expected template flux densities are depicted as horizontal bars in each case and have been obtained by convolution of the spectral response of each individual instrument using appropriate color corrections. While the starburst template poorly fits the global IR photometry if fixed to the 1 mm emission observed, the Mrk 231 model underscores the 160 μm hot dust emission. The redshifted mean obscured quasar SED of Martínez-Sansigre et al. (2009) (green) provides a good fit to the observed data without rescaling if we adopt the warmer of the two alternative gray bodies ($T_{\rm D}$ = 35/47 K, β = 1.6) they suggest to model the cool dust emission. A single component gray body fit to our (sub-)mm data observed yields similar parameters ($T_{\rm D}$ = 42 K, β = 1.5; dashed black curve). Our data, however, cannot constrain the rest-frame mid-IR portion of this model that shows the typical deep silicate absorption features. Given our few photometric data points a simple double component gray body fit ($T_{\rm D}$ = 102/42 K, β = 2.0; solid black curve) represents best the hot and cool components of the dust continuum emission.

radio source is found to be the same at both resolutions while the radio source is nominally unresolved either way. However, the emission appears slightly extended given that the higher resolution map reveals a difference in peak and total flux density. We find that the 1.4 GHz peak flux density corresponds to 65 % of the total 1.4 GHz emission (see Table 6.1). For a point source we should see no difference between peak and total flux emission. This difference might not be entirely explicable by the effect of bandwidth smearing (chromatic

abberation due to the finite bandwidth) but rather by a central point source embedded in a diffuser component.[10] Consequently, we need to quantify the amount of radio flux that can be attributed to star formation. Assuming that the local far-IR radio ratio for star forming systems is not evolving from its local value of $q = 2.64 \pm 0.26$ (e.g. Sargent et al. 2010a,b) we can estimate an upper limit to the radio emission powered by star formation from its lower bound. We follow the definition of Kovács et al. (2006),

$$q = \log\left(\frac{L_{\rm IR}\ [\rm W]}{4.52 \times 10^{12}\ \rm Hz}\right) - \log(L_{1.4\ \rm GHz}\ [\rm W\,Hz^{-1}]), \tag{6.2}$$

which is best suited given the dust properties of Vd-17871. The IR luminosity inferred from our single component gray body is $5.5 \times 10^{12}\ L_{\odot}$ and leads to $F_{1.4\ \rm GHz} \lesssim 20\ \mu$Jy which is indeed roughly consistent with the difference between total and peak radio continuum flux density observed, suggesting this more extended radio continuum component to trace the SFR of Vd-17871. In turn, using the total radio flux observed the $q-$value is 1.9 (1.7) if the rest-frame $(8 - 1000)\ \mu$m luminosity is derived from the Mrk 231 template (the single component gray body). Both results are clearly too low to be consistent with pure star formation activity. For the sake of completeness we derive the SFR from the total radio flux density. The corresponding radio luminosity suggests an SFR of $\sim 3800\ \rm M_{\odot}$/yr (using the Bell 2003b calibration) if – unrealistically – all the radio emission were powered by star formation.

As a caveat to the above interpretation of compact and diffuse radio component we should once again come back to the geometric situation (see Figure 6.7). Given the significant spatial offset of the 1.4 GHz peak – coincident only with the warm dust emission as traced, e.g., at 24 μm – it is plausible that the hot dust and major parts of the radio continuum emission themselves originate from a spatially distinct component, possibly the southern UV-source B in Figure 6.7. In this scenario the AGN host would be distinct from the object harboring the bulk of the molecular gas as well as cool dust and the potentially large amount of AGN-powered 1.4 GHz emission would have shifted the radio centroid away from the main star forming source A. However, as outlined above, the Lyman-α line width suggests source A to be an AGN host. Hence, it appears more likely that both source A and B are radio continuum emitters and, possibly, both AGN hosts. Deeper mm-continuum and CO-data but also higher resolution radio continuum data are required to clarify the geometric situation and to ultimately rule out AGN ionization lines as a cause of the elevated 160 μm flux. Additionally, deep optical spectroscopy at the position of source B might shed light on the existence of an AGN in source B.

6.4. The diversity of extreme starbursts at high redshift

Among the very limited number of $z > 4$ extreme starbursts in the literature for which CO data are available, Vd-17871 is not only at the very high redshift but also at the low luminosity end both with respect to its far-IR as well as its CO emission. It provides the only example known to-date for substantial dust heating by an AGN in a $z > 4$ massive starburst. A criterion to classify a source as a starburst is to compare its specific SFR (SSFR) with the

[10] This is also consistent with the results of Klöckner et al. (2009) who find that – on average – the radio continuum emission of radio-intermediate obscured quasars is core-dominated to a similar level as our source.

average trend for star forming sources. The SSFR of Vd-17871 shows a clear elevation (a factor of 3.5-6.2; see Table 6.1) compared to the suggested limit of $\sim$2.7 Gyr^{-1} for average star forming sources at high-z (Karim et al. 2011a) that is observationally supported (Daddi et al. 2009b; McLure et al. 2011). It is hence valid to call Vd-17871 a massive starburst.

While a major part of the bolometric luminosity emitted by sub-mm bright sources at $z \sim 2$ originates in the far-IR as a consequence of dust heated by recently formed stars, typically 30 % is powered by an AGN (e.g. Pope et al. 2008; Meneux et al. 2009) that substantially contributes at shorter IR wavelengths. Already Coppin et al. (2009) reported that at $z > 4$ a massive starburst might exhibit such a composite nature but they did not find evidence for influence of the potential AGN on the thermal dust. Daddi et al. (2009b) serendipitously detected CO-emission from two $z \sim 4$ starburst of which one is supposed to host an AGN due to its comparatively high radio luminosity. As the example of Vd-17871 now shows it is possible that the composition of the extreme starburst population at all $z > 1$ shows a similar diversity.

More insights in the nature of extreme starbursts at high z compared to the $z \sim 2$ SMG population can be gained from their distribution in the $L'_{\rm CO}/L_{\rm IR}$ plane which is a proxy for the star formation efficiency. Recent results suggest the existence of two modes of star formation (Daddi et al. 2010b; Genzel et al. 2010) that separates starbursts from the global population of normal star forming systems with respect to their star formation efficiency. Typically, these studies suggest that SMGs and mm-bright quasars are simply "scaled-up and more gas-rich" versions of local starbursts (also Tacconi et al. 2006). Already well before their actual discovery it has been suggested that $z > 4$ starbursts should be considered a "high redshift tail" of the typical SMG population (Dannerbauer et al. 2002, e.g.) instead of forming a distinct population. However, no attempt has been made so far to find conclusive insights into the distribution of their star formation efficiencies compared to the $z \sim 2$ sources.

We therefore compiled all available $z > 4$ literature sources and a representative census of $1 < z < 3$ SMGs from the literature (Figure 6.6).[11] At both redshift ranges we also include gravitationally lensed sources and consider the lowest rotational CO-transition published for each source. The rare observational data of low-J CO transitions in high-z starbursts suggest that the use of higher transitions might under-estimate the molecular gas mass by up to a factor of two: Based on observations of the CO(2-1) line with the Expanded VLA in combination with higher-J CO data Carilli et al. (2010); Riechers et al. (2010) find for the sources GN20 ($z = 4.05$) and AzTEC-3 ($z = 5.3$) that the CO-excitation of these extreme starbursts is only poorly fit by a single thermalized molecular gas component. These data suggest that about half of the total gas mass is in a diffuse low-excitation phase, not directly traced by $J > 3$ CO lines. Initial observational results suggest similar trends for sub-mm selected sources at lower-z (Ivison et al. 2011). We therefore indicate in Figure 6.6 how the sources shift if we were to apply this correction.[12] In order to compare like with like we

[11] The data for $z \sim 2$ sources used here are taken from Frayer et al. (1998, 1999); Andreani et al. (2000); Neri et al. (2003); Greve et al. (2003); Genzel et al. (2003); Downes and Solomon (2003); Sheth et al. (2004); Weiß et al. (2005); Greve et al. (2005); Kneib et al. (2005); Hainline et al. (2006); Tacconi et al. (2006); Martínez-Sansigre et al. (2009). Data for $z > 4$ sources have been presented by Schinnerer et al. (2008); Daddi et al. (2009b,a); Coppin et al. (2010); Knudsen et al. (2010); Lestrade et al. (2010); Carilli et al. (2010); Riechers et al. (2010); Cox et al. (2011) as well as in this work.

[12] Note, however, that luminous quasars hosts at high z appear to have no extended molecular gas reservoir but solely a single, highly excited gas component (e.g. Riechers et al. 2006). If an obscured quasar like Vd-

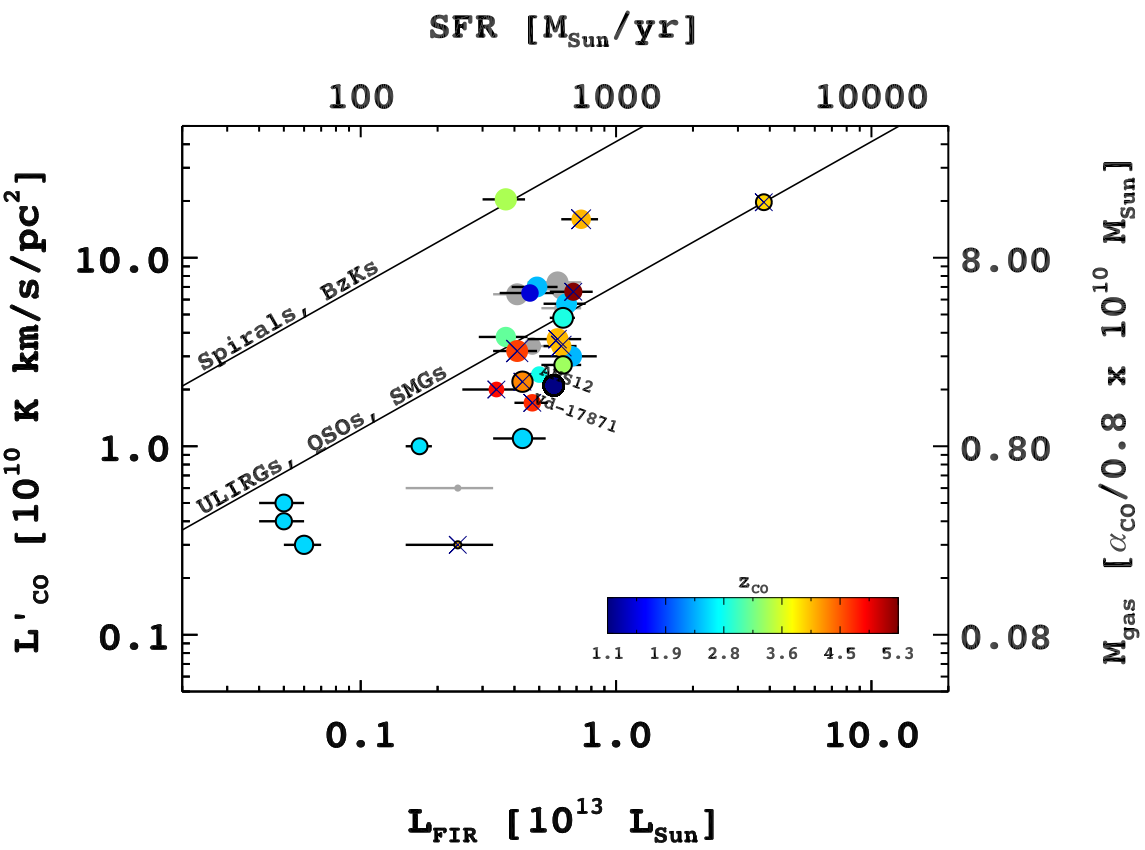

Figure 6.6. – The distribution of $z \sim 2$ sub-millimeter galaxies (SMGs) and $z > 4$ starbursts in the $L'_{\rm CO}/L_{\rm IR}$ plane. The data have been compiled using a representative census of $z \sim 2$ SMGs (filled circles) and all $z > 4$ extreme starbursts (filled circles with crosses) currently available in the literature, both including gravitationally lensed objects. The data points are color coded by their CO-redshift and lensed objects are indicated by an additional black open circle. Symbol sizes scale with the velocity dispersion measured from the FWHM of the CO line emission. In this compilation we always used the lowest rotational CO-transition available for any object. For those sources for which only higher transitions ($J > 3$) have been observed we indicate how they would be shifted along the $L'_{\rm CO}$ axis if a low excitation gas phase were present that contributes 50 % to the total $L'_{\rm CO}$ at the (1-0) transition (gray filled circles; see text for details). Infrared luminosities have been consistently estimated based on the (sub-)mm data published for all objects using a typical dust temperature of 35 K. Black solid lines denote the two sequences for local ULIRGs/distant starbursts/QSOs as well as local disk galaxies/higher z normal star forming sources suggested by Daddi et al. (2010b). Asides rare outliers all sources shown roughly follow the starburst sequence. The obscured quasars Vd-17871 (this work) and AMS12 (Martínez-Sansigre et al. 2009) are labeled by their names and also follow this general trend. No clear redshift trends are apparent, suggesting that starbursts at all $z > 1$ are similar with respect to their star formation efficiency while the population is comprised of intrinsically different objects.

furthermore derive IR luminosities for all sources based on the monochromatic (sub-)mm literature data assuming a single component gray body to be a good model for the cool dust emission heated by star formation. For this we chose a fixed emissivity $\beta = 1.5$ and typical dust temperature of 35 K, a realistic value for the bulk of high z starbursts (e.g.

17871 mainly differs from these sources in orientation with respect to the observers line of sight a different molecular gas excitation is not expected.

Kovács et al. 2006). For the obscured quasars Vd-17871 and AMS12 we adopt the far-IR luminosities reported in this work and by Martínez-Sansigre et al. (2009), respectively.

As apparent from Figure 6.6 both the low- as well as the high-z samples show a wide (1 order of magnitude) spread both in $L'_{\rm CO}$ as well as $L_{\rm IR}$. While for some sources the gravitational lensing magnification factors are uncertain there is a clear trend that all galaxies shown follow the starburst sequence suggested by Daddi et al. (2010b). There are rare outliers that tend to be closer to the "normal" star formation mode with no significant trend. Most interestingly, the distribution of sources in the $L'_{\rm CO}/L_{\rm IR}$ shows no redshift trend suggesting the same principles that underlie the star formation process in starburst environments at all $z > 1$.

As Riechers et al. (2010) argue the different CO-excitation laws observed in high-z quasars (one molecular gas phase) compared to the $z > 4$ starbursts with confirmed two molecular gas phases might point to different evolutionary stages influencing the molecular gas/ISM properties. Assuming that extreme starbursts are mostly triggered by (major) mergers (e.g. Engel et al. 2010) the different states and distribution of the molecular gas could be due to different merger stages observed, thereby explaining the general intrinsic diversity of this source population. This diversity might furthermore be enhanced whenever blending of close pairs of gas-rich[13] but not (yet) merging normal star forming sources occurs due to insufficient spatial resolution in the observations (Hayward et al. 2011a). This would also explain why some sources are closer to the normal star forming sequence of Daddi et al. (2010b). In order to investigate if there is a true star formation bimodality blended normal star forming sources need to be identified among those systems currently classified as starbursts. Initial high resolution studies of CO as well as dust continuum emission at $1 < z < 3$ support these arguments (Engel et al. 2010; Bothwell et al. 2010). It is clear that more high resolution data observations of the molecular gas and dust also in $z > 4$ starbursts are needed to clarify the situation and will be feasible soon with the Atacama Large Millimeter Array.

To summarize, our results – based on global far-IR and CO emission properties – suggest no clear evidence for $z > 4$ massive starbursts to form a distinct population from the well-known $z \sim 2$ SMGs. However, a rich diversity of intrinsically different sources likely comprises the entire population of $z \gg 1$ starbursts. As we showed in this work, in addition to pure starbursts and gas-rich luminous QSOs also obscured quasars can be found in this population even at $z > 4$. Besides J1000+0234 (Capak et al. 2008; Schinnerer et al. 2008) and Vd-17871 we found four more dropout sources with weak radio counterparts in the COSMOS field that qualify as extreme starbursts at $z \gtrsim 4$. Comparing their observed 1.4 GHz and 24 μm flux densities to Vd-17871 suggests at least one object to be of a similar composite nature as this source. For two of them – GISMO-AK03 at $z = 4.757$ as well as the $z = 3.9$ mm-bright source SMA/AzTEC-5 (Scott et al. 2008; Younger et al. 2007) – Keck-/DEIMOS observations confirmed their high redshift nature while only recently (additional) 2 mm continuum observations constrained their cool dust properties. For these sources, however, no CO line are available yet and they will hence be discussed in follow-up work.

[13] Average star forming galaxies at high redshifts are expected to contain large molecular gas fractions (Daddi et al. 2010a; Tacconi et al. 2010).

Table 6.1. Mid-IR-to-millimeter flux densities and derived quantities of Vd-17871

Quantity	Value	Information
$S_{24\ \mu m}$ [μJy]	108±14	$\sim 8\sigma$, from S-COSMOS*
$S_{100\ \mu m}$ [μJy]	< 8	upper limit, from PEP‡
$S_{160\ \mu m}$ [μJy]	11.4±3.4	$\sim 3\sigma$, from PEP‡
$S_{250\ \mu m}$ [μJy]	6.7±1.5 (±2.7)	$> 2\sigma$, from HerMES$^{\mathrm{II}}$
$S_{350\ \mu m}$ [μJy]	9.1±1.7 ±3.4)	$> 2\sigma$, from HerMES$^{\mathrm{II}}$
$S_{500\ \mu m}$ [μJy]	11.4±1.8 ±4.8)	$> 2\sigma$, from HerMES$^{\mathrm{II}}$
$S_{250\ GHz}$ [mJy/beam]	2.5±0.5	$\sim 8\sigma$, from MAMBO-II
$S_{102\ GHz}$ [mJy/beam]	0.13±0.03	$\sim 4\sigma$, from PdBI off-line channels
$S_{1.4\ GHz}$(Peak) [μJy]	57± 12	$>4\sigma$, from VLA-COSMOS†
$S_{1.4\ GHz}$(Total) [μJy]	79± 11	$\sim 7\sigma$, from VLA-COSMOS†
R.A.$_{CO(5-4)}$ (J2000)	10:01:27.080	line peak
Dec.$_{CO(5-4)}$ (J2000)	+02:08:55.80	line peak
R.A.$_{102\ GHz}$ (J2000)	10:01:27.080	continuum peak
Dec.$_{102\ GHz}$ (J2000)	+02:08:55.80	continuum peak
R.A.$_{1.4\ GHz}$ (J2000)	10:01:27.061	continuum peak
Dec.$_{1.4\ GHz}$ (J2000)	+02:08:55.32	continuum peak
L_{IR} [$L_{\odot}$]	8×10^{12}	(8-1000) μm luminosity from scaled Mrk 231 template
L_{IR} [$L_{\odot}$]	1.48×10^{13}	(8-1000) μm luminosity from double component gray body fit
L_{IR} [$L_{\odot}$]	$(4.75 \pm 0.75) \times 10^{12}$	far-IR luminosity (from cool dust)
SFR [$M_{\odot}\,yr^{-1}$]	475 ± 75	derived from cool dust emission
SSFR [Gyr^{-1}]	9.5 ± 1.5	derived from total stellar mass in Vd-17871
SSFR [Gyr^{-1}]	16.8 ± 2.6	derived from stellar mass in source A
$z_{CO(5-4)}$	4.622 ± 0.001	from Gaussian fitting
FWHM$_{CO(5-4)}$ [$km\,s^{-1}$]	397 ± 82	from Gaussian fitting
$S_{CO(5-4)}$ [mJy/beam]	1.3±0.2	Peak line flux, from Gaussian fitting
$I_{CO(5-4)}$ [$Jy\,km\,s^{-1}$]	0.56±0.15	Integral under Gaussian fit
$L_{CO(5-4)}[L_{\odot}]$	$(1.1 \pm 0.3) \times 10^{8}$	from $I_{CO(5-4)}$
$L'_{CO(5-4)}$[$K\,km\,s^{-1}\,pc^{-2}$]	$(1.8 \pm 0.4) \times 10^{10}$	from $I_{CO(5-4)}$
$M_{gas}[M_{\odot}]$	$(1.4 \pm 0.4) \times 10^{10}$	Using $\alpha_{CO} = 0.8$

Note. — The ^{12} CO line luminosity and gas mass of Vd-17871 are derived using the descriptions in Solomon and Vanden Bout (2005) and the findings of Downes and Solomon (1998). The IR luminosity is computed from different templates and gray body models (see Section 6.3.3 for details). The cool dust far-IR emission is the mean value of the best-fit single gray body and the cool component of the double gray body fit. This value is used to constrain the star formation rate (SFR) in Vd-17871. The far-IR based SFR is computed based on Kennicutt (1998b) converted to a Chabrier (2003) IMF resulting in SFR $[M_{\odot}\,yr^{-1}] \sim 1000 \times L_{IR}\ [10^{13}\,L_{\odot}]$. Two values for the specific SFR (SSFR) are stated. The lower value is derived from the total stellar mass content measured for both rest-frame UV components likely comprising a common astronomical system (see Section 6.3.2 for details and mass estimates). The higher value is derived from the stellar mass content of source A which spatially coincides with the bulk of the Lyman-α as well as the ^{12}CO emission.

* Schinnerer et al. (2010)

† Sanders et al. (2007)

‡ Lutz et al. (2011)

II Oliver et al. (in prep.)

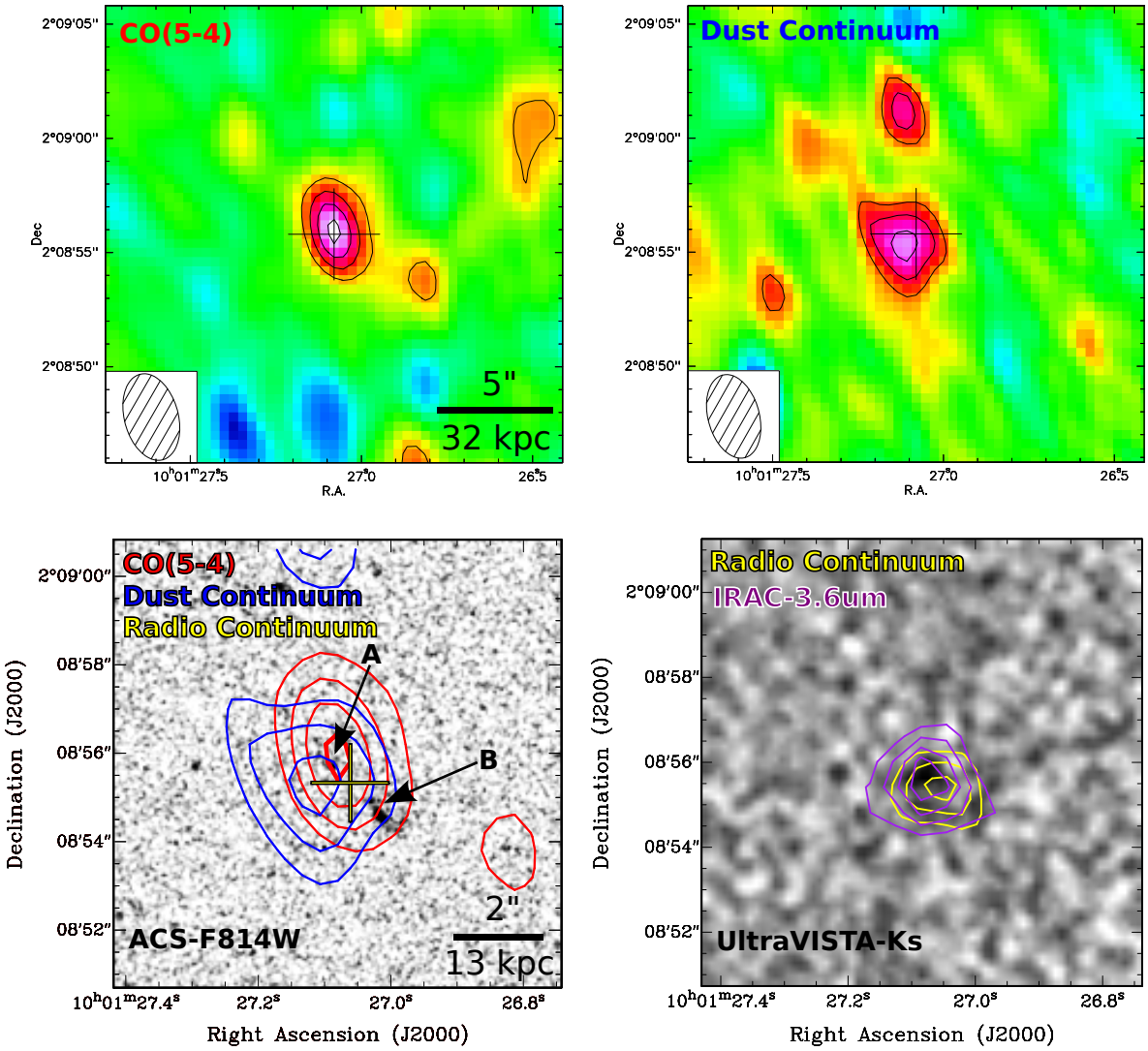

Figure 6.7. – Postage stamps for the Vd-17871 system as seen in different bands. All contours start at 2σ in steps of 1σ. At $z_{\rm CO} = 4.622$, 1" corresponds to a physical scale of 6.52 kpc. By convention, all stamps are oriented such that north is to the top and east is to the left. *Top:* 20" × 20" region around Vd-17871 as seen in ^{12}CO(5-4) emission (left) averaged over 291.429 MHz (850 km/s) and 3 mm dust continuum emission (right) averaged over the remaining ∼3.3 GHz line-free bandwidth the Plateau de Bure Interferometer (PdBI) provides. The images have been CLEANed using the synthesized beams indicated in the lower left. The cross depicts the phase center (source A as introduced below). *Bottom:* The left panel shows a 10" × 10" Hubble Space Telescope/ACS-F814W region around Vd-17871 overlaid with (cool) dust continuum (blue) and ^{12}CO(5-4) (red) contours from our PdBI observations. Two rest-frame UV emission knots are seen (labeled as source A and source B). Within the positional uncertainties the cool dust and gas emission are spatially coincident with source A that was targeted in our Keck/DEIMOS observations. A yellow/black cross denotes the position of the 1.4 GHz counterpart, centered halfway between sources A and B. The right panel shows the same region, this time as seen in the K_S-band (from the UltraVISTA survey) overlaid with Spitzer/IRAC 3.6 μm (purple; covering the Hα line and spatially coincident with source A) and 1.4 GHz radio continuum contours (yellow). Vd-17871 is marginally detected in the K_S-band and the absence of additional bright features rules out a nearby foreground object in our line of sight. The radio emission is spatially offset by $\sim$ 0.6" from the other emission sources except Spitzer/MIPS 24 μm (not shown) tracing the warm dust. The 1.4 GHz peak and warm dust emission are likely powered by an AGN. It is possible that both sources (A and B) are radio emitters blended into a single source since their angular separation equals the 1.5" resolution of our VLA imaging.

7. Summary and outlook

We initially motivated the critical need for direct observational studies of cosmic evolution. We argued that those need to focus on the luminous matter content of the universe which is concentrated in galaxies. We thereby outlined how theoretical models and simulations motivate these observations and why they are, in turn, crucial to constrain them. Within the broad field of galaxy evolution the process of star formation was introduced as a key element in studying the evolution of the interplay between dark and luminous matter over time. In this spirit, the aims of this thesis have been formulated to obtain deeper insights into the evolution of the global cosmic star formation activity.

Here we summarize the methodological and scientific achievements of this thesis and discuss ongoing and potential future research directions related to the individual findings. This Chapter is therefore organized as follows. First we provide essential context information before we recap individual key results and subsequently discuss the related future prospects.

7.1. A newly developed image stacking routine

The method of image stacking has attracted substantial interest over the last years especially in the extragalactic community. It provides a powerful tool to use imaging data beyond their sensitivity limits as long as average trends of observables are of interest and positions of celestial objects are known from ancillary observations.

A goal of this thesis therefore was to design and implement a new image stacking routine that can be used in a flexible and efficient way with a particular focus on radio continuum stacking experiments in deep cosmological survey fields. The resulting routine, described in detail in Chapter 3, has been thoroughly tested at radio wavelengths and provides the fundament for the major scientific results presented in this thesis. A variety of statistical estimators has thereby been implemented and partially developed (see Appendices A.1 and A.2). Additionally, the measurement of total flux densities from radio interferometric imaging has been automated and optimized for the processing of large data sets.

Due to the image processing capabilities implemented this newly developed image stacking routine is, however, not restricted to radio continuum wavelengths. Input imaging is recognized by the routine based on the essential information stored in its FITS-header and astrometric calculations are performed regardless of the nature of the input image. There are flexible input capabilities also with respect to the positions of objects to be stacked and overall the processing options are steered externally by the user in a platform-independent way. The routine can therefore be used in a variety of environments the user prefers and its fast processing capabilities enable an efficient handling of huge data sets as often required. To summarize, the routine at its current stage has proven its abilities and matches the requirements initially formulated.

Full automation of the workflow from arbitrary input data to a total flux measurement is,

however, virtually impossible and perhaps not desirable to achieve. Especially the correct measurement of fluxes needs to be treated differently for different input imaging and is probably most exotic and least straight-forward to perform at radio wavelengths as extensively discussed in this thesis. It is furthermore the interplay between angular resolution and sensitivity of the imaging to be stacked that might lead to blending problems and hence significant inaccuracies in the flux measurement. While the new routine presented here has pre-implemented capabilities to identify noise distortions and interloping detections in order to reject input sources further testing at multiple wavelengths is unavoidable. It is hence an ongoing effort to investigate biases introduced by stacking experiments based on simulations as well as to explore deblending strategies discussed in the recent literature. In its current implementation the routine has, however, proven efficient and valuable especially in the context of large stacking simulation efforts.

A variety of scientific problems is currently being approached and a full overview of current applications of the new image stacking routine at various wavelengths is given in Section 3.3.4. Many more prospects for future application of this routine exist, including those that make use of readily available survey data and imaging. Examples with high relevance for the prospects of this thesis will be highlighted in the next Sections of this Chapter.

7.2. The roughly stellar mass-independent evolution of the average (specific) star formation rate

Recent initial observational results in the local universe (Brinchmann et al. 2004) and at cosmic epochs corresponding to redshifts $z \lesssim 1$ (Noeske et al. 2007b; Elbaz et al. 2007) revealed a surprisingly tight relation between the total star formation rate (SFR) of normal star forming galaxies and their stellar mass content. The localized process of star formation is consequently linked to a global galaxy property, suggesting that star formation histories of individual galaxies are likely not dominated by stochastic processes such as galaxy mergers (e.g. Noeske et al. 2007b). The exact evolutionary properties of this relation are subject to ongoing debates and insights based on a variety of SFR tracers are needed. Especially the measurement of SFRs in a way unaffected from effects of dust are in need in order to obtain an unbiased and (dust) model-independent view of the mass-dependent SFR evolution.

7.2.1. Results presented in this thesis

This motivated an extensive radio-stacking study presented in this thesis (see Chapter 4, Karim et al. 2011a as well as Karim et al. 2011b, for a summary). In order to cover a substantial baseline in cosmic time a rich galaxy sample was needed that remains representative at comparatively low stellar masses out to high redshift. The study is therefore based on the panchromatic datasets from the 2 deg^2 cosmic evolution survey (COSMOS; see Scoville et al. 2007d, for an overview) that have provided very accurate photometric redshifts (photo-z's) and stellar masses for a large mass-selected sample of galaxies (Ilbert et al. 2010). This Spitzer/IRAC ($m_{\rm AB}(3.6\ \mu{\rm m}) \leq 23.9$) selected sample of $\sim$114,000 galaxies with FUV to mid-IR as well as X-ray ancillary data has been used in combination with 1.5" and thus high angular resolution Very Large Array (VLA) radio continuum data in the

COSMOS field (Schinnerer et al. 2007, 2010) to measure the evolution of the average SFR as a function of stellar mass out to $z \sim 3$. SFRs derived from radio continuum emission require only a simple K-correction and no correction for dust extinction, hence matching perfectly the needs formulated above. The high resolution and low detection rate of the VLA-imaging furthermore minimizes the risk of source confusion that would bias the stacking experiment. This is a major advantage compared to far-infrared stacking experiments that also provide a dust-unbiased view.

We have applied various criteria to minimize contaminating radio flux from potential active galactic nuclei and have used the stellar population synthesis template-based, intrinsic rest-frame $(\mathrm{NUV} - \mathrm{r}^{+})_{\mathrm{temp}}$ color from fits to the observed far-UV-mid-IR spectral energy distributions (Ilbert et al. 2010) in order to separate star forming sources from quiescent systems. We have also applied a newly developed scheme (see Appendix A.3) to evaluate the statistical stellar mass-representativeness of the sub-samples resulting from binning the data in stellar mass and redshift.

From the stacked median radio continuum flux densities obtained for each sub-sample we find:

- The evolution of the average (S)SFR of stellar mass selected galaxies is approximately mass-independent at least out to $z \sim 1.5$ where the depth of our data allows the most robust conclusions. A power-law relation between (S)SFR and mass represents well the data at the high mass end.

- The (S)SFR of star forming sources at $z < 3$ also evolves basically independent of mass while a power-law dependence of (S)SFR and mass generally extends over all masses probed. Higher mass galaxies hence have lower SSFRs, regardless if quiescent galaxies are included in the analysis or not.

- There is tentative evidence for an upper bound to the average SSFR preventing a further growth of the SSFR with z, starting at the low-mass end at $z \sim 1.5 - 2$.

A major result of this thesis therefore is that we observe no differential, more rapid evolution of high mass galaxies with respect to their average star formation activity as often claimed before and proposed as one flavor of the so-called ‘downsizing’ paradigm.

The latter of the points listed above is supported by earlier observations at even higher redshifts compared to our work (Stark et al. 2009; González et al. 2010). As an explanation for this behavior we proposed that this upper limit to the average SSFR might represent an effective gas accretion threshold. This is because the limit we find equals about the inverse of a dynamical timescale of typical local but also higher z disk galaxies (e.g. Daddi et al. 2010b). While their dynamical and free-fall times are approximately equal in commonly accepted models of star formation (e.g. Krumholz et al. 2009), normal galaxies are assumed to accrete their gas from their surroundings and to process it into stars at a constant efficiency (e.g. Daddi et al. 2010a). Our proposed scenario has been appreciated and supported in a recent study of the highest redshift normal star forming galaxies in the Hubble Ultra Deep Field observed to-date that confirm the limiting value we find at lower z (McLure et al. 2011).

The rapidness of the SSFR-decline with cosmic time we observe constitutes a challenge for semi-analytical models (Guo and White 2008). Our unprecedented precise measurement

of SFRs over time is therefore used to constrain the next generation models (Somerville et al. in prep.).

Finally, the results we present are consistent with recent far-IR based measurements that draw on substantially smaller samples and therefore, typically, do not yield a consistent view of the evolution of the average mass-dependent SFR over a broad redshift range from a single technique.

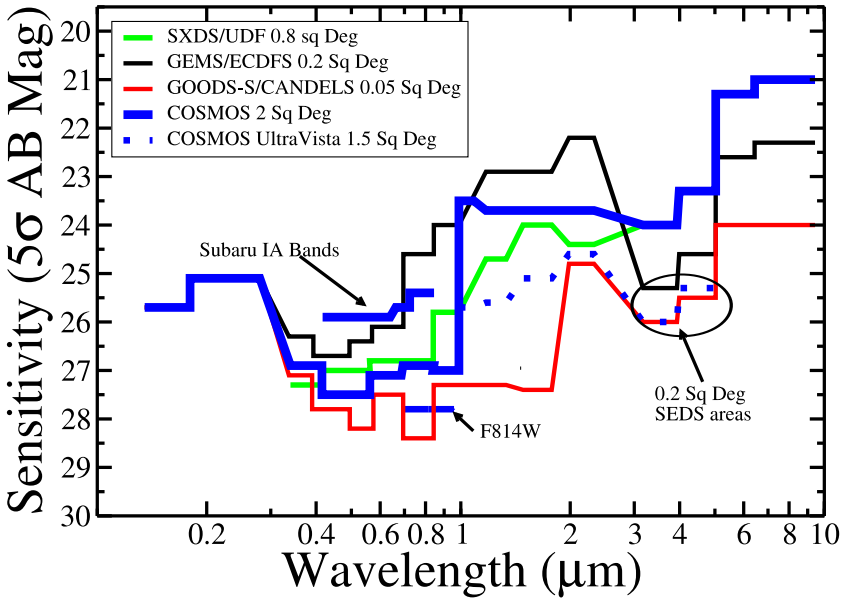

Figure 7.1. – Panchromatic 5σ sensitivities of the COSMOS survey (blue) compared to other deep fields (other colors). The recently released deep near-IR data from the UltraVISTA survey in the COSMOS field (McCracken et al. in prep.) are indicated (blue dotted curve). Image courtesy of Peter Capak (Caltech).

7.2.2. Prospects for ongoing and future research

Clearly not all questions have been answered in our study. While we showed that stellar mass is the determining factor for the average SFR other parameters have not yet been explored based on our approach and the existing data. Especially environmental effects are typically suggested to be of second-highest importance (e.g. Peng et al. 2010; Peng et al. 2011). Studying the evolution of the (S)SFR-sequence with respect to the additional environmental parameter is already feasible with the data in hand.

Extensive environmental information from different diagnostics out to $z \sim 1$ exist in the COSMOS field. In particular galaxy group catalogs based on spectroscopic redshifts and optical selection (Knobel et al. 2009) as well as X-ray selection (Finoguenov et al. in prep.) can be readily used for a radio stacking analysis of the mass-dependent SFR evolution in different environments. The accurate (spectroscopic) measurement of the density field by Kovač et al. (2010) offers yet an alternative approach for such a radio-stacking based study. Given these existing possibilities (including the well-tested image stacking routine) it should soon be undertaken.

Since the radio-view on the SSFR-sequence is dust-unbiased the radio data and stacks can be used to shed light on the stellar-mass dependence of dust correction factors that need to be applied at shorter wavelengths. This project is already possible with the current data and has been recently started (see below).

Further insights in the context of our study require deeper radio continuum data as discussed in the following.

EVLA-COSMOS: new insights from deep radio continuum observations at 3 GHz Recently new 3 GHz radio continuum observations with the Expanded VLA (EVLA; Perley et al. 2011) of the entire COSMOS area have been proposed (principal investigator V. Smolčić, co-investigator A. Karim). The net (total) observing time of 333 (416) hours is supposed to be split in such a way that 90 % of the time the most extended A configuration will be used while 10 % are observed with the C array using all 27 antennas. The resulting sensitivity would be 2 μJy/beam (1σ) while the observations would reach sub-arcsecond resolution (~ 0.65"). The observing strategy is such that two campaigns would be carried out twice per month over the full area and the course of four months. This will allow for variability measurements of bright radio sources in the field.

A main science driver for this outstanding observing program is the study of star formation over time. Based on the results presented in this thesis the sensitivity proposed will be such that the star forming main sequence can be probed out to $z \sim 1.2$ via $\sim 3,000$ direct ($> 5\sigma$) radio detections of star forming galaxies at least down to the characteristic mass for star formation. Detecting these objects means that the intrinsic dispersion of the (S)SFR sequence can be studied out to this redshift in full detail which is out of reach for a stacking-based study. While it is usually claimed that the relation between stellar mass and SFR is tight (intrinsic scatter of ~ 0.3 dex) at all cosmic epochs (e.g. Elbaz et al. 2007) so far no conclusive study over the full stellar mass-range of interest has been conducted outside the local universe to investigate the nature of the scatter: Is it intrinsic, pointing to a physical cause or just a mere effect of too large uncertainties? Is star formation proceeding mainly secular or are major mergers a significant source of contribution?

The new data will allow us to study the star formation–stellar mass relation not only as a function of redshift, but also of environment to unprecedentedly low masses as well as galaxy type (morphology, color) to identify if these other parameters do indeed play a role as well. It has been suggested that the lowest scatter in the star forming main sequence can be achieved if rigorous morphological selection (of pure disks) is applied (Salmi et al. in prep.). Hence, direct detections are critical for any follow-up project that explores morphological information as an additional parameter.

Only recently data from the deep near-infrared UltraVISTA survey (principal investigators Dunlop, Franx, Le Fèvre and Fynbo) in the COSMOS field have been released (see Figure 7.1; McCracken et al. in prep.). It is an ongoing effort to construct source catalogs from those data and to incorporate them in the global photometric catalogs from COSMOS. These deep near-IR imaging will probe significantly lower stellar masses at high redshift than reached with the current stacking study, enabling at the same time vastly improved options for studying the influence of environment on the average star formation rate of galaxies. Clearly, the new EVLA data are also critical to constrain the potential upper limit to the average SSFR proposed in this thesis. Altogether this will substantially improve our understanding of the stellar mass build-up in the universe.

The additional band provided by the 3 GHz observations will furthermore enable detailed studies of the evolution of the synchrotron spectral index for star forming sources when combined with the current 1.4 GHz data in stacking experiments as well as using direct detection. We pointed out in this thesis that the spectral index is important for estimating radio-based SFRs since K-corrections in the radio continuum depend on this quantity. A reliable determination of its non-evolution is still lacking and critically needed to accurately confirm the validity of our results.

In the following we will highlight more applications for these new radio continuum data for future projects related to the scientific projects presented in this thesis.

The mass-dependence of dust-extinction corrections As discussed in this thesis, shorter wavelength SFR indicators than radio emission suffer from uncertain dust extinction corrections. We have also shown that our results are in good agreement with those studies that are based on these alternative indicators and that apply strongly stellar mass-dependent dust corrections (e.g. Gilbank et al. 2010b). It is typically found that the extinction is substantially higher at higher masses.

Particularly Pannella et al. (2009) showed – based on a radio stacking approach – that for BzK-selected galaxies at $z \sim 2$ average SFRs derived from ultraviolet data need to be corrected in a strongly mass-dependent fashion in order to achieve an agreement with the radio-derived ones. With the COSMOS data and our stacking routine in hand this finding can be tested at different redshifts in order to reveal potential evolutionary trends.

However, also direct radio detections are valuable to assess mass-dependent dust corrections based on different diagnostics. Only recently the extensive zCOSMOS (Lilly et al. 2007) spectroscopic sample of 10,000 galaxies with emission line information became available to the COSMOS team. We can use these data to derive SFRs from the Hα ($z < 0.45$) and [OII]λ3727 ($0.75 < z < 1.5$) emission lines (e.g. Moustakas et al. 2006). Additionally, the Hβ emission line can be used at intermediate redshifts. These data can be directly compared to the radio-based SFRs for individual objects. In order to prepare this project the emission line SFRs have already been derived after cleaning the sample from unreliable data using various quality criteria. The resulting catalog has been cross-matched with the deep VLA-COSMOS radio catalog as well as with the multi-wavelength photometric sample including the stellar mass information from the IRAC-selected sample used in this thesis. All following work is currently in progress. The upcoming steps are to force the emission-line derived SFRs to agree with the radio-based ones in order to obtain the mean dust-corrections as a function of stellar mass. Based on this full sample the mean extinction can also be derived from the Hα/Hβ decrement yielding an independent estimate. In total this enables a study of the evolution of dust extinction corrections.

It is clear that any such study of dust correction factors will profit from the deep proposed 3 GHz radio continuum data which will yield a much more extensive sample of direct detections but also enables vastly improved options for a stacking approach.

7.3. The cosmic star formation history over ~ 9 Gyr and a constant characteristic mass for star forming galaxies

The cosmic star formation history (CSFH), i.e. a measure of the global cosmic star formation activity over time in the comoving frame, is of central interest in the research field of galaxy evolution. A number of literature results suggest a rapid (roughly one order of magnitude) decline of the total comoving star formation rate density (SFRD) since a redshift of $z \sim 1$. The CSFH therefore is considered a key manifestation of the impact of cosmic evolution on luminous matter and it is critical to reveal the drivers behind the global trends observed.

7.3.1. Results presented in this thesis

Our measurement of the average star formation rates (SFRs) of star forming galaxies down to a low limiting stellar mass forms the basis of an accurate constraint for the comoving evolution of the global cosmic star formation activity and yields valuable as well as new insights into the relative contribution of differently massive galaxies as a function of time (see Chapter 5, Karim et al. 2011a as well as Karim et al. 2011b, for a summary). The key finding is that the stellar mass distribution function of the SFRD at any epoch is well described by a Schechter function that reveals a constant characteristic mass of star formation since $z \sim 3$. Its integral finally constrains the total SFRD at any redshift probed.

The road to our findings was paved by a combination of our measurement and independent results by Ilbert et al. (2010) on the evolution of the stellar mass distribution (stellar mass function) of star forming galaxies. While star forming sources exhibit this remarkably shape-invariant SSFR-mass relation throughout cosmic time in our study (see above), it is worth noting that their stellar mass functions are found to show a similar constancy of their Schechter profile (e.g. Ilbert et al. 2010). As both phenomena involve a power-law in stellar mass, the product of the SSFR-mass relation and the mass function at a given cosmic epoch also yields a Schechter function for the mass distribution of the comoving SFR density (SFRD).

The potential upper SSFR-limit discussed above might alter the low-mass end shapes significantly only at the highest redshifts, the galaxy mass at which the function peaks at *any* epoch is $M_* \sim 10^{10.6}\ M_\odot$, regardless of the assumption of an SSFR-limit. Galaxies (almost) as massive as our Milky Way have hence always been the main sites of star formation. The existence of this characteristic mass of star forming galaxies challenges a 'downsizing' paradigm in which the dominant contributors to the CSFH have been massive sources in the cosmic past and low-mass galaxies at present times. It does, however, not rule out that low-mass sources gain more relative importance over time.

Literature results from alternative SFR diagnostics at different wavelengths confirm our results while they are mostly restricted to a phenomenological discussion and do not attempt to reveal the underlying analytical functional form. It is also worth noting that no other study to-date constrains the trends out to such high redshifts.

The sum of our direct radio stacking-based measurements of the SFRD for individual mass bins yields lower limits to the total SFRD at any redshift and hence lower constraints to the global CSFH. At a given redshift the Schechter SFRD function enables us to obtain the remainder of the total SFRD, integrated below our observational mass limits. For this

integration we assume the upper bound to the average SSFR motivated above.

Our approach enables a detailed disentangling of the influence of mass and time on the CSFH and therefore indirectly sheds light on its internal drivers as summarized in the following. Since $z \sim 1$ the stellar mass density of star forming galaxies is approximately constant (e.g. Ilbert et al. 2010) and also the relative fractions of objects at different masses within this population are conserved due to the shape-invariance of their mass function. In this redshift range the CSFH is therefore entirely controlled by the mass-uniform evolution of the average SFR. Given a constant star formation efficiency, a strong and global decline in the mass density of molecular gas thus entirely explains the observed decrease of the integrated SFRD with cosmic time. Towards earlier epochs it is predominantly the – again mass-uniform – decrease in star forming stellar mass density that leads to a shallower evolutionary behavior. The CSFH since $z \sim 3$ is hence well described by a broken power-law.

Among the existing and constantly growing number of attempts to constrain the CSFH comparatively few studies use radio continuum emission and its advantages as an SFR tracer. It is thereby worth noting that the agreement between our study and recent far-infrared based measurements is striking, underlining the reliability of radio-based SFRs out to high redshifts. Since our results are outstanding in that they constitute the to-date most extensive and hence statistically most robust study of the CSFH, they are appreciated as such in recent theoretical studies (in particular Leitner 2011) that provide analytical estimates of average star formation histories and evolutionary paths of galaxies.

7.3.2. Prospects for ongoing and future research

Our study – as well as *any* other measurement of the CSFH – relies on extrapolations to the faint (or low mass) end of the galaxy population. This holds true even at comparatively low redshifts ($z < 1$). The depth of the panchromatic COSMOS data especially at near and mid-infrared wavelengths allowed us to reduce the importance of extrapolations and opened a new road to constrain the low mass end. Following this road further, even deeper near-infrared data are needed to constrain the stellar mass function at its low end but also to reveal the positions of a representative sample of low mass galaxies in order to constrain their SFR, e.g., from a stacking experiment.

Deeper CSFH studies using COSMOS data are in reach using the upcoming recently released COSMOS UltraVISTA data. Follow-up studies are certainly not restricted to the COSMOS field but alternative surveys reaching a comparable depth in the selection band typically have substantially less areal coverage and provide hence smaller galaxy samples which leads to significantly worse statistics, in particular in the context of a stacking experiment. The new near-IR data will allow one to constrain the stellar mass functions to higher accuracy and to higher redshifts. The new deep 3 GHz radio continuum observations that have been proposed (see above) in combination with the deep near-IR data will allow us to probe the results presented in this thesis based on direct detections, extend the findings to lower masses via stacking and reach higher redshift limits.

While deeper data in the galaxy sample selection band assure lower limiting masses at all redshifts, low mass extrapolations will, clearly, remain more prominent at high-z. The importance of deeper near-infrared data beyond $z \sim 3$ lies in the improvement of photometric redshifts in order to reliably select clean high redshift samples. Near-IR medium band

filters provide another valuable extension of the COSMOS data sets as the study of Bezanson et al. (2011) shows. These data from the NEWFIRM survey will hence improve the photometric redshift accuracy while only a part of the COSMOS field is covered by these observations.

Constraining the high-mass part of the high redshift SFRD is a valuable and necessary exercise in its own right. The results presented in this thesis suggest that the peak of the CSFH is not yet reached at $z \sim 3$ and it hence remains a puzzle if the SFRD indeed abruptly drops beyond this redshift (a widely accepted scenario; e.g. Bouwens et al. 2009, 2011b), if it keeps increasing as suggested by hydrodynamic simulations (Springel and Hernquist 2003) or reaches an extended plateau. It is worth noting in this context that already the current SFRD measurements at $z \gtrsim 1.6$ lead to an overgrow in stellar mass if compared to the total stellar mass density measured at those epochs (Leitner 2011) which may point to the need for variations of the initial mass function of stars (e.g. Wilkins et al. 2008). Robust dust-unbiased SFRD-limits at $z > 3$, e.g. from deep radio continuum data, are critical, especially to challenge the low dust corrections to UV-based high-z SFRDs currently proposed (e.g. Bouwens et al. 2009, 2011b).

Our result of a constant characteristic stellar mass finally poses the questions whether this corresponds to a constant characteristic dark matter halo mass. This can be expected if the SSFR-sequence originates from the net dark matter halo gas accretion rate which is proportional to the halo mass (Dutton et al. 2010). A telling quantity to compare to the SFRD function we discussed in this thesis is the multiplicity function of star formation which is a dark matter halo mass distribution function of the halo mass normalized star formation rate (Springel and Hernquist 2003). Hydrodynamic simulations (Springel and Hernquist 2003) predict the peak of this function to downsize, unlike the peak of our SFRD function. The same simulations, however, also disagree with the observed CSFH because of a predicted mild evolution at low-z. There is hence a clear potential for new hydrodynamic simulations to challenge the current results.

7.4. Extreme starbursts < 1.5 Gyr after the Big Bang

There is growing evidence that massive elliptical galaxies with little ongoing star formation activity exist already at redshifts as high as $z \sim 3$ (e.g. Kriek et al. 2006, 2008a; Williams et al. 2009; Marchesini et al. 2010). Direct observations of these oldest 'red and dead' systems reveal optical colors that suggest those galaxies to be in a post-starburst phase with ages of < 1 Gyr (e.g. Kriek et al. 2008b).

A progenitor population of massive, probably major merger-driven starbursts might account for this early red sequence. If so, the constituents of this starburst population should resemble the properties of the known population of SMGs (e.g. Blain et al. 2002, for a review), sources first identified at (sub-)millimeter wavelengths that mostly reside at $z \sim 2$ (e.g. Chapman et al. 2005). Those sources typically show large molecular gas fractions with high central densities (e.g. Tacconi et al. 2006, 2008) and are predominantly mergers (e.g. Engel et al. 2010) with extreme SFRs of several hundreds of solar masses per year. These are the ingredients needed to build up the massive quiescent galaxies at even earlier times.

A generally higher importance of merger driven starburst activity at redshifts of $z > 4$ has been postulated (Khochfar and Silk 2010) in order to theoretically reproduce the observed trends of a constant SSFR at $z \gg 1.5$ as suggested in this thesis and also by direct

observations out to $z \sim 7$ (e.g. Stark et al. 2009; González et al. 2010; McLure et al. 2011).

While such starbursts at $z > 4$ have long sought after (e.g. Dannerbauer et al. 2002) they could only been observationally detected around the start of this PhD project (Capak et al. 2008; Schinnerer et al. 2008). Only rare examples of these sources exist to-date and many questions regarding their nature and their relation to the $z \sim 2$ SMGs remain open. These sources provide critical constraints on cosmological models (e.g. Baugh et al. 2005) and could be the signposts of the early galaxy overdensities expected in a hierarchically growing universe, as a first observational example demonstrates (Capak et al. 2011).

7.4.1. Results presented in this thesis

Following the road of pre-selecting high redshift star forming systems at optical wavelengths via the broad-band dropout technique and the subsequent search for radio continuum counterparts we were able to uncover seven candidate sources. For this a newly developed routine to find weak radio counterparts in an efficient and reliable way was used.

A case study of one object (Vd-17871) is presented in this thesis. Its high redshift nature had been confirmed in optical spectroscopic observations. It was furthermore interferometrically detected in its 1.2 mm and 3 mm continuum as well as ^{12}CO (CO in the following) line emission in observations carried out during this thesis work. Together with the extensive COSMOS ancillary data, including the only recently released Herschel/PACS and SPIRE catalogs, this source could be studied in detail (see Chapter 6). As a key result we showed that it is not only a massive and gas-rich star forming object but that it also hosts a powerful and dust-obscured active galactic nucleus (AGN). Due to its hidden nature this AGN could only be revealed by a detailed analysis of the dust and radio continuum emission in combination with Lyman-α diagnostics. This source is the most distant obscured AGN discovered to-date and demonstrates the diversity of the high-z starburst population. Interestingly, the better studied population of $z \sim 2$ SMGs is known to be as diverse. Our source as well as the only nine remaining $z > 4$ starbursts for which CO-data is available in the recent literature appear furthermore indistinguishable from the $z \sim 2$ SMGs with respect to their far-infrared to CO-line luminosity ratio, commonly interpreted as a star formation efficiency indicator. In short, massive starbursts appear homogeneous in their global star forming nature at all $z \gg 1$ while no clear hints exist that the highest redshift objects form a separate population. The intrinsic diversity of this population might, however, point to an evolutionary merger sequence. As the timescales between the different merger stages is expected to be comparatively short, this scenario does not give rise to clear redshift trends. As a result, the state and distribution of the molecular gas in the individual members of the high-z starburst population might, however, be very different as initial literature results suggest (e.g. Carilli et al. 2010; Riechers et al. 2010).

7.4.2. Prospects for ongoing and future research

The aim of this ongoing project is to assemble a comprehensive sample of $z > 4$ starbursts over a contiguous area. Such a sample is needed for a robust observational number density estimate to compare with the predictions of cosmological structure formation models. Large progress has been made during this thesis in consistently selecting these sources and to start the observational follow-up programs needed to confirm their starburst nature. Ob-

servations at these faint levels have been challenging so far even given the comparatively high infrared (IR) luminosities of these sources.

In order to entirely characterize a single source even larger efforts are necessary than those presented in the pilot study of the source in this thesis. As the example of Vd-17871 shows higher spatial resolution is critical to disentangle the individual contributions of the two optical sources that are most likely associated with this astronomical system. This holds true for radio continuum as well as for the far-IR and CO line emission data.

Existing and upcoming instruments such as the Atacama Large Millimeter Array (ALMA), the EVLA but also the next generation bolometer array camera GISMO (Goddard-IRAM Superconducting 2-Millimeter Observer, principal investigator Johannes Staguhn) – currently installed at the IRAM 30 m telescope – will substantially boost our efforts. Detailed observing plans and strategies for these instruments have been worked out already.

More extreme starbursts at $z > 4$ in the COSMOS field Our radio counterpart search to dropout sources revealed seven candidates. Detection of Lyman-α emission in ongoing spectroscopic follow-up observations of five sources revealed three of them to be at $z > 3.9$. The 1.1 mm continuum – tracing the cold dust emission near its peak – of the least redshifted source (AzTEC-5) was previously detected in the combined JCMT/AzTEC (Wilson et al. 2008b) and SMA (Ho et al. 2004) survey of the COSMOS field (Scott et al. 2008; Younger et al. 2007). The other two spectroscopically confirmed sources were detected in subsequent single dish runs at 1.2 mm or 2 mm with the MAMBO-II (Kreysa et al. 1998) respectively GISMO (Staguhn et al. 2008) bolometer arrays installed at the IRAM 30 m telescope. These cold dust continuum detections thus confirmed the massive star forming nature of all sources and thereby the successful selection strategy. The spectroscopically confirmed sources Vd-17871 (presented in this thesis) and AK03 as well as the remaining candidates AK05 and AK06 are shown in Figure 7.2. AK03 is particularly interesting due to its apparent photometric and geometric similarity to Vd-17871. It also shows multiple emission components at rest-frame ultraviolet wavelengths, significant emission at 24 μm and radio continuum emission that appears too high to be powered solely by star formation. This is suggestive that AK03 might also harbor an obscured AGN. With a recent 2 mm detection of 0.8 mJy (3σ) it is comparatively faint at mm wavelengths, yet another similarity to Vd-17871. We have seen, however, that observed far-IR data are critical to constrain the hot dust emission in such sources. AK03 was not detected in the Herschel/PACS observations of the COSMOS field (Lutz et al. 2011). Deeper follow-up observations with the same instrument at 100 μm and 160 μm have been proposed recently (principal investigator P. Capak, co-investigator A. Karim). This explains why only the source with sufficient data coverage (Vd-17871) has been discussed in the case study presented in this thesis.

Clearly, the success rate of our selection strategy does not reach 100 %. Two dropout sources with weak radio continuum counterparts do not belong to the high-z massive starburst population. They are, however, interesting in their own right. The source Vd-9167 is suggested to be a high redshift massive quiescent object probably hosting an AGN (Mobasher et al. in prep.). It was not detected in mm-bolometer observations carried out during this thesis and not at any other observed wavelengths longer than 24 μm. Another source, AK04, is detected at a 3σ level in the LABOCA (Siringo et al. 2009) survey of the central square degree of the COSMOS field (Albrecht et al. in prep.). However, optical spectroscopy revealed that it is a low-z interloper. It therefore seems to be an exceptionally

cold source. The true nature of both sources remains to be clarified.

Other millimeter-bright sources at $z > 4$ are the highest redshift known massive starburst AzTEC-3 (Riechers et al. 2010; Capak et al. 2011) and the brightest source in the JCMT/AzTEC survey of the COSMOS field, AzTEC-1 (Smolčić et al. 2011). AzTEC-3 at $z = 5.3$ could not be found in our automatic counterpart association because of its non-detection in the VLA-COSMOS survey. Deeper radio data such as those that would be obtained in the deep EVLA 3 GHz observations proposed (see above) are hence needed to find much higher redshifted sources based on our approach. AzTEC-1 in turn is firmly detected at radio wavelengths and formally also qualifies as a dropout source. Its nature, however, remains unclear as its largely featureless optical spectrum complicates a robust redshift determination. No CO line emission could be detected in interferometric observations at millimeter wavelengths with the receivers tuned to the purported redshift of $z = 4.64$. Another high-redshift candidate is the source CARMA-1 (Smolčić et al. in prep.) for which high resolution mm-continuum data but currently only photometric evidence for its high redshift nature exists. A blind redshift determination based on multiple CO transitions (following the prescriptions of Weiß et al. 2009a) and using the IRAM 30 m telescope awaits scheduling (principal investigator V. Smolčić, co-investigator A. Karim).

Confronting observations with cosmological models Our combined dropout and radio continuum selection technique provides a well-defined and homogeneous selection function. This is an ideal prerequisite for tests against predictions from semi-analytical cosmological models. These include the evaluation of source properties based on existing models (van Kampen; private communication) as well as robust number count comparison. Also model comparisons with respect to the relative importance of extreme versus average star formation at high redshifts are in reach with a comprehensive, observed $z > 4$ starburst sample in hand. This requires also a representative but clean sample of normal star forming galaxies at these redshifts. Recent advances on the photometric side, in particular deep Subaru z^+ band as well as UltraVISTA near-IR data, in combination with improved V-band dropout criteria (Capak et al. in prep.) will result in an extensive sample with a low level of contamination from $z \sim 1$ interlopers. These data plus the ongoing spectroscopic efforts are also valuable to reveal whether our other extreme starbursts are embedded in proto-cluster structures. Using photometric redshift information first hints exist that the spectroscopically confirmed sources indeed reside in overdensities of dropout sources (Capak et al. in prep.). A precise observational determination of the abundance of such overdense regions provides critical constraints to our understanding of cosmic structure formation.

It has been debated (Baugh et al. 2005) that current models can only reproduce the (sub-)mm source number counts if a top-heavy initial mass function (IMF) for starbursts is assumed with recent theoretical arguments against this scenario (Hayward et al. 2011b). Dwek et al. (2011), however, recently yielded observational support for a top-heavy IMF for an extreme starburst at $z > 4$ and Papadopoulos et al. (2011) provided theoretical arguments for a top-heavy IMF to be generally needed in the densest star forming regions. Coppin et al. (2009) point out that current model predictions (e.g. Baugh et al. 2005) would underscore the number density particularly of the $z > 4$ starbursts by an order of magnitude if all massive quiescent galaxies at $z \gg 2$ had undergone a burst. The current observed number count of the extreme starbursts at $z > 4$, in particular in the COSMOS field, is already in excess of the model predictions.

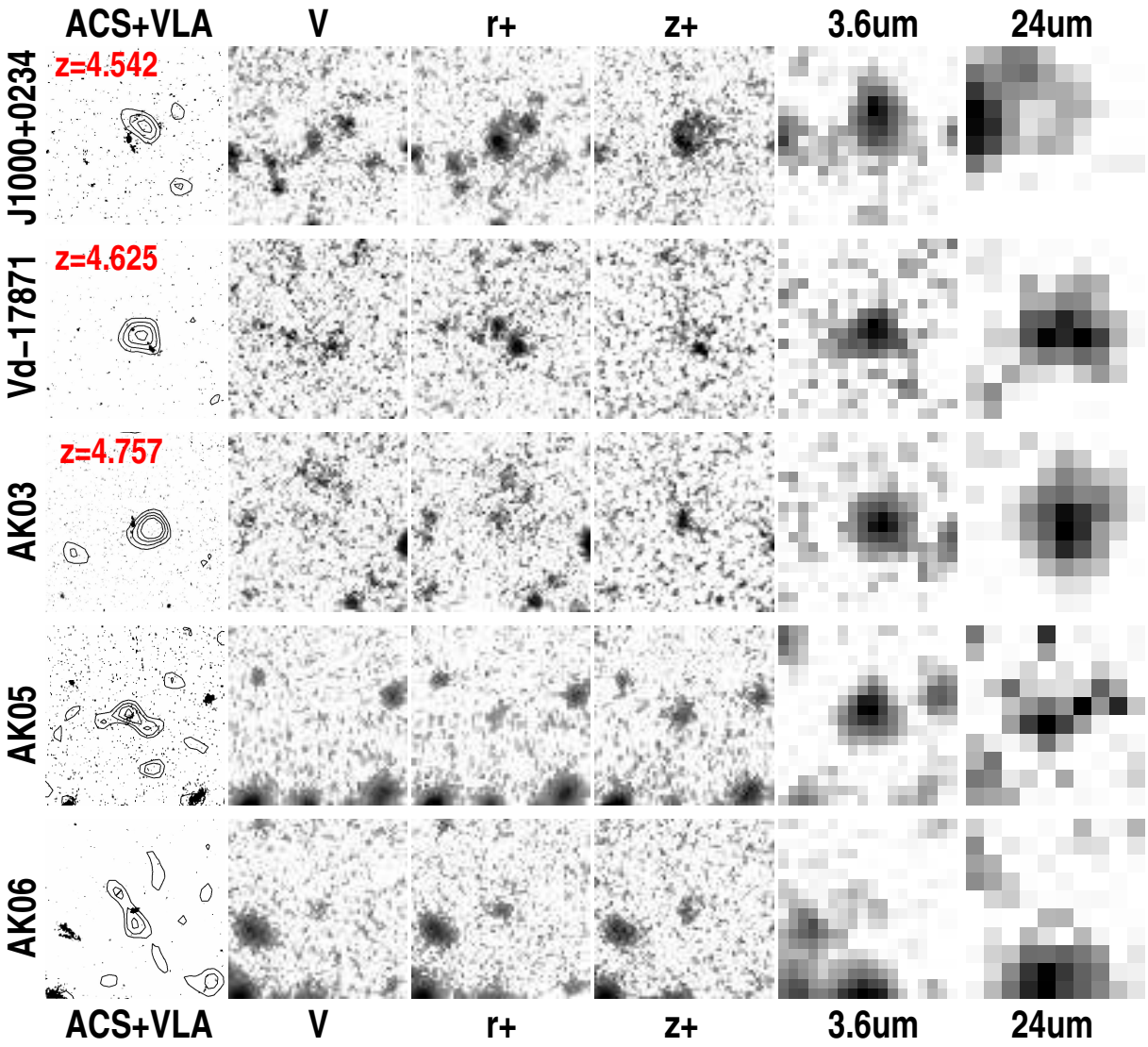

Figure 7.2. – Confirmed, consistently optically selected massive starbursts at $z > 4$ with weak radio continuum counterparts as well as candidates thereof. The postage stamp series shows (from left to right) VLA 1.4 GHz contours (starting at 2σ in steps of 1σ) overlaid on the HST/ACS i-band images centered at the position of the V-band dropout, the Subaru V, r^+ and z^+ bands as well as the Spitzer/IRAC 3.6 μm and MIPS 24 μm channels. All postage stamps are 10" $\times$ 10" in size. Sources with confirmed redshifts from Lyman-α spectroscopy using the DEIMOS spectrograph (Capak et al. in prep.) are labeled with the redshift value (red). The top row shows the first ever discovered $z > 4$ starburst, J1000+0234, (Capak et al. 2008; Schinnerer et al. 2008) which was found only shortly before the start of this thesis project. All other sources (including Vd-17871; see Chapter 6) have been found during this thesis work using a newly written radio continuum counterpart finder (see Section 3.3.3). Follow-up observations using the MAMBO-II (1.2 mm) and GISMO (2 mm) bolometer cameras at the IRAM 30m telescope have been proposed and scheduled during this thesis work. The candidate sources AK05 and AK06 await confirmation from optical spectroscopy as well as from millimeter observations. Not shown is the mm-bright source AzTEC-5 (Younger et al. 2007; Scott et al. 2008) at a Lyman-α based redshift of $z = 3.9$ which has been selected first from (high resolution) sub-mm observations. Formally, it also qualifies as (B-band) dropout with weak radio counterpart so that it forms part of our full sample of $z \gtrsim 4$ massive starbursts.

To summarize, a top-heavy IMF might be theoretically as well as observationally required for extreme starbursts while, independently, models struggle to reproduce the observed number counts of massive starbursts at $z > 4$. Both issues require further efforts from the observers' as well as the modelers' side and demand a robust observed sample of these sources.

Follow-up observations at millimeter and radio wavelengths More observations are needed to comprehensively study massive starbursts at $z > 4$. First of all – based on dust continuum observations at millimeter wavelengths – it needs to be confirmed that the remaining sources show the purported elevated star formation activity. Ideally, high resolution interferometric mm-continuum data would be used to achieve accurate positioning of the cool dust continuum but also morphological information on the dust distribution. These would most vitally be combined with high resolution CO line data that additionally needs to be obtained in order to clarify whether gas emission and dust continuum really arise from the same location or even object since this must not be the case as seen in local ULIRGs (Wilson et al. 2008a). Given the evidence for multiple sources in a system like Vd-17871 such information is essential. Finally we need to constrain the size of the dust emitting, i.e. star forming, region which, due to the overall similarity of our sources to $z \sim 2$ SMGs, is expected to be fairly compact. This allows for estimates of the star formation surface density and will hence shed light on the star formation law in these sources.

Detection of the typically strong (e.g. Stacey et al. 2010) 158 μm [CII] fine-structure line – which is known to be an important coolant for the neutral gas – can be obtained in parallel to high resolution dust continuum observations. Despite hints for a [CII] emission deficit in local IR luminous sources (e.g. Graciá-Carpio et al. 2011), there is evidence that the [CII] line emission is a more reliable tracer for the SFR in their high redshift cousins (e.g. Stacey et al. 2010). Given our consistently selected sample, the [CII] line observations are critical to finally settle whether the ratio of atomic gas to dust emission indeed follows a tight relation for massive but purely star forming sources. In this case, the [CII] line will provide an independent way to estimate the star formation density in our highest redshift targets while its profile compared to the one of the CO line will reveal how closely the star formation activity follows the molecular gas distribution.

Both with respect to angular resolution as well sensitivity all this is already efficiently doable with ALMA in its current state of construction. Less than two hours of on-source integration time would be needed to detect CO line emission in any of our sources while a statistical detection of the [CII] line and its underlying continuum would require less than ten minutes.

Multiple CO transitions, especially at lower J levels are needed in order to shed light on the excitation and state of the molecular gas emission. These data are valuable as (rare) evidence exists at $z > 4$ that massive but purely star forming sources show substantially different gas distribution and excitation properties compared to those extreme starbursts hosting a powerful unobscured QSO (e.g. Riechers et al. 2010). A more diffuse lower-excitation gas component in addition to a higher excited gas phase might be a feature only pure starbursts posses while denser, highly excited gas appears to characterize the unobscured QSOs (e.g. Riechers et al. 2006). Observations of the corresponding emission lines for our sources are feasible with the EVLA but – due to the faint line fluxes expected – still challenging.

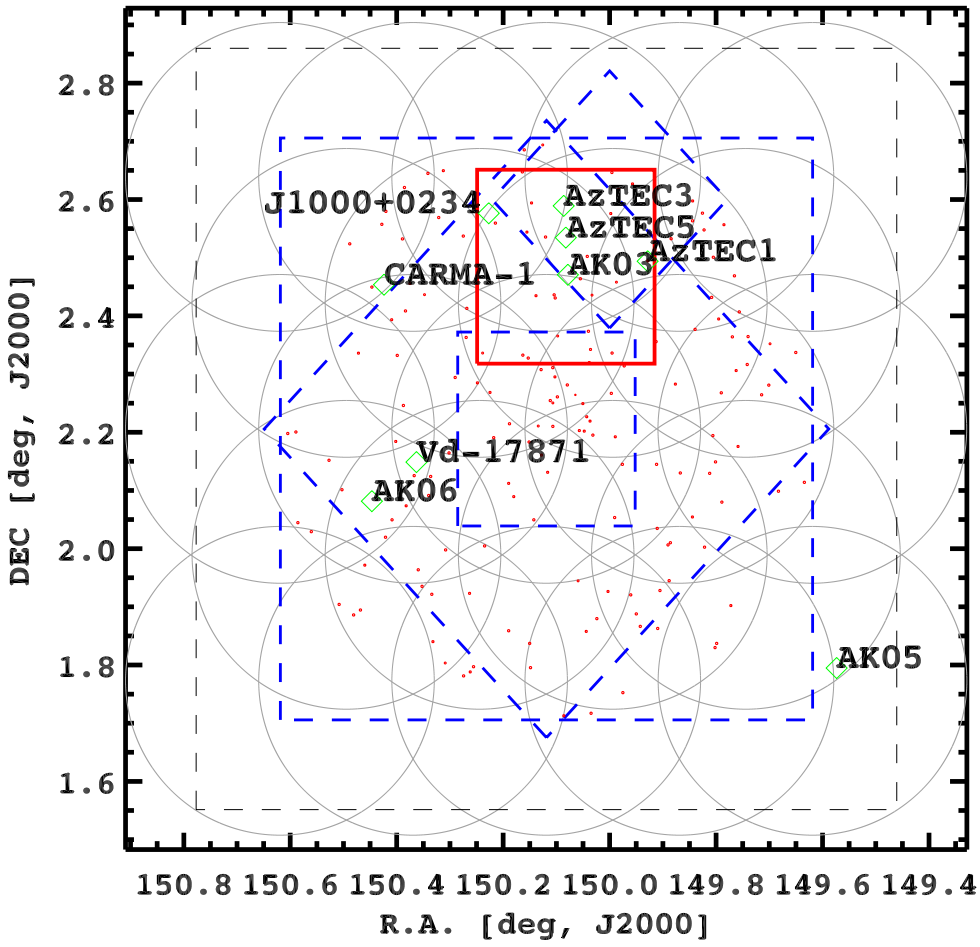

Figure 7.3. – Current and future (sub-)mm surveys in the COSMOS field (east is to the left and north is to the top). Dashed blue lines denote fields with available (sub-)mm data from LABOCA (outer square; Albrecht et al. in prep.), AzTEC/SMA (north western diamond-shaped field; Scott et al. 2008; Younger et al. 2007), AzTEC (large diamond shaped area; Aretxaga et al. 2011) and MAMBO-II (central square; Bertoldi et al. 2007). The proposed region for 2 mm observations (PIs A. Karim & J. Staguhn) with the GISMO bolometer is indicated by solid red lines. LABOCA sources are denoted as red points. Confirmed extreme starbursts at $z > 4$ (Capak et al. 2008; Schinnerer et al. 2008; Riechers et al. 2010; Smolčić et al. 2011 & in prep.; Karim et al. in prep.) as well as candidates are labeled by their names and depicted by green symbols. Among those AzTEC-3 at $z = 5.3$ resides in a proto-cluster region (Capak et al. 2011). Sources found as part of this thesis work are also shown in Figure 7.2. In the background the pointings from the 1.4 GHz VLA COSMOS survey (Schinnerer et al. 2007, 2010) are shown and the outer dashed area marks the low-noise area of the VLA-COSMOS field that has been used for extensive radio stacking experiments as presented in this thesis (see Chapter 4 for the main stacking results as well as Karim et al. 2011a).

Our targets will profit from the higher resolution 3 GHz radio continuum data proposed to be obtained in the COSMOS field using the EVLA (see above). The ~ 0.65" resolution that would be achieved in these observations are sufficient to reveal if the individual radio sources associated with our extreme starbursts consist of multiple blended sources. The source Vd-17871 studied in this thesis is a vital example for the presence of more than one rest-frame ultraviolet sources that are likely part of a single starburst system. At the currently available resolution of 1.5" the associated radio emission is spatially offset from both UV sources and indeed located in between those. Disentangling the actual source geometry at radio wavelengths will yield important insights into the nature of the radio emission, whether it is compact or extended and what fraction each object contributes in case of multiple sources. Globally, the synchrotron spectral index can be studied in detail from multiple frequencies as recently also 610 MHz data became available for the COSMOS field (Klöckner et al. in prep.).[1] This is of special importance for AGN hosts. Depending on the shape of the radio continuum, whether it is steep, flat or gigahertz-peaked the geometry of radio jets and hence the viewing angle towards the AGN can be evaluated as detailed lower redshift studies of, e.g., Martínez-Sansigre et al. (2006a) and Klöckner et al. (2009) show. In some obscured quasars these studies found evidence for AGN obscuration by the cool dust of the host galaxy that is distributed on kpc scales as some of the jets appear to be seen face-on. This suggests that AGN obscuration is not necessarily solely a viewing angle dependent phenomenon as suggested by the unified models (see, e.g., Urry and Padovani 1995, for a review).

A pilot deep field survey in the COSMOS field with the new 2 mm GISMO camera has been proposed recently as shared open and guaranteed time programs (COSMO survey; principal investigators A. Karim & J. Staguhn; see Figure 7.3). It covers an area of $20' \times 20'$ to a 1σ depth of 0.35 mJy and may reach 0.2 mJy within 42 (60) hours of net (total) integration time depending on the final instrument sensitivity and performance. The shallower depth is already sufficient to match those of the existing (sub-)mm surveys in the COSMOS field of (1.2-1.3) mJy (Bertoldi et al. 2007; Scott et al. 2008; Aretxaga et al. 2011) at ~ 1 mm and ~ 4 mJy at 870 μm (Albrecht et al. in prep.). Since the proposed survey area is fully covered by all other facilities hence multiple (sub-)mm colors for all known sources will be available. Together with the extensive ancillary data at other wavelengths and ongoing optical spectroscopic efforts this allows one to break the prominent degeneracy between cool dust temperature and redshift current surveys suffer from (e.g. Greve et al. 2004).

As recent initial deep observations with GISMO in the Hubble Deep Field-North (HDF-N; Staguhn et al. in prep.) suggest, substantially more sources at $z > 4$ could be revealed by the COSMOS 2 mm observations, bearing the potential to even double the current number counts of five sources inside the field proposed. This also demonstrates that the rest-frame far-IR properties of the $z > 4$ sources are not well reflected by typical IR-SED models (e.g. those from Chary and Elbaz 2001, which have been used to estimate the expected 2 mm number counts). The additional 2 mm HDF-N sources are, however, mostly unidentified at other wavelengths so that currently their true nature remains unknown.

Finally, the GISMO map will allow for extensive image stacking experiments using the available COSMOS ancillary data.

[1] Note that the 610 MHz data will be valuable already in the ongoing analysis. Also 327 MHz data are available in the COSMOS field (Smolčić et al. in prep.) but they are too shallow to be conclusive for our $z > 4$ sources.

Appendix

A. Statistical background

Here essential background information on (noise weighted) statistical estimators used in an image stacking experiment (see Chapter 3) and calculation of their uncertainties are presented. For the sample selection process prior to a stacking experiment statistical tools are also needed to assess how representative a flux density limited galaxy sample is with respect to a given galaxy property. The techniques presented here have been implemented in the IDL-package StackAttack as well as in dedicated sample selection routines. Some of these techniques and all software routines themselves have been newly developed during this thesis work.

In the following a set of N pixels will always be written as X_N, regardless if the constituents x_i ($i = 1, \ldots, N$) are noise pixels or a sample of peak flux densities. We will specify at any stage, if we are referring to background noise, in which case we will use the upper case indication 'bg'. Major parts of this Appendix are part of the publication

A. Karim, E. Schinnerer, A. Martínez-Sansigre, M. T. Sargent, A. van der Wel, H.-W. Rix, O. Ilbert, V. Smolčić, C. Carilli, M. Pannella, A. M. Koekemoer, E. F. Bell & M. Salvato, 2011, ApJ, 730, 61, *The star formation history of mass-selected galaxies in the COSMOS field*

A.1. Noise weighted estimators

Due to the often non-uniform noise distribution in a survey map used for a stacking experiment, the input samples used for stacking are ill-defined to some extent. Solely discarding the typically high-noise edge regions does not remedy the fact, that there is significant variation of the rms background noise in the cutout postage stamps originating from a broad spatial distribution across the field. Our aim is to find the best estimator for the representative value of the underlying population. Therefore the sample should consist of a random and independent set of sources drawn from this population under equal circumstances. To approach the last condition, that is not achievable in observational reality, we have to compare the outcome of the stacked sample to that of a weighted sample, in which those stamps gain more influence, that lie in low noise regions.

Regarding the mean-stacking technique it is statistically well known, that appropriate weights are found in the reciprocal variance of each particular stamp's noise pixel sample where the variance of the ith stamp is defined as $\mathrm{Var}_i \equiv \mathrm{Var}\left(X_{N^{\mathrm{bg}}}^{\mathrm{bg},i}\right) = \sigma_{\mathrm{bg}}^2\left(X_{N^{\mathrm{bg}}}^{\mathrm{bg},i}\right)$. As explained above $X_{N^{\mathrm{bg}}}^{\mathrm{bg},i} \equiv \left\{x_{i_1}^{\mathrm{bg}}, \ldots, x_{i_N}^{\mathrm{bg}}\right\}$.
The noise-weighted mean of the sample X_N of peak fluxes can thus be considered the mean of the weighted sample $\widetilde{X}_N$, where the constituents $\widetilde{x}_i$ of $\widetilde{X}_N$ are defined as

$$\widetilde{x}_i = \widetilde{w}_i x_i \equiv N \frac{\mathrm{Var}_i^{-1}}{\sum_i \mathrm{Var}_i^{-1}} x_i \qquad \text{where} \quad x_i \in X_N. \tag{A.1}$$

With the definitions $W_i = \mathrm{Var}_i^{-1}$ and $w_i = W_i / \sum_i W_i$ it is easily shown, that the mean of the $\widetilde{x}_i$ defined in (A.1) indeed equals the noise-weighted mean of the x_i:

$$\langle \widetilde{X} \rangle = \frac{1}{N} \sum_i \widetilde{x}_i = \frac{1}{N} \sum_i \widetilde{w}_i x_i = \sum_i w_i x_i = \frac{\sum_i W_i x_i}{\sum_i W_i}. \tag{A.2}$$

The above discussion leads to the suggestion, that in the presence of varying rms-noise in a given sample, the sample $\widetilde{X}_N$ is the appropriate one to consider not only with respect to the mean value of the sample. It seems reasonable, that also its median is the best estimator for the median of the underlying population, because both computed quantities, the median and the mean, are then referring to the same sample. We will refer to this choice of an estimator in the following as a noise-weighted median.

Little information on weighted medians can be found in the literature and our choice might therefore be rather innovative and, perhaps, cannot be regarded as common statistical practice. An alternative and possibly more common method (D. Hogg, private communication) for computing a weighted median is to sort the sample constituents by increasing value and apply the same sorting scheme to the normalized weights. A normal median, by definition, would be simply the central value in the sorted list, leaving the same number of sample constituents on either side. The weights can now be regarded as distances along a path of unit length due to the normalization. Therefore, adding up the sorted list of weights until the sum reaches the value 0.5 yields an alternative weighted median at the position in the sorted list of sample values corresponding to the position of the last weight added. We implemented both methods and found the results to agree within the uncertainty ranges. For this reason and due to better reliability with respect to numerical stability StackAttack routinely uses the scheme presented first in this Section.

A.2. Bootstrapping

In Sections 3.3.2 and 4.3.1 we justified that neither the observed nor the intrinsic distribution of peak fluxes are expected to be gaussian. This needs to be taken into account no matter if we are looking for an appropriate uncertainty range to the median or mean estimator for a given sample. In order to obtain a 68 % confidence interval not relying on normality of the underlying parent distribution we therefore chose a bootstrapping technique for the statistical parameter of choice. This Section follows closely the descriptions in Lunneborg (2000).[1]

In each case (median or mean statistics) we obtain the limits of the confidence interval by a bootstrapped Student's t-distribution. This technique is called studentizing. A $(1-\alpha)$ confidence interval for a parameter $\overline{X}$ in traditional statistics is given by

$$CI_{\alpha/2} = \overline{X} \pm t_{\alpha/2} \frac{s_{\overline{X}}}{\sqrt{N}}, \qquad s_{\overline{X}}: \text{ standard deviation of } \overline{X}. \tag{A.3}$$

Here $t_{\alpha/2}$ denotes the $\alpha/2$ percentile of the classical t-distribution which is equal to the $(1-\alpha/2)$ percentile due to the symmetry of Student's distribution. Bootstrapping a t-

[1] For a comprehensive summary of the (for our purposes) essential parts of Lunneborg (2000) we refer the reader to http://www.uvm.edu/~dhowell/StatPages/Resampling/Resampling.html.

distribution means to circumvent the assumption of a normally distributed population by deriving the quantity

$$t_i^* = \frac{\overline{X}_i^* - \overline{X}}{s^*_{\overline{X}_i^*}/\sqrt{N}} \tag{A.4}$$

for $i = 1, \ldots, N_{\mathrm{bootstrap}}$ samples drawn from the original sample of peak fluxes with replacement. In case of $\overline{X} \equiv \langle X \rangle$ being the sample mean one thus has to compute the sample mean $\langle X \rangle$ as well as all means of the bootstrapped samples $\langle X^* \rangle_i$ including standard deviations $s^*_{\langle X^* \rangle_i}$. The resulting distribution of $N_{\mathrm{bootstrap}}$ t^*-values is then used to compute the upper and lower confidence limits by taking its $\alpha/2$ and $(1-\alpha/2)$ percentiles:

$$CI^{1-\alpha}_{\mathrm{up}} = \overline{X} + t^*_{\alpha/2}\frac{s_{\overline{X}}}{\sqrt{N}} \tag{A.5}$$

$$CI^{1-\alpha}_{\mathrm{low}} = \overline{X} - t^*_{1-\alpha/2}\frac{s_{\overline{X}}}{\sqrt{N}}, \tag{A.6}$$

where in general we chose $1 - \alpha = 0.68$ obtaining thus a 68 % confidence interval. Here $s_{\overline{X}} \equiv s_{\langle X \rangle}$ still is just the standard deviation of the original sample. In case of $\overline{X} \equiv \mathrm{Med}(X)$ denoting the sample median as the parameter of choice we have to face the problem that the denominator of (A.4) does not provide us with an estimator of the standard error of the median. In order to estimate this latter quantity we need to access the empirical standard deviation of a sample of medians being representative for the median of the current bootstrapped sample. Starting from this sample we thus generate a number of new bootstrapped samples hence performing a bootstrapping within the bootstrapping procedure[2]. The standard deviation $s^*_{Med(X_i^{**})}$ of these subsamples' medians is then used as an estimator for the standard error of the single outer bootstrapped median as given by the denominator of Eq. (A.4). In order to use Eq. (A.5, A.6) we furthermore need the standard error of the original sample's median. This is estimated by computing the median of each outer bootstrapped sample and taking the standard deviation $s_{Med(X^*)}$ of this sample of medians as the standard error.

A.3. A statistical estimator for the stellar mass representativeness of a flux density-limited sample

In principle one could roughly estimate stellar mass completeness limits by visual inspection of Figure 4.1. Given a flux density limit (i.e. $F_{3.6\ \mu\mathrm{m}} \approx 5$ μJy for all and $F_{3.6\ \mu\mathrm{m}} \approx 1$ μJy for star forming (SF) galaxies; see Section 4.2.6) below which no objects of a given spectral type (Section 4.2.4) should be considered one would select by eye a stellar mass limit upward from where there are no objects below the flux density threshold. As pointed out in Section 4.2.6 it is, however, necessary to analytically derive these stellar mass limits in order to ensure that – within a narrow mass-range just at any limiting mass – we are dealing with a distribution of flux densities that can be considered representative for the one of the underlying population. A statistical estimator is needed for obtaining the actual level of representativeness we achieve at a given stellar mass.

[2] The number of outer bootstrapped samples is typically chosen to be an order of magnitude larger compared to the one of the inner bootstrapping.

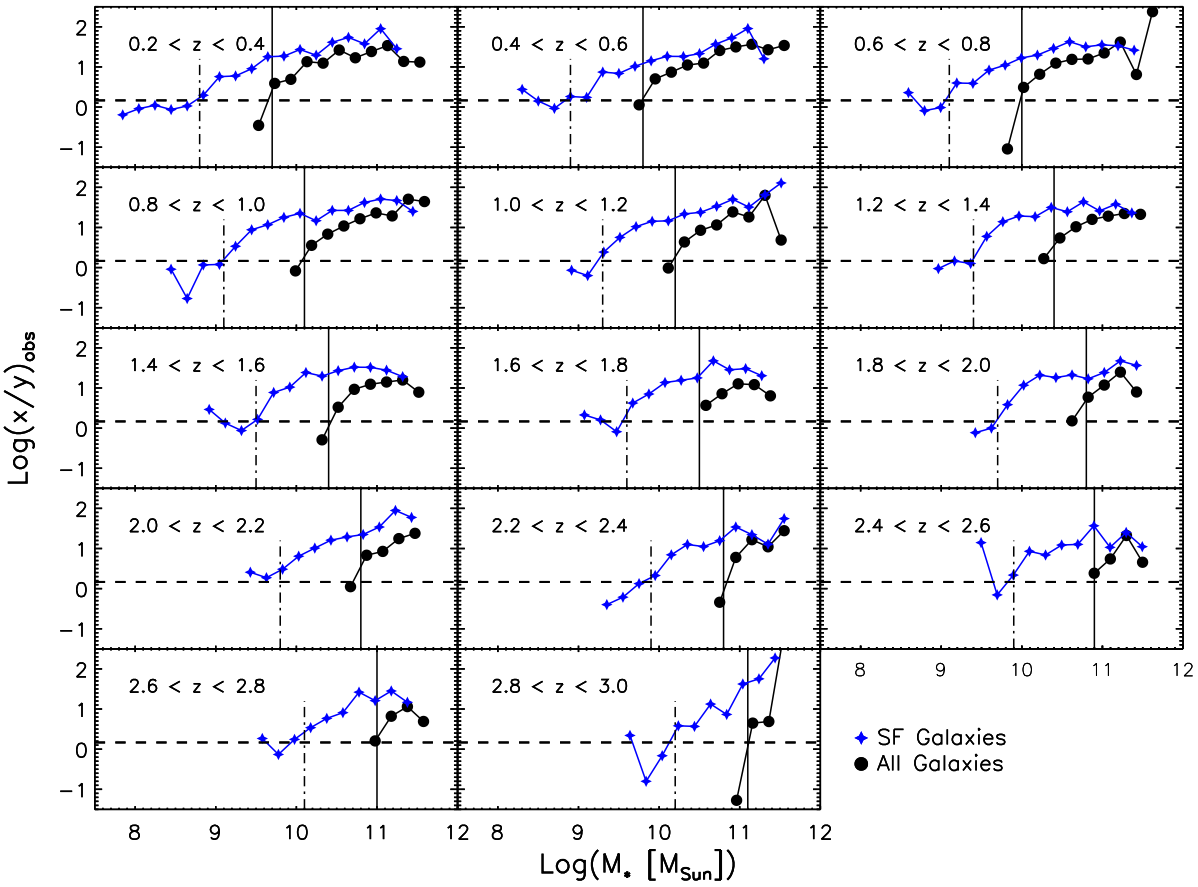

Figure A.1. – Analytic evaluation of the statistical 95 % statistical completeness in different redshift bins, based on a flux density threshold of $F_{3.6\ \mu\mathrm{m}} = 5\ \mu$Jy ($m_{\mathrm{AB}}(3.6\ \mu\mathrm{m}) = 22.15$) corresponding to the 90 % level of intrinsic catalog completeness for all galaxies (black circles). For star forming galaxies (blue stars) the evaluation is based on a flux density threshold of $F_{3.6\ \mu\mathrm{m}} = 1\ \mu$Jy ($m_{\mathrm{AB}}(3.6\ \mu\mathrm{m}) = 23.9$, i.e. the magnitude limit of the catalog). For a detailed discussion of the meaning of statistical completeness, the choice of flux density thresholds and the implications on sample representativeness with respect to star formation see Section 4.2.6. The photometric redshift slices depicted in the individual panels are the same as in Figure 4.1. The quantity $(x/y)_{\mathrm{obs}}$ measures how well the distribution of flux densities at the faint end within a given sample in a narrow mass bin ($\Delta \log(M_*) = 0.2$) follows the decreasing wing of a Gaussian distribution. Where it crosses the dashed horizontal line the Gaussian is cut at the 0.95 percentile and the anticipated statistical completeness limit (vertical lines) is reached. The method is described in detail in Appendix A.3. Lines connecting the data points are meant to guide the eye.

Our aim is to compare the properties of the exponential decline of the *observed* distribution of $3.6\ \mu$m flux densities – i.e. the distribution of low values of flux density towards the flux density limit in our selection band – within a narrow bin in logarithmic stellar mass to the analogously exponentially declining Gaussian distribution. As explained in the following it is sufficient for this comparison to derive the relative distance between *(a)* the 0.95 percentile of the observed distribution of flux densities to the flux density limit and *(a)* the 0.9 to the 0.95 percentile of the same observed distribution. The choice of the two percentiles mentioned is hereby entirely arbitrary.

First we have to derive the corresponding ratio of distances for an arbitrary normal distribution that is cut at a given percentile. This percentile sets the representativeness we want to achieve, i.e. 0.95 in our case. Since the width of and hence the lengthscale defined by a Gaussian is determined by a single parameter σ any ratio of distances between given percentiles is independent of the actual value of σ or the normalization. Given for instance a quantity x defined as the distance between the 0.9025 ($= 0.95 \times 0.95$) percentile of a given normal distribution and its 0.95 percentile as well as a quantity y defined as the distance from the 0.855 ($= 0.95 \times 0.9$) to the 0.9025 percentile of the same distribution, their ratio $(x/y)_{\mathrm{Gauss}}$ yields a value of 1.467 that is universal, i.e. independent of the actually chosen normal distribution. It was obtained by taking advantage of the cumulative distribution function that connects a percentile to the corresponding actual value x_σ defined by the specific Gaussian of width σ centered at μ via the error function (erf):

$$\Phi_{\mu,\sigma}(x_\sigma) = \frac{1}{2}\left[1 + \mathrm{erf}\left(\frac{x_\sigma - \mu}{\sigma\sqrt{2}}\right)\right]. \tag{A.7}$$

Differences in percentiles $\Delta\Phi_{\mu,\sigma} = \Phi_{\mu,\sigma}(x_{\sigma,j}) - \Phi_{\mu,\sigma}(x_{\sigma,i})$ thus translate into physical distances $\Delta x_\sigma = x_{\sigma,j} - x_{\sigma,i}$ solely defined by the scale σ.

Assuming that our data in narrow bins of stellar mass and redshift follows a normal distribution the distance from the 0.95 percentile of the observed distribution of 3.6 μm flux densities to the flux limit of the sample yields a value x_{obs} in units of flux density. Accordingly the distance between the 0.9 and the 0.95 percentiles of the observed distribution defines a value y_{obs} and the dimensionless ratio $(x/y)_{\mathrm{obs}} \equiv x_{\mathrm{obs}}/y_{\mathrm{obs}}$ can be compared to the aforementioned value of $(x/y)_{\mathrm{Gauss}}$. Given the case that the flux density limit is located far in the tail of the observed distribution, $(x/y)_{\mathrm{obs}}$ will exceed $(x/y)_{\mathrm{Gauss}}$ and the observed distribution is statistically representative of the underlying population of objects. As the flux density limit approaches the peak of the observed distribution the observed ratio becomes lower. As soon as it overlaps with the 0.95 percentile of the (unknown) distribution of the underlying population the limiting case of 95 % statistical completeness – and hence the desired lower level of representativeness – is reached so that $(x/y)_{\mathrm{obs}} = (x/y)_{\mathrm{Gauss}}$.

For our sample this effect is shown in Figure A.1 where $(x/y)_{\mathrm{Gauss}}$ is indicated as a dashed horizontal line for individual ranges in photometric redshift. The finally chosen stellar mass representativeness limits are denoted by vertical lines. The data points result from an implementation of the method described in this section that additionally takes into account the detection completeness levels of the catalog as a function of 3.6 μm flux density. Here we therefore obtain the mentioned percentiles using flux densities weighted by the corresponding inverse catalog detection completeness.

It is worth noting that the Gaussian distribution is just one possible parameterization and not a necessary requirement for the method described here. Indeed, the underlying distribution of flux densities is not even required to be symmetric. Our method simply ensures that the observed distribution is smoothly, approximately exponentially declining to low levels of flux density, as one may realistically expect from random processes such as photon noise and confusion. It is simply a practical, quantitative improvement over the alternative method of visual inspection as the latter is, essentially, assuming an unphysical step-function rather than a continuos distribution function.

B. Calculus and formulae

This Appendix summarizes essential formulae used in this thesis and provides background information on fundamental calibrations and calculations.

B.1. Measures of cosmological distances

The need for different cosmological distance measures in an expanding universe arises due to its non-Euclidean nature of space-time on large scales. An excellent summary on cosmological distance measures has been presented by Hogg (1999) to which we refer the reader. Textbook references therein provide the fundaments of all calculations and should be consulted for a thorough introduction into our mathematical understanding of the universe within the physical framework of general relativity. Here, we summarize the most important aspects for this thesis from Hogg (1999) and assume that the universe is homogeneous and isotropic on sufficiently large scales.

The expansion of the universe is conventionally described by a cosmic scale factor $a(t)$. For an individual cosmological object, such as a galaxy, the only direct observable related to expansion[1] is its redshift which is defined by the fractional frequency shift of emitted (e) to observed (o) light[2]:

$$z = \frac{\nu_e - \nu_o}{\nu_o} \iff 1 + z = \frac{\nu_e}{\nu_o} \tag{B.1}$$

which can be re-written in terms of wavelength by using $\nu_{o/e} = c/\lambda_{o/e}$ where c denotes the speed of light. We explicitly assume a cosmological nature for all redshifts reported in this thesis. In this case, redshift and scale factor are related as

$$a(t) = \frac{1}{1+z} \quad \Longrightarrow \quad da(t) = -(1+z)^{-2} dz = -a^2(t) dz. \tag{B.2}$$

We introduce the Hubble function (often called the Hubble parameter) as the logarithmic time derivative of the cosmic scale factor $a(t)$:

$$H(a) = \frac{\dot{a}(t)}{a(t)}. \tag{B.3}$$

The Hubble function is fundamental in that it relates expansion velocity of the universe and its 'size' at a given cosmic epoch.

A cosmology is a parameterization describing the geometry of the universe. The dimensionless matter and vacuum density parameters are given as

[1] For nearby objects redshift can be interpreted as recessional velocity in the sense of a Doppler shift. For this to hold the object's observed redshift must not exceed a value of 10 %.

[2] In the following we will conveniently omit subscripts for quantities in the observed frame and indicated the rest-frame of the light emission with a subscript 'rf' unless indicated otherwise.

$$\Omega_{\mathrm{M}} = \frac{8\pi G\rho_0}{3H_0^2}, \qquad \Omega_\Lambda = \frac{\Lambda c^2}{3H_0^2}, \tag{B.4}$$

where G is the gravitational constant, ρ_0 is the total (dark and baryonic) matter density at the present epoch and Λ is the cosmological constant. We also use the Hubble constant at the present epoch H_0 which, for small redshifts, relates recessional velocity and distance of cosmological objects in an expanding universe. Another dimensionless parameter, $\Omega_k = 1 - \Omega_{\mathrm{M}} - \Omega_\Lambda$, describes the curvature. Here we assume a flat universe, $\Omega_k = 0$, as it is observationally supported (e.g. Komatsu et al. 2009).

In this parameterization and a matter-dominated universe the redshift-dependent Hubble function can be conveniently re-written as

$$H(z) = H_0 E(z) = H_0\sqrt{\Omega_{\mathrm{M}}(1+z)^3 + \Omega_k(1+z)^2 + \Omega_\Lambda} = H_0\sqrt{\Omega_{\mathrm{M}}(1+z)^3 + \Omega_\Lambda} \tag{B.5}$$

which defines the function $E(z)$ where we explicitly use the assumption of a flat universe in the last step. The function $E(z)$ is of central importance for all cosmological distance calculations as we will see in the following

We are seeking for a convenient infinitesimal distance measure in which two nearby objects that partake in the general expansion (the so-called 'Hubble-flow') would have the same value of separation regardless of cosmic epoch. We might call this a comoving distance element. It differs from a proper distance (the separation of the objects in the frame they would be observed at the same time)[3] in that it accounts for the change in scale factors. It can be found by combining Eq. (B.3) and (B.5) as well as using Eq. (B.2):

$$\frac{\dot{a}(t)}{a(t)} = \frac{1}{a(t)}\frac{da(t)}{dz}\frac{dz}{dt} = -a(t)\frac{dz}{dt} = H_0 E(z) \iff \frac{-c\,dt}{a(t)} = \frac{c\,dz}{H_0 E(z)}, \tag{B.6}$$

where the different signs on both sides of the equality reflect the different time 'directions' of redshift and cosmic time t. For a photon whose speed c is constant in all inertial frames $c\,dt$ defines a proper distance corresponding to the infinitesimal redshift interval the photon would have crossed. The last step of Eq. (B.6) therefore defines a comoving distance as it is divided by the scale factor at cosmic time t. Introducing the Hubble distance $D_H = c/H_0$, one obtains the total comoving distance to redshift z along the line of sight by integration:

$$D_C = D_H \int_0^z \frac{dz'}{E(z')}. \tag{B.7}$$

An expression for the lookback time t_{lb} as well as for the cosmic age t_{age} can be found in the same way. The lookback time is the difference between the current cosmic age and the one reported by a distant light emitter at the moment of emission. Therefore we need to solve Eq. (B.6) for dt using Eq. (B.2) in order to obtain the lookback time element and compute the lookback time to redshift z again via integration:

$$t_{\mathrm{lb}} = t_H \int_0^z \frac{dz'}{(1+z')E(z')}, \tag{B.8}$$

[3] In other words, a proper distance from us to another object is the distance of the other object at the time measured in its rest-frame when it emitted the light

where we introduced the Hubble time $t_H = 1/H_0$. The cosmic age at redshift z is obtained by simply integrating from z to infinity.

As Hogg (1999) points out, one can regard the line-of-sight comoving distance D_C – which equals the transverse comoving distance D_M for a flat cosmology – as the fundamental cosmological distance indicator as it relates to all other distances frequently used. The redshift integral over $1/E(z)$ will therefore be frequently needed for measuring cosmological distances and is solved numerically. Clearly, $E(z)$ depends on the cosmology chosen. A reader assuming a flat cosmology but different values than $\Omega_\Lambda = 0.7$ and $H_0 = 70$ (km/s)/Mpc for the vacuum energy density and the Hubble constant, respectively, will compute different distance values and hence also different results for all quantities that depend on the cosmological distances (e.g. luminosities and physical scales) compared to this work.

Throughout this thesis we make frequent use of two common cosmological distance indicators, the angular diameter distance D_A and the luminosity distance D_L. The angular diameter distance at redshift z measures the ratio of the physical (transverse) extent to its observed angular size (in radians) and is related to the comoving distance as

$$D_\mathrm{A} = \frac{d_0}{\theta} = \frac{D_M}{1+z}. \tag{B.9}$$

Intuitively one would assume that D_A should monotonically increase with redshift such that objects at higher redshift would always appear smaller compared to those at lower redshift of the same intrinsic size. This is, however, not the case as D_A reaches a maximum around $z = 1.6$ for the cosmology assumed in this work and decreases towards higher z. Objects hence appear larger beyond this redshift threshold compared to their lower-z siblings. Apparently, in a flat universe the angular diameter distance measures the proper distance from us to an object at the cosmic epoch when the light was emitted.

The luminosity distance is the distance measure for which we can define a standard relation between bolometric luminosity and flux of a spherically emitting source:

$$D_\mathrm{L} = \sqrt{\frac{L}{4\pi F}} = (1+z)^2 D_\mathrm{A} = (1+z) D_M. \tag{B.10}$$

The relation between luminosity distance and angular diameter distance can be derived from the cosmic microwave background. Its emission is close to that of an ideal black body which is known not to change its spectral shape with redshift but only its temperature as $T_\mathrm{rf} = (1+z)T$. According to the Stefan-Boltzmann law the energy per unit surface area emitted by a blackbody is furthermore proportional to the fourth power of its temperature, hence leading to a factor $(1+z)^4$. Accounting for the full emitting spherical surface the total power the cosmic background emitted at a given redshift equals its luminosity which is related to the observed cosmic microwave background flux via the square of the luminosity distance as given in Eq. (B.10). Relating source and angular size by definition only a factor D_A^2 survives together with the factor $(1+z)^4$ mentioned before.

Having found a comoving distance element along the line of sight (Eq. (B.6)) one obtains a comoving volume element by multiplication with a comoving transverse area element. Since the angular diameter distance measures a proper distance an observed infinitesimal solid angle $d\Omega$ is converted into a proper area element by multiplication with D_A^2. Divided

by the square of the scale factor (or multiplied by $(1+z)^2$) this proper area element is converted into a comoving area element so that the comoving volume element reads

$$dV_C = D_H \frac{(1+z)^2 D_\mathrm{A}^2}{E(z)} d\Omega dz. \tag{B.11}$$

Integrating dV_C between redshift slices over a given angular survey area yields the corresponding comoving volume. A given comoving volume will always contain the same number of non-evolving objects partaking in the Hubble flow, regardless of cosmic epoch. Therefore global quantities normalized to unit comoving volume that are observed to evolve are intrinsically evolving, i.e. the underlying galaxy population evolves with respect to this global quantity. A prominent example thoroughly studied in this thesis is the cosmic star formation rate density (see Chapter 5).

B.2. K-corrections at radio continuum and millimeter wavelengths

In Eq. (B.10) we introduced the luminosity distance D_L to relate luminosity and flux as bolometric quantities. It is, however, much more common in observational reality to deal with monochromatic flux densities F_ν (defined per unit frequency) and corresponding differential luminosities L_ν. This is also the case for radio continuum emission frequently used in this thesis. A complication arises since emitted and observed bands are not the same for a cosmologically redshifted source. Intrinsic luminosity and observed flux density are therefore determined at different frequencies and, generally, also through different passbands. One often wishes, however, to determine the source's intrinsic monochromatic luminosity at the observed frequency, e.g., in order to apply standard conversions calibrated in the local universe in a given band. Postulating that energy is conserved one finds

$$F_\nu \, d\nu = \frac{L_{\nu_\mathrm{rf}}}{4\pi D_\mathrm{L}^2} d\nu_\mathrm{rf} \tag{B.12}$$

$$F_\nu = \frac{(1+z) L_{\nu_\mathrm{rf}}}{4\pi D_\mathrm{L}^2} = (1+z) \frac{L_{\nu_\mathrm{rf}}}{L_\nu} \frac{L_\nu}{4\pi D_\mathrm{L}^2}, \tag{B.13}$$

where the rest-frame frequency is given by $\nu_\mathrm{rf} = (1+z)\nu$ and in the last step we made the connection of intrinsic luminosity and observed flux density determined in the same (observed) passband. If the spectrum of the emitter is known and reasonably simple Eq. (B.13) can be determined analytically. At radio continuum frequencies, e.g. at observed 1.4 GHz, where the spectral shape is well described by a power-law and where no (broad) emission or absorption features occur this is the case. As introduced in Section 4.3.2, $L_{\nu_\mathrm{rf}}/L_\nu = (1+z)^{\alpha_\mathrm{rc}}$, the intrinsic 1.4 GHz luminosity can hence be determined from the observed 1.4 GHz flux density using a K-correction that depends on the radio spectral index α_rc (here $\alpha_\mathrm{rc} = -0.8$, e.g. Condon 1992). In convenient units this reads

$$L_{1.4\ \mathrm{GHz}}\ [\mathrm{W/Hz}] = 1.12 \times 10^{14}\, F_{1.4\ \mathrm{GHz}}\ [\mu\mathrm{Jy}] \big(D_\mathrm{L}\ [\mathrm{Mpc}]\big)^2 \left(1+z\right)^{-(1+\alpha_\mathrm{rc})}. \tag{B.14}$$

In general, the situation is more complicated. For a more profound description of this so-called K-correction in the most general case we refer the reader to Hogg et al. (2002). References therein provide the essential background information and original definitions

as well as applications of the K-correction.

Another interesting phenomenon in the context of K-corrections occurs at (sub-)mm wavelengths. As explained below (Section B.5), at sufficiently long rest-frame wavelengths $\gg 100$ μm the thermal dust continuum emission of star forming galaxies also follows a power-law described by a spectral index of $\alpha_{\rm SMM} = 2 + \beta$ with $\beta \gtrsim 1$. At high redshift $z \gg 2$, i.e. well beyond its peak, the angular diameter distance decreases approximately with $(1+z)^{-1}$ for the cosmology assumed here. The luminosity distance therefore increases approximately with $(1 + z)$ according to Eq. (B.10). Assuming a spectral shape and hence differential luminosity for a distant galaxy of a given bolometric luminosity the observed flux is therefore expected to increase with redshift as $(1 + z)^{1+\beta}$ instead of decreasing. This effect is often referred to as negative K-correction (e.g. Blain et al. 2002) and can be fully exploited at very high redshifts (even $z \sim 10$ or more) only if observed at sufficiently long wavelengths ($\sim$ 2 mm). Note that the negative K-correction also affects ^{12}CO rotational emission lines observed at (sub-)mm wavelengths as outlined below (see Section B.4).

B.3. Visualizing luminosity and mass functions in the Schechter representation

Even though appearing mathematically trivial the visual representation of luminosity and mass functions is sometimes a source of confusion. Since in this thesis we are dealing only with mass functions in the Schechter representation it is useful to illustrate the essential steps from the mathematical definition to the actual plot based on this specific function. The transformation discussed below would, however, likewise affect any other parameterization of luminosity functions. To some extent this Appendix covers a broader range of problems as similar transformations would need to be performed if the concern was with other measures of density distributions such as spectral energy distributions of galaxies.

A luminosity function of any form is often represented by a parametric model to reproduce the observed number density of a given galaxy population per unit comoving volume and luminosity interval. This luminosity typically is monochromatic. As a most trivial example for extended application of the luminosity function concept, number densities with respect to galaxy properties that are linearly related to a monochromatic luminosity can hence be represented by the same mathematical function.

In reality, like in this work, a not directly observable quantity like stellar mass might not be linearly derived from a monochromatic luminosity but a number density distribution with respect to this quantity might still follow a parameterization that is well established for luminosity functions. This is the case for the galaxy populations studied in this thesis where (see Chapter 5) the mass functions are well parametrized by a power law with an exponential cutoff at a characteristic mass M^* as introduced by Schechter (1976) of the form of

$$\Phi(M_*)dM_* = \Phi^* \left(M_*/M^*\right)^{\alpha} \times \exp\left(-M_*/M^*\right) d(M_*/M^*). \tag{B.15}$$

The parameter M_* denotes the stellar mass in units of solar mass. However, it is convenient to plot Φ per logarithmic stellar mass (instead of stellar mass) interval as a function of logarithmic stellar mass. Introducing the quantity $\mathcal{M}_* := \log(M_*)$ and the Schechter

parameter $\mathcal{M}^* := \log(M^*)$, i.e. the logarithm of the cutoff (characteristic) stellar mass (in units of $M_\odot$) Eq. (B.15) transforms into

$$\Phi(\mathcal{M}_*)d\mathcal{M}_* = \ln(10)\,\Phi^*\left(10^{(\mathcal{M}_*-\mathcal{M}^*)\times(1+\alpha)}\right) \times \exp\left(10^{(\mathcal{M}_*-\mathcal{M}^*)}\right) d\mathcal{M}_*, \tag{B.16}$$

since $d(M_*/M^*) = \left(10^{(\mathcal{M}_*-\mathcal{M}^*)} \times \ln(10)\right) d\mathcal{M}_*$. The most prominent effect of this transformation therefore is that the power-law slope in logarithmic representation appears different in the plot from what would be expected based on its numerical value: $\alpha \rightarrow (1+\alpha)$. Note that the same effect occurs if a luminosity function is to be represented per unit magnitude interval since absolute magnitude by definition is logarithmically related to luminosity.

B.4. ^{12}CO line emission and its relation to global molecular gas properties in galaxies

In this thesis we derive molecular gas properties of a distant starburst based on its millimeter ^{12}CO line emission. Here we want to introduce the fundamental physics and concepts underlying our calculations. A profound and virtually complete overview on molecular emission lines originating from the interstellar media of (distant) galaxies has been presented in Chapter 2 of Riechers (2007) to which we refer the reader. The review presented by Solomon and Vanden Bout (2005) summarizes all important definitions with respect to molecular line emission properties, the relation between ^{12}CO line emission and the total molecular gas content of galaxies as well as a thorough overview on the detections of molecular gas in distant galaxies. In this Appendix we summarize the most important insights for our work from Riechers (2007) and Solomon and Vanden Bout (2005), hence follow closely the argumentation and notation in both works.

Carbon monoxide (CO) is a linear but electrically asymmetric molecule that hence possesses a permanent dipole moment (meaning its center of mass and center of charge do not coincide). It is highly abundant in the interstellar medium (ISM) of galaxies following closely the distribution of molecular hydrogen H_2. H_2 itself is symmetric and does not have a dipole moment. Observationally, this means that CO will show detectable emission lines if brought into rotation through collisions with other H_2 particles whereas H_2 will not. CO is therefore frequently used by observers to trace the H_2-dominated molecular ISM in galaxies and hence the raw material needed for star formation.

Molecular rotation is quantized, meaning that a given molecule has discrete rotational excitation levels. Rotation is, generally, possible about three mutually perpendicular axes and three corresponding moments of inertia can be defined. In a linear (i.e. cylindrically symmetric) molecule like CO (or H_2) only two distinct moments of inertia, $I_\perp$ and $I_\parallel$, exist where the moment of inertia defined along the binding axis is substantially smaller ($I_\parallel \ll I_\perp$). Since rotational energy scales reciprocally with the moment of inertia, parallel rotation is unlikely to be excited in the environments of interest for this thesis so that we will deal in the following solely with $I \equiv I_\perp$.

The discrete energy levels of molecular rotation, working in the Born-Oppenheimer approximation and hence neglecting higher order terms, are found as energy eigenvalues of

the Schrödinger equation as

$$E_{\rm rot} = \frac{J(J+1)\hbar^2}{2I}, \qquad J = 0, 1, 2, 3 \ldots \tag{B.17}$$

where $\hbar$ is the (reduced) Planck constant ($\hbar = h/2\pi$). The photon energy, $\Delta E_{\rm rot} = h\nu_{\rm if}$, released by radiative de-excitation[4] from the initial level $\mathrm{i} = J$ to the final level $\mathrm{f} = J - 1$ hence reads

$$\Delta E_{\rm rot} = \frac{\hbar^2 J}{2I} \quad \Longleftrightarrow \quad \nu_{\rm if} = \frac{\hbar J}{2\pi I} = \nu_{\rm CO(1-0)} J', \tag{B.18}$$

where $J' = J$ for all $J \geq 2$ and $\nu_{\rm CO(1-0)} = 115.271202$ GHz[5] denotes the fundamental frequency of the CO-spectrum in the sense that all higher J-transitions are harmonics of this lowest possible transition. Within certain restrictions (Riechers 2007) the fundamental frequency for the CO molecule is, hence, solely determined by its dominant moment of inertia.[6] Due to this simple discretization one sometimes refers to such a line spectrum as a rotational ladder.

Given that a main channel for rotational excitation of molecules in a given molecular cloud is through collisions[7], a minimum excitation temperature for any energy level can be derived by equating rotational energy (Eq. (B.17)) and the kinetic temperature of the gas. Generally, higher levels have higher minimum excitation temperatures while also having substantially higher critical densities (Riechers 2007). In the case where more than one gas phase exists along one line of sight[8] towards a given galaxy the $J = 5 \rightarrow 4$ transition studied in this thesis is thus more likely to probe those regions that are denser. Compared to other molecules (such as HCN), however, CO line emission is generally a good tracer for lower density environments while still tracing a broad range of temperatures.

The CO emission line is expected to show some Doppler broadening if one assumes that the molecular gas is observed in a rotating disk and the line profile should hence follow a Gaussian function. However, such an ordered rotation is not necessarily expected in a (possibly merger-driven) starburst environment and there are plenty of other physical reasons that would change the line profile from this simple shape (see Riechers 2007). On the other hand, a Gaussian profile, constituting a one-parameter model, is often the most simple choice to obtain reasonable measures of line peak flux and line width from the typically low signal-to-noise data obtained for such faint emission lines from high redshift objects. In velocity units[9] the model profile of width σ, centered at a reference velocity[10]

[4] Note that quantum mechanical optical selection rules prohibit all transitions except those between neighbored energy levels.

[5] A list of theoretically predicted emission line frequencies and corresponding laboratory measurements is found at http://splatalogue.net/

[6] This statement holds also for other linear molecules which explains why rotational transition lines of various molecular species are found at (sub-)mm wavelengths.

[7] Strictly speaking, collisional excitation dominates only over radiative excitation if the environmental conditions are such that the density is higher than a certain critical density. In this situation the gas is then referred to as being in local thermal equilibrium.

[8] Within the telescope beam, respectively, if we are dealing with unresolved emission.

[9] We could work in frequency units in exactly the same way. It is, however, common practice in molecular studies to state velocity-related quantities.

[10] In this Appendix we denote velocities as v instead of v used elsewhere in this thesis in order to avoid confusion with the frequency ν.

v_0, hence reads

$$\mathcal{G}(\mathsf{v},\sigma) = \frac{A_1}{\sigma\sqrt{2\pi}} e^{\frac{-(\mathsf{v}-\mathsf{v}_0)^2}{2\sigma^2}} + A_2, \tag{B.19}$$

where we introduced two other free parameters, the line peak flux $S_{\rm CO} \equiv A_1$ and the continuum flux level $S_{\rm cont} \equiv A_2$. The full width at half maximum (FWHM) is related to the width of the Gaussian by

$$\Delta\mathsf{v}_{\rm FWHM} = 2\sqrt{2\ln 2}\,\sigma \approx 2.35\,\sigma. \tag{B.20}$$

The integrated line flux, often presented as[11] $S_{\rm CO}\Delta\mathsf{v}$ (in units of $\mathrm{Jy\,km\,s^{-1}}$), is found by analytical integration of the Gaussian profile:

$$S_{\rm CO}\Delta\mathsf{v} = \int_{-\infty}^{\infty} d\mathsf{v}\,\mathcal{G}(\mathsf{v},\sigma) = \frac{\pi}{2\sqrt{\ln 2}}\,S_{\rm CO}\Delta\mathsf{v}_{\rm FWHM} \approx S_{\rm CO}\Delta\mathsf{v}_{\rm FWHM}. \tag{B.21}$$

Using Eq. (B.12) we can derive a luminosity of the CO line by integrating the luminosity over the spectral range covering the line:

$$L_{\rm CO} = \int d\nu_{\rm rf}\,L_{\nu_{\rm rf}} = \int d\nu\,4\pi D_{\rm L}^2\,S_\nu(\nu) \tag{B.22}$$

$$= 4\pi D_{\rm L}^2 \frac{(1+z_{\rm CO})^{-1}\,\nu_{\rm CO}}{c} \int d\mathsf{v}\,S_\nu(\mathsf{v}), \tag{B.23}$$

where we used $c\,d\nu = \nu_{\rm Peak}\,d\mathsf{v} = (1+z_{\rm CO})^{-1}\,\nu_{\rm CO}\,d\mathsf{v}$, relating not only observed frequency and velocity but also the observed peak frequency $\nu_{\rm Peak}$ and the rest-frame (i.e. laboratory) frequency of a given CO-transition.

If we change to convenient units the flux integral in Eq. (B.23) can be expressed (e.g. Solomon and Vanden Bout 2005) in relation to the integrated line flux given by Eq. (B.21):

$$L_{\rm CO}\;[L_\odot] = 1.04\times10^{-3}\,S_{\rm CO}\Delta\mathsf{v}\;[\mathrm{Jy\,km\,s^{-1}}]\,(D_{\rm L}\;[\mathrm{Mpc}])^2\,(1+z_{\rm CO})^{-1}\,\nu_{\rm CO}\;[\mathrm{GHz}], \tag{B.24}$$

where one could also directly use the observed peak frequency $\nu_{\rm Peak}$ for the redshifted rest-frame transition $(1+z_{\rm CO})^{-1}\,\nu_{\rm CO}$.

A particularly useful concept in dealing with ^{12}CO line emission is, however, a luminosity definition in relation to the intrinsic (i.e. rest-frame) source brightness temperature averaged over the source. The concept of brightness temperature is physically meaningful only if we are dealing with an optically thick emitter. In optically thick emitters the brightness temperature and intrinsic temperature of the emitting body are the same as the molecular gas at a given transition level is in thermal equilibrium with its own radiation (and the surrounding medium collisionally exciting it). When several several rotational transition levels are optically thick, emission of all these transitions will be of the same (intrinsic) equilibrium temperature. Line luminosities individually related to this unique temperature will therefore always show mutual ratios of unity. On the other hand, a brightness-temperature related line-ratio other than unity informs us that the intrinsic state of the molecular gas cannot be thermalized up to the higher of the two transitions.

[11] Note that in this thesis we also use the notation $\mathrm{I_{CO}}$ for the observed velocity-integrated line flux.

This alternative line luminosity, $L'_{\rm CO}$, is derived from the product of the velocity-integrated brightness temperature and the (proper) source area (e.g. Solomon and Vanden Bout 2005). The latter is derived from (see Appendix B.1) the product of observed source solid angle and the square of the angular diameter distance, $\Omega D_{\rm A}^2$. For optically thick emission at sufficiently low rest-frame frequencies rest-frame brightness temperature and intrinsic source intensity are related through the Raleigh-Jeans approximation ($h\nu \ll k_{\rm B}T$) of the black body intensity such that rest-frame brightness temperature and observed flux density are related as (e.g. Riechers 2007)

$$T_{\rm rf}^{\rm b} = \frac{(1+z)\,c^2}{2k_{\rm B}\,\nu_{\rm Peak}^2\,\Omega} S_\nu. \tag{B.25}$$

The line rest-frame frequency of < 600 GHz (i.e. a rest-frame wavelength of > 500 μm) we are dealing with in this thesis justifies the above definition of brightness temperature as it is still well within the Raleigh-Jeans tail of any reasonable thermal emission. Brightness temperature hence measures the intrinsic thermal temperature of the emitting body in our case.

Using Eq. (B.25) the line luminosity $L'_{\rm CO}$ can finally be derived:

$$\begin{aligned} L'_{\rm CO} &= \int d\mathrm{v}\, T_{\rm rf}^{\rm b}\, \Omega D_{\rm A}^2 = \frac{c^2}{2k_{\rm B}\,\nu_{\rm Peak}^2} \frac{D_{\rm L}^2}{(1+z_{\rm CO})^3} \int d\mathrm{v}\, S_\nu(\mathrm{v}) && \text{(B.26)} \\ &= \frac{c^2}{2k_{\rm B}\,\nu_{\rm CO}^2} \frac{D_{\rm L}^2}{(1+z_{\rm CO})} \int d\mathrm{v}\, S_\nu(\mathrm{v}) && \text{(B.27)} \\ &= \frac{c^3}{8\pi\, k_{\rm B} \nu_{\rm CO}^3} L_{\rm CO}, && \text{(B.28)} \end{aligned}$$

where the latter step makes the connection to the line luminosity as defined in Eq. (B.23). This translates into (e.g. Solomon and Vanden Bout 2005)

$$L'_{\rm CO}\ [\mathrm{K\,km\,s^{-1}\,pc^2}] = 3.25\times10^7\, S_{\rm CO}\Delta\mathrm{v}\ [\mathrm{Jy\,km\,s^{-1}}]\, \frac{(D_{\rm L}\ [\mathrm{Mpc}])^2}{(1+z_{\rm CO})}\, (\nu_{\rm CO}\ [\mathrm{GHz}])^{-2} \tag{B.29}$$

Note that this relation strictly holds only if the source is smaller than the telescope beam. Otherwise $S_{\rm CO}\Delta\mathrm{v}$ does not measure the total source-averaged brightness temperature. For a source at high redshift – as studied in this thesis – Eq. (B.25) is, however, fully applicable.

As we have seen in Appendix B.2 continuum emission at (sub-)mm wavelengths benefits from a negative K-correction at high redshifts. We see now that the same holds true for molecular line emission in the same observing range since the velocity integrated line flux scales with $D_{\rm L}^{-2}(1+z)^3 \approx (1+z)$ at sufficiently high redshift (as outlined above) for a given $L'_{\rm CO}$. For a given observing window covering a low-J CO-transition at $z = 0$ (e.g. the 3 mm band) a higher transition will be detectable if the source is at a high enough redshift that the line is shifted into the same window. The CO-detection presented in this thesis plus the detections of 35 distant starbursts, about the same number of high-z quasars and some other bolometrically bright objects residing at high redshifts and reported in the literature have observationally proven the usefulness of this concept. As a caveat one should be aware that – for this to be useful – the high-J transitional levels require adequate environments to be thermalized. This does not seem to be the case in local normal star forming objects. Thus blind CO-searches at long mm-wavelengths are hence expected to be biased against

highly excited objects at high redshift, comparable merely to starburst environments in the local universe.

A CO line luminosity is directly converted into a molecular gas mass by a linear relation (e.g. Solomon and Vanden Bout 2005):

$$M_{\rm gas} = \alpha_{\rm CO} L'_{\rm CO}, \tag{B.30}$$

where $M_{\rm gas}$ denotes the total molecular gas mass (incl. H_2 as well as Helium). There is ample evidence that, for the Milky way, $\alpha_{\rm CO} = 4.6\ M_\odot\,(\mathrm{K\,km\,s^{-1}\,pc^2})^{-1}$ holds. This value can be derived from the virial theorem under observationally confirmed assumption on the dynamics of gravitationally bound individual molecular clouds as well as from independent observational diagnostics (see Solomon and Vanden Bout 2005, for a summary of mutually agreeing results).

In local starbursts, however, it has been argued (Downes et al. 1993) that the assumption of an ensemble of virialized clouds might not hold due to the substantially higher central mass densities in such objects. In the centers of massive starbursts we are merely dealing with a single bound medium of gas and stars. Downes et al. (1993) point out that this leads to the fact that the CO line luminosity cannot be regarded as a pure gas mass tracer anymore but rather traces the geometric mean of gas and dynamical mass. The galactic $\alpha_{\rm CO}$ factor introduced before would hence over-predict the gas mass if applied to CO-observations of starbursts. Indeed, the gas masses reported for such extreme objects based on a Galactic conversion factor often exceed the dynamical mass estimates, hence observationally favoring a lower conversion factor (see, e.g., Downes et al. 1993, Solomon and Vanden Bout 2005, and references therein).

A commonly accepted value for local starbursts has been suggested by Downes and Solomon (1998) as $\alpha_{\rm CO} = 0.8\ M_\odot\,(\mathrm{K\,km\,s^{-1}\,pc^2})^{-1}$ and is often used for their high-redshift cousins (e.g. Solomon and Vanden Bout 2005).

In this thesis we make use of the Downes and Solomon (1998) conversion factor for a $z \sim 4.6$ starburst in order to estimate the total molecular gas mass in this object. For similar objects at comparably high redshift this conversion has been used as well. While those rare objects for which the CO excitation could be constrained based on multiple CO transitions (Riechers et al. 2010; Carilli et al. 2010) two distinct gas phases have been reported which, if the starburst conversion applies, contribute about equal amounts to the total gas content in these system. Also for these objects dynamical mass arguments favor a low conversion factor but it remains elusive if the apparently more diffuse lower excitation gas component might not resemble the molecular conditions of local disk galaxies. It should be noted that the dynamical mass estimates themselves are hard to constrain due to the uncertain assumptions on the dark matter distribution in those objects. Molecular gas mass estimates for high redshift objects should therefore be treated with caution.

B.5. Dust emission properties of star forming galaxies and derivation of dust mass

Dust in the interstellar media of galaxies is dominantly composed of amorphous carbon and silicate-like grains (Draine 2003). They are exposed to the interstellar radiation field,

mostly heated by blue UV light emitted from young stars to temperatures of $T \gtrsim 20$ K and they constitute predominantly thermal (in most cases isotropic) emitters. The dust mass in star forming objects is usually dominated by a cool component that can be described by a single temperature (typically < 50 K; e.g. Kovács et al. 2006; Hwang et al. 2010) and assuming a single species of dust grains. If the galaxy hosts an active galactic nucleus (AGN) the dust in its vicinity is dominantly heated by this central engine to temperatures of 100 K or more (peaking at ~ 20 μm in the rest-frame), bolometrically outshining the cool dust component. AGN may, however, also contribute to the heating of the cooler dust grains typically distributed on much larger (kpc) scales (e.g. Martínez-Sansigre et al. 2009, and references therein). In presence of an AGN cool dust emission is hence not necessarily directly proportional to the star formation rate (SFR), rather constraining an upper limit to the SFR.

Mathematically, a single species dust emission is usually well described by a modified black body at a temperature T_D (also referred to as gray body emission). However, at high redshift it is also useful to account for the contribution of the redshifted cosmic microwave background emission of temperature $T_\mathrm{BG} = 2.73\ \mathrm{K} \times (1+z)$ (e.g. Weiß et al. 2007). In total, the flux density in the observed frame then reads

$$F_\nu = \frac{\Omega}{(1+z)^3} \left[B_{\nu_\mathrm{rf}}(T_\mathrm{D}) - B_{\nu_\mathrm{rf}}(T_\mathrm{BG})\right] \left(1 - e^{-\tau_{\nu_\mathrm{rf}}}\right), \tag{B.31}$$

where $\nu_\mathrm{rf} = (1+z)\nu$ denotes the frequency in the rest-frame of the source and ν the observed one. Following the notation in Aravena et al. (2008) we introduced $\Omega = \pi(d_0/D_\mathrm{A})^2$, the solid angle the source subtends on the sky defined by the ratio of the equivalent source size d_0 and the angular diameter distance D_A at the redshift of the source.[12] The emission of a black body B_{ν_rf} at a temperature T is described by the Planck function as

$$B_{\nu_\mathrm{rf}}(T) = \frac{2h\nu_\mathrm{rf}^3}{c^2} \left[\exp\left(\frac{h\nu_\mathrm{rf}}{k_\mathrm{B}T}\right) - 1\right]^{-1}, \tag{B.32}$$

where h is Planck's and k_B is Boltzmann's constant, c denotes the speed of light and we use the rest-frame notation for consistency with Eq. (B.31). The optical depth τ_{ν_rf} introduced in Eq. (B.31) follows a frequency-dependent description proportional to the illuminated dust mass M_D:

$$\tau_{\nu_\mathrm{rf}} = \frac{\kappa_{\nu_\mathrm{rf}} M_\mathrm{D}}{D_\mathrm{A}^2 \Omega}. \tag{B.33}$$

The explicit frequency dependence is thereby contained in the mass-absorption coefficient $\kappa_{\nu_\mathrm{rf}} = \kappa_0(\nu_\mathrm{rf}/\nu_0)^\beta$. Note that this simple power-law description with a dust emissivity index β is valid only within certain limits. Empirically, based on laboratory experiments combined with observational evidence, emissivity curves have been studied for individual dust species. E.g. Draine and Lee (1984) show that the power-law description is a good approximation for silicates/graphites exposed to interstellar radiation fields for rest-frame wavelengths above ∼20/40 μm. There is hence experimental support to model long far-infrared to (sub-)mm data observed for $z > 4$ sources studied in this thesis under this power-law assumption. Observationally, it is hard to constrain the exact value of the index

[12] The factor $(1+z)^{-3}$ in Eq. (B.31) results from the effect of surface brightness dimming, $(1+z)^{-4}$, and the redshifting of the bandpass which produces a factor of $(1+z)$.

β because of degeneracies between colors and temperature (Blain et al. 2003), unless the peak region of the dust emission (and thus the dust temperature) is accurately sampled. For dust-rich sources in the distant universe values of $1 < \beta < 2$ have been reported (e.g. Priddey and McMahon 2001; Kovács et al. 2006, for high redshift quasars as well as e.g. Blain et al. 2002, and references therein for sub-mm galaxies), perhaps with growing evidence that quasars and composite objects cluster somewhat more at the higher end of this range.

The reference value for the mass-absorption κ_0 probably is the most uncertain parameter which explains why inferred dust masses should be treated with caution. Different authors report fairly different values for κ_0 while also probing different reference wavelengths. Extrapolating different measurements to the same reference wavelengths by assuming a typical value for β translates into about a factor of three scatter (Blain et al. 2002). Explicitely, two commonly used literature values are $\kappa_{1.2\mathrm{mm}} = 0.04\ \mathrm{m^2 kg^{-1}}$ (Alton et al. 2004; Kruegel and Siebenmorgen 1994) and $\kappa_{125\mu\mathrm{m}} = 2.64\ \mathrm{m^2 kg^{-1}}$ (Dunne et al. 2003) which nominally agree within a factor of two when extrapolated to the same reference wavelength in the observed frame by assuming a typical value for the index β.

In the presence of N dust components with emissivities β^i at temperatures T_D^i individually described by Eq. (B.31) the (far-)infrared (FIR) luminosity is obtained by integrating over all frequencies and adding up all dust components as

$$L_\mathrm{FIR} = \frac{4\pi\, D_\mathrm{L}^2}{(1+z)} \int d\nu \sum_i^N F_\nu^i(\beta^i, T_\mathrm{D}^i) = 4\pi\, D_\mathrm{A}^2 (1+z)^3 \sum_i^N \int d\nu F_\nu^i(\beta^i, T_\mathrm{D}^i), \tag{B.34}$$

where $D_\mathrm{L} = (1+z)^2 D_\mathrm{A}$ denotes the luminosity distance to redshift z and we exchanged – for convenience – summation and integration in the last step.

Typically, the order of operations starts from fitting gray body components according to Eq. (B.31) to the observed photometry. The fit then delivers the temperatures and masses of the dust components and a luminosity can be estimated according to Eq. (B.34) from the best-fit models. For most objects at high redshifts the data coverage is rather sparse so that, usually, the emissivities β^i are not treated as free parameters in the fit but are fixed to empirically justified values (see above).

Eq. (B.31) explicitly accounts for optically thick ($\tau_{\nu_\mathrm{rf}} > 1$) dust emission. While it is often assumed that dust emission is optically thin at far-infrared wavelengths, Downes et al. (1993) argue that the situation changes in presence of large, spatially concentrated dust reservoirs typically found in (local) starbursts. The limit at which the dust emission becomes optically thick can be derived from Eq. (B.33) in dependence of the source size and dust mass, hence the density of the dust. For example Aravena et al. (2008) find for a $z \sim 1.8$ starburst/QSO composite object – for which a source extent of 1.5 kpc was estimated based on ^{12}CO emission line observations – that the dust mass computed for the dominant cool component suffices to make the dust emission optically thick at rest-frame wavelengths below 130 μm. Given that the cool dust emission from this source peaks around rest-frame wavelengths of ~ 90 μm (i.e. in the typical range for starbursts) only its Raleigh-Jeans tail should be treated in the optically thin approximation. The Raleigh-Jeans approximation for the cool dust component, in turn, directly leads to a sub-mm spectral index of $\alpha_\mathrm{SMM} = 2+\beta$. It is hence a prominent characteristic of a modified black body spectrum at long wavelengths that it falls off significantly steeper than a standard black body.

It should be noted that – due to a current lack of very high-resolution data – little is known about the actual dust distribution in distant starbursts so that the assumption of a single compact dust reservoir might not hold at high-z. In the near future the Atacama Large Millimeter Array (ALMA) will resolve the dust distribution in high redshift objects. One should still generally be cautious when applying the optically thin approximation globally.

In the optically thin approximation, $\tau_{\nu_{\mathrm{rf}}} \ll 1$, at sufficiently long rest-frame wavelengths Eq. (B.31) simplifies to:

$$\begin{aligned} F_\nu &= \frac{\kappa_{\nu_{\mathrm{rf}}} M_{\mathrm{D}}}{D_{\mathrm{A}}^2 (1+z)^3} \left[B_{\nu_{\mathrm{rf}}}(T_{\mathrm{D}}) - B_{\nu_{\mathrm{rf}}}(T_{\mathrm{BG}}) \right] \\ &= \kappa_0 \left(\frac{\nu_{\mathrm{rf}}}{\nu_0} \right)^\beta \frac{M_{\mathrm{D}}(1+z)}{D_{\mathrm{L}}^2} \left[B_{\nu_{\mathrm{rf}}}(T_{\mathrm{D}}) - B_{\nu_{\mathrm{rf}}}(T_{\mathrm{BG}}) \right], \end{aligned} \tag{B.35}$$

which is now independent of the solid angle and, thus, also of the source size. The far-IR luminosity is again computed from Eq. (B.34), this time for a single dust component. With Eq. (B.32) and the substitution $x = h\nu_{\mathrm{rf}}/k_{\mathrm{B}}T$ we arrive at an integral for which an analytic solution exists via the Gamma and Riemann zeta functions (e.g. Martínez-Sansigre et al. 2009):

$$L_{\mathrm{FIR}} \propto \int dx \frac{x^{3+\beta}}{e^x - 1} = \Gamma(4+\beta)\zeta(4+\beta). \tag{B.36}$$

This approach resembles the derivation of the Stefan-Boltzmann law so that pre-factors can be collected to a large extent in the Stefan-Boltzmann constant $\sigma_{\mathrm{SB}} = \frac{2\pi^5 k_{\mathrm{B}}^4}{15c^2h^3}$ while the temperature dependence becomes even stronger pronounced than in the Stefan-Boltzmann law:

$$L_{\mathrm{FIR}} = 4\pi M_{\mathrm{D}} \kappa_0 \left(\frac{k_{\mathrm{B}}}{\nu_0 h} \right)^\beta \frac{\Gamma(4+\beta)\zeta(4+\beta)}{\pi^5/15} \sigma_{\mathrm{SB}} \left(T_{\mathrm{D}}^{4+\beta} - T_{\mathrm{BG}}^{4+\beta} \right), \tag{B.37}$$

where any explicit redshift dependence canceled out since we integrated in the rest-frame.

In practice, Eq. (B.37) is used to substitute the unknown dust mass in Eq. (B.35) yielding a model to fit the observed photometry of the cool dust emission when treating L_{FIR}, T_{D} and β as free parameters. This way also the uncertain reference value κ_0 of the mass absorption coefficient cancels out. This might be regarded as a particular advantage of the optically thin approximation over the full model in Eq. (B.31) because at least the far-infrared luminosity and dust temperature can be estimated without this additional source of error. In turn, a single observed monochromatic flux density can be used to roughly constrain L_{FIR} when fixing the values of β and T_{D}. This is useful in the – at high redshift – common case that for a source only a single measurement, e.g. from (sub-)mm-observations, is available.

For completeness, the full parametric model for the observed flux density in the optically thin approximation at sufficiently long wavelengths reads

$$F_\nu = \frac{L_{\mathrm{FIR}}(1+z)}{4\pi D_{\mathrm{L}}^2} \frac{\pi^5/15}{\sigma_{\mathrm{SB}}} \frac{B_{\nu_{\mathrm{rf}}}(T_{\mathrm{D}}) - B_{\nu_{\mathrm{rf}}}(T_{\mathrm{BG}})}{\Gamma(4+\beta)\zeta(4+\beta)\left(T_{\mathrm{D}}^{4+\beta} - T_{\mathrm{BG}}^{4+\beta} \right)} \left(\frac{h\nu_{\mathrm{rf}}}{k_{\mathrm{B}}} \right)^\beta \tag{B.38}$$

Bearing in mind the caveats discussed above, the cool dust mass is finally estimated by solving Eq. (B.37) using the data-constrained parameters. Alternatively, Eq. (B.35) can be used to estimate the dust mass from any given monochromatic flux density in the observed frame.

C. Fundamental constants, units and definitions

Many of the relations and calibrations that led to the results presented in this work make use of fundamental and convenient (astro-)physical constants. Here we list the numerical values of these constants and, if applicable, their relation to other fundamental constants. Furthermore the list includes distance and flux density units conveniently used in astronomical contexts.

Cosmological quantities used in this thesis are defined in Appendix B.1 along with their numerical values assumed here.

Table C.1. Fundamental physical constants

Constant	Symbol	Value	SI unit
Speed of light (vacuum)	c	299792458	$\mathrm{m\,s^{-1}}$
Elementary charge	e	$1.602176565 \times 10^{-19}$	$\mathrm{As} \stackrel{\mathrm{Def.}}{=} \mathrm{C}$
Newton gravitational constant	G	6.67384×10^{-11}	$\mathrm{m^3\,kg^{-1}\,s^{-2}}$
Planck constant	h	$6.62606957 \times 10^{-34}$	$\mathrm{J\,s}$
Boltzmann constant	k_B	1.380658×10^{-23}	$\mathrm{J\,K^{-1}}$
Stefan-Boltzmann constant	$\sigma_\mathrm{SB} = \frac{2\pi^5 k_\mathrm{B}^4}{15 c^2 h^3}$	5.670373×10^{-8}	$\mathrm{W\,m^{-2}\,K^{-4}}$

Note. — Values taken from P.J. Mohr, B.N. Taylor, and D.B. Newell (2011), *The 2010 CODATA Recommended Values of the Fundamental Physical Constants* (Web Version 6.0). This database was developed by J. Baker, M. Douma, and S. Kotochigova. Available: http://physics.nist.gov/constants. National Institute of Standards and Technology, Gaithersburg, MD 20899.

Table C.2. Astronomical and SI-derived units

Unit	Symbol	Value	(SI) unit / information
Parsec	pc	$3.08568025 \times 10^{16}$	m
Solar mass	$M_\odot$	1.98892×10^{30}	kg
Solar luminosity	$L_\odot$	3.839×10^{26}	W
Erg	erg	10^{-7}	J
Hertz	Hz	1	$\mathrm{s^{-1}}$
Angstrom	Å	10^{-10}	m
Jansky	Jy	10^{-26}	$\mathrm{W\,m^{-2}\,Hz^{-1}}$
		$2.99792458 \times 10^{-5}$	$\mathrm{erg\,s^{-1}\,cm^{-2}\,Å^{-1}} \times (\lambda\ [\mathrm{Å}])^{-2}$
AB magnitude	$\mathrm{m_{AB}}(\nu)$	$-2.5 \log\left(\frac{F_\nu\ [\mathrm{Jy}]}{3631}\right)$	For flux density F_ν
		$\approx -2.5 \log(F_\nu\ [\mu\mathrm{Jy}]) + 23.9$	at observed frequency ν

Note. — Values and definitions can be found in any standard astronomy textbook. For an overview on often used unit conversions in astronomy we refer the reader to http://astro.wku.edu/strolger/UNITS.txt.

Acknowledgments

This thesis started with Kafka and the main street of the village which never reaches the castle. It is known that the protagonist – called K. – will never reach the castle (his purported destination) either. This sounds quite negative and in case of K. it certainly is. The question remains, however, what we can learn from the metaphor for science and perhaps for life. Sometimes it might be better, on the one hand, not to know the ultimate destination. In an astronomical context a famous example for this might be the quite serendipitous observational discovery of the cosmic microwave background. On the other hand, sometimes it might be better not to follow the main road. Be aware, however, that finding the most promising alternative way demands a good portion of creativity, actual talent as well as some luck and hence courage. The author of this thesis lacks the self confidence and perhaps the arrogance to claim those traits for himself in sufficient amount. He might have often looked for the side streets anyway. Leaving the main road often (maybe naturally?) also means to leave the straight way. It is the author's opinion that this thesis profited from this approach in some parts. In others it might have dramatically failed. In which fraction did it fail or did it work? In equal parts? Even worse? I am glad that higher powers than me have to judge this.

I wish to thank Professor Hans-Walter Rix and Professor Ralf Klessen for having taken over the challenge to be those higher powers. Thanks to Dr. Henrik Beuther and Professor Luca Amendola the committee for my doctoral exam is complete and I am glad that both found time in their certainly tight schedules. I thank my advisor, Dr. Eva Schinnerer, for having given me the opportunity to work in the exciting and most familiar environment the Max-Planck-Instute for Astronomy offers. She was brave enough to accept me as her student given that my scientific background was on tiny scales compared to any astronomical context (let alone cosmic evolution!). I also thank her for sharing her unchallenged scientific intuition with me. She furthermore introduced me into how science works. I often tried to compensate her efforts in returning my opinion on how science should work. I hope nobody became desperate from these debates for longer periods of time.

I thank all my colleagues and the entire COSMOS collaboration – consisting of more than a hundred scientists around the globe – who contributed to this work in several ways, in particular in providing data products, making suggestions and giving guidance. Those who are listed as co-authors of the published (and soon to be published) parts of this thesis thereby deserve special acknowledgment. Particularly, I thank Dr. Mark Sargent, Dr. Alejo Martínez-Sansigre, Dr. Vernesa Smolčić, Dr. Arjen van der Wel and Dr. Manuel Aravena for their support, their help and for countless hours of their time before and around proposal deadlines as well as before paper and thesis submissions. Many thanks also to Chris Carilli for his enlightening suggestions and, not less, for simply being Chris Carilli. I want to thank Dr. Brent Groves and Dr. Andrea Maccio for reading parts of this manuscript (Appendix and Introduction) and providing helpful suggestions which certainly improved the text. Another 'thank you' to Dr. Johannes Staguhn for making me a GISMO team member. I am sure

GISMO and its successor will rock the world! Finally, I thank Professor Ian Smail for giving me the opportunity to carry out my future work at Durham University.

Thanks to Dr. Julian Merten for providing the LaTeX-style file for this thesis (I hope he is fine with the numerous modifications I applied). I thank him and all my friends in Heidelberg for the great time we had together and all my friends in larger distances (however, not yet comparable with the distances this thesis is dealing with) for being sufficiently patient with respect to my rare presence. This group of friends includes Dr. Arno Witzel and Gunther Witzel who gave me invaluable support as well as guidance along my scientific way, especially when I was looking for the right direction after the defense of my diploma thesis.

Abschließend, jedoch sicherlich nicht zuletzt, danke ich meiner Familie für jegliche Unterstützung auf meinem bisherigen Weg. Wie schon meine Diplomarbeit sei diese Dissertation Clemens und Leonie, den Kindern meiner Schwester Dagmar und ihres Mannes Stephan Epe gewidmet, da sie ihren (Paten)onkel nach wie vor zu selten sehen. Meine Eltern, Monika und Dr. Ayad Karim, haben mich stets nach Kräften unterstützt und sämtliche Etappen wohlwollend und geduldig begleitet. Für viel Verständnis und noch mehr Unterstützung danke ich Dir, Lisa, ganz besonders.[1]

[1] Finally, I must not forget to thank Mr. M, Mr. R, Mr. G and all other members of their gang. Those who should will understand...

References

Alexander, D. M., Bauer, F. E., Brandt, W. N., Schneider, D. P., Hornschemeier, A. E., Vignali, C., Barger, A. J., Broos, P. S., Cowie, L. L., Garmire, G. P., Townsley, L. K., Bautz, M. W., Chartas, G., and Sargent, W. L. W. (2003). The Chandra Deep Field North Survey. XIII. 2 Ms Point-Source Catalogs. *AJ*, 126:539–574.

Alton, P. B., Xilouris, E. M., Misiriotis, A., Dasyra, K. M., and Dumke, M. (2004). The emissivity of dust grains in spiral galaxies. *A&A*, 425:109–120.

Andreani, P., Cimatti, A., Loinard, L., and Röttgering, H. (2000). CO detection of the extremely red galaxy HR10. *A&A*, 354:L1–L5.

Antonucci, R. (1993). Unified models for active galactic nuclei and quasars. *ARA&A*, 31:473–521.

Aravena, M., Bertoldi, F., Schinnerer, E., Weiss, A., Jahnke, K., Carilli, C. L., Frayer, D., Henkel, C., Brusa, M., Menten, K. M., Salvato, M., and Smolcic, V. (2008). Properties of the molecular gas in a starbursting QSO at z = 1.83 in the COSMOS field. *A&A*, 491:173–181.

Aretxaga, I., Wilson, G. W., Aguilar, E., Alberts, S., Scott, K. S., Scoville, N., Yun, M. S., Austermann, J., Downes, T. P., Ezawa, H., Hatsukade, B., Hughes, D. H., Kawabe, R., Kohno, K., Oshima, T., Perera, T. A., Tamura, Y., and Zeballos, M. (2011). AzTEC millimetre survey of the COSMOS field - III. Source catalogue over 0.72 deg^2 and plausible boosting by large-scale structure. *MNRAS*, 415:3831–3850.

Arnouts, S., Moscardini, L., Vanzella, E., Colombi, S., Cristiani, S., Fontana, A., Giallongo, E., Matarrese, S., and Saracco, P. (2002). Measuring the redshift evolution of clustering: the Hubble Deep Field South. *MNRAS*, 329:355–366.

Arnouts, S., Walcher, C. J., Le Fèvre, O., Zamorani, G., Ilbert, O., Le Brun, V., Pozzetti, L., Bardelli, S., Tresse, L., Zucca, E., Charlot, S., Lamareille, F., McCracken, H. J., Bolzonella, M., Iovino, A., Lonsdale, C., Polletta, M., Surace, J., Bottini, D., Garilli, B., Maccagni, D., Picat, J. P., Scaramella, R., Scodeggio, M., Vettolani, G., Zanichelli, A., Adami, C., Cappi, A., Ciliegi, P., Contini, T., de la Torre, S., Foucaud, S., Franzetti, P., Gavignaud, I., Guzzo, L., Marano, B., Marinoni, C., Mazure, A., Meneux, B., Merighi, R., Paltani, S., Pellò, R., Pollo, A., Radovich, M., Temporin, S., and Vergani, D. (2007). The SWIRE-VVDS-CFHTLS surveys: stellar mass assembly over the last 10 Gyr. Evidence for a major build up of the red sequence between z = 2 and z = 1. *A&A*, 476:137–150.

Baldry, I. K. and Glazebrook, K. (2003). Constraints on a Universal Stellar Initial Mass Function from Ultraviolet to Near-Infrared Galaxy Luminosity Densities. *ApJ*, 593:258–271.

Baldry, I. K., Glazebrook, K., Brinkmann, J., Ivezić, Ž., Lupton, R. H., Nichol, R. C., and Szalay, A. S. (2004). Quantifying the Bimodal Color-Magnitude Distribution of Galaxies. *ApJ*, 600:681–694.

Bartelmann, M. and Schneider, P. (2001). Weak gravitational lensing. *Phys. Rep.*, 340:291–472.

Bauer, A. E., Drory, N., Hill, G. J., and Feulner, G. (2005). Specific Star Formation Rates to Redshift 1.5. *ApJ*, 621:L89–L92.

Baugh, C. M., Lacey, C. G., Frenk, C. S., Granato, G. L., Silva, L., Bressan, A., Benson, A. J., and Cole, S. (2005). Can the faint submillimetre galaxies be explained in the Λ cold dark matter model? *MNRAS*, 356:1191–1200.

Beckwith, S. V. W., Stiavelli, M., Koekemoer, A. M., Caldwell, J. A. R., Ferguson, H. C., Hook, R., Lucas, R. A., Bergeron, L. E., Corbin, M., Jogee, S., Panagia, N., Robberto, M., Royle, P., Somerville, R. S., and Sosey, M. (2006). The Hubble Ultra Deep Field. *AJ*, 132:1729–1755.

Beelen, A., Cox, P., Benford, D. J., Dowell, C. D., Kovács, A., Bertoldi, F., Omont, A., and Carilli, C. L. (2006). 350 μm Dust Emission from High-Redshift Quasars. *ApJ*, 642:694–701.

Bell, A. R. (1978a). The acceleration of cosmic rays in shock fronts. I. *MNRAS*, 182:147–156.

Bell, A. R. (1978b). The acceleration of cosmic rays in shock fronts. II. *MNRAS*, 182:443–455.

Bell, E. F. (2003a). Estimating Star Formation Rates from Infrared and Radio Luminosities: The Origin of the Radio-Infrared Correlation. *ApJ*, 586:794–813.

Bell, E. F. (2003b). Estimating Star Formation Rates from Infrared and Radio Luminosities: The Origin of the Radio-Infrared Correlation. *ApJ*, 586:794–813.

Bell, E. F. and de Jong, R. S. (2001). Stellar Mass-to-Light Ratios and the Tully-Fisher Relation. *ApJ*, 550:212–229.

Bell, E. F., McIntosh, D. H., Katz, N., and Weinberg, M. D. (2003). The Optical and Near-Infrared Properties of Galaxies. I. Luminosity and Stellar Mass Functions. *ApJS*, 149:289–312.

Bell, E. F., Wolf, C., Meisenheimer, K., Rix, H., Borch, A., Dye, S., Kleinheinrich, M., Wisotzki, L., and McIntosh, D. H. (2004). Nearly 5000 Distant Early-Type Galaxies in COMBO-17: A Red Sequence and Its Evolution since z$\sim$1. *ApJ*, 608:752–767.

Bell, E. F., Zheng, X. Z., Papovich, C., Borch, A., Wolf, C., and Meisenheimer, K. (2007). Star Formation and the Growth of Stellar Mass. *ApJ*, 663:834–843.

Bertin, E. and Arnouts, S. (1996). SExtractor: Software for source extraction. *A&AS*, 117:393–404.

Bertoldi, F., Carilli, C., Aravena, M., Schinnerer, E., Voss, H., Smolcic, V., Jahnke, K., Scoville, N., Blain, A., Menten, K. M., Lutz, D., Brusa, M., Taniguchi, Y., Capak, P., Mobasher, B., Lilly, S., Thompson, D., Aussel, H., Kreysa, E., Hasinger, G., Aguirre, J., Schlaerth, J., and Koekemoer, A. (2007). COSBO: The MAMBO 1.2 Millimeter Imaging Survey of the COSMOS Field. *ApJS*, 172:132–149.

Best, P. N., Kauffmann, G., Heckman, T. M., and Ivezić, Ž. (2005). A sample of radio-loud active galactic nuclei in the Sloan Digital Sky Survey. *MNRAS*, 362:9–24.

Bezanson, R., van Dokkum, P. G., Franx, M., Brammer, G. B., Brinchmann, J., Kriek, M., Labbé, I., Quadri, R. F., Rix, H.-W., van de Sande, J., Whitaker, K. E., and Williams, R. J. (2011). Redshift Evolution of the Galaxy Velocity Dispersion Function. *ApJ*, 737:L31+.

Bigiel, F., Leroy, A., Walter, F., Brinks, E., de Blok, W. J. G., Madore, B., and Thornley, M. D. (2008). The Star Formation Law in Nearby Galaxies on Sub-Kpc Scales. *AJ*, 136:2846–2871.

Bîrzan, L., McNamara, B. R., Nulsen, P. E. J., Carilli, C. L., and Wise, M. W. (2008). Radiative Efficiency and Content of Extragalactic Radio Sources: Toward a Universal Scaling Relation between Jet Power and Radio Power. *ApJ*, 686:859–880.

Blain, A. W., Barnard, V. E., and Chapman, S. C. (2003). Submillimetre and far-infrared spectral energy distributions of galaxies: the luminosity-temperature relation and consequences for photometric redshifts. *MNRAS*, 338:733–744.

Blain, A. W., Smail, I., Ivison, R. J., Kneib, J.-P., and Frayer, D. T. (2002). Submillimeter galaxies. *Phys. Rep.*, 369:111–176.

Boissier, S., Buat, V., and Ilbert, O. (2010). Stellar Mass and Velocity Functions of Galaxies: Backward evolution and the fate of Milky Way siblings. *ArXiv e-prints*.

Bolzonella, M., Miralles, J.-M., and Pelló, R. (2000). Photometric redshifts based on standard SED fitting procedures. *A&A*, 363:476–492.

Bondi, M., Ciliegi, P., Schinnerer, E., Smolčić, V., Jahnke, K., Carilli, C., and Zamorani, G. (2008). The VLA-COSMOS Survey. III. Further Catalog Analysis and the Radio Source Counts. *ApJ*, 681:1129–1135.

Bothwell, M. S., Chapman, S. C., Tacconi, L., Smail, I., Ivison, R. J., Casey, C. M., Bertoldi, F., Beswick, R., Biggs, A., Blain, A. W., Cox, P., Genzel, R., Greve, T. R., Kennicutt, R., Muxlow, T., Neri, R., and Omont, A. (2010). High-resolution CO and radio imaging of ULIRGs: extended CO structures and implications for the universal star formation law. *MNRAS*, 405:219–233.

Bouché, N., Cresci, G., Davies, R., Eisenhauer, F., Förster Schreiber, N. M., Genzel, R., Gillessen, S., Lehnert, M., Lutz, D., Nesvadba, N., Shapiro, K. L., Sternberg, A., Tacconi, L. J., Verma, A., Cimatti, A., Daddi, E., Renzini, A., Erb, D. K., Shapley, A., and Steidel, C. C. (2007). Dynamical Properties of z ˜ 2 Star-forming Galaxies and a Universal Star Formation Relation. *ApJ*, 671:303–309.

Bouché, N., Dekel, A., Genzel, R., Genel, S., Cresci, G., Förster Schreiber, N. M., Shapiro, K. L., Davies, R. I., and Tacconi, L. (2010). The Impact of Cold Gas Accretion Above a Mass Floor on Galaxy Scaling Relations. *ApJ*, 718:1001–1018.

Bournaud, F., Elmegreen, B. G., Teyssier, R., Block, D. L., and Puerari, I. (2010). ISM properties in hydrodynamic galaxy simulations: turbulence cascades, cloud formation, role of gravity and feedback. *MNRAS*, 409:1088–1099.

Bourne, N., Dunne, L., Ivison, R. J., Maddox, S. J., Dickinson, M., and Frayer, D. T. (2010). Evolution of the FIR-Radio Correlation and Infrared SEDs of Massive Galaxies over z = 0 - 2. *ArXiv e-prints*.

Bouwens, R. J., Illingworth, G. D., Franx, M., Chary, R., Meurer, G. R., Conselice, C. J., Ford, H., Giavalisco, M., and van Dokkum, P. (2009). UV Continuum Slope and Dust Obscuration from z ˜ 6 to z ˜ 2: The Star Formation Rate Density at High Redshift. *ApJ*, 705:936–961.

Bouwens, R. J., Illingworth, G. D., Labbe, I., Oesch, P. A., Trenti, M., Carollo, C. M., van Dokkum, P. G., Franx, M., Stiavelli, M., González, V., Magee, D., and Bradley, L. (2011a). A candidate redshift z˜10 galaxy and rapid changes in that population at an age of 500Myr. *Nature*, 469:504–507.

Bouwens, R. J., Illingworth, G. D., Oesch, P. A., Labbé, I., Trenti, M., van Dokkum, P., Franx, M., Stiavelli, M., Carollo, C. M., Magee, D., and Gonzalez, V. (2011b). Ultraviolet Luminosity Functions from 132 z ˜ 7 and z ˜ 8 Lyman-break Galaxies in the Ultra-deep HUDF09 and Wide-area Early Release Science WFC3/IR Observations. *ApJ*, 737:90–+.

Brammer, G. B., Whitaker, K. E., van Dokkum, P. G., Marchesini, D., Labbé, I., Franx, M., Kriek, M., Quadri, R. F., Illingworth, G., Lee, K., Muzzin, A., and Rudnick, G. (2009). The Dead Sequence: A Clear Bimodality in Galaxy Colors from z = 0 to z = 2.5. *ApJ*, 706:L173–L177.

Brinchmann, J., Charlot, S., White, S. D. M., Tremonti, C., Kauffmann, G., Heckman, T., and Brinkmann, J. (2004). The physical properties of star-forming galaxies in the low-redshift Universe. *MNRAS*, 351:1151–1179.

Brusa, M., Civano, F., Comastri, A., Miyaji, T., Salvato, M., Zamorani, G., Cappelluti, N., Fiore, F., Hasinger, G., Mainieri, V., Merloni, A., Bongiorno, A., Capak, P., Elvis, M., Gilli, R., Hao, H., Jahnke, K., Koekemoer, A. M., Ilbert, O., Floc'h, E. L., Lusso, E., Mignoli, M., Schinnerer, E., Silverman, J. D., Treister, E., Trump, J. D., Vignali, C., Zamojski, M., Aldcroft, T., Aussel, H., Bardelli, S., Bolzonella, M., Cappi, A., Caputi, K., Contini, T., Finoguenov, A., Fruscione, A., Garilli, B., Impey, C. D., Iovino, A., Iwasawa, K., Kampczyk, P., Kartaltepe, J., Kneib, J. P., Knobel, C., Kovac, K., Lamareille, F., Leborgne, J.-F., Brun, V. L., Fevre, O. L., Lilly, S. J., Maier, C., McCracken, H. J., Pello, R., Peng, Y.-J., Perez-Montero, E., de Ravel, L., Sanders, D., Scodeggio, M., Scoville, N. Z., Tanaka, M., Taniguchi, Y., Tasca, L., de la Torre, S., Tresse, L., Vergani, D., and Zucca, E. (2010). The xmm-newton wide-field survey in the cosmos field (xmm-cosmos): demography and multiwavelength properties of obscured and unobscured luminous agn. *eprint arXiv*, 1004:2790.

Bruzual, G. (2007). Stellar Populations: High Spectral Resolution Libraries. Improved TP-AGB Treatment. In A. Vallenari, R. Tantalo, L. Portinari, & A. Moretti, editor, *From Stars to Galaxies: Building the Pieces to Build Up the Universe*, volume 374 of *Astronomical Society of the Pacific Conference Series*, pages 303–+.

Bruzual, G. and Charlot, S. (2003). Stellar population synthesis at the resolution of 2003. *MNRAS*, 344:1000–1028.

Bundy, K., Ellis, R. S., Conselice, C. J., Taylor, J. E., Cooper, M. C., Willmer, C. N. A., Weiner, B. J., Coil, A. L., Noeske, K. G., and Eisenhardt, P. R. M. (2006). The Mass Assembly History of Field Galaxies: Detection of an Evolving Mass Limit for Star-Forming Galaxies. *ApJ*, 651:120–141.

Calzetti, D., Armus, L., Bohlin, R. C., Kinney, A. L., Koornneef, J., and Storchi-Bergmann, T. (2000). The Dust Content and Opacity of Actively Star-forming Galaxies. *ApJ*, 533:682–695.

Calzetti, D. and Kennicutt, R. C. (2009). The New Frontier: Galactic-Scale Star Formation. *PASP*, 121:937–941.

Calzetti, D., Kinney, A. L., and Storchi-Bergmann, T. (1994). Dust extinction of the stellar continua in starburst galaxies: The ultraviolet and optical extinction law. *ApJ*, 429:582–601.

Capak, P., Aussel, H., Ajiki, M., McCracken, H. J., Mobasher, B., Scoville, N., Shopbell, P., Taniguchi, Y., Thompson, D., Tribiano, S., Sasaki, S., Blain, A. W., Brusa, M., Carilli, C., Comastri, A., Carollo, C. M., Cassata, P., Colbert, J., Ellis, R. S., Elvis, M., Giavalisco, M., Green, W., Guzzo, L., Hasinger, G., Ilbert, O., Impey, C., Jahnke, K., Kartaltepe, J., Kneib, J.-P., Koda, J., Koekemoer, A., Komiyama, Y., Leauthaud, A., Lefevre, O., Lilly, S., Liu, C., Massey, R., Miyazaki, S., Murayama, T., Nagao, T., Peacock, J. A., Pickles, A., Porciani, C., Renzini, A., Rhodes, J., Rich, M., Salvato, M., Sanders, D. B., Scarlata, C., Schiminovich, D., Schinnerer, E., Scodeggio, M., Sheth, K., Shioya, Y., Tasca, L. A. M., Taylor, J. E., Yan, L., and Zamorani, G. (2007). The First Release COSMOS Optical and Near-IR Data and Catalog. *ApJS*, 172:99–116.

Capak, P., Carilli, C. L., Lee, N., Aldcroft, T., Aussel, H., Schinnerer, E., Wilson, G. W., Yun, M. S., Blain, A., Giavalisco, M., Ilbert, O., Kartaltepe, J., Lee, K.-S., McCracken, H., Mobasher, B., Salvato, M., Sasaki, S., Scott, K. S., Sheth, K., Shioya, Y., Thompson, D., Elvis, M., Sanders, D. B., Scoville, N. Z., and Tanaguchi, Y. (2008). Spectroscopic Confirmation of an Extreme Starburst at Redshift 4.547. *ApJ*, 681:L53–L56.

Capak, P. L., Riechers, D., Scoville, N. Z., Carilli, C., Cox, P., Neri, R., Robertson, B., Salvato, M., Schinnerer, E., Yan, L., Wilson, G. W., Yun, M., Civano, F., Elvis, M., Karim, A., Mobasher, B., and Staguhn, J. G. (2011). A massive protocluster of galaxies at a redshift of z˜5.3. *Nature*, 470:233–235.

Carilli, C. L., Daddi, E., Riechers, D., Walter, F., Weiss, A., Dannerbauer, H., Morrison, G. E., Wagg, J., Davé, R., Elbaz, D., Stern, D., Dickinson, M., Krips, M., and Aravena, M. (2010). Imaging the Molecular Gas in a Submillimeter Galaxy at z = 4.05: Cold Mode Accretion or a Major Merger? *ApJ*, 714:1407–1417.

Carilli, C. L., Kohno, K., Kawabe, R., Ohta, K., Henkel, C., Menten, K. M., Yun, M. S., Petric, A., and Tutui, Y. (2002). High-Resolution Imaging of Molecular Line Emission from High-Redshift QSOs. *AJ*, 123:1838–1846.

Carilli, C. L., Lee, N., Capak, P., Schinnerer, E., Lee, K.-S., McCraken, H., Yun, M. S., Scoville, N., Smolčić, V., Giavalisco, M., Datta, A., Taniguchi, Y., and Urry, C. M. (2008). Star Formation Rates in Lyman Break Galaxies: Radio Stacking of LBGs in the COSMOS Field and the Sub-μJy Radio Source Population. *ApJ*, 689:883–888.

Chabrier, G. (2003). Galactic Stellar and Substellar Initial Mass Function. *PASP*, 115:763–795.

Chapman, S. C., Blain, A. W., Smail, I., and Ivison, R. J. (2005). A Redshift Survey of the Submillimeter Galaxy Population. *ApJ*, 622:772–796.

Charlot, S. and Fall, S. M. (2000). A Simple Model for the Absorption of Starlight by Dust in Galaxies. *ApJ*, 539:718–731.

Chary, R. and Elbaz, D. (2001). Interpreting the Cosmic Infrared Background: Constraints on the Evolution of the Dust-enshrouded Star Formation Rate. *ApJ*, 556:562–581.

Chary, R.-R. and Pope, A. (2010). New Observational Constraints and Modeling of the Infrared Background: Dust Obscured Star-Formation at z>1 and Dust in the Outer Solar System. *ArXiv e-prints*.

Cimatti, A., Daddi, E., Renzini, A., Cassata, P., Vanzella, E., Pozzetti, L., Cristiani, S., Fontana, A., Rodighiero, G., Mignoli, M., and Zamorani, G. (2004). Old galaxies in the young Universe. *Nature*, 430:184–187.

Cirasuolo, M., McLure, R. J., Dunlop, J. S., Almaini, O., Foucaud, S., and Simpson, C. (2010). A new measurement of the evolving near-infrared galaxy luminosity function out to z ˜= 4: a continuing challenge to theoretical models of galaxy formation. *MNRAS*, 401:1166–1176.

Cisternas, M., Jahnke, K., Inskip, K. J., Kartaltepe, J., Koekemoer, A. M., Lisker, T., Robaina, A. R., Scodeggio, M., Sheth, K., Trump, J. R., Andrae, R., Miyaji, T., Lusso, E., Brusa, M., Capak, P., Cappelluti, N., Civano, F., Ilbert, O., Impey, C. D., Leauthaud, A., Lilly, S. J., Salvato, M., Scoville, N. Z., and Taniguchi, Y. (2011). The Bulk of the Black Hole Growth Since z ˜ 1 Occurs in a Secular Universe: No Major Merger-AGN Connection. *ApJ*, 726:57–+.

Comastri, A. (2004). Compton-Thick AGN: The Dark Side of the X-Ray Background. In A. J. Barger, editor, *Supermassive Black Holes in the Distant Universe*, volume 308 of *Astrophysics and Space Science Library*, pages 245–+.

Condon, J. J. (1989). The 1.4 gigahertz luminosity function and its evolution. *ApJ*, 338:13–23.

Condon, J. J. (1992). Radio emission from normal galaxies. *ARA&A*, 30:575–611.

Condon, J. J. (1997). Errors in Elliptical Gaussian FITS. *PASP*, 109:166–172.

Condon, J. J., Cotton, W. D., and Broderick, J. J. (2002). Radio Sources and Star Formation in the Local Universe. *AJ*, 124:675–689.

Coppin, K. E. K., Chapman, S. C., Smail, I., Swinbank, A. M., Walter, F., Wardlow, J. L., Weiss, A., Alexander, D. M., Brandt, W. N., Dannerbauer, H., De Breuck, C., Dickinson, M., Dunlop, J. S., Edge, A. C., Emonts, B. H. C., Greve, T. R., Huynh, M., Ivison, R. J., Knudsen, K. K., Menten, K. M., Schinnerer, E., and van der Werf, P. P. (2010). Detection of molecular gas in a distant submillimetre galaxy at z = 4.76 with Australia Telescope Compact Array. *MNRAS*, 407:L103–L107.

Coppin, K. E. K., Smail, I., Alexander, D. M., Weiss, A., Walter, F., Swinbank, A. M., Greve, T. R., Kovacs, A., De Breuck, C., Dickinson, M., Ibar, E., Ivison, R. J., Reddy, N., Spinrad, H., Stern, D., Brandt, W. N., Chapman, S. C., Dannerbauer, H., van Dokkum, P., Dunlop, J. S., Frayer, D., Gawiser, E., Geach, J. E., Huynh, M., Knudsen, K. K., Koekemoer, A. M., Lehmer, B. D., Menten, K. M., Papovich, C., Rix, H.-W., Schinnerer, E., Wardlow, J. L., and van der Werf, P. P. (2009). A submillimetre galaxy at z = 4.76 in the LABOCA survey of the Extended Chandra Deep Field-South. *MNRAS*, 395:1905–1914.

Coppin, K. E. K., Swinbank, A. M., Neri, R., Cox, P., Alexander, D. M., Smail, I., Page, M. J., Stevens, J. A., Knudsen, K. K., Ivison, R. J., Beelen, A., Bertoldi, F., and Omont, A. (2008). Testing the evolutionary link between submillimetre galaxies and quasars: CO observations of QSOs at z ˜ 2. *MNRAS*, 389:45–62.

Cowie, L. L. and Barger, A. J. (2008). An Integrated Picture of Star Formation, Metallicity Evolution, and Galactic Stellar Mass Assembly. *ApJ*, 686:72–116.

Cowie, L. L., Songaila, A., Hu, E. M., and Cohen, J. G. (1996). New Insight on Galaxy Formation and Evolution From Keck Spectroscopy of the Hawaii Deep Fields. *AJ*, 112:839–+.

Cox, P., Krips, M., Neri, R., Omont, A., Gusten, R., Menten, K. M., Wyrowski, F., Weiss, A., Beelen, A., Gurwell, M. A., Dannerbauer, H., Ivison, R. J., Negrello, M., Aretxaga, I., Hughes, D. H., Auld, R., Baes, M., Blundell, R., Buttiglione, S., Cava, A., Cooray, A., Dariush, A., Dunne, L., Dye, S., Eales, S. A., Frayer, D., Fritz, J., Gavazzi, R., Hopwood, R., Ibar, E., Jarvis, M., Maddox, S., Michalowski, M., Pascale, E., Pohlen, M., Rigby, E., Smith, D. J. B., Swinbank, A. M., Temi, P., Valtchanov, I., van der Werf, P., and de Zotti, G. (2011). Gas and dust in a submillimeter galaxy at z = 4.24 from the Herschel ATLAS. *ArXiv e-prints*.

Croton, D. J., Springel, V., White, S. D. M., De Lucia, G., Frenk, C. S., Gao, L., Jenkins, A., Kauffmann, G., Navarro, J. F., and Yoshida, N. (2006). The many lives of active galactic nuclei: cooling flows, black holes and the luminosities and colours of galaxies. *MNRAS*, 365:11–28.

Daddi, E., Bournaud, F., Walter, F., Dannerbauer, H., Carilli, C. L., Dickinson, M., Elbaz, D., Morrison, G. E., Riechers, D., Onodera, M., Salmi, F., Krips, M., and Stern, D. (2010a). Very High Gas Fractions and Extended Gas Reservoirs in z = 1.5 Disk Galaxies. *ApJ*, 713:686–707.

Daddi, E., Cimatti, A., Renzini, A., Fontana, A., Mignoli, M., Pozzetti, L., Tozzi, P., and Zamorani, G. (2004). A New Photometric Technique for the Joint Selection of Star-forming and Passive Galaxies at 1.4 <˜ z <˜ 2.5. *ApJ*, 617:746–764.

Daddi, E., Dannerbauer, H., Krips, M., Walter, F., Dickinson, M., Elbaz, D., and Morrison, G. E. (2009a). A CO Emission Line from the Optical and Near-IR Undetected Submillimeter Galaxy GN10. *ApJ*, 695:L176–L180.

Daddi, E., Dannerbauer, H., Stern, D., Dickinson, M., Morrison, G., Elbaz, D., Giavalisco, M., Mancini, C., Pope, A., and Spinrad, H. (2009b). Two Bright Submillimeter Galaxies in a z = 4.05 Protocluster in Goods-North, and Accurate Radio-Infrared Photometric Redshifts. *ApJ*, 694:1517–1538.

Daddi, E., Dickinson, M., Morrison, G., Chary, R., Cimatti, A., Elbaz, D., Frayer, D., Renzini, A., Pope, A., Alexander, D. M., Bauer, F. E., Giavalisco, M., Huynh, M., Kurk, J., and Mignoli, M. (2007). Multiwavelength Study of Massive Galaxies at z˜2. I. Star Formation and Galaxy Growth. *ApJ*, 670:156–172.

Daddi, E., Elbaz, D., Walter, F., Bournaud, F., Salmi, F., Carilli, C., Dannerbauer, H., Dickinson, M., Monaco, P., and Riechers, D. (2010b). Different Star Formation Laws for Disks Versus Starbursts at Low and High Redshifts. *ApJ*, 714:L118–L122.

Damen, M., Förster Schreiber, N. M., Franx, M., Labbé, I., Toft, S., van Dokkum, P. G., and Wuyts, S. (2009a). Star Formation in the Chandra Deep Field South: Observations Confront Simulations. *ApJ*, 705:617–623.

Damen, M., Labbé, I., Franx, M., van Dokkum, P. G., Taylor, E. N., and Gawiser, E. J. (2009b). The Evolution of the Specific Star Formation Rate of Massive Galaxies to z ˜ 1.8 in the Extended Chandra Deep Field South. *ApJ*, 690:937–943.

Damen, M., Labbe, I., van Dokkum, P. G., Franx, M., Taylor, E. N., Brandt, W. N., Dickinson, M., Gawiser, E., Illingworth, G. D., Kriek, M., Marchesini, D., Muzzin, A., Papovich, C., and Rix, H. (2010). The SIMPLE survey: observations, reduction, and catalog. *ArXiv e-prints*.

Dannerbauer, H., Lehnert, M. D., Lutz, D., Tacconi, L., Bertoldi, F., Carilli, C., Genzel, R., and Menten, K. (2002). Properties of Millimeter Galaxies: Constraints from K-Band Blank Fields. *ApJ*, 573:473–484.

De Breuck, C., van Breugel, W., Stanford, S. A., Röttgering, H., Miley, G., and Stern, D. (2002). Optical and Near-Infrared Imaging of Ultra-Steep-Spectrum Radio Sources: The K-z Diagram of Radio-selected and Optically Selected Galaxies. *AJ*, 123:637–677.

Dib, S. (2011). Feedback-regulated Star Formation: Implications for the Kennicutt-Schmidt Law. *ApJ*, 737:L20+.

Donoso, E., Best, P. N., and Kauffmann, G. (2009). Evolution of the radio-loud galaxy population. *MNRAS*, 392:617–629.

Downes, D. and Solomon, P. M. (1998). Rotating Nuclear Rings and Extreme Starbursts in Ultraluminous Galaxies. *ApJ*, 507:615–654.

Downes, D. and Solomon, P. M. (2003). Molecular Gas and Dust at z=2.6 in SMM J14011+0252: A Strongly Lensed Ultraluminous Galaxy, Not a Huge Massive Disk. *ApJ*, 582:37–48.

Downes, D., Solomon, P. M., and Radford, S. J. E. (1993). Molecular gas mass and far-infrared emission from distant luminous galaxies. *ApJ*, 414:L13–L16.

Draine, B. T. (2003). Interstellar Dust Grains. *ARA&A*, 41:241–289.

Draine, B. T. and Lee, H. M. (1984). Optical properties of interstellar graphite and silicate grains. *ApJ*, 285:89–108.

Dumas, G., Schinnerer, E., Tabatabaei, F. S., Beck, R., Velusamy, T., and Murphy, E. (2011). The Local Radio-IR Relation in M51. *AJ*, 141:41–+.

Dunne, L., Eales, S. A., and Edmunds, M. G. (2003). A census of metals at high and low redshift and the connection between submillimetre sources and spheroid formation. *MNRAS*, 341:589–598.

Dunne, L., Ivison, R. J., Maddox, S., Cirasuolo, M., Mortier, A. M., Foucaud, S., Ibar, E., Almaini, O., Simpson, C., and McLure, R. (2009). The star formation history of K-selected galaxies. *MNRAS*, 394:3–20.

Dutton, A. A., van den Bosch, F. C., and Dekel, A. (2010). On the origin of the galaxy star-formation-rate sequence: evolution and scatter. *MNRAS*, 405:1690–1710.

Dwek, E., Staguhn, J. G., Arendt, R. G., Capak, P. L., Kovacs, A., Benford, D. J., Fixsen, D., Karim, A., Leclercq, S., Maher, S. F., Moseley, S. H., Schinnerer, E., and Sharp, E. H. (2011). Star and Dust Formation Activities in AzTEC-3, a Starburst Galaxy at z = 5.3. *ApJ*, 738:36–+.

Elbaz, D., Daddi, E., Le Borgne, D., Dickinson, M., Alexander, D. M., Chary, R., Starck, J., Brandt, W. N., Kitzbichler, M., MacDonald, E., Nonino, M., Popesso, P., Stern, D., and Vanzella, E. (2007). The reversal of the star formation-density relation in the distant universe. *A&A*, 468:33–48.

Elbaz, D., Dickinson, M., Hwang, H. S., Diaz-Santos, T., Magdis, G., Magnelli, B., Le Borgne, D., Galliano, F., Pannella, M., Chanial, P., Armus, L., Charmandaris, V., Daddi, E., Aussel, H., Popesso, P., Kartaltepe, J., Altieri, B., Valtchanov, I., Coia, D., Dannerbauer, H., Dasyra, K., Leiton, R., Mazzarella, J., Buat, V., Burgarella, D., Chary, R. ., Gilli, R., Ivison, R. J., Juneau, S., LeFloc'h, E., Lutz, D., Morrison, G. E., Mullaney, J., Murphy, E., Pope, A., Scott, D., Alexander, D., Brodwin, M., Calzetti, D., Cesarsky, C., Charlot, S., Dole, H., Eisenhardt, P., Ferguson, H. C., Foerster-Schreiber, N., Frayer, D., Giavalisco, M., Huynh, M., Koekemoer, A. M., Papovich, C., Reddy, N., Surace, C., Teplitz, H., Yun, M. S., and Wilson, G. (2011). GOODS-Herschel: an infrared main sequence for star-forming galaxies. *ArXiv e-prints*.

Elbaz, D., Hwang, H. S., Magnelli, B., Daddi, E., Aussel, H., Altieri, B., Amblard, A., Andreani, P., Arumugam, V., Auld, R., Babbedge, T., Berta, S., Blain, A., Bock, J., Bongiovanni, A., Boselli, A., Buat, V., Burgarella, D., Castro-Rodriguez, N., Cava, A., Cepa, J., Chanial, P., Chary, R., Cimatti, A., Clements, D. L., Conley, A., Conversi, L., Cooray, A., Dickinson, M., Dominguez, H., Dowell, C. D., Dunlop, J. S., Dwek, E., Eales, S., Farrah, D., Förster Schreiber, N., Fox, M., Franceschini, A., Gear, W., Genzel, R., Glenn, J., Griffin,

M., Gruppioni, C., Halpern, M., Hatziminaoglou, E., Ibar, E., Isaak, K., Ivison, R. J., Lagache, G., Le Borgne, D., Le Floc'h, E., Levenson, L., Lu, N., Lutz, D., Madden, S., Maffei, B., Magdis, G., Mainetti, G., Maiolino, R., Marchetti, L., Mortier, A. M. J., Nguyen, H. T., Nordon, R., O'Halloran, B., Okumura, K., Oliver, S. J., Omont, A., Page, M. J., Panuzzo, P., Papageorgiou, A., Pearson, C. P., Perez Fournon, I., Pérez García, A. M., Poglitsch, A., Pohlen, M., Popesso, P., Pozzi, F., Rawlings, J. I., Rigopoulou, D., Riguccini, L., Rizzo, D., Rodighiero, G., Roseboom, I. G., Rowan-Robinson, M., Saintonge, A., Sanchez Portal, M., Santini, P., Sauvage, M., Schulz, B., Scott, D., Seymour, N., Shao, L., Shupe, D. L., Smith, A. J., Stevens, J. A., Sturm, E., Symeonidis, M., Tacconi, L., Trichas, M., Tugwell, K. E., Vaccari, M., Valtchanov, I., Vieira, J., Vigroux, L., Wang, L., Ward, R., Wright, G., Xu, C. K., and Zemcov, M. (2010). Herschel unveils a puzzling uniformity of distant dusty galaxies. *A&A*, 518:L29+.

Elvis, M., Civano, F., Vignali, C., Puccetti, S., Fiore, F., Cappelluti, N., Aldcroft, T. L., Fruscione, A., Zamorani, G., Comastri, A., Brusa, M., Gilli, R., Miyaji, T., Damiani, F., Koekemoer, A. M., Finoguenov, A., Brunner, H., Urry, C. M., Silverman, J., Mainieri, V., Hasinger, G., Griffiths, R., Carollo, M., Hao, H., Guzzo, L., Blain, A., Calzetti, D., Carilli, C., Capak, P., Ettori, S., Fabbiano, G., Impey, C., Lilly, S., Mobasher, B., Rich, M., Salvato, M., Sanders, D. B., Schinnerer, E., Scoville, N., Shopbell, P., Taylor, J. E., Taniguchi, Y., and Volonteri, M. (2009). The Chandra COSMOS Survey. I. Overview and Point Source Catalog. *ApJS*, 184:158–171.

Engel, H., Tacconi, L. J., Davies, R. I., Neri, R., Smail, I., Chapman, S. C., Genzel, R., Cox, P., Greve, T. R., Ivison, R. J., Blain, A., Bertoldi, F., and Omont, A. (2010). Most Submillimeter Galaxies are Major Mergers. *ApJ*, 724:233–243.

Erb, D. K., Steidel, C. C., Shapley, A. E., Pettini, M., Reddy, N. A., and Adelberger, K. L. (2006). Hα Observations of a Large Sample of Galaxies at z ˜ 2: Implications for Star Formation in High-Redshift Galaxies. *ApJ*, 647:128–139.

Faber, S. M., Phillips, A. C., Kibrick, R. I., Alcott, B., Allen, S. L., Burrous, J., Cantrall, T., Clarke, D., Coil, A. L., Cowley, D. J., Davis, M., Deich, W. T. S., Dietsch, K., Gilmore, D. K., Harper, C. A., Hilyard, D. F., Lewis, J. P., McVeigh, M., Newman, J., Osborne, J., Schiavon, R., Stover, R. J., Tucker, D., Wallace, V., Wei, M., Wirth, G., and Wright, C. A. (2003). The DEIMOS spectrograph for the Keck II Telescope: integration and testing. In M. Iye & A. F. M. Moorwood, editor, *Society of Photo-Optical Instrumentation Engineers (SPIE) Conference Series*, volume 4841 of *Society of Photo-Optical Instrumentation Engineers (SPIE) Conference Series*, pages 1657–1669.

Faber, S. M., Willmer, C. N. A., Wolf, C., Koo, D. C., Weiner, B. J., Newman, J. A., Im, M., Coil, A. L., Conroy, C., Cooper, M. C., Davis, M., Finkbeiner, D. P., Gerke, B. F., Gebhardt, K., Groth, E. J., Guhathakurta, P., Harker, J., Kaiser, N., Kassin, S., Kleinheinrich, M., Konidaris, N. P., Kron, R. G., Lin, L., Luppino, G., Madgwick, D. S., Meisenheimer, K., Noeske, K. G., Phillips, A. C., Sarajedini, V. L., Schiavon, R. P., Simard, L., Szalay, A. S., Vogt, N. P., and Yan, R. (2007). Galaxy Luminosity Functions to z˜1 from DEEP2 and COMBO-17: Implications for Red Galaxy Formation. *ApJ*, 665:265–294.

Fanaroff, B. L. and Riley, J. M. (1974). The morphology of extragalactic radio sources of high and low luminosity. *MNRAS*, 167:31P–36P.

Feulner, G., Gabasch, A., Salvato, M., Drory, N., Hopp, U., and Bender, R. (2005a). Specific Star Formation Rates to Redshift 5 from the FORS Deep Field and the GOODS-S Field. *ApJ*, 633:L9–L12.

Feulner, G., Goranova, Y., Drory, N., Hopp, U., and Bender, R. (2005b). The connection between star formation and stellar mass: specific star formation rates to redshift one. *MNRAS*, 358:L1–L5.

Filho, M. E., Barthel, P. D., and Ho, L. C. (2006). A radio census of nuclear activity in nearby galaxies. *A&A*, 451:71–83.

Finkelstein, S. L., Papovich, C., Giavalisco, M., Reddy, N. A., Ferguson, H. C., Koekemoer, A. M., and Dickinson, M. (2009). On the Stellar Populations and Evolution of Star-Forming Galaxies at $6.3 < z < 8.6$. *ArXiv e-prints*.

Firmani, C., Avila-Reese, V., and Rodríguez-Puebla, A. (2010). Can galaxy outflows and re-accretion produce a downsizing in the specific star-formation rate of late-type galaxies? *MNRAS*, 404:1100–1110.

Fontanot, F., De Lucia, G., Monaco, P., Somerville, R. S., and Santini, P. (2009). The many manifestations of downsizing: hierarchical galaxy formation models confront observations. *MNRAS*, 397:1776–1790.

Forbes, D. A. and Kroupa, P. (2011). What Is a Galaxy? Cast Your Vote Here. *PASA*, 28:77–82.

Ford, H. C., Clampin, M., Hartig, G. F., Illingworth, G. D., Sirianni, M., Martel, A. R., Meurer, G. R., McCann, W. J., Sullivan, P. C., Bartko, F., Benitez, N., Blakeslee, J., Bouwens, R., Broadhurst, T., Brown, R. A., Burrows, C. J., Campbell, D., Cheng, E. S., Feldman, P. D., Franx, M., Golimowski, D. A., Gronwall, C., Kimble, R. A., Krist, J. E., Lesser, M. P., Magee, D., Miley, G., Postman, M., Rafal, M. D., Rosati, P., Sparks, W. B., Tran, H. D., Tsvetanov, Z. I., Volmer, P., White, R. L., and Woodruff, R. A. (2003). Overview of the Advanced Camera for Surveys on-orbit performance. In J. C. Blades & O. H. W. Siegmund, editor, *Society of Photo-Optical Instrumentation Engineers (SPIE) Conference Series*, volume 4854 of *Society of Photo-Optical Instrumentation Engineers (SPIE) Conference Series*, pages 81–94.

Frayer, D. T., Ivison, R. J., Scoville, N. Z., Evans, A. S., Yun, M. S., Smail, I., Barger, A. J., Blain, A. W., and Kneib, J.-P. (1999). Molecular Gas in the Z = 2.565 Submillimeter Galaxy SMM J14011+0252. *ApJ*, 514:L13–L16.

Frayer, D. T., Ivison, R. J., Scoville, N. Z., Yun, M., Evans, A. S., Smail, I., Blain, A. W., and Kneib, J.-P. (1998). Molecular Gas in the Z = 2.8 Submillimeter Galaxy SMM 02399-0136. *ApJ*, 506:L7–L10.

Freedman, W. L., Madore, B. F., Gibson, B. K., Ferrarese, L., Kelson, D. D., Sakai, S., Mould, J. R., Kennicutt, Jr., R. C., Ford, H. C., Graham, J. A., Huchra, J. P., Hughes, S. M. G., Illingworth, G. D., Macri, L. M., and Stetson, P. B. (2001). Final Results from the Hubble Space Telescope Key Project to Measure the Hubble Constant. *ApJ*, 553:47–72.

Frenk, C. S., Colberg, J. M., Couchman, H. M. P., Efstathiou, G., Evrard, A. E., Jenkins, A., MacFarland, T. J., Moore, B., Peacock, J. A., Pearce, F. R., Thomas, P. A., White, S. D. M., and Yoshida, N. (2000). Public Release of N-body simulation and related data by the Virgo consortium. *ArXiv Astrophysics e-prints*.

Gallerani, S., Maiolino, R., Juarez, Y., Nagao, T., Marconi, A., Bianchi, S., Schneider, R., Mannucci, F., Oliva, T., Willott, C. J., Jiang, L., and Fan, X. (2010). The extinction law at high redshift and its implications. *ArXiv e-prints*.

Garn, T. and Alexander, P. (2009). Radio source stacking and the infrared/radio correlation at μJy flux densities. *MNRAS*, 394:105–116.

Genzel, R., Baker, A. J., Tacconi, L. J., Lutz, D., Cox, P., Guilloteau, S., and Omont, A. (2003). Spatially Resolved Millimeter Interferometry of SMM J02399-0136: AVery Massive Galaxy at z = 2.8. *ApJ*, 584:633–642.

Genzel, R., Tacconi, L. J., Gracia-Carpio, J., Sternberg, A., Cooper, M. C., Shapiro, K., Bolatto, A., Bouche, N., Bournaud, F., Burkert, A., Combes, F., Comerford, J., Cox, P., Davis, M., Foerster Schreiber, N. M., Garcia-Burillo, S., Lutz, D., Naab, T., Neri, R., Omont, A., Shapley, A., and Weiner, B. (2010). A Study of the Gas-Star Formation Relation over Cosmic Time. *ArXiv e-prints*.

Giacconi, R., Rosati, P., Tozzi, P., Nonino, M., Hasinger, G., Norman, C., Bergeron, J., Borgani, S., Gilli, R., Gilmozzi, R., and Zheng, W. (2001). First Results from the X-Ray and Optical Survey of the Chandra Deep Field South. *ApJ*, 551:624–634.

Giavalisco, M., Ferguson, H. C., Koekemoer, A. M., Dickinson, M., Alexander, D. M., Bauer, F. E., Bergeron, J., Biagetti, C., Brandt, W. N., Casertano, S., Cesarsky, C., Chatzichristou, E., Conselice, C., Cristiani, S., Da Costa, L., Dahlen, T., de Mello, D., Eisenhardt, P., Erben, T., Fall, S. M., Fassnacht, C., Fosbury, R., Fruchter, A., Gardner, J. P., Grogin, N., Hook, R. N., Hornschemeier, A. E., Idzi, R., Jogee, S., Kretchmer, C., Laidler, V., Lee, K. S., Livio, M., Lucas, R., Madau, P., Mobasher, B., Moustakas, L. A., Nonino, M., Padovani, P., Papovich, C., Park, Y., Ravindranath, S., Renzini, A., Richardson, M., Riess, A., Rosati, P., Schirmer, M., Schreier, E., Somerville, R. S., Spinrad, H., Stern, D., Stiavelli, M., Strolger, L., Urry, C. M., Vandame, B., Williams, R., and Wolf, C. (2004). The Great Observatories Origins Deep Survey: Initial Results from Optical and Near-Infrared Imaging. *ApJ*, 600:L93–L98.

Gilbank, D. G., Baldry, I. K., Balogh, M. L., Glazebrook, K., and Bower, R. G. (2010a). The local star formation rate density: assessing calibrations using [OII], H and UV luminosities. *MNRAS*, 405:2594–2614.

Gilbank, D. G., Balogh, M. L., Glazebrook, K., Bower, R. G., Baldry, I. K., Davies, G. T., Hau, G. K. T., Li, I. H., and McCarthy, P. (2010b). The Redshift One LDSS-3 Emission line Survey (ROLES): survey method and z ˜ 1 mass-dependent star formation rate density. *MNRAS*, 405:2419–2438.

Glover, S. C. O. and Clark, P. C. (2011). Is molecular gas necessary for star formation? *ArXiv e-prints*.

González, V., Labbé, I., Bouwens, R. J., Illingworth, G., Franx, M., Kriek, M., and Brammer, G. B. (2010). The Stellar Mass Density and Specific Star Formation Rate of the Universe at z ˜ 7. *ApJ*, 713:115–130.

Gorgas, J., Cardiel, N., Pedraz, S., and González, J. J. (1999). Empirical calibration of the lambda 4000 Å break. *A&AS*, 139:29–41.

Graciá-Carpio, J., Sturm, E., Hailey-Dunsheath, S., Fischer, J., Contursi, A., Poglitsch, A., Genzel, R., González-Alfonso, E., Sternberg, A., Verma, A., Christopher, N., Davies, R., Feuchtgruber, H., de Jong, J. A., Lutz, D., and Tacconi, L. J. (2011). Far-infrared Line Deficits in Galaxies with Extreme L_{FIR}/M_{H_{2}} Ratios. *ApJ*, 728:L7+.

Greve, T. R., Bertoldi, F., Smail, I., Neri, R., Chapman, S. C., Blain, A. W., Ivison, R. J., Genzel, R., Omont, A., Cox, P., Tacconi, L., and Kneib, J.-P. (2005). An interferometric CO survey of luminous submillimetre galaxies. *MNRAS*, 359:1165–1183.

Greve, T. R., Ivison, R. J., Bertoldi, F., Stevens, J. A., Dunlop, J. S., Lutz, D., and Carilli, C. L. (2004). A 1200-μm MAMBO survey of ELAISN2 and the Lockman Hole - I. Maps, sources and number counts. *MNRAS*, 354:779–797.

Greve, T. R., Ivison, R. J., and Papadopoulos, P. P. (2003). Gas and Dust in the Extremely Red Object ERO J164502+4626.4. *ApJ*, 599:839–846.

Greve, T. R., Weiβ, A., Walter, F., Smail, I., Zheng, X. Z., Knudsen, K. K., Coppin, K. E. K., Kovács, A., Bell, E. F., de Breuck, C., Dannerbauer, H., Dickinson, M., Gawiser, E., Lutz, D., Rix, H.-W., Schinnerer, E., Alexander, D., Bertoldi, F., Brandt, N., Chapman, S. C., Ivison, R. J., Koekemoer, A. M., Kreysa, E., Kurczynski, P., Menten, K., Siringo, G., Swinbank, M., and van der Werf, P. (2010). A LABOCA Survey of the Extended Chandra Deep Field South – Submillimeter Properties of Near-infrared Selected Galaxies. *ApJ*, 719:483–496.

Griffith, R. L. and Stern, D. (2010). Morphologies of Radio-, X-ray-, and Mid-infrared-selected Active Galactic Nuclei. *AJ*, 140:533–545.

Gruppioni, C., Pozzi, F., Andreani, P., Rodighiero, G., Cimatti, A., Altieri, B., Aussel, H., Berta, S., Bongiovanni, A., Brisbin, D., Cava, A., Cepa, J., Daddi, E., Dominguez-Sanchez, H., Elbaz, D., Förster Schreiber, N., Genzel, R., Le Floc'h, E., Lutz, D., Magdis, G., Magliocchetti, M., Magnelli, B., Maiolino, R., Nordon, R., Peréz-García, A. M., Poglitsch, A., Popesso, P., Riguccini, L., Saintonge, A., Sanchez-Portal, M., Santini, P., Shao, L., Sturm, E., Tacconi, L., and Valtchanov, I. (2010). PEP: First Herschel probe of dusty galaxy evolution up to z ˜ 3. *A&A*, 518:L27+.

Guilloteau, S., Delannoy, J., Downes, D., Greve, A., Guelin, M., Lucas, R., Morris, D., Radford, S. J. E., Wink, J., Cernicharo, J., Forveille, T., Garcia-Burillo, S., Neri, R., Blondel, J., Perrigourad, A., Plathner, D., and Torres, M. (1992). The IRAM interferometer on Plateau de Bure. *A&A*, 262:624–633.

Guilloteau, S. and Lucas, R. (2000). Imaging at the IRAM Plateau de Bure Interferometer. In J. G. Mangum & S. J. E. Radford, editor, *Imaging at Radio through Submillimeter Wavelengths*, volume 217 of *Astronomical Society of the Pacific Conference Series*, pages 299–+.

Guo, Q. and White, S. D. M. (2008). Galaxy growth in the concordance ÎŻcdm cosmology. *Monthly Notices of the Royal Astronomical Society*, 384:2.

Haarsma, D. B., Partridge, R. B., Windhorst, R. A., and Richards, E. A. (2000). Faint Radio Sources and Star Formation History. *ApJ*, 544:641–658.

Hainline, L. J., Blain, A. W., Greve, T. R., Chapman, S. C., Smail, I., and Ivison, R. J. (2006). Observing Cold Gas in Submillimeter Galaxies: Detection of CO (1-0) Emission in SMM J13120+4242 with the Green Bank Telescope. *ApJ*, 650:614–623.

Hasinger, G., Cappelluti, N., Brunner, H., Brusa, M., Comastri, A., Elvis, M., Finoguenov, A., Fiore, F., Franceschini, A., Gilli, R., Griffiths, R. E., Lehmann, I., Mainieri, V., Matt, G., Matute, I., Miyaji, T., Molendi, S., Paltani, S., Sanders, D. B., Scoville, N., Tresse, L., Urry, C. M., Vettolani, P., and Zamorani, G. (2007). The XMM-Newton Wide-Field Survey in the COSMOS Field. I. Survey Description. *ApJS*, 172:29–37.

Hauser, M. G. and Dwek, E. (2001). The Cosmic Infrared Background: Measurements and Implications. *ARA&A*, 39:249–307.

Hayward, C. C., Kereš, D., Jonsson, P., Narayanan, D., Cox, T. J., and Hernquist, L. (2011a). What Does a Submillimeter Galaxy Selection Actually Select? The Dependence of Submillimeter Flux Density on Star Formation Rate and Dust Mass. *ArXiv e-prints*.

Hayward, C. C., Narayanan, D., Jonsson, P., Cox, T. J., Kereš, D., Hopkins, P. F., and Hernquist, L. (2011b). Do Sub-Millimeter Galaxy Number Counts Provide Evidence for a Top-Heavy IMF? In M. Treyer, T. Wyder, J. Neill, M. Seibert, & J. Lee, editor, *UP2010: Have Observations Revealed a Variable Upper End of the Initial Mass Function?*, volume 440 of *Astronomical Society of the Pacific Conference Series*, pages 369–+.

Helou, G., Soifer, B. T., and Rowan-Robinson, M. (1985). Thermal infrared and nonthermal radio - Remarkable correlation in disks of galaxies. *ApJ*, 298:L7–L11.

Hickox, R. C., Jones, C., Forman, W. R., Murray, S. S., Kochanek, C. S., Eisenstein, D., Jannuzi, B. T., Dey, A., Brown, M. J. I., Stern, D., Eisenhardt, P. R., Gorjian, V., Brodwin, M., Narayan, R., Cool, R. J., Kenter, A., Caldwell, N., and Anderson, M. E. (2009). Host Galaxies, Clustering, Eddington Ratios, and Evolution of Radio, X-Ray, and Infrared-Selected AGNs. *ApJ*, 696:891–919.

Ho, P. T. P., Moran, J. M., and Lo, K. Y. (2004). The Submillimeter Array. *ApJ*, 616:L1–L6.

Hogg, D. W. (1999). Distance measures in cosmology. *ArXiv Astrophysics e-prints*.

Hogg, D. W., Baldry, I. K., Blanton, M. R., and Eisenstein, D. J. (2002). The K correction. *ArXiv Astrophysics e-prints*.

Hopkins, A. M. (2004). On the Evolution of Star-forming Galaxies. *ApJ*, 615:209–221.

Hopkins, A. M., Afonso, J., Chan, B., Cram, L. E., Georgakakis, A., and Mobasher, B. (2003). The Phoenix Deep Survey: The 1.4 GHz Microjansky Catalog. *AJ*, 125:465–477.

Hopkins, A. M. and Beacom, J. F. (2006). On the Normalization of the Cosmic Star Formation History. *ApJ*, 651:142–154.

Hwang, H. S., Elbaz, D., Magdis, G., Daddi, E., Symeonidis, M., Altieri, B., Amblard, A., Andreani, P., Arumugam, V., Auld, R., Aussel, H., Babbedge, T., Berta, S., Blain, A., Bock, J., Bongiovanni, A., Boselli, A., Buat, V., Burgarella, D., Castro-Rodríguez, N., Cava, A., Cepa, J., Chanial, P., Chapin, E., Chary, R.-R., Cimatti, A., Clements, D. L., Conley, A., Conversi, L., Cooray, A., Dannerbauer, H., Dickinson, M., Dominguez, H., Dowell, C. D., Dunlop, J. S., Dwek, E., Eales, S., Farrah, D., Schreiber, N. F., Fox, M., Franceschini, A., Gear, W., Genzel, R., Glenn, J., Griffin, M., Gruppioni, C., Halpern, M., Hatziminaoglou, E., Ibar, E., Isaak, K., Ivison, R. J., Jeong, W.-S., Lagache, G., Le Borgne, D., Le Floc'h, E., Lee, H. M., Lee, J. C., Lee, M. G., Levenson, L., Lu, N., Lutz, D., Madden, S., Maffei, B., Magnelli, B., Mainetti, G., Maiolino, R., Marchetti, L., Mortier, A. M. J., Nguyen, H. T., Nordon, R., O'Halloran, B., Okumura, K., Oliver, S. J., Omont, A., Page, M. J., Panuzzo, P., Papageorgiou, A., Pearson, C. P., Pérez-Fournon, I., García, A. M. P., Poglitsch, A., Pohlen, M., Popesso, P., Pozzi, F., Rawlings, J. I., Rigopoulou, D., Riguccini, L., Rizzo, D., Rodighiero, G., Roseboom, I. G., Rowan-Robinson, M., Saintonge, A., Portal, M. S., Santini, P., Sauvage, M., Schulz, B., Scott, D., Seymour, N., Shao, L., Shupe, D. L., Smith, A. J., Stevens, J. A., Sturm, E., Tacconi, L., Trichas, M., Tugwell, K. E., Vaccari, M., Valtchanov, I., Vieira, J. D., Vigroux, L., Wang, L., Ward, R., Wright, G., Xu, C. K., and Zemcov, M. (2010). Evolution of dust temperature of galaxies through cosmic time as seen by Herschel. *MNRAS*, 409:75–82.

Ilbert, O., Arnouts, S., McCracken, H. J., Bolzonella, M., Bertin, E., Le Fèvre, O., Mellier, Y., Zamorani, G., Pellò, R., Iovino, A., Tresse, L., Le Brun, V., Bottini, D., Garilli, B., Maccagni, D., Picat, J. P., Scaramella, R., Scodeggio, M., Vettolani, G., Zanichelli, A., Adami, C., Bardelli, S., Cappi, A., Charlot, S., Ciliegi, P., Contini, T., Cucciati, O., Foucaud, S., Franzetti, P., Gavignaud, I., Guzzo, L., Marano, B., Marinoni, C., Mazure, A., Meneux, B., Merighi, R., Paltani, S., Pollo, A., Pozzetti, L., Radovich, M., Zucca, E., Bondi, M., Bongiorno, A., Busarello, G., de La Torre, S., Gregorini, L., Lamareille, F., Mathez, G., Merluzzi, P., Ripepi, V., Rizzo, D., and Vergani, D. (2006). Accurate photometric redshifts for the CFHT legacy survey calibrated using the VIMOS VLT deep survey. *A&A*, 457:841–856.

Ilbert, O., Capak, P., Salvato, M., Aussel, H., McCracken, H. J., Sanders, D. B., Scoville, N., Kartaltepe, J., Arnouts, S., Floc'h, E. L., Mobasher, B., Taniguchi, Y., Lamareille, F., Leauthaud, A., Sasaki, S., Thompson, D., Zamojski, M., Zamorani, G., Bardelli, S., Bolzonella, M., Bongiorno, A., Brusa, M., Caputi, K. I., Carollo, C. M., Contini, T., Cook, R., Coppa, G., Cucciati, O., de la Torre, S., de Ravel, L., Franzetti, P., Garilli, B., Hasinger, G., Iovino, A., Kampczyk, P., Kneib, J.-P., Knobel, C., Kovac, K., LeBorgne, J. F., LeBrun, V., Fèvre, O. L., Lilly, S., Looper, D., Maier, C., Mainieri, V., Mellier, Y., Mignoli, M., Murayama, T., Pellò, R., Peng, Y., Pérez-Montero, E., Renzini, A., Ricciardelli, E., Schiminovich, D., Scodeggio, M., Shioya, Y., Silverman, J., Surace, J., Tanaka, M., Tasca, L., Tresse, L., Vergani, D., and Zucca, E. (2009). Cosmos Photometric Redshifts with 30-Bands for 2-deg^2. *ApJ*, 690:1236–1249.

Ilbert, O., Salvato, M., Le Floc'h, E., Aussel, H., Capak, P., McCracken, H. J., Mobasher, B., Kartaltepe, J., Scoville, N., Sanders, D. B., Arnouts, S., Bundy, K., Cassata, P., Kneib, J., Koekemoer, A., Le Fèvre, O., Lilly, S., Surace, J., Taniguchi, Y., Tasca, L., Thompson,

D., Tresse, L., Zamojski, M., Zamorani, G., and Zucca, E. (2010). Galaxy Stellar Mass Assembly Between 0.2 < z < 2 from the S-COSMOS Survey. *ApJ*, 709:644–663.

Ilbert, O., Tresse, L., Zucca, E., Bardelli, S., Arnouts, S., Zamorani, G., Pozzetti, L., Bottini, D., Garilli, B., Le Brun, V., Le Fèvre, O., Maccagni, D., Picat, J., Scaramella, R., Scodeggio, M., Vettolani, G., Zanichelli, A., Adami, C., Arnaboldi, M., Bolzonella, M., Cappi, A., Charlot, S., Contini, T., Foucaud, S., Franzetti, P., Gavignaud, I., Guzzo, L., Iovino, A., McCracken, H. J., Marano, B., Marinoni, C., Mathez, G., Mazure, A., Meneux, B., Merighi, R., Paltani, S., Pello, R., Pollo, A., Radovich, M., Bondi, M., Bongiorno, A., Busarello, G., Ciliegi, P., Lamareille, F., Mellier, Y., Merluzzi, P., Ripepi, V., and Rizzo, D. (2005). The VIMOS-VLT deep survey. Evolution of the galaxy luminosity function up to z = 2 in first epoch data. *A&A*, 439:863–876.

Ivison, R. J., Papadopoulos, P. P., Smail, I., Greve, T. R., Thomson, A. P., Xilouris, E. M., and Chapman, S. C. (2011). Tracing the molecular gas in distant submillimetre galaxies via CO(1-0) imaging with the Expanded Very Large Array. *MNRAS*, 412:1913–1925.

Iwata, I., Ohta, K., Tamura, N., Akiyama, M., Aoki, K., Ando, M., Kiuchi, G., and Sawicki, M. (2007). Differential evolution of the UV luminosity function of Lyman break galaxies from z ˜ 5 to 3. *MNRAS*, 376:1557–1576.

Juneau, S., Glazebrook, K., Crampton, D., McCarthy, P. J., Savaglio, S., Abraham, R., Carlberg, R. G., Chen, H., Le Borgne, D., Marzke, R. O., Roth, K., Jørgensen, I., Hook, I., and Murowinski, R. (2005). Cosmic Star Formation History and Its Dependence on Galaxy Stellar Mass. *ApJ*, 619:L135–L138.

Karim, A., Schinnerer, E., Martínez-Sansigre, A., Sargent, M. T., van der Wel, A., Rix, H.-W., Ilbert, O., Smolčić, V., Carilli, C., Pannella, M., Koekemoer, A. M., Bell, E. F., and Salvato, M. (2011a). The Star Formation History of Mass-selected Galaxies in the COSMOS Field. *ApJ*, 730:61–91.

Karim, A., Schinnerer, E., and the VLA-COSMOS and COSMOS collaborations (2011b). A constant characteristic mass for star forming galaxies since $z \sim 3$ revealed by radio emission in the COSMOS field. *ArXiv e-prints*.

Kauffmann, G., Colberg, J. M., Diaferio, A., and White, S. D. M. (1999). Clustering of galaxies in a hierarchical universe - I. Methods and results at z=0. *MNRAS*, 303:188–206.

Kennicutt, Jr., R. C. (1998a). Star Formation in Galaxies Along the Hubble Sequence. *ARA&A*, 36:189–232.

Kennicutt, Jr., R. C. (1998b). The Global Schmidt Law in Star-forming Galaxies. *ApJ*, 498:541–552.

Kereš, D., Katz, N., Weinberg, D. H., and Davé, R. (2005). How do galaxies get their gas? *MNRAS*, 363:2–28.

Khochfar, S. and Silk, J. (2010). Understanding the specific star formation rate of high redshift galaxies: the case for two modes of star formation. *ArXiv e-prints*.

Klöckner, H.-R., Martínez-Sansigre, A., Rawlings, S., and Garrett, M. A. (2009). High-redshift obscured quasars: radio emission at sub-kiloparsec scales. *MNRAS*, 398:176–188.

Kneib, J.-P., Neri, R., Smail, I., Blain, A., Sheth, K., van der Werf, P., and Knudsen, K. K. (2005). Molecular gas in a z∼2.5 triply-imaged, sub-mJy submillimetre galaxy typical of the cosmic far-infrared background. *A&A*, 434:819–825.

Knobel, C., Lilly, S. J., Iovino, A., Porciani, C., Kovač, K., Cucciati, O., Finoguenov, A., Kitzbichler, M. G., Carollo, C. M., Contini, T., Kneib, J.-P., Le Fèvre, O., Mainieri, V., Renzini, A., Scodeggio, M., Zamorani, G., Bardelli, S., Bolzonella, M., Bongiorno, A., Caputi, K., Coppa, G., de la Torre, S., de Ravel, L., Franzetti, P., Garilli, B., Kampczyk, P., Lamareille, F., Le Borgne, J.-F., Le Brun, V., Maier, C., Mignoli, M., Pello, R., Peng, Y., Perez Montero, E., Ricciardelli, E., Silverman, J. D., Tanaka, M., Tasca, L., Tresse, L., Vergani, D., Zucca, E., Abbas, U., Bottini, D., Cappi, A., Cassata, P., Cimatti, A., Fumana, M., Guzzo, L., Koekemoer, A. M., Leauthaud, A., Maccagni, D., Marinoni, C., McCracken, H. J., Memeo, P., Meneux, B., Oesch, P., Pozzetti, L., and Scaramella, R. (2009). An Optical Group Catalog to z = 1 from the zCOSMOS 10 k Sample. *ApJ*, 697:1842–1860.

Knudsen, K. K., Kneib, J.-P., Richard, J., Petitpas, G., and Egami, E. (2010). Physical Properties and Morphology of a Newly Identified Compact z = 4.04 Lensed Submillimeter Galaxy in Abell 2218. *ApJ*, 709:210–217.

Koekemoer, A. M., Aussel, H., Calzetti, D., Capak, P., Giavalisco, M., Kneib, J.-P., Leauthaud, A., Le Fèvre, O., McCracken, H. J., Massey, R., Mobasher, B., Rhodes, J., Scoville, N., and Shopbell, P. L. (2007). The COSMOS Survey: Hubble Space Telescope Advanced Camera for Surveys Observations and Data Processing. *ApJS*, 172:196–202.

Komatsu, E., Dunkley, J., Nolta, M. R., Bennett, C. L., Gold, B., Hinshaw, G., Jarosik, N., Larson, D., Limon, M., Page, L., Spergel, D. N., Halpern, M., Hill, R. S., Kogut, A., Meyer, S. S., Tucker, G. S., Weiland, J. L., Wollack, E., and Wright, E. L. (2009). Five-Year Wilkinson Microwave Anisotropy Probe Observations: Cosmological Interpretation. *ApJS*, 180:330–376.

Kovács, A., Chapman, S. C., Dowell, C. D., Blain, A. W., Ivison, R. J., Smail, I., and Phillips, T. G. (2006). SHARC-2 350 μm Observations of Distant Submillimeter-selected Galaxies. *ApJ*, 650:592–603.

Kovač, K., Lilly, S. J., Cucciati, O., Porciani, C., Iovino, A., Zamorani, G., Oesch, P., Bolzonella, M., Knobel, C., Finoguenov, A., Peng, Y., Carollo, C. M., Pozzetti, L., Caputi, K., Silverman, J. D., Tasca, L. A. M., Scodeggio, M., Vergani, D., Scoville, N. Z., Capak, P., Contini, T., Kneib, J.-P., Le Fèvre, O., Mainieri, V., Renzini, A., Bardelli, S., Bongiorno, A., Coppa, G., de la Torre, S., de Ravel, L., Franzetti, P., Garilli, B., Guzzo, L., Kampczyk, P., Lamareille, F., Le Borgne, J.-F., Le Brun, V., Maier, C., Mignoli, M., Pello, R., Perez Montero, E., Ricciardelli, E., Tanaka, M., Tresse, L., Zucca, E., Abbas, U., Bottini, D., Cappi, A., Cassata, P., Cimatti, A., Fumana, M., Koekemoer, A. M., Maccagni, D., Marinoni, C., McCracken, H. J., Memeo, P., Meneux, B., and Scaramella, R. (2010). The Density Field of the 10k zCOSMOS Galaxies. *ApJ*, 708:505–533.

Kreysa, E., Gemuend, H.-P., Gromke, J., Haslam, C. G., Reichertz, L., Haller, E. E., Beeman, J. W., Hansen, V., Sievers, A., and Zylka, R. (1998). Bolometer array development at the Max-Planck-Institut fuer Radioastronomie. In T. G. Phillips, editor, *Society of Photo-Optical Instrumentation Engineers (SPIE) Conference Series*, volume 3357 of *Presented at the Society of Photo-Optical Instrumentation Engineers (SPIE) Conference*, pages 319–325.

Kriek, M., van der Wel, A., van Dokkum, P. G., Franx, M., and Illingworth, G. D. (2008a). The Detection of a Red Sequence of Massive Field Galaxies at z ˜ 2.3 and Its Evolution to z ˜ 0. *ApJ*, 682:896–906.

Kriek, M., van Dokkum, P. G., Franx, M., Illingworth, G. D., Marchesini, D., Quadri, R., Rudnick, G., Taylor, E. N., Förster Schreiber, N. M., Gawiser, E., Labbé, I., Lira, P., and Wuyts, S. (2008b). A Near-Infrared Spectroscopic Survey of K-selected Galaxies at z ˜ 2.3: Redshifts and Implications for Broadband Photometric Studies. *ApJ*, 677:219–237.

Kriek, M., van Dokkum, P. G., Franx, M., Quadri, R., Gawiser, E., Herrera, D., Illingworth, G. D., Labbé, I., Lira, P., Marchesini, D., Rix, H., Rudnick, G., Taylor, E. N., Toft, S., Urry, C. M., and Wuyts, S. (2006). Spectroscopic Identification of Massive Galaxies at z ˜ 2.3 with Strongly Suppressed Star Formation. *ApJ*, 649:L71–L74.

Kroupa, P. (2001). On the variation of the initial mass function. *MNRAS*, 322:231–246.

Kruegel, E. and Siebenmorgen, R. (1994). Dust in protostellar cores and stellar disks. *A&A*, 288:929–941.

Krumholz, M. R. and McKee, C. F. (2005). A General Theory of Turbulence-regulated Star Formation, from Spirals to Ultraluminous Infrared Galaxies. *ApJ*, 630:250–268.

Krumholz, M. R., McKee, C. F., and Tumlinson, J. (2009). The Star Formation Law in Atomic and Molecular Gas. *ApJ*, 699:850–856.

Kurczynski, P. and Gawiser, E. (2010). A Simultaneous Stacking and Deblending Algorithm for Astronomical Images. *AJ*, 139:1592–1599.

Lacki, B. C. and Thompson, T. A. (2010). The Physics of the Far-infrared-Radio Correlation. II. Synchrotron Emission as a Star Formation Tracer in High-redshift Galaxies. *ApJ*, 717:196–208.

Lacki, B. C., Thompson, T. A., and Quataert, E. (2010). The Physics of the Far-infrared-Radio Correlation. I. Calorimetry, Conspiracy, and Implications. *ApJ*, 717:1–28.

Lee, N., Le Floc'h, E., Sanders, D. B., Frayer, D. T., Arnouts, S., Ilbert, O., Aussel, H., Salvato, M., Scoville, N. Z., and Kartaltepe, J. S. (2010). A Far-infrared Characterization of 24 μm Selected Galaxies at $0 < z < 2.5$ using Stacking at 70 μm and 160 μm in the COSMOS Field. *ApJ*, 717:175–182.

LeFloc'h, E., Aussel, H., Ilbert, O., Riguccini, L., Frayer, D. T., Salvato, M., Arnouts, S., Surace, J., Feruglio, C., Rodighiero, G., Capak, P., Kartaltepe, J., Heinis, S., Sheth, K., Yan, L., McCracken, H. J., Thompson, D., Sanders, D., Scoville, N., and Koekemoer, A. (2009). Deep spitzer 24 Îijm cosmos imaging. i. the evolution of luminous dusty galaxies—confronting the models. *The Astrophysical Journal*, 703:222.

LeFloc'h, E., Papovich, C., Dole, H., Bell, E. F., Lagache, G., Rieke, G. H., Egami, E., Pérez-González, P. G., Alonso-Herrero, A., Rieke, M. J., Blaylock, M., Engelbracht, C. W., Gordon, K. D., Hines, D. C., Misselt, K. A., Morrison, J. E., and Mould, J. (2005). Infrared luminosity functions from the chandra deep field-south: The spitzer view on the history of dusty star formation at $0 < z < 1$. *The Astrophysical Journal*, 632:169.

Leitner, S. N. (2011). On the Last 10 Billion Years of Stellar Mass Growth in Star Forming Galaxies. *ArXiv e-prints*.

Leroy, A. K., Walter, F., Brinks, E., Bigiel, F., de Blok, W. J. G., Madore, B., and Thornley, M. D. (2008). The Star Formation Efficiency in Nearby Galaxies: Measuring Where Gas Forms Stars Effectively. *AJ*, 136:2782–2845.

Lestrade, J.-F., Combes, F., Salomé, P., Omont, A., Bertoldi, F., André, P., and Schneider, N. (2010). Discovery of an extremely bright submillimeter galaxy at $z = 3.93$. *A&A*, 522:L4+.

Lilly, S. J., Le Brun, V., Maier, C., Mainieri, V., Mignoli, M., Scodeggio, M., Zamorani, G., Carollo, M., Contini, T., Kneib, J., Le Fèvre, O., Renzini, A., Bardelli, S., Bolzonella, M., Bongiorno, A., Caputi, K., Coppa, G., Cucciati, O., de la Torre, S., de Ravel, L., Franzetti, P., Garilli, B., Iovino, A., Kampczyk, P., Kovac, K., Knobel, C., Lamareille, F., Le Borgne, J., Pello, R., Peng, Y., Pérez-Montero, E., Ricciardelli, E., Silverman, J. D., Tanaka, M., Tasca, L., Tresse, L., Vergani, D., Zucca, E., Ilbert, O., Salvato, M., Oesch, P., Abbas, U., Bottini, D., Capak, P., Cappi, A., Cassata, P., Cimatti, A., Elvis, M., Fumana, M., Guzzo, L., Hasinger, G., Koekemoer, A., Leauthaud, A., Maccagni, D., Marinoni, C., McCracken, H., Memeo, P., Meneux, B., Porciani, C., Pozzetti, L., Sanders, D., Scaramella, R., Scarlata, C., Scoville, N., Shopbell, P., and Taniguchi, Y. (2009). The zCOSMOS 10k-Bright Spectroscopic Sample. *ApJS*, 184:218–229.

Lilly, S. J., Le Fevre, O., Hammer, F., and Crampton, D. (1996). The Canada-France Redshift Survey: The Luminosity Density and Star Formation History of the Universe to Z approximately 1. *ApJ*, 460:L1+.

Lilly, S. J., Le Fèvre, O., Renzini, A., Zamorani, G., Scodeggio, M., Contini, T., Carollo, C. M., Hasinger, G., Kneib, J.-P., Iovino, A., Le Brun, V., Maier, C., Mainieri, V., Mignoli, M., Silverman, J., Tasca, L. A. M., Bolzonella, M., Bongiorno, A., Bottini, D., Capak, P., Caputi, K., Cimatti, A., Cucciati, O., Daddi, E., Feldmann, R., Franzetti, P., Garilli, B., Guzzo, L., Ilbert, O., Kampczyk, P., Kovac, K., Lamareille, F., Leauthaud, A., Borgne, J.-F. L., McCracken, H. J., Marinoni, C., Pello, R., Ricciardelli, E., Scarlata, C., Vergani, D., Sanders, D. B., Schinnerer, E., Scoville, N., Taniguchi, Y., Arnouts, S., Aussel, H., Bardelli, S., Brusa, M., Cappi, A., Ciliegi, P., Finoguenov, A., Foucaud, S., Franceschini, R., Halliday, C., Impey, C., Knobel, C., Koekemoer, A., Kurk, J., Maccagni, D., Maddox, S., Marano, B., Marconi, G., Meneux, B., Mobasher, B., Moreau, C., Peacock, J. A., Porciani, C., Pozzetti, L., Scaramella, R., Schiminovich, D., Shopbell, P., Smail, I., Thompson, D., Tresse, L., Vettolani, G., Zanichelli, A., and Zucca, E. (2007). zCOSMOS: A Large VLT/VIMOS Redshift Survey Covering $0 < z < 3$ in the COSMOS Field. *ApJS*, 172:70–85.

Lilly, S. J., Tresse, L., Hammer, F., Crampton, D., and Le Fevre, O. (1995). The Canada-France Redshift Survey. VI. Evolution of the Galaxy Luminosity Function to Z approximately 1. *ApJ*, 455:108–+.

Lisenfeld, U., Voelk, H. J., and Xu, C. (1996). A quantitative model of the FIR/radio correlation for normal late-type galaxies. *A&A*, 306:677–+.

Lunneborg, C. E. (2000). *Data analysis by resampling: Concepts and applications*. Duxbury Press, Belmont, CA.

Lutz, D., Poglitsch, A., Altieri, B., Andreani, P., Aussel, H., Berta, S., Bongiovanni, A., Brisbin, D., Cava, A., Cepa, J., Cimatti, A., Daddi, E., Dominguez-Sanchez, H., Elbaz, D., Forster Schreiber, N. M., Genzel, R., Grazian, A., Gruppioni, C., Harwit, M., Le Floc'h, E., Magdis, G., Magnelli, B., Maiolino, R., Nordon, R., Perez Garcia, A. M., Popesso, P., Pozzi, F., Riguccini, L., Rodighiero, G., Saintonge, A., Sanchez Portal, M., Santini, P., Shao, L., Sturm, E., Tacconi, L. J., Valtchanov, I., Wetzstein, M., and Wieprecht, E. (2011). PACS Evolutionary Probe (PEP) - A Herschel Key Program. *ArXiv e-prints*.

Mac Low, M.-M. and Klessen, R. S. (2004). Control of star formation by supersonic turbulence. *Reviews of Modern Physics*, 76:125–194.

Macciò, A. V., Moore, B., and Stadel, J. (2006). The Origin of Polar Ring Galaxies: Evidence for Galaxy Formation by Cold Accretion. *ApJ*, 636:L25–L28.

Machalski, J. and Godlowski, W. (2000). 1.4 GHz luminosity function of galaxies in the Las Campanas redshift survey and its evolution. *A&A*, 360:463–471.

Madau, P., Ferguson, H. C., Dickinson, M. E., Giavalisco, M., Steidel, C. C., and Fruchter, A. (1996). High-redshift galaxies in the Hubble Deep Field: colour selection and star formation history to z˜4. *MNRAS*, 283:1388–1404.

Magdis, G. E., Elbaz, D., Daddi, E., Morrison, G. E., Dickinson, M., Rigopoulou, D., Gobat, R., and Hwang, H. S. (2010). A Multi-wavelength View of the Star Formation Activity at z ˜ 3. *ApJ*, 714:1740–1745.

Marchesini, D., van Dokkum, P. G., Förster Schreiber, N. M., Franx, M., Labbé, I., and Wuyts, S. (2009). The Evolution of the Stellar Mass Function of Galaxies from z = 4.0 and the First Comprehensive Analysis of its Uncertainties: Evidence for Mass-Dependent Evolution. *ApJ*, 701:1765–1796.

Marchesini, D., Whitaker, K. E., Brammer, G., van Dokkum, P. G., Labbé, I., Muzzin, A., Quadri, R. F., Kriek, M., Lee, K.-S., Rudnick, G., Franx, M., Illingworth, G. D., and Wake, D. (2010). The Most Massive Galaxies at 3.0 <= z < 4.0 in the Newfirm Medium-band Survey: Properties and Improved Constraints on the Stellar Mass Function. *ApJ*, 725:1277–1295.

Martin, D. C., Small, T., Schiminovich, D., Wyder, T. K., Pérez-González, P. G., Johnson, B., Wolf, C., Barlow, T. A., Forster, K., Friedman, P. G., Morrissey, P., Neff, S. G., Seibert, M., Welsh, B. Y., Bianchi, L., Donas, J., Heckman, T. M., Lee, Y., Madore, B. F., Milliard, B., Rich, R. M., Szalay, A. S., Yi, S. K., Meisenheimer, K., and Rieke, G. (2007a). The Star Formation and Extinction Coevolution of UV-Selected Galaxies over 0.05<z<1.2. *ApJS*, 173:415–431.

Martin, D. C., Wyder, T. K., Schiminovich, D., Barlow, T. A., Forster, K., Friedman, P. G., Morrissey, P., Neff, S. G., Seibert, M., Small, T., Welsh, B. Y., Bianchi, L., Donas, J., Heckman, T. M., Lee, Y., Madore, B. F., Milliard, B., Rich, R. M., Szalay, A. S., and Yi, S. K. (2007b). The UV-Optical Galaxy Color-Magnitude Diagram. III. Constraints on Evolution from the Blue to the Red Sequence. *ApJS*, 173:342–356.

Martínez-Sansigre, A., Karim, A., Schinnerer, E., Omont, A., Smith, D. J. B., Wu, J., Hill, G. J., Klöckner, H., Lacy, M., Rawlings, S., and Willott, C. J. (2009). Millimeter Observations of a Sample of High-Redshift Obscured Quasars. *ApJ*, 706:184–202.

Martínez-Sansigre, A., Lacy, M., Sajina, A., and Rawlings, S. (2008). Mid-Infrared Spectroscopy of High-Redshift Obscured Quasars. *ApJ*, 674:676–685.

Martínez-Sansigre, A., Rawlings, S., Garn, T., Green, D. A., Alexander, P., Klöckner, H.-R., and Riley, J. M. (2006a). A population of high-redshift type 2 quasars - II. Radio properties. *MNRAS*, 373:L80–L84.

Martínez-Sansigre, A., Rawlings, S., Lacy, M., Fadda, D., Jarvis, M. J., Marleau, F. R., Simpson, C., and Willott, C. J. (2006b). A population of high-redshift type 2 quasars - I. Selection criteria and optical spectra. *MNRAS*, 370:1479–1498.

Martínez-Sansigre, A., Rawlings, S., Lacy, M., Fadda, D., Marleau, F. R., Simpson, C., Willott, C. J., and Jarvis, M. J. (2005). The obscuration by dust of most of the growth of supermassive black holes. *Nature*, 436:666–669.

Mauch, T. and Sadler, E. M. (2007). Radio sources in the 6dFGS: local luminosity functions at 1.4GHz for star-forming galaxies and radio-loud AGN. *MNRAS*, 375:931–950.

Mauersberger, R. (2003). Highlights from the IRAM-30m Telescope. In *1er Congreso Nacional de Astrofísica Molecular: Una visión general del potencial de los grupos de química españoles anters los nuevos desafíos de la Astrofísica*, pages 13–+.

McCracken, H. J., Capak, P., Salvato, M., Aussel, H., Thompson, D., Daddi, E., Sanders, D. B., Kneib, J.-P., Willott, C. J., Mancini, C., Renzini, A., Cook, R., Fèvre, O. L., Ilbert, O., Kartaltepe, J., Koekemoer, A. M., Mellier, Y., Murayama, T., Scoville, N. Z., Shioya, Y., and Tanaguchi, Y. (2010). The cosmos-wircam near-infrared imaging survey. i. bzk-selected passive and star-forming galaxy candidates at z gsim 1.4. *The Astrophysical Journal*, 708:202.

McKee, C. F. and Ostriker, E. C. (2007). Theory of Star Formation. *ARA&A*, 45:565–687.

McLure, R. J., Dunlop, J. S., Cirasuolo, M., Koekemoer, A. M., Sabbi, E., Stark, D. P., Targett, T. A., and Ellis, R. S. (2010). Galaxies at z = 6-9 from the WFC3/IR imaging of the Hubble Ultra Deep Field. *MNRAS*, 403:960–983.

McLure, R. J., Dunlop, J. S., de Ravel, L., Cirasuolo, M., Ellis, R. S., Schenker, M., Robertson, B. E., Koekemoer, A. M., Stark, D. P., and Bowler, R. A. A. (2011). A robust sample of galaxies at redshifts 6.0<z<8.7: stellar populations, star-formation rates and stellar masses. *ArXiv e-prints*.

Meneux, B., Guzzo, L., de la Torre, S., Porciani, C., Zamorani, G., Abbas, U., Bolzonella, M., Garilli, B., Iovino, A., Pozzetti, L., Zucca, E., Lilly, S. J., Le Fèvre, O., Kneib, J., Carollo, C. M., Contini, T., Mainieri, V., Renzini, A., Scodeggio, M., Bardelli, S., Bongiorno, A., Caputi, K., Coppa, G., Cucciati, O., de Ravel, L., Franzetti, P., Kampczyk, P., Knobel, C., Kovač, K., Lamareille, F., Le Borgne, J., Le Brun, V., Maier, C., Pellò, R., Peng, Y., Perez Montero, E., Ricciardelli, E., Silverman, J. D., Tanaka, M., Tasca, L., Tresse, L., Vergani, D., Bottini, D., Cappi, A., Cimatti, A., Cassata, P., Fumana, M., Koekemoer, A. M., Leauthaud, A., Maccagni, D., Marinoni, C., McCracken, H. J., Memeo, P., Oesch, P., and Scaramella, R. (2009). The zCOSMOS survey. The dependence of clustering on luminosity and stellar mass at z=0.2-1. *A&A*, 505:463–482.

Messias, H., Afonso, J., Hopkins, A., Mobasher, B., Dominici, T., and Alexander, D. M. (2010). A multi-wavelength approach to the properties of Extremely Red Galaxy populations: I - Contribution to the Star Formation Rate density and AGN content. *ArXiv e-prints*.

Michałowski, M. J., Watson, D., and Hjorth, J. (2010). Rapid Dust Production in Submillimeter Galaxies at z>4? *ApJ*, 712:942–950.

Mo, H., Bosch, F., and White, S. (2010). *Galaxy Formation and Evolution*. Galaxy Formation and Evolution. Cambridge University Press.

Moster, B. P., Somerville, R. S., Maulbetsch, C., van den Bosch, F. C., Macciò, A. V., Naab, T., and Oser, L. (2010). Constraints on the Relationship between Stellar Mass and Halo Mass at Low and High Redshift. *ApJ*, 710:903–923.

Moustakas, J., Kennicutt, Jr., R. C., and Tremonti, C. A. (2006). Optical Star Formation Rate Indicators. *ApJ*, 642:775–796.

Muxlow, T. W. B., Pedlar, A., Wilkinson, P. N., Axon, D. J., Sanders, E. M., and de Bruyn, A. G. (1994). The Structure of Young Supernova Remnants in M82. *MNRAS*, 266:455–+.

Nenkova, M., Sirocky, M. M., Ivezić, Ž., and Elitzur, M. (2008a). AGN Dusty Tori. I. Handling of Clumpy Media. *ApJ*, 685:147–159.

Nenkova, M., Sirocky, M. M., Nikutta, R., Ivezić, Ž., and Elitzur, M. (2008b). AGN Dusty Tori. II. Observational Implications of Clumpiness. *ApJ*, 685:160–180.

Neri, R., Genzel, R., Ivison, R. J., Bertoldi, F., Blain, A. W., Chapman, S. C., Cox, P., Greve, T. R., Omont, A., and Frayer, D. T. (2003). Interferometric Observations of Powerful CO Emission from Three Submillimeter Galaxies at z=2.39, 2.51, and 3.35. *ApJ*, 597:L113–L116.

Noeske, K. G. (2009). Star Formation Histories and Stellar Mass Growth out to z>1. *ArXiv e-prints*.

Noeske, K. G., Faber, S. M., Weiner, B. J., Koo, D. C., Primack, J. R., Dekel, A., Papovich, C., Conselice, C. J., Le Floc'h, E., Rieke, G. H., Coil, A. L., Lotz, J. M., Somerville, R. S., and Bundy, K. (2007a). Star Formation in AEGIS Field Galaxies since z=1.1: Staged Galaxy Formation and a Model of Mass-dependent Gas Exhaustion. *ApJ*, 660:L47–L50.

Noeske, K. G., Weiner, B. J., Faber, S. M., Papovich, C., Koo, D. C., Somerville, R. S., Bundy, K., Conselice, C. J., Newman, J. A., Schiminovich, D., Le Floc'h, E., Coil, A. L., Rieke, G. H., Lotz, J. M., Primack, J. R., Barmby, P., Cooper, M. C., Davis, M., Ellis, R. S., Fazio, G. G., Guhathakurta, P., Huang, J., Kassin, S. A., Martin, D. C., Phillips, A. C., Rich, R. M., Small, T. A., Willmer, C. N. A., and Wilson, G. (2007b). Star Formation in AEGIS Field Galaxies since z=1.1: The Dominance of Gradually Declining Star Formation, and the Main Sequence of Star-forming Galaxies. *ApJ*, 660:L43–L46.

Obreschkow, D. and Rawlings, S. (2009). The Cosmic Decline in the H_2/H I Ratio in Galaxies. *ApJ*, 696:L129–L132.

Oliver, S., Frost, M., Farrah, D., Gonzalez-Solares, E., Shupe, D. L., Henriques, B., Roseboom, I., Alfonso-Luis, A., Babbedge, T. S. R., Frayer, D., Lencz, C., Lonsdale, C. J., Masci, F., Padgett, D., Polletta, M., Rowan-Robinson, M., Siana, B., Smith, H. E., Surace, J. A., and Vaccari, M. (2010). Specific star formation and the relation to stellar mass from $0 < z < 2$ as seen in the far-infrared at 70 and 160 μm. *MNRAS*, 405:2279–2294.

Omont, A., Petitjean, P., Guilloteau, S., McMahon, R. G., Solomon, P. M., and Pécontal, E. (1996). Molecular gas and dust around a radio-quiet quasar at redshift 4.69. *Nature*, 382:428–431.

Overzier, R. A., Bouwens, R. J., Cross, N. J. G., Venemans, B. P., Miley, G. K., Zirm, A. W., Benítez, N., Blakeslee, J. P., Coe, D., Demarco, R., Ford, H. C., Homeier, N. L., Illingworth, G. D., Kurk, J. D., Martel, A. R., Mei, S., Oliveira, I., Röttgering, H. J. A., Tsvetanov, Z. I., and Zheng, W. (2008). Lyman Break Galaxies, Lyα Emitters, and a Radio Galaxy in a Protocluster at z = 4.1. *ApJ*, 673:143–162.

Overzier, R. A., Miley, G. K., Bouwens, R. J., Cross, N. J. G., Zirm, A. W., Benítez, N., Blakeslee, J. P., Clampin, M., Demarco, R., Ford, H. C., Hartig, G. F., Illingworth, G. D., Martel, A. R., Röttgering, H. J. A., Venemans, B., Ardila, D. R., Bartko, F., Bradley, L. D., Broadhurst, T. J., Coe, D., Feldman, P. D., Franx, M., Golimowski, D. A., Goto, T., Gronwall, C., Holden, B., Homeier, N., Infante, L., Kimble, R. A., Krist, J. E., Mei, S., Menanteau, F., Meurer, G. R., Motta, V., Postman, M., Rosati, P., Sirianni, M., Sparks, W. B., Tran, H. D., Tsvetanov, Z. I., White, R. L., and Zheng, W. (2006). Clustering of Star-forming Galaxies Near a Radio Galaxy at z=5.2. *ApJ*, 637:58–73.

Owen, F. N. and Morrison, G. E. (2008). The Deep Swire Field. I. 20 cm Continuum Radio Observations: A Crowded Sky. *AJ*, 136:1889–1900.

Padmanabhan, T. (1993). *Structure Formation in the Universe*. Cambridge University Press, Cambridge, UK.

Pannella, M., Carilli, C. L., Daddi, E., McCracken, H. J., Owen, F. N., Renzini, A., Strazzullo, V., Civano, F., Koekemoer, A. M., Schinnerer, E., Scoville, N., Smolčić, V., Taniguchi, Y., Aussel, H., Kneib, J. P., Ilbert, O., Mellier, Y., Salvato, M., Thompson, D., and Willott, C. J. (2009). Star Formation and Dust Obscuration at $z \approx 2$: Galaxies at the Dawn of Downsizing. *ApJ*, 698:L116–L120.

Papadopoulos, P. P., Thi, W.-F., Miniati, F., and Viti, S. (2011). Extreme cosmic ray dominated regions: a new paradigm for high star formation density events in the Universe. *MNRAS*, 414:1705–1714.

Peng, Y., Lilly, S. J., Kovac, K., Bolzonella, M., Pozzetti, L., Renzini, A., Zamorani, G., Ilbert, O., Knobel, C., Iovino, A., Maier, C., Cucciati, O., Tasca, L., Carollo, C. M., Silverman, J., Kampczyk, P., de Ravel, L., Sanders, D., Scoville, N., Contini, T., Mainieri, V., Scodeggio, M., Kneib, J.-P., Fevre, O. L., Bardelli, S., Bongiorno, A., Caputi, K., Coppa, G., de la Torre, S., Franzetti, P., Garilli, B., Lamareille, F., Borgne, J.-F. L., Brun, V. L., Mignoli, M., Montero, E. P., Pello, R., Ricciardelli, E., Tanaka, M., Tresse, L., Vergani, D., Welikala, N., Zucca, E., Oesch, P., Abbas, U., Barnes, L., Bordoloi, R., Bottini, D., Cappi, A., Cassata, P., Cimatti, A., Fumana, M., Hasinger, G., Koekemoer, A., Leauthaud, A., Maccagni, D., Marinoni, C., McCracken, H., Memeo, P., Meneux, B., Nair, P., Porciani, C., Presotto, V., and Scaramella, R. (2010). Mass and environment as drivers of galaxy evolution in sdss and zcosmos and the origin of the schechter function. *The Astrophysical Journal*, 721(1):193.

Peng, Y., Lilly, S. J., Renzini, A., and Carollo, M. (2011). Mass and Environment as Drivers of Galaxy Evolution II: The quenching of satellite galaxies as the origin of environmental effects. *ArXiv e-prints*.

Penzias, A. A. and Wilson, R. W. (1965). A Measurement of Excess Antenna Temperature at 4080 Mc/s. *ApJ*, 142:419–421.

Pérez-González, P. G., Rieke, G. H., Villar, V., Barro, G., Blaylock, M., Egami, E., Gallego, J., Gil de Paz, A., Pascual, S., Zamorano, J., and Donley, J. L. (2008). The Stellar Mass Assembly of Galaxies from z = 0 to z = 4: Analysis of a Sample Selected in the Rest-Frame Near-Infrared with Spitzer. *ApJ*, 675:234–261.

Perley, R. A., Chandler, C. J., Butler, B. J., and Wrobel, J. M. (2011). The Expanded Very Large Array: A New Telescope for New Science. *ApJ*, 739:L1+.

Poglitsch, A., Waelkens, C., Geis, N., Feuchtgruber, H., Vandenbussche, B., Rodriguez, L., Krause, O., Renotte, E., van Hoof, C., Saraceno, P., Cepa, J., Kerschbaum, F., Agnèse, P., Ali, B., Altieri, B., Andreani, P., Augueres, J.-L., Balog, Z., Barl, L., Bauer, O. H., Belbachir, N., Benedettini, M., Billot, N., Boulade, O., Bischof, H., Blommaert, J., Callut, E., Cara, C., Cerulli, R., Cesarsky, D., Contursi, A., Creten, Y., De Meester, W., Doublier, V., Doumayrou, E., Duband, L., Exter, K., Genzel, R., Gillis, J.-M., Grözinger, U., Henning, T., Herreros, J., Huygen, R., Inguscio, M., Jakob, G., Jamar, C., Jean, C., de Jong, J., Katterloher, R., Kiss, C., Klaas, U., Lemke, D., Lutz, D., Madden, S., Marquet, B., Martignac, J., Mazy, A., Merken, P., Montfort, F., Morbidelli, L., Müller, T., Nielbock, M., Okumura, K., Orfei, R., Ottensamer, R., Pezzuto, S., Popesso, P., Putzeys, J., Regibo, S., Reveret, V., Royer, P., Sauvage, M., Schreiber, J., Stegmaier, J., Schmitt, D., Schubert, J., Sturm, E., Thiel, M., Tofani, G., Vavrek, R., Wetzstein, M., Wieprecht, E., and Wiezorrek, E. (2010). The Photodetector Array Camera and Spectrometer (PACS) on the Herschel Space Observatory. *A&A*, 518:L2+.

Polletta, M., Tajer, M., Maraschi, L., Trinchieri, G., Lonsdale, C. J., Chiappetti, L., Andreon, S., Pierre, M., Le Fèvre, O., Zamorani, G., Maccagni, D., Garcet, O., Surdej, J., Franceschini, A., Alloin, D., Shupe, D. L., Surace, J. A., Fang, F., Rowan-Robinson, M., Smith, H. E., and Tresse, L. (2007). Spectral Energy Distributions of Hard X-Ray Selected Active Galactic Nuclei in the XMM-Newton Medium Deep Survey. *ApJ*, 663:81–102.

Pope, A., Chary, R.-R., Alexander, D. M., Armus, L., Dickinson, M., Elbaz, D., Frayer, D., Scott, D., and Teplitz, H. (2008). Mid-Infrared Spectral Diagnosis of Submillimeter Galaxies. *ApJ*, 675:1171–1193.

Pozzetti, L., Bolzonella, M., Zucca, E., Zamorani, G., Lilly, S., Renzini, A., Moresco, M., Mignoli, M., Cassata, P., Tasca, L., Lamareille, F., Maier, C., Meneux, B., Halliday, C., Oesch, P., Vergani, D., Caputi, K., Kovac, K., Cimatti, A., Cucciati, O., Iovino, A., Peng, Y., Carollo, M., Contini, T., Kneib, J. P., Le F'evre, O., Mainieri, V., Scodeggio, M., Bardelli, S., Bongiorno, A., Coppa, G., de la Torre, S., de Ravel, L., Franzetti, P., Garilli, B., Kampczyk, P., Knobel, C., Le Borgne, J. F., Le Brun, V., Pell'o, R., Perez Montero, E., Ricciardelli, E., Silverman, J. D., Tanaka, M., Tresse, L., Abbas, U., Bottini, D., Cappi, A., Guzzo, L., Koekemoer, A. M., Leauthaud, A., Maccagni, D., Marinoni, C., McCracken, H. J., Memeo, P., Porciani, C., Scaramella, R., Scarlata, C., and Scoville, N. (2009). zCOSMOS - 10k-bright spectroscopic sample. The bimodality in the Galaxy Stellar Mass Function: exploring its evolution with redshift. *ArXiv e-prints*.

Priddey, R. S. and McMahon, R. G. (2001). The far-infrared-submillimetre spectral energy distribution of high-redshift quasars. *MNRAS*, 324:L17–L22.

Quadri, R. F. and Williams, R. J. (2009). Quantifying Photometric Redshift Errors in the Absence of Spectroscopic Redshifts. *ArXiv e-prints*.

Reddy, N. A. and Steidel, C. C. (2009). A Steep Faint-End Slope of the UV Luminosity Function at z ˜ 2-3: Implications for the Global Stellar Mass Density and Star Formation in Low-Mass Halos. *ApJ*, 692:778–803.

Riechers, D. A. (2007). *The molecular ISM of Quasar Host Galaxies in the early Universe*. PhD thesis, Universität Heidelberg.

Riechers, D. A. (2011). Molecular Gas in Lensed z>2 Quasar Host Galaxies and the Star Formation Law for Galaxies with Luminous Active Galactic Nuclei. *ApJ*, 730:108–+.

Riechers, D. A., Capak, P. L., Carilli, C. L., Cox, P., Neri, R., Scoville, N. Z., Schinnerer, E., Bertoldi, F., and Yan, L. (2010). A Massive Molecular Gas Reservoir in the z = 5.3 Submillimeter Galaxy AzTEC-3. *ApJ*, 720:L131–L136.

Riechers, D. A., Walter, F., Carilli, C. L., Bertoldi, F., and Momjian, E. (2008). Formation of a Quasar Host Galaxy through a Wet Merger 1.4 Billion Years after the Big Bang. *ApJ*, 686:L9–L12.

Riechers, D. A., Walter, F., Carilli, C. L., Knudsen, K. K., Lo, K. Y., Benford, D. J., Staguhn, J. G., Hunter, T. R., Bertoldi, F., Henkel, C., Menten, K. M., Weiss, A., Yun, M. S., and Scoville, N. Z. (2006). CO(1-0) in z$\gtrsim$4 Quasar Host Galaxies: No Evidence for Extended Molecular Gas Reservoirs. *ApJ*, 650:604–613.

Rix, H.-W., Barden, M., Beckwith, S. V. W., Bell, E. F., Borch, A., Caldwell, J. A. R., Häussler, B., Jahnke, K., Jogee, S., McIntosh, D. H., Meisenheimer, K., Peng, C. Y., Sanchez, S. F., Somerville, R. S., Wisotzki, L., and Wolf, C. (2004). GEMS: Galaxy Evolution from Morphologies and SEDs. *ApJS*, 152:163–173.

Robaina, A. R., Bell, E. F., Skelton, R. E., McIntosh, D. H., Somerville, R. S., Zheng, X., Rix, H.-W., Bacon, D., Balogh, M., Barazza, F. D., Barden, M., Böhm, A., Caldwell, J. A. R., Gallazzi, A., Gray, M. E., Häussler, B., Heymans, C., Jahnke, K., Jogee, S., van Kampen, E., Lane, K., Meisenheimer, K., Papovich, C., Peng, C. Y., Sánchez, S. F., Skibba, R., Taylor, A., Wisotzki, L., and Wolf, C. (2009). Less Than 10 Percent of Star Formation in z ˜ 0.6 Massive Galaxies is Triggered by Major Interactions. *ApJ*, 704:324–340.

Rodighiero, G., Cimatti, A., Gruppioni, C., Popesso, P., Andreani, P., Altieri, B., Aussel, H., Berta, S., Bongiovanni, A., Brisbin, D., Cava, A., Cepa, J., Daddi, E., Dominguez-Sanchez, H., Elbaz, D., Fontana, A., Förster Schreiber, N., Franceschini, A., Genzel, R., Grazian, A., Lutz, D., Magdis, G., Magliocchetti, M., Magnelli, B., Maiolino, R., Mancini, C., Nordon, R., Perez Garcia, A. M., Poglitsch, A., Santini, P., Sanchez-Portal, M., Pozzi, F., Riguccini, L., Saintonge, A., Shao, L., Sturm, E., Tacconi, L., Valtchanov, I., Wetzstein, M., and Wieprecht, E. (2010a). The first Herschel view of the mass-SFR link in high-z galaxies. *A&A*, 518:L25+.

Rodighiero, G., Daddi, E., Baronchelli, I., Cimatti, A., Renzini, A., Aussel, H., Popesso, P., Lutz, D., Andreani, P., Berta, S., Cava, A., Elbaz, D., Feltre, A., Fontana, A., Forster Schreiber, N. M., Franceschini, A., Genzel, R., Grazian, A., Gruppioni, C., Ilbert, O., Le Floch, E., Magdis, G., Magliocchetti, M., Magnelli, B., Maiolino, R., McCracken, H., Nordon, R., Poglitsch, A., Santini, P., Pozzi, F., Riguccini, L., Tacconi, L. J., Wuyts, S., and Zamorani, G. (2011). The lesser role of starbursts for star formation at z=2. *ArXiv e-prints*.

Rodighiero, G., Vaccari, M., Franceschini, A., Tresse, L., Le Fevre, O., Le Brun, V., Mancini, C., Matute, I., Cimatti, A., Marchetti, L., Ilbert, O., Arnouts, S., Bolzonella, M., Zucca, E., Bardelli, S., Lonsdale, C. J., Shupe, D., Surace, J., Rowan-Robinson, M., Garilli, B., Zamorani, G., Pozzetti, L., Bondi, M., de La Torre, S., Vergani, D., Santini, P., Grazian, A., and Fontana, A. (2010b). Mid- and far-infrared luminosity functions and galaxy evolution from multiwavelength Spitzer observations up to z ˜ 2.5. *A&A*, 515:A8+.

Rujopakarn, W., Eisenstein, D. J., Rieke, G. H., Papovich, C., Cool, R. J., Moustakas, J., Jannuzi, B. T., Kochanek, C. S., Rieke, M. J., Dey, A., Eisenhardt, P., Murray, S. S., Brown, M. J. I., and Le Floc'h, E. (2010). The Evolution of the Star Formation Rate of Galaxies at 0.0 <= z <= 1.2. *ApJ*, 718:1171–1185.

Sadler, E. M., Cannon, R. D., Mauch, T., Hancock, P. J., Wake, D. A., Ross, N., Croom, S. M., Drinkwater, M. J., Edge, A. C., Eisenstein, D., Hopkins, A. M., Johnston, H. M., Nichol, R., Pimbblet, K. A., de Propris, R., Roseboom, I. G., Schneider, D. P., and Shanks, T. (2007). Radio galaxies in the 2SLAQ Luminous Red Galaxy Survey - I. The evolution of low-power radio galaxies to z ˜ 0.7. *MNRAS*, 381:211–227.

Sadler, E. M., Jackson, C. A., Cannon, R. D., McIntyre, V. J., Murphy, T., Bland-Hawthorn, J., Bridges, T., Cole, S., Colless, M., Collins, C., Couch, W., Dalton, G., De Propris, R., Driver, S. P., Efstathiou, G., Ellis, R. S., Frenk, C. S., Glazebrook, K., Lahav, O., Lewis, I., Lumsden, S., Maddox, S., Madgwick, D., Norberg, P., Peacock, J. A., Peterson, B. A., Sutherland, W., and Taylor, K. (2002). Radio sources in the 2dF Galaxy Redshift Survey - II. Local radio luminosity functions for AGN and star-forming galaxies at 1.4 GHz. *MNRAS*, 329:227–245.

Salim, S., Rich, R. M., Charlot, S., Brinchmann, J., Johnson, B. D., Schiminovich, D., Seibert, M., Mallery, R., Heckman, T. M., Forster, K., Friedman, P. G., Martin, D. C., Morrissey, P., Neff, S. G., Small, T., Wyder, T. K., Bianchi, L., Donas, J., Lee, Y.-W., Madore, B. F., Milliard, B., Szalay, A. S., Welsh, B. Y., and Yi, S. K. (2007). Uv star formation rates in the local universe. *The Astrophysical Journal Supplement Series*, 173:267.

Salpeter, E. E. (1955). The Luminosity Function and Stellar Evolution. *ApJ*, 121:161–+.

Salvato, M., Hasinger, G., Ilbert, O., Zamorani, G., Brusa, M., Scoville, N. Z., Rau, A., Capak, P., Arnouts, S., Aussel, H., Bolzonella, M., Buongiorno, A., Cappelluti, N., Caputi, K., Civano, F., Cook, R., Elvis, M., Gilli, R., Jahnke, K., Kartaltepe, J. S., Impey, C. D., Lamareille, F., LeFloch, E., Lilly, S., Mainieri, V., McCarthy, P., McCracken, H., Mignoli, M., Mobasher, B., Murayama, T., Sasaki, S., Sanders, D. B., Schiminovich, D., Shioya, Y., Shopbell, P., Silverman, J., Smolčić, V., Surace, J., Taniguchi, Y., Thompson, D., Trump, J. R., Urry, M., and Zamojski, M. (2009). Photometric Redshift and Classification for the XMM-COSMOS Sources. *ApJ*, 690:1250–1263.

Sanders, D. B., Salvato, M., Aussel, H., Ilbert, O., Scoville, N., Surace, J. A., Frayer, D. T., Sheth, K., Helou, G., Brooke, T., Bhattacharya, B., Yan, L., Kartaltepe, J. S., Barnes, J. E., Blain, A. W., Calzetti, D., Capak, P., Carilli, C., Carollo, C. M., Comastri, A., Daddi, E., Ellis, R. S., Elvis, M., Fall, S. M., Franceschini, A., Giavalisco, M., Hasinger, G., Impey, C., Koekemoer, A., Le Fèvre, O., Lilly, S., Liu, M. C., McCracken, H. J., Mobasher, B., Renzini, A., Rich, M., Schinnerer, E., Shopbell, P. L., Taniguchi, Y., Thompson, D. J., Urry, C. M., and Williams, J. P. (2007). S-COSMOS: The Spitzer Legacy Survey of the Hubble Space Telescope ACS 2 $\deg^2$ COSMOS Field I: Survey Strategy and First Analysis. *ApJS*, 172:86–98.

Sanders, D. B., Soifer, B. T., Elias, J. H., Madore, B. F., Matthews, K., Neugebauer, G., and Scoville, N. Z. (1988). Ultraluminous infrared galaxies and the origin of quasars. *ApJ*, 325:74–91.

Santini, P., Fontana, A., Grazian, A., Salimbeni, S., Fiore, F., Fontanot, F., Boutsia, K., Castellano, M., Cristiani, S., de Santis, C., Gallozzi, S., Giallongo, E., Menci, N., Nonino, M., Paris, D., Pentericci, L., and Vanzella, E. (2009). Star formation and mass assembly in high redshift galaxies. *A&A*, 504:751–767.

Sargent, M. T., Schinnerer, E., Murphy, E., Aussel, H., Le Floc'h, E., Frayer, D. T., Martínez-Sansigre, A., Oesch, P., Salvato, M., Smolčić, V., Zamorani, G., Brusa, M., Cappelluti, N., Carilli, C. L., Carollo, C. M., Ilbert, O., Kartaltepe, J., Koekemoer, A. M., Lilly, S. J., Sanders, D. B., and Scoville, N. Z. (2010a). The VLA-COSMOS Perspective on the Infrared-Radio Relation. I. New Constraints on Selection Biases and the Non-Evolution of the Infrared/Radio Properties of Star-Forming and Active Galactic Nucleus Galaxies at Intermediate and High Redshift. *ApJS*, 186:341–377.

Sargent, M. T., Schinnerer, E., Murphy, E., Carilli, C. L., Helou, G., Aussel, H., Le Floc'h, E., Frayer, D. T., Ilbert, O., Oesch, P., Salvato, M., Smolčić, V., Kartaltepe, J., and Sanders, D. B. (2010b). No Evolution in the IR-Radio Relation for IR-luminous Galaxies at $z < 2$ in the COSMOS Field. *ApJ*, 714:L190–L195.

Schaerer, D. and de Barros, S. (2010). On the physical properties of z ≈ 6-8 galaxies. *A&A*, 515:A73+.

Schechter, P. (1976). An analytic expression for the luminosity function for galaxies. *Astrophys. J.*, 203:297. A&AA ID. AAA017.158.009.

Scheuer, P. A. G. and Williams, P. J. S. (1968). Radio Spectra. *ARA&A*, 6:321–+.

Schiminovich, D., Ilbert, O., Arnouts, S., Milliard, B., Tresse, L., Le Fèvre, O., Treyer, M., Wyder, T. K., Budavári, T., Zucca, E., Zamorani, G., Martin, D. C., Adami, C., Arnaboldi, M., Bardelli, S., Barlow, T., Bianchi, L., Bolzonella, M., Bottini, D., Byun, Y.-I., Cappi, A., Contini, T., Charlot, S., Donas, J., Forster, K., Foucaud, S., Franzetti, P., Friedman, P. G., Garilli, B., Gavignaud, I., Guzzo, L., Heckman, T. M., Hoopes, C., Iovino, A., Jelinsky, P., Le Brun, V., Lee, Y.-W., Maccagni, D., Madore, B. F., Malina, R., Marano, B., Marinoni, C., McCracken, H. J., Mazure, A., Meneux, B., Morrissey, P., Neff, S., Paltani, S., Pellò, R., Picat, J. P., Pollo, A., Pozzetti, L., Radovich, M., Rich, R. M., Scaramella, R., Scodeggio, M., Seibert, M., Siegmund, O., Small, T., Szalay, A. S., Vettolani, G., Welsh, B., Xu, C. K., and Zanichelli, A. (2005). The GALEX-VVDS Measurement of the Evolution of the Far-Ultraviolet Luminosity Density and the Cosmic Star Formation Rate. *ApJ*, 619:L47–L50.

Schiminovich, D., Wyder, T. K., Martin, D. C., Johnson, B. D., Salim, S., Seibert, M., Treyer, M. A., Budavári, T., Hoopes, C., Zamojski, M., Barlow, T. A., Forster, K. G., Friedman, P. G., Morrissey, P., Neff, S. G., Small, T. A., Bianchi, L., Donas, J., Heckman, T. M., Lee, Y., Madore, B. F., Milliard, B., Rich, R. M., Szalay, A. S., Welsh, B. Y., and Yi, S. (2007). The UV-Optical Color Magnitude Diagram. II. Physical Properties and Morphological Evolution On and Off of a Star-forming Sequence. *ApJS*, 173:315–341.

Schinnerer, E., Carilli, C. L., Capak, P., Martinez-Sansigre, A., Scoville, N. Z., Smolčić, V., Taniguchi, Y., Yun, M. S., Bertoldi, F., Le Fevre, O., and de Ravel, L. (2008). Molecular Gas in a Submillimeter Galaxy at z = 4.5: Evidence for a Major Merger at 1 Billion Years after the Big Bang. *ApJ*, 689:L5–L8.

Schinnerer, E., Carilli, C. L., Scoville, N. Z., Bondi, M., Ciliegi, P., Vettolani, P., Le Fèvre, O., Koekemoer, A. M., Bertoldi, F., and Impey, C. D. (2004). The VLA-COSMOS Survey. I. Radio Identifications from the Pilot Project. *AJ*, 128:1974–1989.

Schinnerer, E., Sargent, M. T., Bondi, M., Smolčić, V., Datta, A., Carilli, C. L., Bertoldi, F., Blain, A., Ciliegi, P., Koekemoer, A., and Scoville, N. Z. (2010). The VLA-COSMOS Survey. IV. Deep Data and Joint Catalog. *ApJS*, 188:384–404.

Schinnerer, E., Smolčić, V., Carilli, C. L., Bondi, M., Ciliegi, P., Jahnke, K., Scoville, N. Z., Aussel, H., Bertoldi, F., Blain, A. W., Impey, C. D., Koekemoer, A. M., Le Fevre, O., and Urry, C. M. (2007). The VLA-COSMOS Survey. II. Source Catalog of the Large Project. *ApJS*, 172:46–69.

Schmidt, M. (1959). The Rate of Star Formation. *ApJ*, 129:243–+.

Scott, K. S., Austermann, J. E., Perera, T. A., Wilson, G. W., Aretxaga, I., Bock, J. J., Hughes, D. H., Kang, Y., Kim, S., Mauskopf, P. D., Sanders, D. B., Scoville, N., and Yun, M. S. (2008). AzTEC millimetre survey of the COSMOS field - I. Data reduction and source catalogue. *MNRAS*, 385:2225–2238.

Scoville, N., Abraham, R. G., Aussel, H., Barnes, J. E., Benson, A., Blain, A. W., Calzetti, D., Comastri, A., Capak, P., Carilli, C., Carlstrom, J. E., Carollo, C. M., Colbert, J., Daddi, E., Ellis, R. S., Elvis, M., Ewald, S. P., Fall, M., Franceschini, A., Giavalisco, M., Green, W., Griffiths, R. E., Guzzo, L., Hasinger, G., Impey, C., Kneib, J.-P., Koda, J., Koekemoer, A., Lefevre, O., Lilly, S., Liu, C. T., McCracken, H. J., Massey, R., Mellier, Y., Miyazaki, S., Mobasher, B., Mould, J., Norman, C., Refregier, A., Renzini, A., Rhodes, J., Rich, M., Sanders, D. B., Schiminovich, D., Schinnerer, E., Scodeggio, M., Sheth, K., Shopbell, P. L., Taniguchi, Y., Tyson, N. D., Urry, C. M., Van Waerbeke, L., Vettolani, P., White, S. D. M., and Yan, L. (2007a). COSMOS: Hubble Space Telescope Observations. *ApJS*, 172:38–45.

Scoville, N., Abraham, R. G., Aussel, H., Barnes, J. E., Benson, A., Blain, A. W., Calzetti, D., Comastri, A., Capak, P., Carilli, C., Carlstrom, J. E., Carollo, C. M., Colbert, J., Daddi, E., Ellis, R. S., Elvis, M., Ewald, S. P., Fall, M., Franceschini, A., Giavalisco, M., Green, W., Griffiths, R. E., Guzzo, L., Hasinger, G., Impey, C., Kneib, J.-P., Koda, J., Koekemoer, A., Lefevre, O., Lilly, S., Liu, C. T., McCracken, H. J., Massey, R., Mellier, Y., Miyazaki, S., Mobasher, B., Mould, J., Norman, C., Refregier, A., Renzini, A., Rhodes, J., Rich, M., Sanders, D. B., Schiminovich, D., Schinnerer, E., Scodeggio, M., Sheth, K., Shopbell, P. L., Taniguchi, Y., Tyson, N. D., Urry, C. M., Van Waerbeke, L., Vettolani, P., White, S. D. M., and Yan, L. (2007b). COSMOS: Hubble Space Telescope Observations. *ApJS*, 172:38–45.

Scoville, N., Aussel, H., Benson, A., Blain, A., Calzetti, D., Capak, P., Ellis, R. S., El-Zant, A., Finoguenov, A., Giavalisco, M., Guzzo, L., Hasinger, G., Koda, J., Le Fèvre, O., Massey, R., McCracken, H. J., Mobasher, B., Renzini, A., Rhodes, J., Salvato, M., Sanders, D. B., Sasaki, S. S., Schinnerer, E., Sheth, K., Shopbell, P. L., Taniguchi, Y., Taylor, J. E., and Thompson, D. J. (2007c). Large Structures and Galaxy Evolution in COSMOS at $z < 1.1$. *ApJS*, 172:150–181.

Scoville, N., Aussel, H., Brusa, M., Capak, P., Carollo, C. M., Elvis, M., Giavalisco, M., Guzzo, L., Hasinger, G., Impey, C., Kneib, J.-P., LeFevre, O., Lilly, S. J., Mobasher, B., Renzini, A., Rich, R. M., Sanders, D. B., Schinnerer, E., Schminovich, D., Shopbell, P., Taniguchi, Y., and Tyson, N. D. (2007d). The Cosmic Evolution Survey (COSMOS): Overview. *ApJS*, 172:1–8.

Serjeant, S., Gruppioni, C., and Oliver, S. (2002). The local star formation rate and radio luminosity density. *MNRAS*, 330:621–624.

Shapley, A. E., Steidel, C. C., Pettini, M., and Adelberger, K. L. (2003). Rest-Frame Ultraviolet Spectra of z˜3 Lyman Break Galaxies. *ApJ*, 588:65–89.

Sheth, K., Blain, A. W., Kneib, J.-P., Frayer, D. T., van der Werf, P. P., and Knudsen, K. K. (2004). Detection of CO from SMM J16359+6612, the Multiply Imaged Submillimeter Galaxy behind A2218. *ApJ*, 614:L5–L8.

Siringo, G., Kreysa, E., Kovács, A., Schuller, F., Weiß, A., Esch, W., Gemünd, H.-P., Jethava, N., Lundershausen, G., Colin, A., Güsten, R., Menten, K. M., Beelen, A., Bertoldi, F., Beeman, J. W., and Haller, E. E. (2009). The Large APEX BOlometer CAmera LABOCA. *A&A*, 497:945–962.

Smolčić, V., Capak, P., Ilbert, O., Blain, A. W., Salvato, M., Aretxaga, I., Schinnerer, E., Masters, D., Morić, I., Riechers, D. A., Sheth, K., Aravena, M., Aussel, H., Aguirre, J., Berta,

S., Carilli, C. L., Civano, F., Fazio, G., Huang, J., Hughes, D., Kartaltepe, J., Koekemoer, A. M., Kneib, J.-P., LeFloc'h, E., Lutz, D., McCracken, H., Mobasher, B., Murphy, E., Pozzi, F., Riguccini, L., Sanders, D. B., Sargent, M., Scott, K. S., Scoville, N. Z., Taniguchi, Y., Thompson, D., Willott, C., Wilson, G., and Yun, M. (2011). The Redshift and Nature of AzTEC/COSMOS 1: A Starburst Galaxy at z = 4.6. *ApJ*, 731:L27.

Smolčić, V., Schinnerer, E., Zamorani, G., Bell, E. F., Bondi, M., Carilli, C. L., Ciliegi, P., Mobasher, B., Paglione, T., Scodeggio, M., and Scoville, N. (2009a). The Dust-Unbiased Cosmic Star-Formation History from the 20 CM VLA-COSMOS Survey. *ApJ*, 690:610–618.

Smolčić, V., Zamorani, G., Schinnerer, E., Bardelli, S., Bondi, M., Bîrzan, L., Carilli, C. L., Ciliegi, P., Elvis, M., Impey, C. D., Koekemoer, A. M., Merloni, A., Paglione, T., Salvato, M., Scodeggio, M., Scoville, N., and Trump, J. R. (2009b). Cosmic Evolution of Radio Selected Active Galactic Nuclei in the Cosmos Field. *ApJ*, 696:24–39.

Smoot, G. F., Bennett, C. L., Kogut, A., Wright, E. L., Aymon, J., Boggess, N. W., Cheng, E. S., de Amici, G., Gulkis, S., Hauser, M. G., Hinshaw, G., Jackson, P. D., Janssen, M., Kaita, E., Kelsall, T., Keegstra, P., Lineweaver, C., Loewenstein, K., Lubin, P., Mather, J., Meyer, S. S., Moseley, S. H., Murdock, T., Rokke, L., Silverberg, R. F., Tenorio, L., Weiss, R., and Wilkinson, D. T. (1992). Structure in the COBE differential microwave radiometer first-year maps. *ApJ*, 396:L1–L5.

Solomon, P. M. and Vanden Bout, P. A. (2005). Molecular Gas at High Redshift. *ARA&A*, 43:677–725.

Somerville, R. S., Hopkins, P. F., Cox, T. J., Robertson, B. E., and Hernquist, L. (2008). A semi-analytic model for the co-evolution of galaxies, black holes and active galactic nuclei. *MNRAS*, 391:481–506.

Spergel, D. N., Bean, R., Doré, O., Nolta, M. R., Bennett, C. L., Dunkley, J., Hinshaw, G., Jarosik, N., Komatsu, E., Page, L., Peiris, H. V., Verde, L., Halpern, M., Hill, R. S., Kogut, A., Limon, M., Meyer, S. S., Odegard, N., Tucker, G. S., Weiland, J. L., Wollack, E., and Wright, E. L. (2007). Three-Year Wilkinson Microwave Anisotropy Probe (WMAP) Observations: Implications for Cosmology. *ApJS*, 170:377–408.

Spergel, D. N., Verde, L., Peiris, H. V., Komatsu, E., Nolta, M. R., Bennett, C. L., Halpern, M., Hinshaw, G., Jarosik, N., Kogut, A., Limon, M., Meyer, S. S., Page, L., Tucker, G. S., Weiland, J. L., Wollack, E., and Wright, E. L. (2003). First-Year Wilkinson Microwave Anisotropy Probe (WMAP) Observations: Determination of Cosmological Parameters. *ApJS*, 148:175–194.

Springel, V., Frenk, C. S., and White, S. D. M. (2006). The large-scale structure of the Universe. *Nature*, 440:1137–1144.

Springel, V. and Hernquist, L. (2003). The history of star formation in a Λ cold dark matter universe. *MNRAS*, 339:312–334.

Springel, V., White, S. D. M., Jenkins, A., Frenk, C. S., Yoshida, N., Gao, L., Navarro, J., Thacker, R., Croton, D., Helly, J., Peacock, J. A., Cole, S., Thomas, P., Couchman, H., Evrard, A., Colberg, J., and Pearce, F. (2005). Simulations of the formation, evolution and clustering of galaxies and quasars. *Nature*, 435:629–636.

Stacey, G. J., Hailey-Dunsheath, S., Ferkinhoff, C., Nikola, T., Parshley, S. C., Benford, D. J., Staguhn, J. G., and Fiolet, N. (2010). A 158 μm [C II] Line Survey of Galaxies at z$\sim$1-2: An Indicator of Star Formation in the Early Universe. *ApJ*, 724:957–974.

Staguhn, J., Allen, C., Benford, D., Sharp, E., Ames, T., Arendt, R., Chuss, D., Dwek, E., Kovacs, A., Maher, S., Marx, C., Miller, T., Moseley, S. H., Navarro, S., Sievers, A., Voellmer, G., and Wollack, E. (2008). GISMO, a 2 mm Bolometer Camera Optimized for the Study of High Redshift Galaxies. *Journal of Low Temperature Physics*, 151:709–714.

Stark, D. P., Ellis, R. S., Bunker, A., Bundy, K., Targett, T., Benson, A., and Lacy, M. (2009). The Evolutionary History of Lyman Break Galaxies Between Redshift 4 and 6: Observing Successive Generations of Massive Galaxies in Formation. *ApJ*, 697:1493–1511.

Steidel, C. C., Giavalisco, M., Pettini, M., Dickinson, M., and Adelberger, K. L. (1996). Spectroscopic Confirmation of a Population of Normal Star-forming Galaxies at Redshifts z$>$3. *ApJ*, 462:L17+.

Steidel, C. C., Pettini, M., and Hamilton, D. (1995). Lyman Imaging of High-Redshift Galaxies.III.New Observations of Four QSO Fields. *AJ*, 110:2519–+.

Strateva, I., Ivezić, Ž., Knapp, G. R., Narayanan, V. K., Strauss, M. A., Gunn, J. E., Lupton, R. H., Schlegel, D., Bahcall, N. A., Brinkmann, J., Brunner, R. J., Budavári, T., Csabai, I., Castander, F. J., Doi, M., Fukugita, M., Győry, Z., Hamabe, M., Hennessy, G., Ichikawa, T., Kunszt, P. Z., Lamb, D. Q., McKay, T. A., Okamura, S., Racusin, J., Sekiguchi, M., Schneider, D. P., Shimasaku, K., and York, D. (2001). Color Separation of Galaxy Types in the Sloan Digital Sky Survey Imaging Data. *AJ*, 122:1861–1874.

Tacconi, L. J., Genzel, R., Neri, R., Cox, P., Cooper, M. C., Shapiro, K., Bolatto, A., Bouché, N., Bournaud, F., Burkert, A., Combes, F., Comerford, J., Davis, M., Schreiber, N. M. F., Garcia-Burillo, S., Gracia-Carpio, J., Lutz, D., Naab, T., Omont, A., Shapley, A., Sternberg, A., and Weiner, B. (2010). High molecular gas fractions in normal massive star-forming galaxies in the young Universe. *Nature*, 463:781–784.

Tacconi, L. J., Genzel, R., Smail, I., Neri, R., Chapman, S. C., Ivison, R. J., Blain, A., Cox, P., Omont, A., Bertoldi, F., Greve, T., Förster Schreiber, N. M., Genel, S., Lutz, D., Swinbank, A. M., Shapley, A. E., Erb, D. K., Cimatti, A., Daddi, E., and Baker, A. J. (2008). Submillimeter Galaxies at z$\sim$2: Evidence for Major Mergers and Constraints on Lifetimes, IMF, and CO-H_2 Conversion Factor. *ApJ*, 680:246–262.

Tacconi, L. J., Neri, R., Chapman, S. C., Genzel, R., Smail, I., Ivison, R. J., Bertoldi, F., Blain, A., Cox, P., Greve, T., and Omont, A. (2006). High-Resolution Millimeter Imaging of Submillimeter Galaxies. *ApJ*, 640:228–240.

Taniguchi, Y., Scoville, N., Murayama, T., Sanders, D. B., Mobasher, B., Aussel, H., Capak, P., Ajiki, M., Miyazaki, S., Komiyama, Y., Shioya, Y., Nagao, T., Sasaki, S. S., Koda, J., Carilli, C., Giavalisco, M., Guzzo, L., Hasinger, G., Impey, C., LeFevre, O., Lilly, S., Renzini, A., Rich, M., Schinnerer, E., Shopbell, P., Kaifu, N., Karoji, H., Arimoto, N., Okamura, S., and Ohta, K. (2007). The Cosmic Evolution Survey (COSMOS): Subaru Observations of the HST Cosmos Field. *ApJS*, 172:9–28.

Taylor, E. N., Franx, M., van Dokkum, P. G., Bell, E. F., Brammer, G. B., Rudnick, G., Wuyts, S., Gawiser, E., Lira, P., Urry, C. M., and Rix, H. (2009). The Rise of Massive Red Galaxies: The Color-Magnitude and Color-Stellar Mass Diagrams for $z_{\rm phot} \lesssim 2$ from the Multiwavelength Survey by Yale-Chile. *ApJ*, 694:1171–1199.

Thompson, A. R., Clark, B. G., Wade, C. M., and Napier, P. J. (1980). The Very Large Array. *ApJS*, 44:151–167.

Treister, E. and Urry, C. M. (2005). Active Galactic Nuclei Unification and the X-Ray Background. *ApJ*, 630:115–121.

Trump, J. R., Impey, C. D., McCarthy, P. J., Elvis, M., Huchra, J. P., Brusa, M., Hasinger, G., Schinnerer, E., Capak, P., Lilly, S. J., and Scoville, N. Z. (2007). Magellan Spectroscopy of AGN Candidates in the COSMOS Field. *ApJS*, 172:383–395.

Ueda, Y., Akiyama, M., Ohta, K., and Miyaji, T. (2003). Cosmological Evolution of the Hard X-Ray Active Galactic Nucleus Luminosity Function and the Origin of the Hard X-Ray Background. *ApJ*, 598:886–908.

Urry, C. M. and Padovani, P. (1995). Unified Schemes for Radio-Loud Active Galactic Nuclei. *PASP*, 107:803–+.

Voelk, H. J. (1989). The correlation between radio and far-infrared emission for disk galaxies - A calorimeter theory. *A&A*, 218:67–70.

Walcher, C. J., Lamareille, F., Vergani, D., Arnouts, S., Buat, V., Charlot, S., Tresse, L., Le Fèvre, O., Bolzonella, M., Brinchmann, J., Pozzetti, L., Zamorani, G., Bottini, D., Garilli, B., Le Brun, V., Maccagni, D., Milliard, B., Scaramella, R., Scodeggio, M., Vettolani, G., Zanichelli, A., Adami, C., Bardelli, S., Cappi, A., Ciliegi, P., Contini, T., Franzetti, P., Foucaud, S., Gavignaud, I., Guzzo, L., Ilbert, O., Iovino, A., McCracken, H. J., Marano, B., Marinoni, C., Mazure, A., Meneux, B., Merighi, R., Paltani, S., Pellò, R., Pollo, A., Radovich, M., Zucca, E., Lonsdale, C., and Martin, C. (2008). The VVDS-SWIRE-GALEX-CFHTLS surveys: physical properties of galaxies at z below 1.2 from photometric data. *A&A*, 491:713–730.

Walter, F., Bertoldi, F., Carilli, C., Cox, P., Lo, K. Y., Neri, R., Fan, X., Omont, A., Strauss, M. A., and Menten, K. M. (2003). Molecular gas in the host galaxy of a quasar at redshift z = 6.42. *Nature*, 424:406–408.

Weedman, D. W., Hao, L., Higdon, S. J. U., Devost, D., Wu, Y., Charmandaris, V., Brandl, B., Bass, E., and Houck, J. R. (2005). Mid-Infrared Spectra of Classical AGNs Observed with the Spitzer Space Telescope. *ApJ*, 633:706–716.

Weiß, A., Downes, D., Neri, R., Walter, F., Henkel, C., Wilner, D. J., Wagg, J., and Wiklind, T. (2007). Highly-excited CO emission in APM 08279+5255 at z = 3.9. *A&A*, 467:955–969.

Weiß, A., Downes, D., Walter, F., and Henkel, C. (2005). Multiple CO lines in SMM J16359+6612 - further evidence for a merger. *A&A*, 440:L45–L49.

Weiß, A., Ivison, R. J., Downes, D., Walter, F., Cirasuolo, M., and Menten, K. M. (2009a). First Redshift Determination of an Optically/Ultraviolet Faint Submillimeter Galaxy Using CO Emission Lines. *ApJ*, 705:L45–L47.

Weiß, A., Kovács, A., Coppin, K., Greve, T. R., Walter, F., Smail, I., Dunlop, J. S., Knudsen, K. K., Alexander, D. M., Bertoldi, F., Brandt, W. N., Chapman, S. C., Cox, P., Dannerbauer, H., De Breuck, C., Gawiser, E., Ivison, R. J., Lutz, D., Menten, K. M., Koekemoer, A. M., Kreysa, E., Kurczynski, P., Rix, H.-W., Schinnerer, E., and van der Werf, P. P. (2009b). The Large Apex Bolometer Camera Survey of the Extended Chandra Deep Field South. *ApJ*, 707:1201–1216.

White, R. L., Helfand, D. J., Becker, R. H., Glikman, E., and de Vries, W. (2007). Signals from the Noise: Image Stacking for Quasars in the FIRST Survey. *ApJ*, 654:99–114.

White, S. D. M. and Rees, M. J. (1978). Core condensation in heavy halos - A two-stage theory for galaxy formation and clustering. *MNRAS*, 183:341–358.

Wilkins, S. M., Bunker, A. J., Ellis, R. S., Stark, D., Stanway, E. R., Chiu, K., Lorenzoni, S., and Jarvis, M. J. (2010). Probing $\sim L_*$ Lyman-break galaxies at $z \sim 7$ in GOODS-South with WFC3 on Hubble Space Telescope. *MNRAS*, 403:938–944.

Wilkins, S. M., Hopkins, A. M., Trentham, N., and Tojeiro, R. (2008). Extragalactic constraints on the initial mass function. *MNRAS*, 391:363–368.

Williams, R. E., Blacker, B., Dickinson, M., Dixon, W. V. D., Ferguson, H. C., Fruchter, A. S., Giavalisco, M., Gilliland, R. L., Heyer, I., Katsanis, R., Levay, Z., Lucas, R. A., McElroy, D. B., Petro, L., Postman, M., Adorf, H.-M., and Hook, R. (1996). The Hubble Deep Field: Observations, Data Reduction, and Galaxy Photometry. *AJ*, 112:1335–+.

Williams, R. J., Quadri, R. F., and Franx, M. (2011). The Diminishing Importance of Major Galaxy Mergers at Higher Redshifts. *ApJ*, 738:L25+.

Williams, R. J., Quadri, R. F., Franx, M., van Dokkum, P., and Labbé, I. (2009). Detection of Quiescent Galaxies in a Bicolor Sequence from Z = 0-2. *ApJ*, 691:1879–1895.

Willott, C. J., Rawlings, S., Blundell, K. M., Lacy, M., and Eales, S. A. (2001). The radio luminosity function from the low-frequency 3CRR, 6CE and 7CRS complete samples. *MNRAS*, 322:536–552.

Wilson, C. D., Petitpas, G. R., Iono, D., Baker, A. J., Peck, A. B., Krips, M., Warren, B., Golding, J., Atkinson, A., Armus, L., Cox, T. J., Ho, P., Juvela, M., Matsushita, S., Mihos, J. C., Pihlstrom, Y., and Yun, M. S. (2008a). Luminous Infrared Galaxies with the Submillimeter Array. I. Survey Overview and the Central Gas to Dust Ratio. *ApJS*, 178:189–224.

Wilson, G. W., Austermann, J. E., Perera, T. A., Scott, K. S., Ade, P. A. R., Bock, J. J., Glenn, J., Golwala, S. R., Kim, S., Kang, Y., Lydon, D., Mauskopf, P. D., Predmore, C. R., Roberts, C. M., Souccar, K., and Yun, M. S. (2008b). The AzTEC mm-wavelength camera. *MNRAS*, 386:807–818.

Windhorst, R. A., van Heerde, G. M., and Katgert, P. (1984). A deep Westerbork survey of areas with multicolor Mayall 4 M plates. I - The 1412 MHz catalogue, source counts and angular size statistics. *A&AS*, 58:1–37.

Wolf, C., Dye, S., Kleinheinrich, M., Meisenheimer, K., Rix, H.-W., and Wisotzki, L. (2001). Deep BVR photometry of the Chandra Deep Field South from the COMBO-17 survey. *A&A*, 377:442–449.

Wyder, T. K., Martin, D. C., Schiminovich, D., Seibert, M., Budavári, T., Treyer, M. A., Barlow, T. A., Forster, K., Friedman, P. G., Morrissey, P., Neff, S. G., Small, T., Bianchi, L., Donas, J., Heckman, T. M., Lee, Y., Madore, B. F., Milliard, B., Rich, R. M., Szalay, A. S., Welsh, B. Y., and Yi, S. K. (2007). The UV-Optical Galaxy Color-Magnitude Diagram. I. Basic Properties. *ApJS*, 173:293–314.

Yabe, K., Ohta, K., Iwata, I., Sawicki, M., Tamura, N., Akiyama, M., and Aoki, K. (2009). The Stellar Populations of Lyman Break Galaxies at z ˜ 5. *ApJ*, 693:507–533.

York, D. G., Adelman, J., Anderson, Jr., J. E., Anderson, S. F., Annis, J., Bahcall, N. A., Bakken, J. A., Barkhouser, R., Bastian, S., Berman, E., Boroski, W. N., Bracker, S., Briegel, C., Briggs, J. W., Brinkmann, J., Brunner, R., Burles, S., Carey, L., Carr, M. A., Castander, F. J., Chen, B., Colestock, P. L., Connolly, A. J., Crocker, J. H., Csabai, I., Czarapata, P. C., Davis, J. E., Doi, M., Dombeck, T., Eisenstein, D., Ellman, N., Elms, B. R., Evans, M. L., Fan, X., Federwitz, G. R., Fiscelli, L., Friedman, S., Frieman, J. A., Fukugita, M., Gillespie, B., Gunn, J. E., Gurbani, V. K., de Haas, E., Haldeman, M., Harris, F. H., Hayes, J., Heckman, T. M., Hennessy, G. S., Hindsley, R. B., Holm, S., Holmgren, D. J., Huang, C.-h., Hull, C., Husby, D., Ichikawa, S.-I., Ichikawa, T., Ivezić, Ž., Kent, S., Kim, R. S. J., Kinney, E., Klaene, M., Kleinman, A. N., Kleinman, S., Knapp, G. R., Korienek, J., Kron, R. G., Kunszt, P. Z., Lamb, D. Q., Lee, B., Leger, R. F., Limmongkol, S., Lindenmeyer, C., Long, D. C., Loomis, C., Loveday, J., Lucinio, R., Lupton, R. H., MacKinnon, B., Mannery, E. J., Mantsch, P. M., Margon, B., McGehee, P., McKay, T. A., Meiksin, A., Merelli, A., Monet, D. G., Munn, J. A., Narayanan, V. K., Nash, T., Neilsen, E., Neswold, R., Newberg, H. J., Nichol, R. C., Nicinski, T., Nonino, M., Okada, N., Okamura, S., Ostriker, J. P., Owen, R., Pauls, A. G., Peoples, J., Peterson, R. L., Petravick, D., Pier, J. R., Pope, A., Pordes, R., Prosapio, A., Rechenmacher, R., Quinn, T. R., Richards, G. T., Richmond, M. W., Rivetta, C. H., Rockosi, C. M., Ruthmansdorfer, K., Sandford, D., Schlegel, D. J., Schneider, D. P., Sekiguchi, M., Sergey, G., Shimasaku, K., Siegmund, W. A., Smee, S., Smith, J. A., Snedden, S., Stone, R., Stoughton, C., Strauss, M. A., Stubbs, C., SubbaRao, M., Szalay, A. S., Szapudi, I., Szokoly, G. P., Thakar, A. R., Tremonti, C., Tucker, D. L., Uomoto, A., Vanden Berk, D., Vogeley, M. S., Waddell, P., Wang, S.-i., Watanabe, M., Weinberg, D. H., Yanny, B., and Yasuda, N. (2000). The Sloan Digital Sky Survey: Technical Summary. *AJ*, 120:1579–1587.

Younger, J. D., Fazio, G. G., Huang, J.-S., Yun, M. S., Wilson, G. W., Ashby, M. L. N., Gurwell, M. A., Lai, K., Peck, A. B., Petitpas, G. R., Wilner, D. J., Iono, D., Kohno, K., Kawabe, R., Hughes, D. H., Aretxaga, I., Webb, T., Martínez-Sansigre, A., Kim, S., Scott, K. S., Austermann, J., Perera, T., Lowenthal, J. D., Schinnerer, E., and Smolčić, V. (2007). Evidence for a Population of High-Redshift Submillimeter Galaxies from Interferometric Imaging. *ApJ*, 671:1531–1537.

Yun, M. S., Reddy, N. A., and Condon, J. J. (2001). Radio Properties of Infrared-selected Galaxies in the IRAS 2 Jy Sample. *ApJ*, 554:803–822.

Zamojski, M. A., Schiminovich, D., Rich, R. M., Mobasher, B., Koekemoer, A. M., Capak, P., Taniguchi, Y., Sasaki, S. S., McCracken, H. J., Mellier, Y., Bertin, E., Aussel, H., Sanders, D. B., Le Fèvre, O., Ilbert, O., Salvato, M., Thompson, D. J., Kartaltepe, J. S., Scoville, N., Barlow, T. A., Forster, K., Friedman, P. G., Martin, D. C., Morrissey, P., Neff, S. G., Seibert,

M., Small, T., Wyder, T. K., Bianchi, L., Donas, J., Heckman, T. M., Lee, Y.-W., Madore, B. F., Milliard, B., Szalay, A. S., Welsh, B. Y., and Yi, S. K. (2007). Deep GALEX Imaging of the COSMOS HST Field: A First Look at the Morphology of z ˜ 0.7 Star-forming Galaxies. *ApJS*, 172:468–493.

Zheng, X. Z., Bell, E. F., Papovich, C., Wolf, C., Meisenheimer, K., Rix, H.-W., Rieke, G. H., and Somerville, R. (2007a). The Dependence of Star Formation on Galaxy Stellar Mass. *ApJ*, 661:L41–L44.

Zheng, X. Z., Bell, E. F., Rix, H.-W., Papovich, C., Le Floc'h, E., Rieke, G. H., and Pérez-González, P. G. (2006). Detecting Faint Galaxies by Stacking at 24 μm. *ApJ*, 640:784–800.

Zheng, X. Z., Dole, H., Bell, E. F., Le Floc'h, E., Rieke, G. H., Rix, H.-W., and Schiminovich, D. (2007b). Infrared Spectral Energy Distributions of z ˜ 0.7 Star-forming Galaxies. *ApJ*, 670:301–312.

Zucca, E., Ilbert, O., Bardelli, S., Tresse, L., Zamorani, G., Arnouts, S., Pozzetti, L., Bolzonella, M., McCracken, H. J., Bottini, D., Garilli, B., Le Brun, V., Le Fèvre, O., Maccagni, D., Picat, J. P., Scaramella, R., Scodeggio, M., Vettolani, G., Zanichelli, A., Adami, C., Arnaboldi, M., Cappi, A., Charlot, S., Ciliegi, P., Contini, T., Foucaud, S., Franzetti, P., Gavignaud, I., Guzzo, L., Iovino, A., Marano, B., Marinoni, C., Mazure, A., Meneux, B., Merighi, R., Paltani, S., Pellò, R., Pollo, A., Radovich, M., Bondi, M., Bongiorno, A., Busarello, G., Cucciati, O., Gregorini, L., Lamareille, F., Mathez, G., Mellier, Y., Merluzzi, P., Ripepi, V., and Rizzo, D. (2006). The VIMOS VLT Deep Survey. Evolution of the luminosity functions by galaxy type up to z = 1.5 from first epoch data. *A&A*, 455:879–890.